Transactions of the ASME, Journal of Heat Transfer (ISSN 0022-1481) is published monthly by The American Society of Mechanical Engineers, Three Park Avenue, New York, NY 10016. Periodicals postage paid at New York, NY and additional mailing offices. POSTMASTER: Send address changes to Transactions of the ASME, Journal of Heat Transfer, c/o THE AMERICAN SOCIETY OF MECHANICAL ENGINEERS, 22 Law Drive, Box 2300, Fairfield, NJ 07007-2300. **CHANGES OF ADDRESS** must be received at Society headquarters seven weeks before they are to be effective. Please send old label and new address. **STATEMENT from By-Laws.** The Society shall not be responsible for statements or opinions advanced in papers or ... printed in its publications (B7.1, Para. 3).

Journal of Heat Transfer

Published Monthly by ASME

VOLUME 127 • NUMBER 10 • OCTOBER 2005

RESEARCH PAPERS

Bubbles, Particles and Droplets

1077 **An Experimental Investigation of the Influence of Gas and Solid Particle Interaction on the Heat Transfer Effectiveness of a Falling-Bed Heat Exchanger**
Matthew J. Frain, David P. Schmidt, and Woodrow A. Fiveland

1087 **Enhancement of Heat Transfer by an Electric Field for a Drop Translating at Intermediate Reynolds Number**
Rajkumar Subramanian and M. A. Jog

Micro/Nanoscale Heat Transfer

1096 **A Theory of Film Condensation in Horizontal Noncircular Section Microchannels**
Hua Sheng Wang and John W. Rose

1106 **Reduced Pressure Boiling Heat Transfer in Rectangular Microchannels With Interconnected Reentrant Cavities**
Ali Koşar, Chih-Jung Kuo, and Yoav Peles

Radiative Heat Transfer

1115 **Radiative Heat Transfer Using Isotropic Scaling Approximation: Application to Fibrous Medium**
Hervé Thierry Kamdem Tagne and Dominique Doermann Baillis

1124 **Smoothing Monte Carlo Exchange Factors Through Constrained Maximum Likelihood Estimation**
K. J. Daun, D. P. Morton, and J. R. Howell

1129 **Monte Carlo Simulation of Silicon Nanowire Thermal Conductivity**
Yunfei Chen, Deyu Li, Jennifer R. Lukes, and Arun Majumdar

Forced Convection

1138 **Accurate Boundary Element Solutions for Highly Convective Unsteady Heat Flows**
M. M. Grigoriev and G. F. Dargush

1151 **Turbulent Three-Dimensional Air Flow and Heat Transfer in a Cross-Corrugated Triangular Duct**
Li-Zhi Zhang

Heat Transfer in Manufacturing

1159 **Boundary/Finite Element Modeling of Three-Dimensional Electromagnetic Heating During Microwave Food Processing**
Y. Huo and B. Q. Li

1167 **Improved Two-Temperature Model and Its Application in Ultrashort Laser Heating of Metal Films**
Lan Jiang and Hai-Lung Tsai

(Contents continued on inside back cover)

This journal is printed on acid-free paper, which exceeds the ANSI Z39.48-1992 specification for permanence of paper and library materials. ♾™
♻ 85% recycled content, including 10% post-consumer fibers.

(**Contents continued**)

Journal of Heat Transfer **Volume 127, Number 10** **OCTOBER 2005**

TECHNICAL BRIEFS

1174 Frost-Air Interface Characterization Under Natural Convection
Y. L. Hao, J. Iragorry, and Y.-X. Tao

1181 Natural Convection Patterns in Right-Angled Triangular Cavities With Heated Vertical Sides and Cooled Hypotenuses
El Hassan Ridouane, Antonio Campo, and Jane Y. Chang

ANNOUNCEMENT

1187 9th Joint AIAA/ASME Thermophysics and Heat Transfer Conference

The ASME Journal of Heat Transfer is abstracted and indexed in the following:

Applied Science and Technology Index, Chemical Abstracts, Chemical Engineering and Biotechnology Abstracts (Electronic equivalent of Process and Chemical Engineering), Civil Engineering Abstracts, Compendex (The electronic equivalent of Engineering Index), Corrosion Abstracts, Current Contents, E & P Health, Safety, and Environment, Ei EncompassLit, Engineered Materials Abstracts, Engineering Index, Enviroline (The electronic equivalent of Environment Abstracts), Environment Abstracts, Environmental Engineering Abstracts, Environmental Science and Pollution Management, Fluidex, Fuel and Energy Abstracts, Index to Scientific Reviews, INSPEC, International Building Services Abstracts, Mechanical & Transportation Engineering Abstracts, Mechanical Engineering Abstracts, METADEX (The electronic equivalent of Metals Abstracts and Alloys Index), Petroleum Abstracts, Process and Chemical Engineering, Referativnyi Zhurnal, Science Citation Index, SciSearch (The electronic equivalent of Science Citation Index), Theoretical Chemical Engineering

An Experimental Investigation of the Influence of Gas and Solid Particle Interaction on the Heat Transfer Effectiveness of a Falling-Bed Heat Exchanger

Matthew J. Frain

David P. Schmidt
e-mail: schmidt@ecs.umass.edu

Department of Mechanical and Industrial Engineering, University of Massachusetts Amherst, Engineering Laboratory, Box 32210, Amherst, MA 01003-2210

Woodrow A. Fiveland
ALSTOM Power Inc., 2000 Day Hill Road, Windsor, CT 06095

The objective of this investigation is to quantify and understand the performance of falling-bed heat exchangers. Experimental steady-state heat transfer data, whose quality is demonstrated with an accurate energy balance between the gas and particle streams, are presented. Measured temperatures, pressures, and overall heat transfer rates are compared to predicted values from a one-dimensional analytical model, and the capabilities and deficiencies of the model are discussed. In addition, the effect of a particle distributor on the performance of the falling-bed heat exchanger is measured. While the model is shown to be unable to provide a quantitatively accurate prediction of the performance of the heat exchanger, it does provide an estimate of the maximum possible effectiveness of the heat exchanger. A simple particle distributor is shown to provide relatively poor effectiveness, while the use of a more complex distributor causes the effectiveness of the heat exchanger to approach the upper bound. The combination of experimental data and model results offers useful insight for developing falling-bed heat exchangers and provides a useful test case for future modeling efforts. [DOI: 10.1115/1.2033904]

Keywords: Heat Exchanger, Falling-Bed, Solid Particles, Distributor, Effectiveness

1 Introduction

Heat exchangers incorporating fixed, moving, and fluidized beds of solid particles are commonly used in industrial applications. These arrangements provide very large areas for heat exchange in a small volume, and make for very compact and effective heat exchangers. The ability to predict the heat transfer rate between the gas and particles accurately is a critical factor in the design process for chemical reactors and heat exchangers.

The subject of the current research is a method of heat exchange between gas and solids commonly called a falling bed. In this arrangement, solid particles fall through a vertical column against a counterflowing gas stream flowing with a superficial velocity less than the terminal velocity of the particle. Heat is exchanged between the falling particles and rising gas. This arrangement has been proposed for heat recovery and regeneration in power plants and other process applications.

The heat transfer between the gas and solid particles in falling-bed heat exchangers, as well as between a continuous fluid and dispersed droplets in liquid-liquid direct contact heat exchangers and spray columns, has typically been modeled by assuming steady-state and ideal, uniform, one-dimensional flow of the continuous fluid and the particle or droplets (Decher [1], Gat [2], Park et al. [3], Patnaik [4], Thayer and Sekins [5], Thynell and Manchor [6], Thynell and Patnaik [7]). This analytical model, sometimes called the plug flow model, is referred to as the uniform mixing model in this study.

In many previous experimental studies, the uniform mixing model has been assumed to describe the interaction between the continuous fluid and particles or droplets. This assumption is implied by the use of the log-mean temperature difference (LMTD), which is derived assuming a constant heat exchange coefficient U and isolated heat transfer between the two streams (Incropera and DeWitt [8]). With the measurement of the LMTD and the heat transfer rate q between the streams, the product of the apparent coefficient U and the area available for heat exchange A is determined. The coefficient U is finally isolated by a measurement or estimate of the surface area A, possibly by direct photographic measurement as in Pierce et al. [9]. This coefficient U is assumed to be equivalent to the heat transfer coefficient h for a spherical particle, and is usually presented in the form of a Nusselt number correlation as a function of measured or estimated particle relative Reynolds number. These experimental data are then compared to accepted Nusselt number correlations for single isolated spheres, such as that presented by Ranz and Marshall [10]. In most of these comparisons, the agreement between the experimental data and the single particle correlation is poor, with the measured values typically lower than the correlation at the same apparent Reynolds number. In some of the studies, it is acknowledged that the heat transfer between the streams was not isolated from the surroundings owing to steady-state or transient heat exchange with the walls of the test apparatus (Islam [11], Pierce et al. [9]). However, in several instances where the interaction between the dispersed and continuous phases was visible, it was observed that significant maldistributions in the flow of both phases were observed. These maldistributions were posited as the explanation for the poor agreement between the data and the isolated particle correlations (Inaba et al. [12], Pierce et al. [9]). These observed maldistributions, by themselves, indicate the use of the uniform mixing model is suspect. In Inaba et al. [12], direct measurements of the

Contributed by the Heat Transfer Division of ASME for publication in the JOURNAL OF HEAT TRANSFER. Manuscript received November 3, 2004; final manuscript received May 13, 2005. Review conducted by John H. Lienhard V.

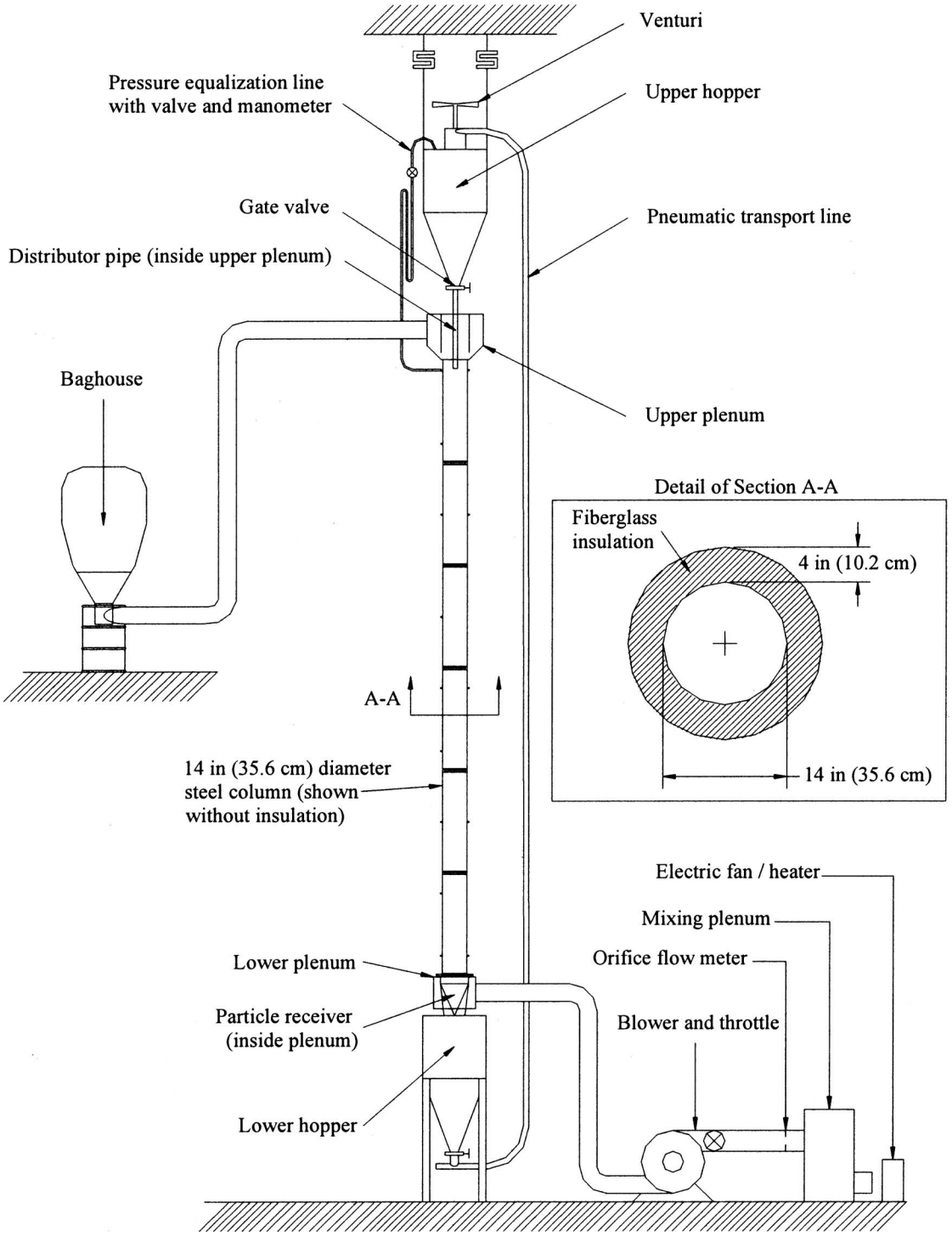

Fig. 1 ALSTOM power plant laboratory enhanced heat transfer (EHT) facility

dispersed and continuous phase velocity profiles suggested that the isolated particle correlations were appropriate if the entrainment of the continuous phase by the drag of the dispersed phase were accounted for.

The objective of this investigation is to quantify the performance of a falling-bed heat exchanger. Experimental data are presented for a test falling-bed heat exchanger. Measured temperatures, pressures, and overall heat transfer rates are reported and compared to predicted values from the analytical uniform mixing model. Both the capabilities and deficiencies of this model are discussed. In addition, the effect of a particle distributor on the performance of the falling-bed heat exchanger is measured.

2 Experimental Work

2.1 Apparatus. Experiments were performed using the ALSTOM Power Plant Laboratory Enhanced Heat Transfer (EHT) facility (Fig. 1). This facility was comprised of a test falling-bed heat exchanger utilizing a steel column constructed with six 1.5 m (5 ft.) sections of 0.45 mm (26 gauge) thick galvanized steel

stovepipe. When assembled, the column had a net height of 8.9 m (29.2 ft.). The inner diameter of this column was 35.6 cm (14 in.). A number of brass couplings were soldered onto the column to provide access for temperature and pressure instrumentation. The column was wrapped in two layers of 5.1 cm (2 in.) fiberglass blanket.

A 42 kW (75 hp) Lamson centrifugal blower provided the airflow. The air entering the column was heated primarily by the mechanical work of the blower. This heating was augmented with an electric fan and heater that warmed the air before it entered the blower. The air then passed through a duct into the lower plenum, then through a perforated plate that spanned the 10.2 cm (4 in.) gap between the bottom of the column and the particle receiver. The air flowed vertically through the column and exited into another plenum, from which the air was directed into baghouses to capture any entrained particles. The mass flow rate of the air was measured with an orifice flow meter located between the electric heater and the blower.

Particles were introduced from a hopper at the top of the column through a gate valve that controlled the mass flow rate of the particles. The particles fell from the pipe or distributor through the upward-flowing gas in the column and into a particle receiver located within the bottom plenum. The receiver directed the particles into a storage hopper below the lower plenum. The hoppers could accommodate approximately 900 kg (2000 lbs.) of solid particles, and the particle flow rate could be varied from zero to 1.5 kg/s (12,000 lb./h). Higher particle flow rates were possible, but at higher particle flow rates the test duration was so short that the column could not reach thermal equilibrium before the upper hopper emptied.

2.2 Particle Distributors. Two different arrangements were used to introduce particles into the column. In the first series of tests the particles were directed through the upper plenum through a 5.1 cm (2 in.) inner diameter Schedule 40 steel pipe that extended to a point just below the top of the column. In another series of tests, this steel pipe was replaced with an identical length of 5.1 cm (2 in.) inner diameter chlorinated polyvinyl chloride (CPVC) pipe. A particle distributor (Fig. 2), formed by a CPVC reducer and a basket formed by four crossed bands of 1.2 cm (0.5 in.) wide sheet metal, was attached to the end of this pipe in order to spread the particles into eight separate streams. This basket distributor was designed with the intention of improving the mixing and overall heat transfer rate between the gas and the particles.

2.3 Particle Properties. The solid material used in these tests was bauxite, a sintered ceramic material consisting mostly of alumina and silica compounds (Fig. 3). The volume mean diameter, determined by sieve analysis, was 700 μm. The density of the bauxite ρ_s, determined by helium displacement, was measured to be 3600 kg/m^3. The specific heat of bauxite c_s was determined by a composition analysis and calculation of the weighted average specific heats of the compounds that constitute bauxite using the method of mixtures. A simple polynomial expression [Eq. (1)] was determined from this analysis in order to integrate the heat pickup by the solids accurately over the possible range of particle temperatures T_s (300–400 K)

$$c_s(T_s) = -115.41 + 3.9413T_s - 0.0034T_s^2 \ (\text{J/kg K}) \qquad (1)$$

The thermal conductivity of the major constituent of bauxite, alumina, is approximately 36 W/m K. The Biot number for these particles, assuming the particle is falling at its terminal Reynolds number, was much less than 0.1, indicating that the particles were essentially isothermal.

2.4 Instrumentation. Temperatures of the gas and particles were measured at various positions in the test apparatus. Type K thermocouples with a resolution of ±1.0 K were used. The maximum air temperature entering the lower plenum was approximately 350 K (630 R), and the entering particles were at ambient room temperature, approximately 300 K (540 R).

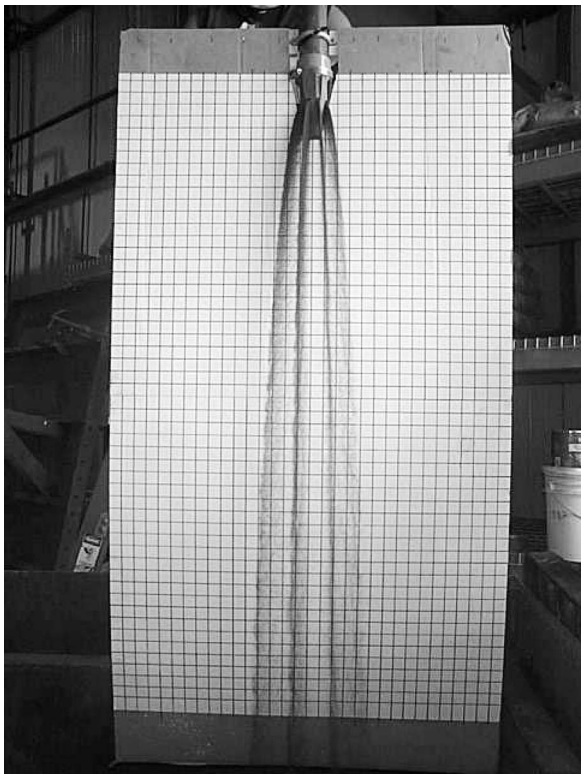

Fig. 2 Image of particle flow from the basket distributor. Grid squares are 2.54 cm (1 in.) wide.

The particle inlet temperature $T_{s,i}$ was measured with a 3.2 mm (1/8 in.) diameter thermocouple inserted through the wall of the upper hopper just above the gate valve. The temperature of the particles exiting the bottom of the column $T_{s,o}$ was the average of the measurements recorded from two 1.6 mm (1/16 in.) diameter thermocouples, each soldered into a half section of a 1.3 cm (0.5 in.) diameter copper pipe. The open side of this pipe received the falling particles, which immersed the thermocouple. These particles flowed along the pipe section and fell into the particle receiver. The particles in the pipe were constantly replaced by

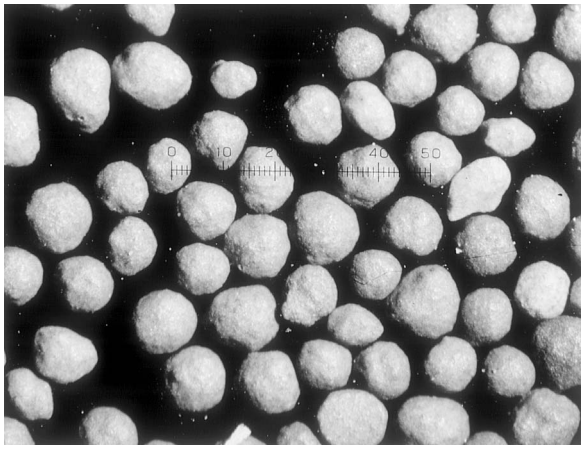

Fig. 3 Photograph of 700 μm bauxite. Scale gradation is in increments of 60 μm.

fresh falling particles.

A number of thermocouples were installed to measure the air temperature along the centerline of the column. During tests with the distributor installed, the thermocouples were shielded from the falling particles by a 9.5 mm (3/8 in.) diameter steel tube, cut in half lengthwise with the open side facing downward. The thermocouple was prevented from contacting the steel tube by small beads of room temperature vulcanizing (RTV) silicone compound. In tests where the distributor was removed, it was thought that these relatively large thermocouple arrangements would have interfered with the dense stream of particles passing down the center of the column. For this reason, these thermocouples were removed and were replaced with thin 0.8 mm (1/32 in.) diameter thermocouples passed through a 2.4 mm (3/32 in.) diameter steel tube to shield it from the falling particles. The tip of the thermocouple was bent downward under the steel tube to minimize particle contact with the falling particles. In addition to these centerline measurements, an unshielded 3.2 mm (1/8 in.) diameter thermocouple was installed at the 8.80 m (28.9 ft.) elevation with the tip inserted 8.9 cm (3.5 in.) in from the inner wall of the column. This thermocouple could not be inserted to the centerline of the column, as it would have interfered with the particle inlet distributor.

A separate series of six Type K thermocouples was also used. Five of these thermocouples, with diameters of 0.8 mm (1/32 in.), were used to construct a rake that could measure the radial gas temperature variation at a certain elevation in the column. These thermocouples were shielded from falling particles by a 6.4 mm (1/4 in.) diameter wooden dowel. The sixth thermocouple measured the air temperature upstream of the orifice flow meter.

Differential pressure measurements were made with a Pressure Systems Inc. ESP-16BP pressure scanner, incorporating piezoelectric pressure transducers with a static uncertainty of ±0.25 Pa. Differential pressure measurements were made for four separate sections of the column, and one overall measurement was made over the full height of the column. This scanner was also used to measure the pressure differential across the orifice flow meter and the static pressure relative to the atmospheric upstream of the orifice. The atmospheric pressure was measured with a Rosemount pressure transducer.

The mass flow rate of the particles was determined by measurements of the mass of the hopper, using two load cells. The rate of change of this measured mass over time determined the particle flow rate. The uncertainty in the particle mass flow rate was less than ±0.01 kg/s.

The thermocouples, load cells, and ambient atmospheric pressure measurements were scanned with a Fluke 2400B data scanner. The data were recorded over time with Labview software on a laptop computer. The output of the pressure scanner and the data acquisition board associated with the thermocouple rake and the orifice temperature were recorded with Labview on a separate computer.

2.5 Experimental Procedure. At the start of the test, the piezoelectric pressure transducers were zeroed against a common pressure reference. Data logging was started on both computers. The air heater and Lamson blower were then turned on and the throttle adjusted to maintain the desired air flow rate. Up to 2 h of blower operation were required for the gas temperatures to reach a steady value, due primarily to the need to heat the thick steel casing of the Lamson compressor stages and the steel walls of the lower plenum.

Once the temperatures stabilized, compressed air was passed through the cyclone inlet at the top of the upper hopper and exhausted from the outlet side of the venturi. The resistance of the venturi to the gas flow pressurized the upper hopper. The compressed air flow was adjusted until a manometer indicated zero static pressure differential between the upper hopper and the top of the column. This was done to prevent the backflow of hot gas within the column up through the distributor into the upper hopper.

Once the static pressure was equalized, the gate valve was opened and particles were introduced into the column. The test duration was determined by the mass flow rate of particles and by the amount of particles in the upper hopper. At the end of the particle flow, the air heater and blower were shut off and the data were written to files for later reduction. The particles were generally allowed to cool overnight before being pneumatically transported to the upper hopper for the next test.

2.6 Data Analysis. The temperatures that were recorded from all of the thermocouples after the apparatus reached thermal equilibrium were averaged both before the start of particle flow and during the particle flow.

All of the averaged axial and radial temperatures in the column before the introduction of particles were generally the same within the experimental resolution of the thermocouples, indicating that the heat exchanger was at steady state, not exchanging a measurable amount of heat with the ambient, and that the gas entering the bottom of the column was well mixed.

The centerline column temperature at the 0.30 m (12 in.) elevation in the column, recorded before the start of the particle flow, was considered to be the inlet temperature of the hot gas $T_{g,i}$ for heat transfer calculations. When the particle flow started and the temperatures stabilized again, the average temperature recorded by the thermocouple at the 8.80 m (28.9 ft.) elevation was considered to be the outlet temperature of the gas $T_{g,o}$. These values were used to calculate the rate of heat transfer from the gas q_{gas}.

The measurements of the particle inlet and outlet temperatures, averaged over the same period of time, were used to calculate the rate of heat transfer to the particles $q_{\text{particles}}$. The rate of heat transfer from the gas q_{gas} and heat transfer rate to the particles $q_{\text{particles}}$ were calculated by the following equations:

$$q_{\text{gas}} = \dot{m}_g c_g (T_{g,i} - T_{g,o}) \quad \text{for air} \tag{2a}$$

$$q_{\text{particles}} = \int_{T_{s,i}}^{T_{s,o}} \dot{m}_s c_s(T_s) dT_s \quad \text{for particles} \tag{2b}$$

Note that the specific heat of the air was approximately constant (1006 J/kg K) over the range of temperatures encountered in this experiment. However, the specific heat of the bauxite varies by more than 12% over the same temperature range. Failure to account for this change by integrating the specific heat curve over the temperature range would have caused a significant error in the measured rate of energy absorption by the particles $q_{\text{particles}}$.

The recorded differential pressures from the column were each averaged both before and during particle flow. These differential pressures had to be corrected for the hydrostatic weight of air in the lines leading from the column to the pressure scanner. The density of the air in the lines was calculated by using the ideal gas law with the measured atmospheric pressure and ambient laboratory temperature. The actual pressure difference between two vertical points on the column ΔP_{column} separated by a height z was related to the recorded differential pressure $\Delta P_{\text{recorded}}$ by

$$\Delta P_{\text{column}} = \Delta P_{\text{recorded}} + \rho_g g z \tag{3}$$

3 Analytical Model

The uniform mixing model has been used by many researchers in order to estimate the heat transfer area A available in a given bed configuration. In this model, the heat exchanger coefficient U is approximated by the heat transfer coefficient h for a sphere falling at terminal velocity. The heat exchanger surface area A is equal to the total surface area of the spherical particles suspended by drag within the column.

The amount of particles supported by the gas is estimated with knowledge of the gas superficial velocity u_o, particle terminal velocity v_T, and mass flow rate $\dot{m}_S$ of particles. The terminal velocity is calculated by equating the weight of the particle to the drag force on the particle falling at terminal velocity, using the drag correlation of Morsi and Alexander [13]

$$C_D = a_1 + \frac{a_2}{\mathrm{Re}_d} + \frac{a_3}{\mathrm{Re}_d^2} \tag{4}$$

The constants for this correlation are expressed for discrete ranges of Reynolds numbers as follows:

$0 < \mathrm{Re}_d \leqslant 0.1$	$a_1 = 0.0$	$a_2 = 18.0$	$a_3 = 0.0$
$0.1 < \mathrm{Re}_d \leqslant 1.0$	$a_1 = 1.222$	$a_2 = 29.1667$	$a_3 = -3.8889$
$1.0 < \mathrm{Re}_d \leqslant 10.0$	$a_1 = 3.690$	$a_2 = 22.73$	$a_3 = 0.0903$
$10.0 < \mathrm{Re}_d \leqslant 100.0$	$a_1 = 0.6167$	$a_2 = 46.5$	$a_3 = -116.67$
$100.0 < \mathrm{Re}_d \leqslant 1000.0$	$a_1 = 0.3644$	$a_2 = 98.33$	$a_3 = -2778.0$
$1000.0 < \mathrm{Re}_d \leqslant 5000.0$	$a_1 = 0.357$	$a_2 = 148.62$	$a_3 = -47500$
$5000.0 < \mathrm{Re}_d \leqslant 10000.0$	$a_1 = 0.46$	$a_2 = -490.55$	$a_3 = 578700$
$10000.0 < \mathrm{Re}_d$	$a_1 = 0.5191$	$a_2 = -1662.5$	$a_3 = 5416700$

From the definition of the mass flow rate of particles

$$\dot{m}_S = \alpha \rho_S A_C (v_T - u_o) \tag{5}$$

where α is the average volume fraction of the particles, ρ_S is the density of the solid material, and A_C is the cross-sectional area of the column. From this expression, we can solve for the particle volume fraction

$$\alpha = \frac{\dot{m}_S}{\rho_S A_C (v_T - u_o)} \tag{6}$$

The temperatures in the experiment ranged from 300 K (laboratory ambient, the inlet temperature of the solid particles) to 360 K (inlet gas temperature). Calculation of the particle terminal velocities at these extremes, using the ideal gas law for density and the Sutherland law for viscosity, yields a difference of 3% in terminal velocity. The corresponding change in average solid fraction calculated in the model is similarly small. In the calculation, the average of the gas and particle inlet temperatures was used for the evaluation of air properties.

The effect of interparticle spacing on drag was investigated in detail and found to be negligible. In the tests conducted with the simple injector, at the highest flow rates, the maximum solid fraction at the point of introduction was around 0.02 (2%). Using the solid fraction drag correction of Wen and Yu [14], the change in drag coefficient was less than 10%, with a corresponding change in terminal velocity of around 5%. The local solids fraction decreases as the particle stream spreads. On average, the solids fraction near the bottom of the column at the highest solids loading would not exceed 0.001 (0.1%).

Average values of the Reynolds number and solid fraction were calculated for use with the uniform mixing model. For the bauxite particles used in this study, the terminal Reynolds number, calculated using the Morsi and Alexander drag correlation, was approximately 230, with a corresponding terminal velocity of 6.6 m/s. The average solids volume fraction, calculated using Eq. (6), varied from 0.0001 to 0.001.

The holdup area A can then be estimated by multiplying the volume fraction of particles by the volume of the column (A_cL, where L is the height of the column), and then multiplying by the surface area to volume ratio of a spherical particle ($6/d$)

$$A = \frac{\dot{m}_S}{\rho_S A_c (v_T - u_o)} (A_c L) \frac{6}{d} = 6 \frac{\dot{m}_S}{\rho_S (v_T - u_o)} \frac{L}{d} \tag{7}$$

The pressure gradient in the column can also be calculated using the mixture density in the hydrostatic equation

$$\nabla p = (\alpha \rho_s + (1 - \alpha)\rho_g) g \tag{8}$$

where g is the acceleration of gravity. The gas density ρ_g is calculated using the ideal gas law for air in conjunction with the average gas temperature in the column.

The overall heat exchanger coefficient U is assumed to be equal to the heat transfer coefficient h for the particle falling at its terminal Reynolds number. The heat transfer coefficient is determined using the Nusselt number correlation of Ranz and Marshall [10]

$$\mathrm{Nu} = 2 + 0.6 \mathrm{Re}_d^{1/2} \mathrm{Pr}^{1/3} \tag{9}$$

The heat transfer effectiveness ε can be estimated with the ε-*NTU* method. The ε-*NTU* method is derived by assuming that the heat exchanger is isolated from its surroundings, that the overall heat transfer coefficient U is constant, and that the specific heats of both streams are constant. The expression for the theoretical effectiveness ε of a counterflow heat exchanger is given by (Incropera and DeWitt [8])

$$\varepsilon = \frac{1 - \exp[-NTU(1 - C_r)]}{1 - C_r \exp[-NTU(1 - C_r)]} \quad C_r < 1$$

$$\varepsilon = \frac{NTU}{1 + NTU} \quad C_r = 1 \tag{10}$$

The number of transfer units *NTU* is given by

$$NTU = \frac{UA}{C_{\min}}, \tag{11}$$

where $C_{\min}$ is the limiting heat capacity rate of the heat exchanger, defined as:

$$C_{\min} = \min(\dot{m}_g c_g, \dot{m}_s c_s) \tag{12}$$

where $\dot{m}_i$ is the mass flow rate of the stream, and c_i is the specific heat capacity of the stream material. C_r is the ratio of the minimum to the maximum heat capacity rates

$$C_r = \frac{C_{\min}}{C_{\max}} \tag{13}$$

For a given application where the inlet temperatures of both streams are prescribed, the maximum possible heat transfer rate $q_{\max}$ may be determined by

$$q_{\max} = C_{\min}(T_{g,i} - T_{s,i}) \tag{14}$$

The heat transfer rate for the uniform mixing model q_{umm} between the particles and the gas may then be estimated by the definition of the heat exchanger effectiveness

$$q_{\mathrm{umm}} = \varepsilon q_{\max} \tag{15}$$

The nonconstant specific heat of the bauxite will generally not permit the use of the ε-*NTU* method to calculate the heat transfer rate. The temperature dependence of the specific heat of bauxite introduces a nonlinearity into the heat exchange equations that will not permit the derivation of a closed form expression for effectiveness. An iterative numerical shooting method was used in order to determine the temperature profiles and net heat exchange rate between the gas and particles q_{umm}.

4 Results

In order to evaluate the quality of the heat transfer and temperature data, the heat transfer rates from the gas and to the particles were evaluated using Eqs. (2*a*) and (2*b*), respectively, using the measured inlet and outlet temperatures and mass flow rates of both streams. These gas and particle heat transfer rates are plotted against each other in Fig. 4. The solid line in this figure indicates a slope of one where the gas and particle heat transfer rates are equal. The proximity of the data to this line indicates that for the majority of the tests a satisfactory energy balance was achieved.

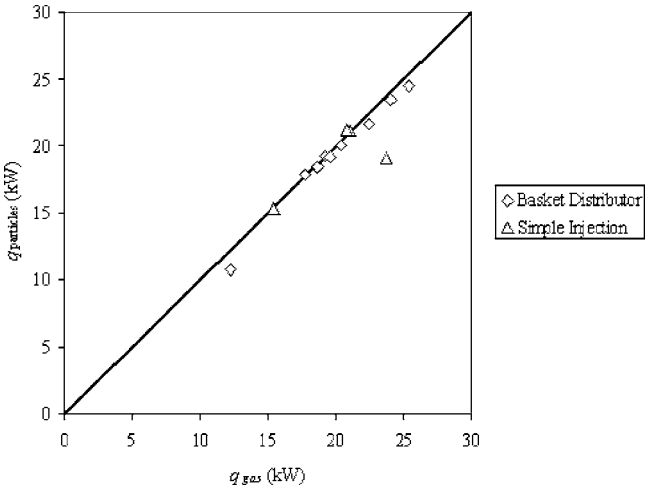

Fig. 4 Heat transfer rate balance between gas and particles

In one instance the solids flow rate was so high that thermal equilibrium could not be achieved, and the resulting heat imbalance is shown in Fig. 4. The heat transfer data from this particular test was rejected, but the corresponding pressure measurements were retained as the density of the air was not strongly affected by changes in temperature in this experiment.

The measured gas and particle heat transfer rates calculated using Eqs. (2*a*) and (2*b*) were averaged and plotted against the analogous model predictions (Fig. 5). As can be seen, the predictions of the uniform mixing model generally overpredict the measured heat transfer rates. The apparent agreement between the data and the model at the high and low extremes of heat transfer rate is due to the fact that the falling-bed heat exchanger effectiveness approaches unity at low values of the thermal capacitance ratio C_r.

The averaged axial gas temperature data for tests conducted without a basket distributor are shown in Fig. 6. Data are presented for three representative tests at high, low, and midrange solid flow rates. Gas flow rates were approximately constant from test to test. These data are plotted against the gas temperature profiles predicted by the uniform mixing model. While the model appears to follow the crude trend of the axial temperature data at higher solid flow rates [Figs. 6(*a*) and 6(*b*)], the predicted axial gas temperature significantly overpredicts the centerline temperature at lower solids flow rates [Fig. 6(*c*)]. At this flow rate, the

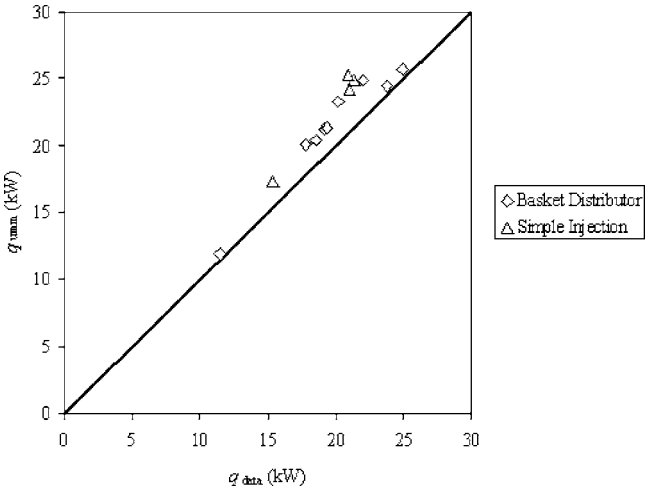

Fig. 5 Comparison of measured gas and particle heat transfer rates to predictions of uniform mixing model

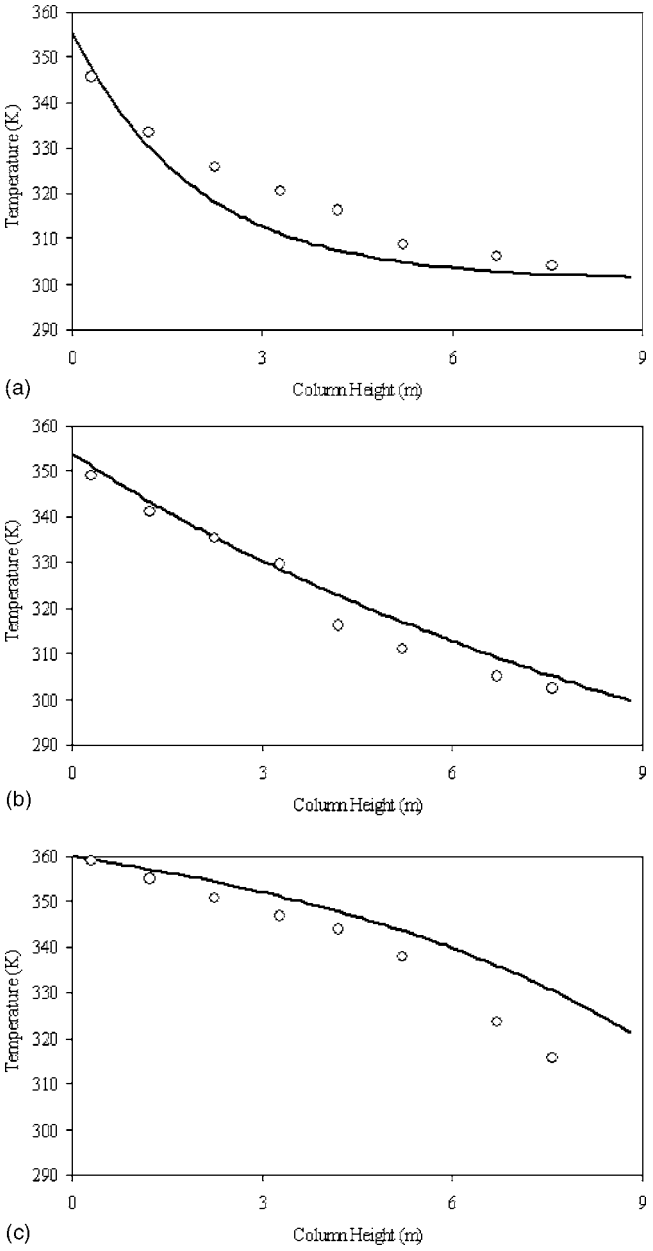

Fig. 6 Axial temperature profiles for tests with simple particle injection. Measured temperatures (symbols) plotted against prediction of uniform mixing model (solid line). The respective particle and gas mass flow rates are (a) 1.05 and 0.45 kg/s, (b) 0.67 and 0.46 kg/s, and (c) 0.39 and 0.44 kg/s.

capacitance ratio is close to one, which from *ε-NTU* theory corresponds to an operating condition of minimum effectiveness. This reduced effectiveness causes the predicted gas temperature at the top of the column to be measurably different from the inlet solids temperature, therefore providing a more challenging comparison to corresponding experimental data.

The measured pressure gradients for the same tests conducted without the basket distributor installed are shown in Fig. 7. These data were corrected for pressure line effects as described in Eq. (3). These pressures were measured relative to the static pressure measurement taken at the 0.30 m elevation in the column. Lines indicating the pressure gradient predicted using the uniform mixing model [Eq. (8)] and the estimated hydrostatic gradient of the air only are also plotted in these figures. It can be seen at the top of the column that the pressure gradient is close to the hydrostatic

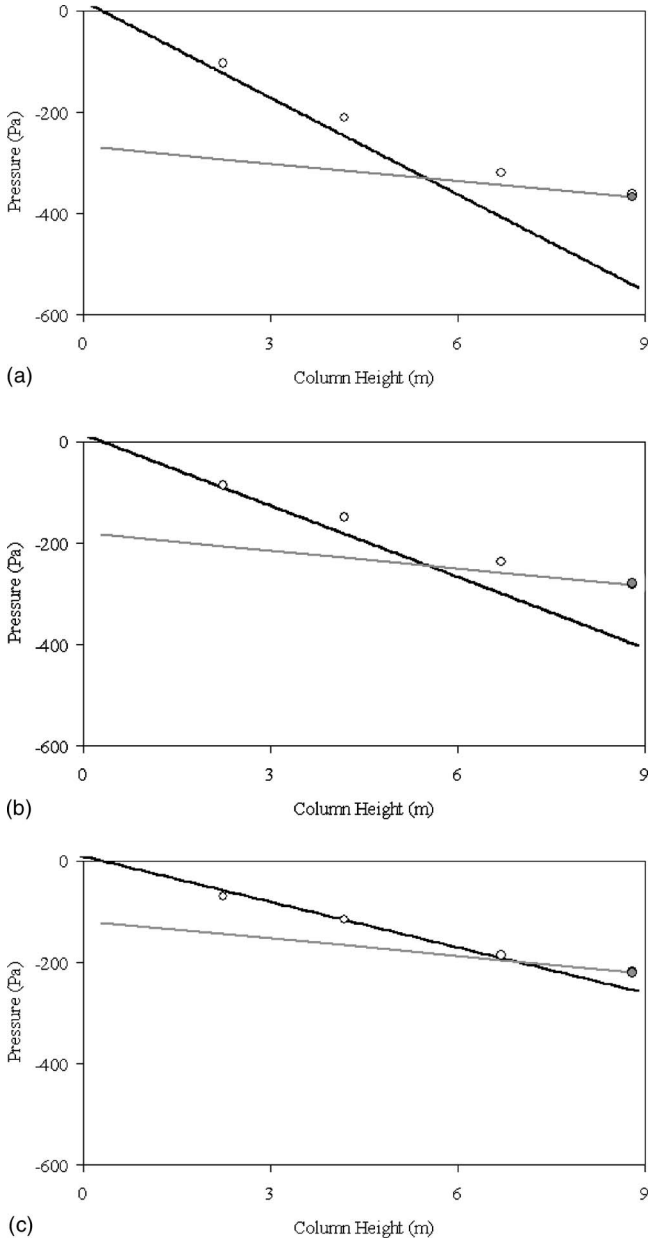

Fig. 7 Axial pressure profiles for tests with simple particle injection. Measured pressures plotted against prediction of uniform mixing model (black line) and hydrostatic gradient of air only (gray line). Open symbols are the sum of the measured pressure differences up to that elevation. The gray symbol is the pressure difference over the entire column. The respective particle and gas mass flow rates are (a) 1.05 and 0.45 kg/s, (b) 0.67 and 0.46 kg/s, and (c) 0.39 and 0.44 kg/s.

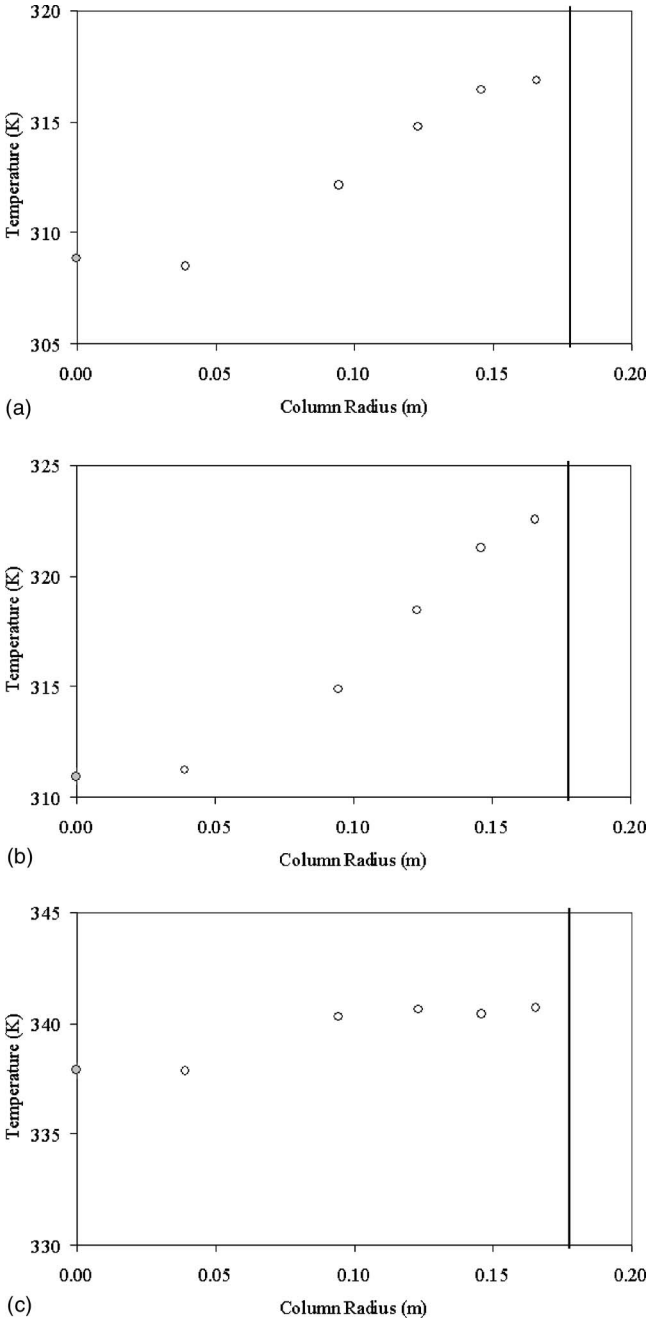

Fig. 8 Radial temperature profiles for tests with simple particle injection. The solid vertical line is the location of the column wall. The respective particle and gas mass flow rates are (a) 1.05 and 0.45 kg/s, (b) 0.67 and 0.46 kg/s, and (c) 0.39 and 0.44 kg/s.

gradient of the air, suggesting that very little drag interaction occurs in this area. Closer to the bottom of the column, the pressure gradient asymptotes to the pressure gradient predicted by the uniform mixing model. The location of this transition appears to be a function of particle flow rate, with the transition occurring farther down the column as the particle flow rate increases.

The measured radial gas temperature profile for the same tests is shown in Fig. 8, taken at the 5.2 m elevation in the column. Note that significant radial temperature gradients are observed in these tests. This profile shows that the gas in the center of the column is cooler than the gas near the column walls, suggesting that the structure of the falling stream of particles was intact at this column elevation. The presence of a structured stream of particles was confirmed by qualitative measurements of the radial particle concentration using two copper pipe sections, cut in half and filled with silicone adhesive, to collect falling particles. These measurements were performed at two elevations (5.2 and 7.6 m) in the column. The measurements at the 7.6 m elevation did clearly show the structure of the stream of solids falling from the simple injector. This structure was not observed in the profile taken at the 5.2 m elevation in the column. The existence of these temperature and particle concentration gradients contradicts the assumptions used to develop the uniform mixing model, and therefore the uniform mixing model is not accurate for this situation.

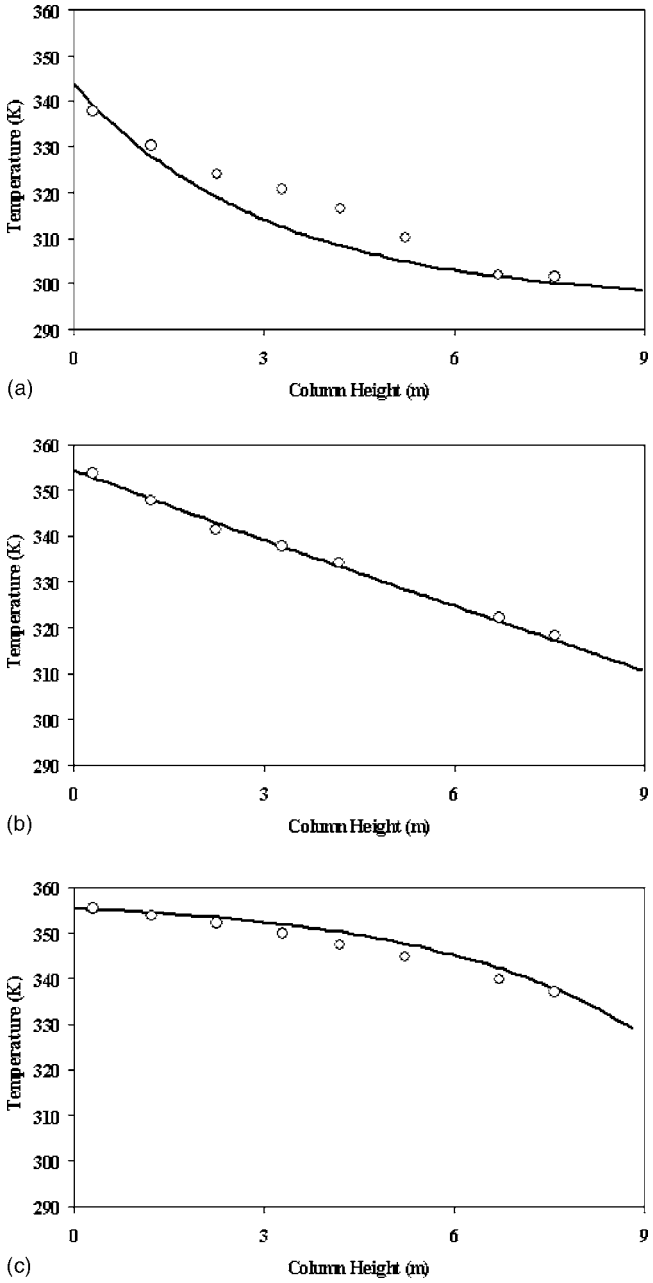

Fig. 9 Axial gas temperature profiles for tests with basket distributor. Measured temperatures (symbols) plotted against prediction of uniform mixing model (solid line). The respective particle and gas mass flow rates are (a) 0.94 and 0.47 kg/s, (b) 0.58 and 0.45 kg/s, and (c) 0.28 and 0.45 kg/s.

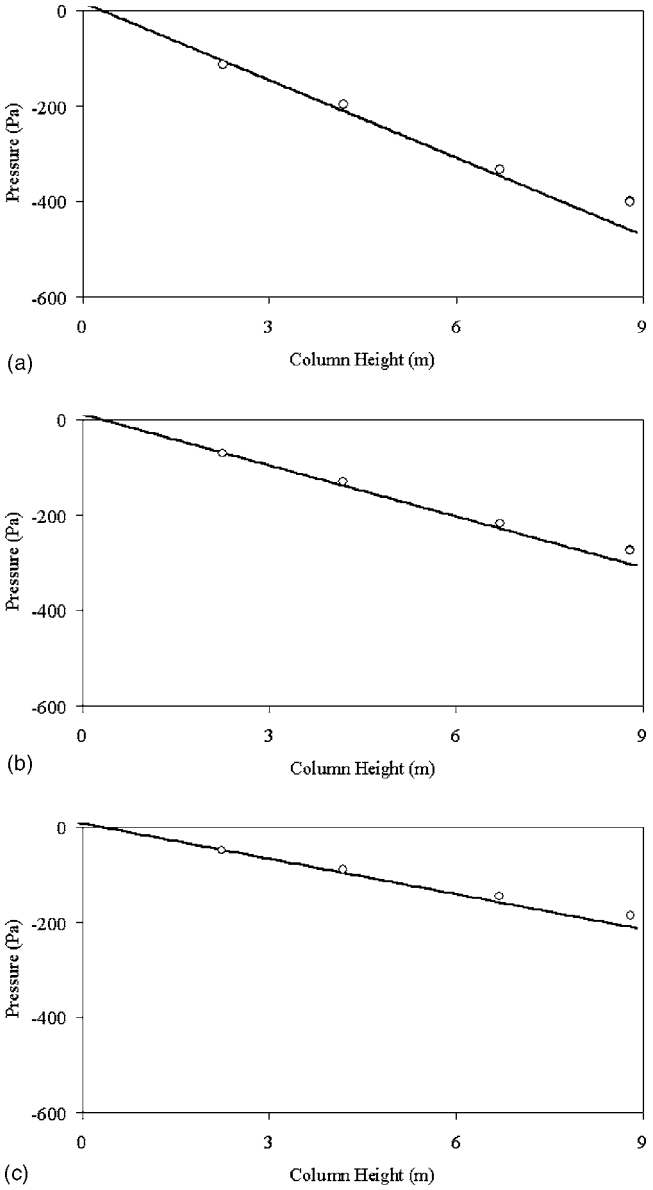

Fig. 10 Axial pressure profiles for tests with basket distributor. Measured pressures plotted against prediction of uniform mixing model (black line). Open symbols are the sum of the measured pressure differences up to that elevation. The gray symbol is the pressure difference over the entire column. The respective particle and gas mass flow rates are (a) 0.94 and 0.47 kg/s, (b) 0.58 and 0.45 kg/s, and (c) 0.28 and 0.45 kg/s.

The averaged axial gas temperature data for tests conducted with the basket distributor are shown in Fig. 9, presented for three representative tests at high, low, and midrange solid flow rates. Gas flow rates were approximately constant from test to test. These data are plotted against the gas temperature profiles predicted by the uniform mixing model. Better agreement between the measured temperature data and the model predictions is observed. This improved agreement is due largely to the increased spreading and mixing of the gas and particles in the column by the basket distributor, causing the conditions of the experiment to agree more closely with the uniform mixing model. This improved mixing is also observed in plots of the measured pressure profiles in the column (Fig. 10). The profiles more closely approximate the linear hydrostatic profile predicted by the uniform mixing model, though imperfect mixing due to local particle maldistributions near the distributor is still observed at the top of the column.

In order to evaluate the performance of the falling-bed heat exchanger it is useful to make estimates of the apparent effectiveness ε. Approximations to the various parameters of the heat exchanger are presented for the purposes of illustration only, as the nature of the falling-bed heat exchanger and the temperature-dependent specific heat of the bauxite violate some of the assumptions used in the derivation of the theoretical ε-NTU expression [Eq. (10)]. The effective thermal capacities of both streams are estimated by

$$C_{\text{particles}} = \frac{\int_{T_{s,i}}^{T_{s,o}} \dot{m}_s c_s(T_s) dT_s}{T_{g,i} - T_{s,i}} \tag{16}$$

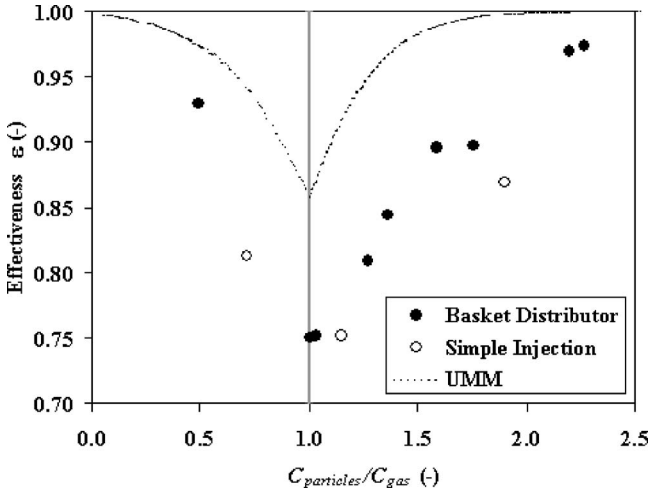

Fig. 11 Comparison of apparent experimental effectiveness of falling-bed heat exchanger with and without basket distributor to uniform mixing model as a function of ratio of particle to gas stream thermal capacities. Vertical gray line indicates a capacitance ratio C_r of one. Dotted line represents the uniform mixing model assuming a constant specific heat of bauxite.

$$C_{\text{gas}} = \dot{m}_g c_g \tag{17}$$

The corresponding thermal capacitance ratio C_r, effectiveness ε, and maximum theoretical heat transfer rate $q_{\max}$ are defined in the same manner as the theoretical model. Note that this method of comparison would not be useful if the effectiveness of the heat exchanger without the distributor was close to unity. In that situation, the relative performance would need to be evaluated with a comparison of the temperature profiles within the column.

In order to observe the effect of the particle distributor on the heat transfer performance of the falling-bed heat exchanger, the temperatures or heat transfer rates for experiments performed both with and without the distributor must be compared at the same operating point of gas and particle flow rates. This comparison was accomplished by plotting the measured apparent effectiveness of both sets of experiments against the ratio of particle to gas thermal capacities (Fig. 11). Due to the imperfections in mixing, the simple distributor does not come close to the effectiveness predicted by the model. However, it can be seen that the effectiveness of the falling-bed heat exchanger is enhanced by the addition of the basket distributor. The performance of the falling-bed heat exchanger with the basket distributor is closer to the effectiveness predicted by the uniform mixing model.

5 Conclusions and Discussion

Designers of falling-bed heat exchangers are typically trying to achieve a certain heat transfer effectiveness for the lowest structural cost. Once the particle material and mass flows have been determined, the column diameter is generally scaled to keep the mean gas velocity below the terminal velocity of particles. At this point in the design process, the only variables available to optimize the performance of the heat exchanger are the column height and the method of particle distribution. A good particle distributor design can mean a shorter column for the same effectiveness, and therefore reduced structural costs.

The uniform mixing model represents the "perfect" or "ideal" falling-bed heat exchanger where the rate of radial mixing of gas temperature and momentum is infinite. The amount of particle area available for heat exchange is a maximum, and the highest possible temperature difference is maintained, and therefore the predicted heat transfer rate is the highest possible value. The uniform mixing model cannot generally describe the falling-bed heat exchanger, as it cannot account for differences in particle distributor design, or in any other source of radial maldistribution. As can be seen in Fig. 5, the uniform mixing model consistently overestimates the heat transfer rate, for both cases with and without the particle distributor basket.

Despite these shortcomings, the uniform mixing model establishes an upper bound that describes the maximum possible effectiveness of the falling-bed heat exchanger, as the model assumes the perfect distribution and mixing of the gas and particles. The experimental performance of a particular distributor design can be compared to this bound, and a judgment can be made by the designer as to whether further cost and effort is warranted to improve the performance of the design. For example, this model can be utilized by designers to determine the maximum possible heat transfer effectiveness, to which the performance of various particle distribution methods can be compared and evaluated.

In this study it has been determined that the discrepancy between the predicted and measured performance is not attributable to solid volume fraction effects on particle drag and heat transfer. This discrepancy in performance has been shown to be a function of the method of introducing the particles into the bed. This observation suggests the importance of modeling the gradients in the flow, and further suggests the need to incorporate the effects of viscosity and turbulence into any realistic model of the falling-bed heat exchanger. Previous experimental experience suggests that accepted single particle correlations for drag and heat transfer are appropriate if these maldistributions can be properly modeled. The use of computational fluid dynamics (CFD) would permit the modeling of turbulence and permit the resolution of spatial maldistributions in the flow.

The experimental data presented above are intended to serve the development and validation of two-phase CFD modeling, as well. A very good energy balance has been obtained, indicating that steady-state conditions and a good isolation from the environment were achieved. The boundary conditions have been carefully controlled and faithfully reported. The geometry has been kept simple, to simplify modeling efforts. It is expected that this experiment will be a good test case for two-phase turbulence and heat transfer models.

Acknowledgment

Funding and support by ALSTOM Power Inc. for this study is gratefully acknowledged.

Nomenclature

a_1, a_2, a_3 = coefficients for Morsi and Alexander drag correlation [−]
A = available surface for heat exchange [m^2]
A_c = column cross sectional area [m^2]
c_g, c_s = specific heats of gas and solids [J/kg K]
C_D = drag coefficient [−]
C_{gas} = stream heat capacity rate of gas [W/K]
$C_{\min}$ = minimum stream heat capacity rate [W/K]
$C_{\max}$ = maximum stream heat capacity rate [W/K]
$C_{\text{particles}}$ = stream heat capacity rate of particles [W/K]
C_r = ratio of specific heat capacities ($C_{\min}/C_{\max}$) [−]
d = spherical particle diameter [m]
g = acceleration of gravity at Earth's surface [9.81 m/s^2]
h = heat transfer coefficient [W/m^2 K]
k_g = thermal conductivity of air [W/m K]
L = column height [m]
LMTD = Log mean temperature difference [K]
$\dot{m}_g$, $\dot{m}_s$ = mass flow rates of gas and solids [kg/s]
Nu = Nusselt number for particle (hd/k_g) [−]
NTU = Number of transfer units [−]
Pr = Prandtl number of air [−]
q = heat transfer rate between gas and solids [W]

q_{data} = average of measured heat transfer q_{gas} and $q_{particles}$ [W]
q_{gas} = measured heat transfer rate from gas [W]
q_{max} = maximum possible heat transfer rate in a heat exchanger $C_{min}(T_{h,i}-T_{c,i})$ [W]
$q_{particles}$ = measured heat transfer rate to particles [W]
q_{umm} = heat transfer rate predicted using uniform mixing model [W]
Re_d = Reynolds number based on particle diameter and terminal velocity $(\rho_g d v_t/\mu)$ [−]
T_g = temperature of gas stream in heat exchanger [K]
T_s = temperature of solids stream in heat exchanger [K]
$T_{g,i}$, $T_{g,o}$ = inlet and outlet temperatures of gas stream in heat exchanger [K]
$T_{s,i}$, $T_{s,o}$ = inlet and outlet temperatures of solids stream in heat exchanger [K]
U = heat exchanger coefficient [$W/m^2 K$]
u_o = superficial gas velocity relative to column [m/s]
V_c = column volume [m^3]
v_t = particle terminal velocity relative to gas [m/s]
z = distance between two vertical points [m]
∇p = pressure gradient [Pa/m]

Greek Letters

α = volume fraction of solids in a gas-solid suspension [−], thermal diffusivity of gas [m^2/s]
Δp_{column} = pressure difference between two vertical points in column [Pa]
$\Delta p_{recorded}$ = pressure difference measured by differential pressure transducer [Pa]
ε = heat exchanger effectiveness (q/q_{max}) [−]
μ = viscosity of air [Pa s]
ρ_g, ρ_s = density of gas and solids [kg/m^3]

References

[1] Decher, R., 1981, "The Falling Bead Dry Cooling Tower," AIAA J. Energy, **5**, p. 321.
[2] Gat, N., 1987, "The Circulating Balls Heat Exchanger (CIBEX)," Int. J. Thermophys., **1**, pp. 105–111.
[3] Park, J., Baek, S., and Kwon, S., 1998, "Analysis of a Gas-Particle Direct-Contact Heat Exchanger with Two-Phase Radiation Effect," Numer. Heat Transfer, Part A, **33**, pp. 701–721.
[4] Patnaik, V., 1990, "Study of Waste Heat Recovery Using Phase-Change Particles," Master's thesis, Pennsylvania State University.
[5] Thayer, W., and Sekins, K., 1985, "High Temperature Heat Recovery by Particle or Droplet Heat Exchangers," *Proc. 20th Intersociety Energy Conversion Engineering Conf.*, pp. 2.253–2.258.
[6] Thynell, S., and Manchor, J., 1994, "Effect of Radiation on Stage Performance of the Falling Particle Heat Exchanger," *Proc. 6th AIAA/ASME Thermophysics and Heat Transfer Conference* ASME HTD, **276**, pp. 121–130.
[7] Thynell, S., and Patnaik, V., 1990, "Study of Waste Heat Recovery Using Phase Change Particles," *Proc. Thermophysics and Heat Transfer Conf.* ASME HTD, **129**, pp. 71–79.
[8] Incropera, F., and DeWitt, D., 1996, *Fundamentals of Heat and Mass Transfer*, Wiley, New York.
[9] Pierce, R., Dwyer, O., and Martin, J., 1959, "Heat Transfer and Fluid Dynamics in Mercury-Water Spray Columns," AIChE J., **5**, pp. 257–262.
[10] Ranz, W., and Marshall, W., Jr., 1952, "Evaporation from Drops-Part I," Chem. Eng. Prog., **48**, pp. 141–146.
[11] Islam, M., 1972, "Heat Transfer from Gases to Solid Particles," Ph.D. dissertation, University of Newcastle upon Tyne.
[12] Inaba, H., Horibe, A., Ozaki, K., and Yokoyama, N., 2000, "Liquid-Liquid Direct Contact Heat Exchange Using a Perfluorocarbon Liquid for Waste Heat Recovery," JSME Int. J., Ser. B, **43**, pp. 52–61.
[13] Morsi, S., and Alexander, A., 1972, "An Investigation of Particle Trajectories in Two-Phase Flow Systems," J. Fluid Mech., **55**, pp. 193–208.
[14] Wen, C., and Yu, Y., 1966, "Mechanics of Fluidization," Chem. Eng. Prog., Symp. Ser., **62**, pp. 100–111.

Enhancement of Heat Transfer by an Electric Field for a Drop Translating at Intermediate Reynolds Number

Rajkumar Subramanian

M. A. Jog[1]
e-mail: milind.jog@uc.edu

Department of Mechanical, Industrial, and Nuclear Engineering,
University of Cincinnati,
Cincinnati, OH 45221-0072

The enhancement of heat transfer by an electric field to a spherical droplet translating at intermediate Reynolds number is numerically investigated using a finite volume method. Two heat transfer limits are considered. The first limit is the external problem where the bulk of the resistance is assumed to be in the continuous phase. Results show that the external Nusselt number significantly increases with electric field strength at all Reynolds numbers. Also, the drag coefficient increases with electric field strength. The enhancement in heat transfer is higher with lower ratio of viscosity of the dispersed phase to the viscosity of the continuous phase. The second heat transfer limit is the internal problem where the bulk of the resistance is assumed to be in the dispersed phase. Results show that the steady state Nusselt number for a combined electrically induced and translational flow is substantially greater than that for purely translational flow. Furthermore, for a drop moving at intermediate Reynolds number, the maximum steady state Nusselt number for a combined electrically induced and translational flow is slightly greater than that for a purely electric field driven motion in a suspended drop.
[DOI: 10.1115/1.2033906]

Keywords: Heat Transfer Enhancement, Electric Field, Droplet, Numerical Analysis

Introduction

When an electrical field is applied to a dielectric drop, the electric field induces stresses on the drop surface. The tangential stresses produce circulatory fluid motion in the drop and the continuous phase which results in increase in the heat or mass transfer rate. Taylor [1] was perhaps the first to experimentally demonstrate electrically induced flow in a suspended drop of silicone oil in a mixture of castor oil and corn oil. Based on a leaky dielectric model, he calculated the induced stresses at the drop surface due to applied electric field. In Stokes flow regime, he derived the stream function for flow in the drop interior and that in the continuous phase. His analytical solutions for the flow field have been extensively used to study the heat transfer to a suspended drop [2].

Heat and/or mass transfer studies of a droplet in electric field have typically considered two limits based on the relative magnitude of the resistance to heat transfer in the continuous and the dispersed phase. One limit, where the bulk of the resistance to the heat transport is in the dispersed phase, is known as the internal problem. The other limit, where the resistance to heat transfer is mainly in the continuous phase, is known as the external problem. The steady-state Nusselt number for a conjugate problem, where the heat transfer resistances in the two phases are comparable, can be estimated from the individual Nusselt numbers for the internal and external problem as described by Abramzon and Borde [3]. When the time scale for the external Nusselt number to approach its steady-state value is small compared to the time scale for temperature change in the drop interior, the heat transport in the continuous phase can be considered to be quasi-steady, and the steady state results obtained for the external problem can be used.

Oliver, Carleson, and Chung [4] carried out a numerical solution to the unsteady heat transfer to a droplet suspended in an electric field. A fully developed flow field was assumed and the droplet was suddenly exposed to a step change in the ambient temperature with the bulk of the resistance being in the droplet. Initially it was found that the Nusselt number oscillates for larger values of Peclet numbers. As time increases the Nusselt number approaches a steady value. At low values of Peclet numbers, the steady-state Nusselt number was found to be close to the pure diffusion limit of 6.6. As Peclet number increases, the steady-state Nusselt number becomes independent of Peclet number for large Peclet numbers and approaches 29.8 at high Peclet number [2]. This is considerably greater than the steady state internal Nusselt number of 17.66 for a purely translating drop under creeping flow.

The transient heat transfer in a fluid sphere translating in an electric field was analyzed by Chung and Oliver [5] in creeping flow regime with thermal resistance being in the dispersed phase. The electric field strength was expressed in terms of a parameter E, defined as the ratio of electrically induced to translation-induced maximum surface velocity. It was shown that at high Peclet number, the electric field effects are negligible for E less than 0.5 while translation is unimportant for E greater than 10.

Griffiths and Morrison [6] analyzed the external heat transfer from a drop in an electric field at low Peclet number using a regular perturbation expansion. It was found that a perturbation about the zero flow solution was everywhere valid for analysis of transport due to the low Peclet number creeping flow generated by an electric field. These solutions were accurate up to a Peclet number of 60. Sharpe and Morrison [7] investigated the external steady-state heat or mass transfer to a drop in an electric field at low values of the Reynolds number. The overall Nusselt number was found to increase monotonically with the Peclet number.

Chang and Berg [8] analyzed the fluid flow and mass transfer behavior of a droplet translating in an electric field at intermediate Reynolds numbers. They adopted an approximate Galerkin method to solve the external problem and predicted drag coefficients for a range of Reynolds numbers and viscosity ratios. However, it appears that the contribution from the normal viscous

[1]To whom correspondence should be addressed.

Contributed by the Heat Transfer Division of ASME for publication in the JOURNAL OF HEAT TRANSFER. Manuscript received September 11, 2004; final manuscript received May 5, 2005. Review conducted by Jacob Chung.

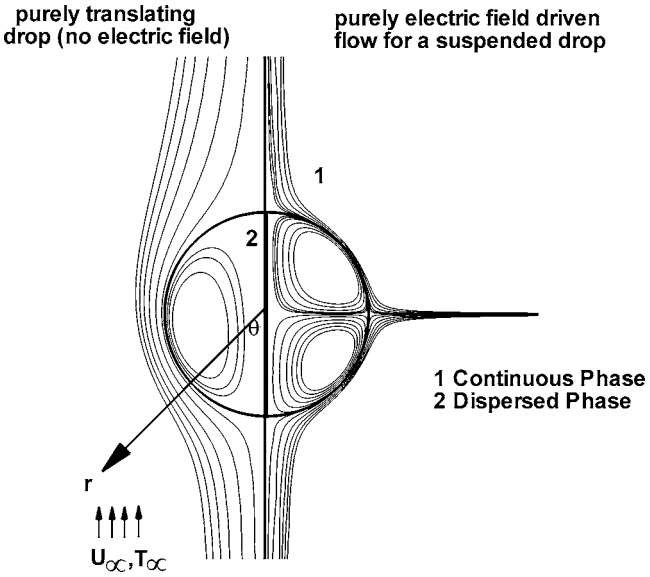

Fig. 1 Schematic diagram showing the coordinate system and streamlines for purely translating drop and for purely electric field driven flow for a suspended drop

stress on the drop surface was not considered in the drag force calculation. The external mass transfer rates were obtained for very high Peclet numbers. Their mass transfer calculations were based on a thin boundary layer approximation and restricted to very high Peclet numbers. The electric field effect was characterized by a dimensionless parameter *W*, which was defined as the ratio of electrical and gravitational effects. They concluded that, for a substantial increase in the rate of transport due to the electric field, the value for this dimensionless parameter should be significantly greater than unity. For negative *W* the electrically induced flow is from the equator to the pole on the drop surface. It was found that even at moderate negative values of *W*, enhancement in mass transfer was not obtained. As such, we have considered only positive values of *W* in this study.

In this paper we address the situation that would be applicable in direct-contact heat exchange application of a droplet moving in a continuous medium in intermediate Reynolds number regime. The analysis removes the earlier restrictions of the creeping flow limit and the restriction of the very high Peclet number limit.

Formulation

Consider a spherical droplet moving steadily in a uniform electric field. The flow field is considered axi-symmetric with the origin of the coordinate system at the center of the drop and the thermophysical properties are considered constant. The flow in the two phases and the external heat transfer are considered steady whereas the heat transfer in the internal problem is considered as transient. We note that the internal heat transfer must be considered transient as no nontrivial steady solution exits for the droplet temperature variation. A schematic of the problem is shown in the left half of Fig. 1 with typical stream lines for purely translational motion. The right half of Fig. 1 shows typical stream lines for purely electric field induced flow in a suspended drop. The assumption of spherical drop shape needs some discussion. The drop distortion from sphericity is governed by the Reynolds, Weber, Eotvos, and capillary numbers. The drop may deform at elevated Reynolds number. Additionally at high electric field strengths, the drop may deform in a prolate or an oblate shape based on Taylor's discriminating function which is related to the thermophysical properties of the two phases. As such for some combination of thermophysical properties, the deformation due to hydrodynamic and electrical effects may nearly cancel each other keeping the drop nearly spherical. However, in some cases, the two effects may be additive, leading to significant deviations of drop shape from a sphere. The exact calculation of the drop shape is computationally challenging task even for a suspended drop [9]. As such we have considered a spherical drop in our model.

Governing Equations

In terms of the following dimensionless parameters $U_i = U^*/U_\infty$, $\nabla = R\nabla^*$, $p = (p^* - p_\infty)/(1/2)\rho_1 U_\infty^2$, $\mathrm{Re} = U_\infty 2R/\nu_1$, $T_1 = (T_1^* - T_\infty)/(T_s - T_\infty)$, $t = t^*\alpha_2/R^2$, and $T_2 = (T_2^* - T_0)/(T_\infty - T_0)$, the governing equations are:

Continuous phase

$$\nabla \cdot \vec{U}_1 = 0 \tag{1}$$

$$\vec{U}_1 \cdot \nabla \vec{U}_1 = -\frac{1}{2}\nabla p_1 + \frac{2}{\mathrm{Re}}\nabla^2 \vec{U}_1 \tag{2}$$

$$\vec{U}_1 \cdot \nabla T_1 = \frac{2}{Pe_1}\nabla^2 T_1 \tag{3}$$

Dispersed phase

$$\nabla \cdot \vec{U}_2 = 0 \tag{4}$$

$$\vec{U}_2 \cdot \nabla \vec{U}_2 = -\frac{1}{2}\nabla p_2 + \frac{2}{\mathrm{Re}}k_\nu \nabla^2 \vec{U}_2 \tag{5}$$

$$\frac{\partial T_2}{\partial t} + \frac{\mathrm{Pe}_2}{2k_\nu}(U_2 \cdot \nabla T_2) = \nabla^2 T_2 \tag{6}$$

The equations are transformed in terms of vorticity and stream function. The stream function is introduced such that

$$U_r = -\frac{1}{r^2 \sin\theta}\frac{\partial \psi}{\partial \theta} \quad \text{and} \quad U_\theta = \frac{1}{r \sin\theta}\frac{\partial \psi}{\partial r} \tag{7}$$

The vorticity is

$$\vec{\omega} = \nabla \times \vec{U} = \left[\frac{1}{r}\frac{\partial}{\partial r}\left(\frac{1}{\sin\theta}\frac{\partial \psi}{\partial r}\right) + \frac{1}{r^3}\frac{\partial}{\partial \theta}\left(\frac{1}{\sin\theta}\frac{\partial \psi}{\partial \theta}\right)\right]\vec{i}_\phi \tag{8}$$

Since the flow is assumed to be axi-symmetric, we have $\vec{\omega} = \omega \cdot \vec{i}_\Phi$.

The momentum conservation equations in terms of stream function and vorticity become

$$\vec{U}_1 \cdot \nabla \vec{\omega}_1 - (\vec{\omega}_1 \cdot \nabla)\vec{U}_1 = \frac{2}{\mathrm{Re}}\nabla^2 \vec{\omega}_1 \tag{9}$$

$$(\vec{U}_2 \cdot \nabla \vec{\omega}_2) - (\vec{\omega}_2 \cdot \nabla)\vec{U}_2 = \frac{2}{\mathrm{Re}}k_\nu \nabla^2 \vec{\omega}_2 \tag{10}$$

Equations (3), (6), and (8)–(10) are the final governing equations for the problem. These are subject to the following boundary conditions. At infinity, uniform flow, zero vorticity, and uniform temperature are specified.

As $r \to \infty$, $\psi_1 \to (1/2)r^2 \sin^2\theta$; $\omega_1 \to 0$; $T_1 \to 0$.

At $\theta = 0$ and $\theta = \pi$, the symmetry condition gives $0 = \psi_1 = \psi_2 = \omega_1 = \omega_2 = \partial T_1/\partial\theta = \partial T_2/\partial\theta$.

At the interface $r = 1$, zero normal velocity condition gives $\psi_1 = \psi_2 = 0$.

Using the continuity of tangential velocity, the shear stress balance at the interface, $\tau_{Er\theta}^* + \tau_{1r\theta}^* = \tau_{2r\theta}^*$, can be written as

$$\frac{R}{U_\infty \mu_2}\tau_{Er\theta}^* + \frac{\mu_1}{\mu_2}\omega_1 + 2\left(1 - \frac{\mu_1}{\mu_2}\right)U_\theta = \omega_2 \tag{11}$$

where $U_\theta = U_{1\theta} = U_{2\theta}$.

The shear stress caused by the electric field $\tau^*_{Er\theta}$ is given by Taylor [1] and can be written in terms of the maximum surface velocity induced by the electric field (V) for a suspended drop as

$$\tau^*_{Er\theta} = 10V^* \frac{\mu_1 + \mu_2}{R} \cos\theta \sin\theta \tag{12}$$

$$V^* = V\, U_\infty = \frac{9E^2 R d_2}{8\pi(2+\sigma_1/\sigma_2)^2} \frac{[1-(\sigma_1 d_1)/(\sigma_2 d_2)]}{5(\mu_1+\mu_2)} \tag{13}$$

Hence, in earlier studies in the creeping flow regime, the relative strength of the electric field was defined in terms of a parameter

$$\hat{W} = \frac{U_{\theta,\max(r=1)} \text{due to purely electric field driven flow in suspended drop}}{U_{\theta,\max(r=1)} \text{due to purely translational motion in creeping flow}} \tag{14}$$

$$\hat{W} = \frac{4V^*(1+k_\mu)}{U_\infty} \tag{15}$$

$$\omega_2 = \frac{\omega_1}{k_\mu} + \frac{2(k_\mu - 1)}{k_\mu} U_\theta + \frac{10\hat{W}}{4k_\mu} \sin\theta\cos\theta \tag{16}$$

However, the above equation provides the ratio of maximum surface velocities by purely electrically induced flow to purely translational flow *only in the limit of creeping flow*. For the intermediate Reynolds number, the maximum velocity on the drop surface due to pure translational motion must be evaluated numerically. For each Reynolds number considered, the program is executed for a purely translational flow without applied electric field and the maximum velocity surface is obtained. We introduce the term W, to indicate the ratio of maximum electric field induced surface velocity to that due to purely translational motion in intermediate Reynolds number flow. The boundary condition can be written in terms of W by writing, $\hat{W}=aW$. Here a is a parameter defined such that $W=1$ corresponds to equal electric field driven velocity and purely translational maximum surface velocity. For creeping flow, $a=1$. In this manner the equation is consistent with earlier work and is appropriate for the intermediate Reynolds number regime. Therefore the condition of continuity of shear stress can be written as

$$\omega_2 = \frac{\omega_1}{k_\mu} + \frac{2(k_\mu - 1)}{k_\mu} U_\theta + \frac{10aW}{4k_\mu} \sin\theta\cos\theta \tag{17}$$

The transient temperature distribution in the dispersed phase is solved using Eq. (6). The initial temperature in the drop interior is considered uniform at T_0. In dimensionless form this condition is $T_2(t=0)=0$. For a conjugate problem, the interface conditions at the drop surface are: continuity of temperature $T^*_1(R,\theta) = T^*_2(R,\theta)$ and equality of heat flux $-k_1(\partial T^*_1/\partial r^*) = -k_2(\partial T^*_2/\partial r^*)$. However, a conjugate problem is not addressed here. We have considered two limits based on the relative resistance to heat transfer in both phases. The heat transfer resistances are dependent on the ratio of thermal diffusivities in the two phases. When the thermal diffusivity of the continuous phase is much larger than that of the dispersed phase, the resistance to heat transfer is very small in the continuous phase. This is the internal problem. In such case, the drop surface temperature will be close to the far field temperature.

Therefore, for the internal problem, we consider: $T_2(r=1)=1$.

The external problem is treated by the steady form of the energy equation. The drop surface temperature is prescribed for the external problem.

Hence, for the external problem, in dimensionless form: $T_1(r=1)=1$.

As shown by Abramzon and Borde [3], the external heat transfer can be considered steady when the time scale of drop heating (or cooing) is much larger than the time required for the continuous phase to reach the steady state solution. They showed that this condition is met when $\rho_2 c_2/\rho_1 c_1 \gg 1$. One example of such condition is a liquid drop moving in a gaseous environment. Moreover, Abramzon and Borde [3] also showed that the overall Nusselt number for a conjugate problem can be obtained using steady state external Nusselt number as $1/\mathrm{Nu} \cong (k_2/k_1)(1/\mathrm{Nu}_{\text{internal}}) + 1/\mathrm{Nu}_{\text{steady,external}}$. As such, a time-independent solution of the external problem provides useful information.

Drag Coefficients. A drag force is experienced by the fluid sphere due to the net force in the direction of flow owing to the pressure and shear stress

$$C_D = C_{\mathrm{Dp}} + C_{\mathrm{Df}} \tag{18}$$

where the pressure drag is given by

$$C_{\mathrm{Dp}} = \int_0^\pi 2p \sin\theta\cos\theta d\theta \tag{19}$$

The stagnation pressure is obtained by integrating the r component of the momentum equation along $\theta=0$ from $r=\infty$ to 1. The pressure variation along the surface is obtained by integrating the θ component of the momentum equation along $r=1$ [10]

The friction drag is

$$C_{\mathrm{Df}} = \frac{\int_0^\pi (\tau_{r\theta}{}^* \sin\theta - \tau_{rr}{}^* \cos\theta) 2\pi R \sin\theta\, R\, d\theta}{(1/2)\rho_1 U_\infty{}^2 \pi R^2}$$

In dimensionless form it becomes

$$C_{\mathrm{Df}} = \frac{8}{\mathrm{Re}} \int_0^\pi \left[\left(\frac{\partial U_{1\theta}}{\partial r} - U_{1\theta} \right) \sin\theta - 2\frac{\partial U_{1r}}{\partial r} \cos\theta \right] \sin\theta\, d\theta. \tag{20}$$

Nusselt Numbers. For the continuous phase the average Nusselt number is given by

$$\overline{\mathrm{Nu}} = \int_0^\pi -\frac{\partial T_1}{\partial r} \sin\theta\, d\theta \tag{21}$$

Local nusselt number $\mathrm{Nu}_{\mathrm{loc}} = h_{\mathrm{loc}} 2R/k_1 = -2(\partial T_1/\partial r)$.

The Nusselt number for the dispersed phase can be written in terms of the bulk temperature by overall heat balance for the drop as [5]

$$\mathrm{Nu} = \frac{2}{3} \frac{1}{(1-T_b)} \frac{dT_b}{dt}. \tag{22}$$

The bulk temperature is calculated as

$$T_b = \frac{3}{2} \int_0^1 \int_0^\pi T_2 r^2 \sin\theta\, d\theta\, dr. \tag{23}$$

Table 1 Validation of results for drag coefficient for a rigid sphere. Pr=0.7.

Re	20	40	50	60	100
Cd (Model)	2.79	1.83	1.61	1.46	1.10
Cd (Comer & Kleinstreuer)[13]		1.80	1.58	1.43	1.09
Cd (Clift et al.[12])	2.71	1.79	1.57	1.42	1.09
Nu (Model)		5.031	5.453	5.836	7.06
Nu (Comer & Kleinstreuer[13])		5.007	5.398	5.749	6.906
Nu (Clift et al.[12])		5.077	5.457	5.795	6.894

Numerical Solution and Model Validation

We solve the external problem with an exponential transformation, $r=e^z$, whereas the internal flow and energy equations are solved in the regular spherical coordinate system. The governing equations are discretized using a finite volume approach with the power-law scheme of Patankar [11]. In both phases, 60×200 grid points were used in the tangential and radial directions, respectively. The results were obtained by doubling the grid in both directions to make sure that the results are grid independent. The changes in Nusselt number and drag coefficient were substantially less than 1%. The computational infinity is located at $z=5$ or $r_\infty=148.41$. Earlier numerical analyses of heat/mass transfer to a drop translating in the intermediate Reynolds number regime indicate that the computational infinity located beyond 20 diameters is adequate [2]. To check the sensitivity of r_∞, we doubled the value of r_∞ and executed a case for Re=100, Pr=0.7 for a solid sphere. The change in results was negligible ($<0.5\%$).

The model was validated by comparing results for several limiting cases where numerical and experimental results are available in published literature. These include flow over a solid sphere (Clift et al. [12], and Comer and Kleinstreuer [13]) in Table 1, flow over a liquid drop with $k_\mu>1$(Comer and Kleinstruer [14]) in Table 2, and flow over a liquid drop with $k_\mu<1$(Oliver and Chung [15]) in Table 3. Furthermore, the surface velocity profiles for different Reynolds numbers and viscosity ratios were calculated and were found to match closely with those of Oliver and Chung [15] for $k_\mu=0.3$ and 3. Comparison of steady state Nusselt number for heat transfer in a drop suspended in uniform electric field is shown in Table 4 for internal problem (Oliver et al. [4]) and in Table 5 for external problem (Sharpe and Morrison [7]). The above comparisons validate our numerical model for the limiting cases of $W=0$ and $W=\infty$. For finite values of W, results are compared with those of Chung and Oliver [5]. Chung and Oliver use a different notation (E instead of W) to indicate the relative strength of the electric field. Figure 2 shows the transient variation of Nusselt number for two values of E plotted with the results from Ref. [5]. Table 6 provides a comparison of the steady state Nusslet number for three values of E. It is clear from Tables 1–6 and Fig. 2, that in all of these cases our results for drag coefficients and Nusselt numbers agree very closely with published results. The excellent agreement of our results with earlier numerical results and experimental correlations discussed above can be considered as validation of our computational model.

Table 2 Validation of results for C_d and Nusselt Number for a fluid sphere (k_μ=40.2)

Re	50	70	90	110
Cd	1.56	1.28	1.11	0.99
Cd (Comer & Kleinstreuer[14])	1.57	1.27	1.13	1.01
Nu	5.36	6.04	6.62	7.14
Nu (Comer & Kleinstreuer[14])	5.43	6.11	6.70	7.24

Table 3 Validation of results for C_d for a liquid sphere (k_μ =0.3)

Re	5	10	20	50
Cd	4.98	2.81	1.63	0.84
Cd (Oliver & Chung [15])	4.89	2.87	1.71	0.89

Results and Discussion

Results were obtained for the Reynolds number based on the external flow of 20, 50, 80, and 100; $Pr_1=5$, and the density ratio of 1. The electric field parameter W is varied from 0 (for no electric field) to 10 for high electric field.

Table 4 Comparison of results for internal steady state Nusselt number

Peclet Number	Steady state Nu (Model)	Steady state Nu (Oliver et al. [4])
10	6.69	6.6
50	7.53	7.5
100	10.21	10.0
500	25.43	25.6
750	28.01	28.0
1000	28.82	29.0

Table 5 Comparison of results for average external Nusselt number

Peclet Number	Average Nu (Model)	Average Nu (Sharpe & Morrison [7])
1	4.83	4.80
10	5.06	5.10
50	7.68	7.55
100	9.53	9.50
500	22.16	22.00
750	35.64	35.20

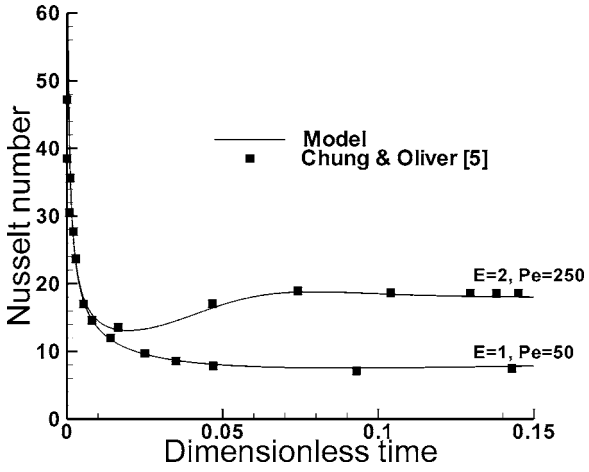

Fig. 2 Comparison of the transient variation of Nusslet number with Chung and Oliver (Ref. [5]). Chung and Oliver have used a notation where the relative electric field strength is called *E* (instead of *W*).

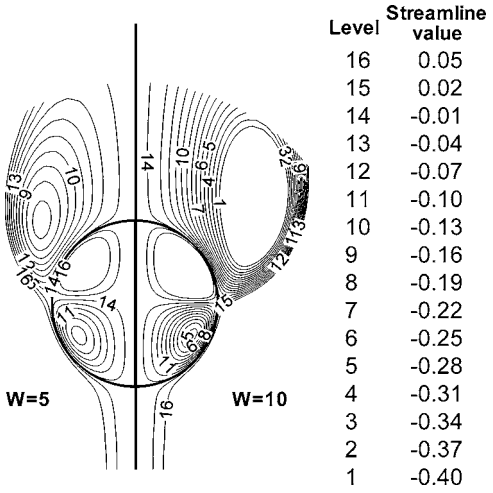

Level	Streamline value
16	0.05
15	0.02
14	-0.01
13	-0.04
12	-0.07
11	-0.10
10	-0.13
9	-0.16
8	-0.19
7	-0.22
6	-0.25
5	-0.28
4	-0.31
3	-0.34
2	-0.37
1	-0.40

Fig. 4 Internal and external streamlines for $W=5$ and 10, Re $=50$, $k_\mu=3$

Effect of Electric Field on the Flow

In Figs. 3 and 4, the streamlines are plotted for different values of $W=0$, 1, 5, and 10 for translational Reynolds number of 50. As discussed by Oliver and Chung [15], unlike the flow over a solid sphere, for $k_\mu=3$, the flow does not have a large circulatory vortex in the drop rear for a purely translating drop at Re$=50$. This is seen in left hand side of the Fig. 3. The applied electric field develops shear stress that produces a flow field with two vortices in the drop interior. For positive values of W, the electrically induced flow is from the poles to the equator. Therefore, when applied to a translating drop, the electric field tends to strengthen the internal circulation in the front half of the drop and introduces a weaker vortex in the rear half of the drop. This vortex in the rear half of the drop produces a large recirculating pattern downstream of the drop. This is seen in the right half of Fig. 3. As W is increased further, the magnitude of the electrically induced stress on the surface increases and consequently the strength of the recirculation in the drop increases. As evident in Fig. 4, at very high electric field with $W=10$, the flow in the drop interior resembles the flow in a drop suspended in electric field. However, at this high electric field strength, the outer flow retains the effect of translational motion away from the drop surface.

Figure 5 shows the surface pressure variation for $W=0$ and 1. It is observed that as the applied electric field increases the stagnation pressure decreases. With no electric field, we see that the surface pressure drops from stagnation pressure to a minimum and then recovers to a value much lower than the front stagnation pressure. From the graph, it is clear that the surface pressure at

Table 6 Comparison of results for Pe=250 (based on surface velocity) with Chung and Oliver (Ref. [5])

Ratio of surface velocity with electric field to that with purely translational motion (E in the notation of Ref. 5)	Steady state Nu (Chung & Oliver [5])	Steady state Nu (Model)
1	17.33	17.41
2	18.70	18.79
6	23.20	23.13

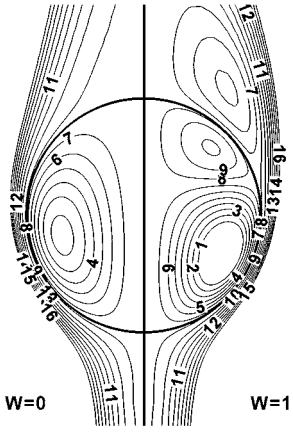

Level	Streamline values
16	0.063
15	0.055
14	0.048
13	0.040
12	0.033
11	0.025
10	0.018
9	0.010
8	0.003
7	-0.005
6	-0.013
5	-0.020
4	-0.028
3	-0.035
2	-0.043
1	-0.050

Fig. 3 Internal and external streamlines for $W=0$ and 1, Re $=50$, $k_\mu=3$

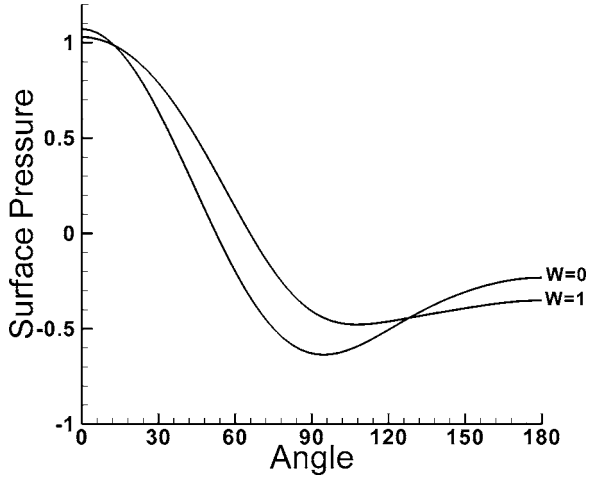

Fig. 5 Variation of surface pressure for $W=0$ and 1, Re=50, and $k_\mu=3$

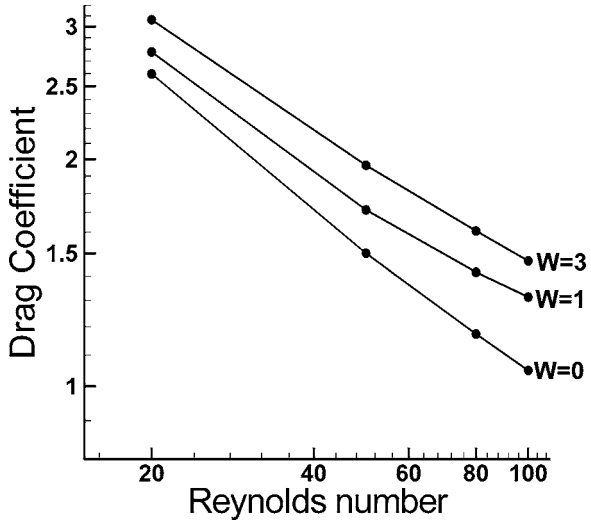

Fig. 6 Variation of drag coefficient with Reynolds numbers for different values of W with $k_\mu=3$

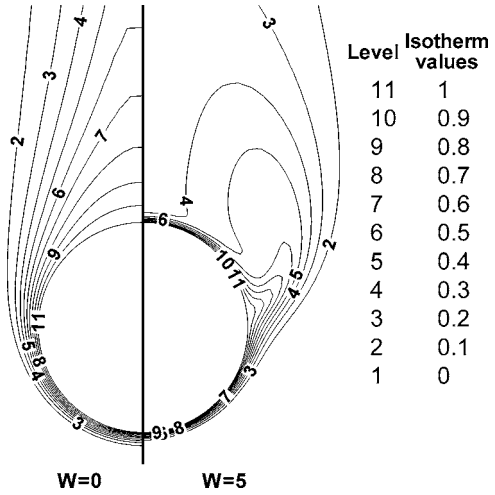

Fig. 7 External isotherms for $W=0$ and 5 at $Re=50$, $Pr_1=5$, and $k_\mu=3$

$W=1$ maintains a higher value than that for $W=0$ at at the front side of the drop. This leads to an increase in pressure difference between the front and the rear half of the drop. Thus the pressure drag coefficient increases as W increases. The tangential shear stress will significantly increase with application of electric field in the rear half of the drop but decrease slightly in the front half of the drop. This is due to the change in the surface velocity with the application of the electric field. Once the electric field is applied, the surface velocity increases in the front half of the drop. This decreases the shear stress experienced by the drop in the front half. The surface velocity in the rear half of the drop is in the opposite direction of the flow which leads to higher shear stress in the rear half of the drop. The overall effect is an increase in the friction drag with increase in W. The variation of the coefficient of drag with Reynolds number is shown in Fig. 6 for different values of W. It is found that, at a given flow Reynolds number, the drag coefficient increases with the applied electric field. In general, for particular electric field strength the drag coefficients decrease with increase in Reynolds number.

Heat Transfer

The External Problem. We first consider the external heat transfer problem with the limit of majority of the heat transfer resistance being in the continuous phase. Figure 7 shows the isotherms for $W=0$ and 5, for $Re=50$. In both cases, as expected, the temperature contours are dense near the front stagnation point, indicating high temperature gradients. With $W=5$, the large recirculation in the drop rear brings hot fluid close to the drop surface, and hence, the temperature gradients are high at the rear part of the drop as well. The variation of the local Nusselt number with application of electric field is shown in Fig. 8 for Reynolds numbers of 50. With no applied electric field, $W=0$, the local Nusselt number decreases monotonically along the drop surface at this Reynolds number and at lower Re. However, higher Reynolds number, the local Nusselt number decreases to a minimum value and then increases slightly in the rear portion of the drop due to a recirculatory vortex that is present even without the application of the electric field at high Reynolds number. The recirculation tends to bring fluid close to the drop surface and consequently increasing the local Nusselt number slightly in the rear of the drop. This phenomenon is significantly increased with application of electric field. At higher W, the circulation in drop rear is so large and strong that the local Nusselt number increases to values closer to those found at the front stagnation point. Moreover, with applied electric field, with increased surface velocity in the front half of the drop, the Nusselt number in the front of the drop increases as well. The net effect of higher heat transfer rate both in the front and the rear, results in a significant increase in the overall Nusselt number with increasing W. Figure 9 shows the enhancement in heat transfer with increase in W at different Reynolds number. It is seen from the figure that significant enhancement in heat transfer is obtained for $W>1$. The increase in Nusselt number with increase in W is more pronounced at higher Reynolds number.

The Internal Problem. The transient internal temperature variation is solved using an alternating direction implicit scheme. The steady state Nusselt number is then computed using the bulk mean temperature. Figure 10 shows the variation of Nusslet number with dimensionless time for different vales of W. We note that increase in W results in increase in the maximum tangential velocity at the drop surface. In all earlier work, the results were presented in terms of Peclet number based on the maximum surface velocity. For all values of W, conduction is the dominant heat transfer mechanism at short times. This is due to the steep temperature gradients near the drop surface. For low W, conduction is the dominant mechanism at all times. At higher W, which corresponds to higher Peclet number based on the surface velocity, the Nusselt number first decreases for short times and starts increas-

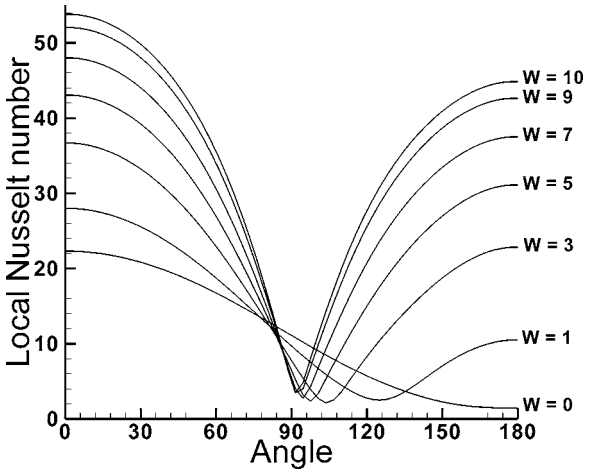

Fig. 8 Local Nusselt number variation with application of electric field at $Re=50$, $Pr_1=5$, and $k_\mu=3$

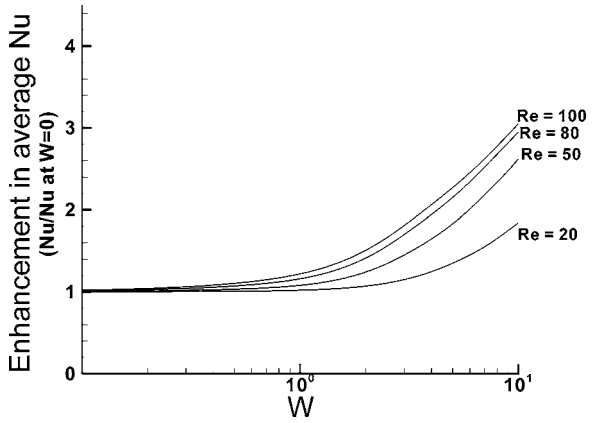

Fig. 9 Enhancement in average Nusselt number with W for different values of Reynolds number (20, 50, 80, and 100), Pr_1 =5, and k_μ=3

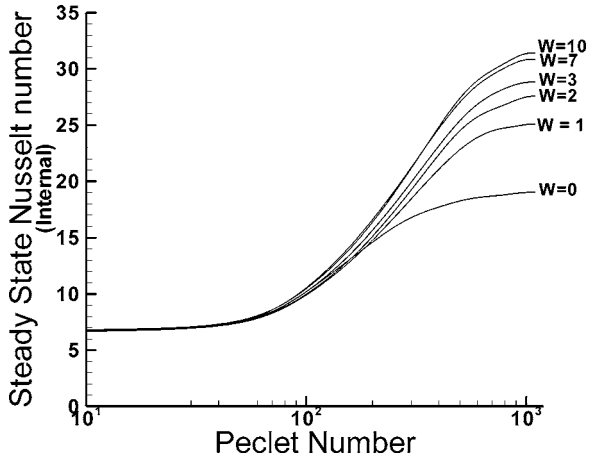

Fig. 11 Variation of steady state Nusselt number with Peclet number, Re=80, and k_μ=3

ing thereafter. This is because the cold fluid from the drop interior is brought near the drop surface due to the circulatory motion. This results in the oscillation of the Nusselt number before it reaches a steady value. These oscillations are more pronounced for higher values of W. As a result of fluid convection, the temperature gradients along each streamline diminish. Then the heat transport is mainly in the direction perpendicular to the streamlines. Hence, the Nusselt number variation attains a steady state.

Figure 11 shows the variation of the steady state Nusselt number with Peclet number based on the maximum surface velocity for different electric field strengths. It is observed that at lower Peclet numbers, the steady state Nusselt number does not vary much with the electric field strength. At high Peclet numbers, the increase in the steady state Nusselt number with the increase of the applied electric field is high. We note that the maximum steady state Nusselt number due to purely electric field induced flow for a suspended drop is 30 in creeping flow regime. We see that the maximum steady state Nusselt number obtained here at very high values of W is more than that for a pure electric field driven flow. This is because the internal streamlines are shifted towards the boundary at higher Reynolds number due to the larger velocity gradients at higher Reynolds number. Figure 12 compares the internal streamlines in our case with that of a pure electric field driven flow. At high Peclet number, the temperature becomes uniform along each streamline very quickly and the heat transfer continues primarily perpendicular to the streamlines. The rate of heat transfer is inversely proportional to the distance of the vortex center to the drop surface. With a slight decrease in this distance at higher Reynolds number, the Nusselt numbers are correspondingly higher than the maximum Nusselt number of 30 obtained for creeping flow. Such increase in the maximum Nusselt number was reported by Hader and Jog [16,17] for deformed drops.

Effect of Viscosity Ratio (k_μ)

Different values of k_μ=0.7, 1.1, 3, 5, and 10 are used to study the effect of viscosity ratio on the flow and heat transport properties. The change in the coefficient of drag is computed and is plotted in Fig. 13 for these values of viscosity ratios. Without electric field, the drag coefficient is higher with higher viscosity ratio. However, at high W, the trend is reversed. The maximum tangential velocity of the drop surface is higher at lower viscosity ratio. Therefore increasing W has a larger effect for k_μ=3 than for k_μ=10. The Nusselt numbers in the five values of viscosity ratio are plotted in Fig. 14. It is observed that the average Nusselt number at a particular value of the applied electric field strength decreases as the viscosity ratio k_μ increases. This is because, as k_μ increases, the dispersed phase fluid becomes more viscous than the continuous phase fluid and the strength of the internal circulation decreases with higher viscosity ratio. At low values of electric field strength, the difference in Nusselt number is less than that at higher values of electric field strength. We note that the maximum tangential surface velocities for k_μ<1 are substantially

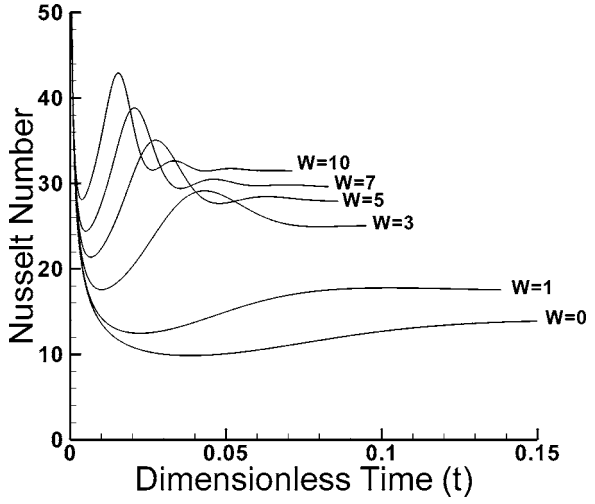

Fig. 10 Variation of Nusselt number with dimensionless time $t=t^*\alpha_2/R^2$ for Re=50, Pr_2=21.21, and k_μ=3

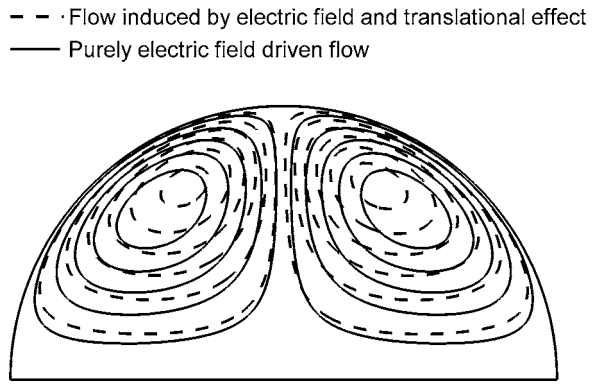

Fig. 12 Comparison of internal stream lines for flow due to electric field and translational motion at Re=80 (dashed lines), and internal stream lines for purely electric field driven flow for a suspended drop (solid lines)

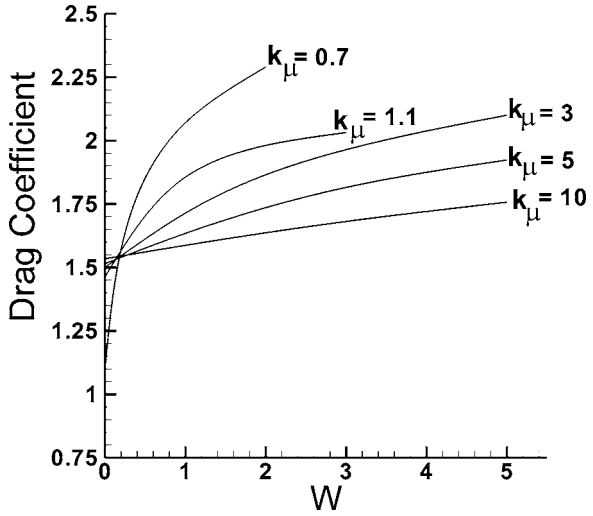

Fig. 13 Variation of drag coefficient with *W* for different viscosity ratios k_μ=0.7, 1.1, 3, 5, and 10, Re=50

greater than those obtained with $k_\mu > 1$. As *W* indicates the ratio of maximum surface velocity with electric field to that with purely translational motion, for $k_\mu < 1$, even for moderate values of *W*, the surface velocity becomes greater than the free stream velocity. In an intermediate Reynolds number regime, it is doubtful if a stable, axi-symmetric (as assumed in the formulation) flow would be obtained under such conditions. For k_μ=0.7, we were not able to obtain stable solutions for $W > 4$.

Conclusions

The heat transfer to a spherical droplet translating in an electric field has been studied in the intermediate Reynolds number regime. The external and the internal heat transfer problems were considered. From this study we can draw the following conclusions:

- The applied electric field induces shear stress at the drop surface that produces a flow field with two vortices in the drop interior for a translating drop. It strengthens the internal circulation in the front half of the drop and creates a weaker vortex in the rear. The magnitude of the electrically induced stress on the surface increases and consequently the strength of the recirculation in the drop increases as the magnitude of the electric field is increased. With increase in electric field strength, the flow separation at the drop rear is more pronounced.
- The overall drag coefficient increases with increasing electric field strength. The change in the drag coefficient is lower at higher viscosity ratio between the dispersed and the continuous phase.
- With no applied electric field, the local Nusselt number decreases monotonically from the front stagnation point. With application of the electric field, the local Nusselt number increases both in the front and the rear half of the drop. The increase in the local Nusselt number is significantly higher in the rear part of the drop compared to the front part of the drop. Consequently, the average Nusselt number increases with increase in the applied electric field.
- For a fixed value of *W*, the increase in average Nusselt number is higher at higher Reynolds numbers.
- In the internal problem, the maximum steady state Nusselt number attained at high Peclet numbers were substantially higher than those obtained for a purely translational motion. Moreover, the maximum steady state Nusselt numbers at high Peclet numbers for a drop moving in an electric field were found to be more than those obtained for a purely electric field driven flow.
- For a given electric field strength, the average Nusselt number decreases as the viscosity ratio increases.

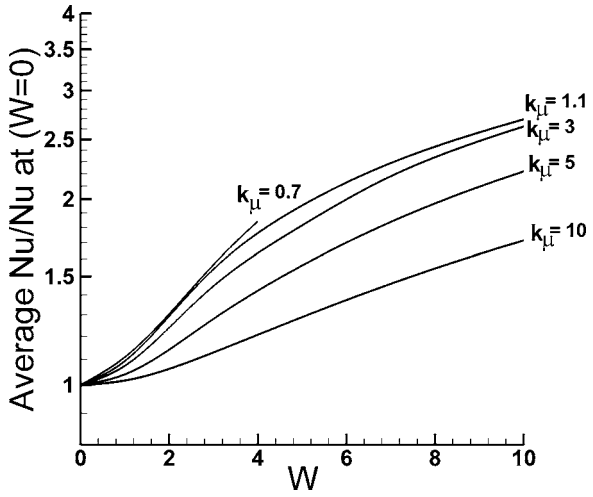

Fig. 14 Enhancement of heat transfer with W for different viscosity ratios k_μ=0.7, 1.1, 3, 5, and 10, Re=50, and Pr_1=5

Nomenclature

a = parameter in Eq. (17)
C_d = drag coefficient
d = dielectric constant
h = heat transfer coefficient
k = thermal conductivity
k_ν = kinematic viscosity ratio, ν_2/ν_1
k_μ = dynamic viscosity ratio, μ_2/μ_1
Nu = Nusselt number based on drop diameter, $h\,2R/k$
p = pressure
Pe = Peclet number based on drop diameter, $U_\infty 2R/\alpha$
Pr = Prandtl number, ν/α
r = radial coordiante
R = radius of the spherical droplet
Re = Translational Reynolds number, $U_\infty 2R/\nu_1$
t = time
T = temperature
U = velocity
V = maximum electric field induced tangential velocity
$\hat{W}$ = ratio of maximum electric field induced surface velocity for a suspended drop to that for a purely translating drop in creeping flow $4V^*(1+k_\mu)/U_\infty$
W = ratio of maximum electric field induced surface velocity for a suspended drop to that for a purely translating drop in intermediate Reynolds number regime
(r, θ, ϕ) = spherical coordinates

Greek symbols

α = thermal diffusivity
μ = dynamic viscosity
ν = kinematic viscosity
ρ = density
σ = electrical resistivity
τ = stress
ψ = stream function
ω = vorticity

Subscripts

0 = initial
1 = continuous phase
2 = dispersed phase
b = bulk
s = surface
∞ = far field

Superscripts

$*$ = dimensional quantities

References

[1] Taylor, G. I., 1966, "Studies in Electrohydrodynamics: the Circulation Produced in a Drop by an Electric Field," Proc. R. Soc. London, Ser. A **291**, pp. 159–166.

[2] Sadhal, S. S., Ayyaswamy, P. S., and Chung, J. N., 1997, *Transport Phenomena with Drops and Bubbles*, Springer New York.

[3] Abramzon, B., and Borde, I., 1980, "Conjugate Unsteady Heat Transfer From a Droplet in Creeping Flow," AIChE J., **26**, pp. 536–544.

[4] Oliver, D. L. R., Carleson, T. E., and Chung, J. N., 1985, "Transient Heat Transfer to a Fluid Sphere Suspended in an Electric Field," Int. J. Heat Mass Transfer, **28**, pp. 1005–1009.

[5] Chung, J. N., and Oliver, D. L. R., 1990, "Transient Heat Transfer in a Fluid Sphere Translating in an Electric Field," ASME J. Heat Transfer, **112**, pp. 84–91.

[6] Griffiths, S. K., and Morrison, F. A., Jr., 1979, "Low Peclet Number Heat and Mass Transfer From a Drop in an Electric Field," ASME J. Heat Transfer, **101**, pp. 484–488.

[7] Sharpe, L., Jr., and Morrison, F. A., Jr., 1984, "Numerical Analysis of Heat and Mass Transfer From Fluid Spheres in an Electric Field," ASME J. Heat Transfer, **108**, pp. 337–342.

[8] Chang, L. S., and Berg, J. C., 1983, "Fluid Flow and Transfer Behavior of a Drop Translating in an Electric Field at Intermediate Reynolds Numbers," Int. J. Heat Mass Transfer, **26**, pp. 823–831.

[9] Feng, J. Q., and Scott, T. C., 1996, "A Computational Analysis of Electrohydrodynamics of a Leaky Dielectric Drop in an Electric Field," J. Fluid Mech., **311**, pp. 289–326.

[10] Subramanian, R., 2005, "Heat Transfer to a Droplet Translating in an Electric Field," M.S. thesis, University of Cincinnati.

[11] Patankar, S. V., 1980, *Numerical Heat Transfer and Fluid Flow*, McGraw-Hill, New York.

[12] Clift, R., Grace, J. R., and Weber, M. E., 1978, *Bubbles, Drops, and Particles*, Academic, New York.

[13] Comer, J. K., and Kleinstreuer, C., 1995, "A Numerical Investigation of Laminar Flow Past Nonspherical Solids and Droplets," ASME J. Fluids Eng., **117**, pp. 170–175.

[14] Comer, J. K., and Kleinstreuer, C., 1995, "Computational Analysis of Convection Heat Transfer to Non-spherical Particles," Int. J. Heat Mass Transfer, **38**, pp. 3171–3180.

[15] Oliver, D. L. R., and Chung, J. N., 1987, "Flow About a Fluid Sphere at Low to Moderate Reynolds Numbers," J. Fluid Mech., **177**, pp. 1–18.

[16] Jog, M. A., and Hader, M. A., 1997, "Transient Heat Transfer to a Spheroidal Liquid Drop Suspended in an Electric Field," Int. J. Heat Fluid Flow, **18**, pp. 411–418.

[17] Hader, M. A., and Jog, M. A., 1998, "Effect of Drop Deformation on Heat Transfer to a Drop Suspended in an Electric Field," ASME J. Heat Transfer, **120**, pp. 682–689.

A Theory of Film Condensation in Horizontal Noncircular Section Microchannels

Hua Sheng Wang
e-mail: h.s.wang@qmul.ac.uk

John W. Rose
e-mail: j.w.rose@qmul.ac.uk

Department of Engineering,
Queen Mary,
University of London,
London E1 4NS, United Kingdom

The paper presents a theoretical model to predict film condensation heat transfer from a vapor flowing in horizontal square and equilateral triangular section minichannels or microchannels. The model is based on fundamental analysis which assumes laminar condensate flow on the channel walls and takes account of surface tension, interfacial shear stress, and gravity. Results are given for channel sizes (side of square or triangle) in the range of 0.5–5 mm and for refrigerants R134a, R22, and R410A. The cases considered here are where the channel wall temperature is uniform and the vapor is saturated at the inlet. The general behavior of the condensate flow pattern (spanwise and streamwise profiles of the condensate film), as well as streamwise variation of local mean (over section perimeter) heat-transfer coefficient and vapor mass quality, are qualitatively in accord with expectations on physical grounds. The magnitudes of the calculated heat-transfer coefficients are in general agreement with experimental data for similar, but nonidentical, channel geometry and flow parameters. [DOI: 10.1115/1.2033905]

Keywords: Condensation, Heat Transfer Enhancement, Microchannel, Noncircular Tube, Theory, Surface Tension, R134a, R22, R410A, Refrigerant

Introduction

Heat transfer in microchannels has received increasing attention in recent years. Earlier single-phase flow measurements indicated unexpected results for channel dimensions of around 1 mm. These are now thought to be attributable to experimental error and surface roughness (see Palm [1]); only at much smaller hydraulic diameters are methods for larger channels inappropriate in single phase flow. For condensation, however, special effects due to surface tension become important for *noncircular* channels with hydraulic diameters around 1 mm. This is due to the so-called "Gregorig effect" [2] where changes in the condensate surface curvature, in conjunction with surface tension, lead to pressure gradients in the condensate film and enhanced heat transfer. This has received considerable attention in connection with condensation on low-finned and inside microfinned tubes (these are discussed together with other surface tension affected condensation problems by Rose [3]).

Recent work on condensation in small channels has been reviewed by Cavallini et al. [4]. Heat-transfer measurements for condensation in microchannels have been made by Yang and Webb [5], Vardhan and Dunn [6], Yan and Lin [7], Kim et al. [8], Zhang and Webb [9], Webb and Ermis [10], Wang et al. [11], Garimella and Bandhauer [12], Ermis and Ekmekci [13], Kim et al. [14], Kim et al. [15], and Baird et al. [16]. In most of these investigations the vapor-side, heat-transfer coefficients are based on overall measurements using "Wilson plots" and consequently have large uncertainty (see Rose [17]).

The fact that heat transfer for condensation in small channels has been found to be largely independent of orientation of the tube suggests that the flow regime may be essentially annular for a significant portion of the channel where most of the heat transfer takes place. Increase in the extent of the annular flow regime with decrease in hydraulic diameter for adiabatic air-water flow and for condensation of R134a have been demonstrated (see Coleman [18], Coleman and Garimella [19–21], and Garimella [22]). Thus, for small diameter channels, uncertainties in calculation methods associated with stratified, wavy, and slug/plug flow regimes found with larger tubes, are reduced, making the problem more amenable to theoretical analysis. However, as discussed below, surface tension greatly complicates theoretical analysis through the involvement of curvature of the condensate surface.

More recently, experimental investigations have been made in which the tube wall temperature has been measured. Measurements using multimicrochannel tubes with channels having hydraulic diameters of around 1 mm have been made by Koyama et al. [23,24] and Cavallini et al. [25,26]. Data are reported for R134a and R410A. Available empirical and semi-empirical models underpredict these data except at the lowest vapor mass fluxes.

The important mechanism of heat transfer enhancement during condensation in noncircular microchannels is the surface tension generated transverse pressure gradient in the condensate film. This leads to condensate flow towards the corners and thins the film along the sides of the channel giving rise to high heat-transfer and condensation rates. The transverse pressure gradient arises from variation of condensate surface curvature along the side of the channel. Maximum thinning of the film occurs at approach to the corners where the interface curvature changes abruptly. When the channel dimension is small (microchannel) the ultrathin portion of the film may occupy a significant part of the channel surface. A theoretical approach along similar lines to the present work has been reported by Zhao and Liao [27]. Zhao and Liao consider downflow in a vertical triangular channel and give specimen numerical results for condensation of steam. Other differences of detail between the Zhao and Liao model and the present work are discussed by Wang and Rose [28].

The present work relates to condensation in horizontal square and triangular microchannels. Preliminary results have been reported (Wang et al. [29], Wang and Rose [28,30]). The overall objective of the research program is to establish methods for determination of the optimum channel shape and dimensions for given duty.

Theoretical Model

As in the treatment of Honda et al. [31] for condensation in microfin tubes, the condensate film on the channel walls is treated

Contributed by the Heat Transfer Division of ASME for publication in the JOURNAL OF HEAT TRANSFER. Manuscript received by the Heat Transfer Division September 14, 2002; revision received June 16, 2005. Review conducted by: J. Chung.

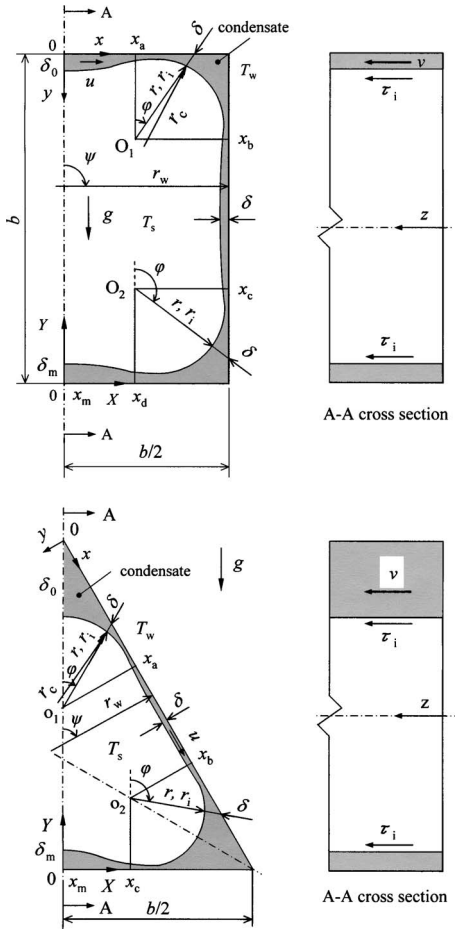

Fig. 1 Physical model and coordinates for horizontal microchannels

by including surface tension and surface curvature effects together with the Nusselt approximations for the condensate film, that is, laminar flow with neglect of inertia and convection terms. The problem and coordinates for square and triangular section microchannels are illustrated in Fig. 1. X and Y are fixed orthogonal coordinates with the origin at the center of the lower channel surface. x is measured along the channel surface from the center of the top surface of the square section or the top corner of the triangular section along the channel surface, y is measured normally outward from the channel surface, and z is measured along the channel in the direction of vapor flow. x_a, x_b, x_c, and x_d are the x coordinates at the foot of the perpendicular from origins O_1 and O_2 of the polar coordinates. r is the radial polar coordinate measured from origins O_1 and O_2 and φ is the polar angle shown in Fig. 1. r_i is the r coordinate of the condensate surface. The values of x_a, x_b, x_c, and x_d are chosen so that origins O_1 and O_2 are located in the vapor space. b is the side length of the channel cross section. As described below and shown in Fig. 1, the condensate flow on the channel walls is treated coupling orthogonal coordinates (x,y) for the flow on the sidewalls and polar coordinates (r,φ) for the flow at the corners.

Condensation on Sidewalls. On the sidewalls of the channel ($0 \leqslant x \leqslant x_a$, $x_b \leqslant x \leqslant x_c$, and $x_d \leqslant x \leqslant x_m$ for square section; $x_a \leqslant x \leqslant x_b$ and $x_c \leqslant x \leqslant x_m$ for triangular section), the condensate film thickness δ is defined normal to the channel surface as shown in Fig. 1. Neglecting the surface tension-induced pressure gradient in the z direction, the momentum equation for the condensate film on the side walls in the x direction and in the z direction are, respectively

$$\mu_l \frac{\partial^2 u}{\partial y^2} + (\rho_l - \rho_v) g \sin \Psi = \frac{\partial P}{\partial x} \tag{1}$$

$$\mu_l \frac{\partial^2 v}{\partial y^2} = \frac{\partial P_l}{\partial z} \tag{2}$$

where u and v are the velocity components in the x direction and in the z direction, respectively, μ_l is the dynamic viscosity of condensate, ρ_l and ρ_v are the densities of condensate and vapor, respectively, g is the specific force of gravity, Ψ is the angle of the normal to the channel surface to the Y coordinate (see Fig. 1), and P is the pressure difference (liquid side minus vapor side) between the condensate and vapor due to the effect of surface tension given by

$$P = -\sigma / r_c \tag{3}$$

where σ is the surface tension and r_c is the local radius of the curvature of condensate surface measured on the vapor side in the plane normal to the channel given by

$$\frac{1}{r_c} = \frac{\partial^2 \delta / \partial x^2}{\{1 + (\partial \delta / \partial x)^2\}^{3/2}}$$

for $0 \leqslant x \leqslant x_a$, $x_b \leqslant x \leqslant x_c$

and $x_d \leqslant x \leqslant x_m$ for square section

for $x_a \leqslant x \leqslant x_b$ and $x_c \leqslant x \leqslant x_m$ for triangular section (4)

P_l is the pressure in the condensate film. Neglecting streamwise variation of the condensate surface curvature

$$\frac{\partial P_l}{\partial z} = \frac{dP_v}{dz} \tag{5}$$

where P_v is the vapor pressure and dP_v/dz is obtained from a momentum balance for one-dimensional vapor flow

$$\frac{dP_v}{dz} + \frac{\rho_v}{A_v} \frac{d}{dz}(U_v^2 A_v) + \frac{\tau_i S_i}{A_v} = 0 \tag{6}$$

where A_v and S_i are the area of vapor flow and perimeter of the vapor-liquid interface in channel cross section, respectively, U_v is taken as the local average velocity of the vapor which is calculated from the inlet mass flow minus the condensation rate up to the position in question, τ_i is the streamwise interfacial shear stress.

Neglecting transverse interfacial shear stress, the boundary conditions for Eqs. (1) and (2) are

$$u = v = 0 \quad \text{at} \quad y = 0 \tag{7}$$

$$\partial u / \partial y = 0 \quad \text{at} \quad y = \delta \tag{8}$$

$$\mu_l \partial v / \partial y = \tau_i \quad \text{at} \quad y = \delta \tag{9}$$

The effect of condensation (suction) is taken into account by using the approach suggested by Mickley et al. [32] for flow over a flat plate with suction and described in Kays, Crawford, and Weigand [33]. The approach was also used to treat condensation in tube by Cavallini et al. [34]. The interfacial surface shear stress is

$$\tau_i = \frac{1}{2} f \rho_v U_v^2 \tag{10}$$

where

$$f = \frac{\phi}{e^{\phi} - 1} f_v \tag{11}$$

$$\phi = -\frac{2m}{f_v \rho_v U_v} \tag{12}$$

m is the condensation flux, f_v is the zero transpiration friction factor obtained by the Churchill [35] equation

$$f_v = 2\left[\left(\frac{8}{\mathrm{Re}_v}\right)^{12} + \frac{1}{(A+B)^{3/2}}\right]^{1/12} \tag{13}$$

where

$$A = \left\{-4\sqrt{2}\log\left[\left(\frac{6.9}{\mathrm{Re}_v}\right)^{0.9} + \frac{k}{3.71 d_{\mathrm{hv}}}\right]\right\}^{16} \tag{14}$$

$$B = \left(\frac{37530}{\mathrm{Re}_v}\right)^{16} \tag{15}$$

$\mathrm{Re}_v (=\rho_v U_v d_{\mathrm{hv}}/\mu_v)$ is taken as the local Reynolds number of vapor flow, k is the surface roughness here taken as zero, d_{hv} is the hydraulic diameter of the vapor flow area calculated from the local condensate surface profile. In evaluating τ_i, the local value of U_v was used in Eq. (10) and in Re_v in Eqs. (11)–(15).

Integrating Eqs. (1) and (2) subject to boundary conditions (7)–(9) across the condensate film in the y direction yields

$$u = \frac{1}{\mu_l}\left[(\rho_l - \rho_v) g \sin\Psi + \sigma\frac{\partial}{\partial x}\left(\frac{1}{r_c}\right)\right]\delta^2\left[\left(\frac{y}{\delta}\right) - \frac{1}{2}\left(\frac{y}{\delta}\right)^2\right] \tag{16}$$

$$v = \frac{\tau_i}{\mu_l} y - \frac{1}{\mu_l}\left(\frac{dP_v}{dz}\right)\delta^2\left[\left(\frac{y}{\delta}\right) - \frac{1}{2}\left(\frac{y}{\delta}\right)^2\right] \tag{17}$$

For condensation on the sidewalls ($0 \leqslant x \leqslant x_a$, $x_b \leqslant x \leqslant x_c$ and $x_d \leqslant x \leqslant x_m$ for square section; $x_a \leqslant x \leqslant x_b$ and $x_c \leqslant x \leqslant x_m$ for triangular section), the condensate flow rates per length in the x direction m_x and in the z direction m_z are given by

$$m_x = \int_0^\delta \rho_l u dy = \frac{1}{3\nu_l}\left[(\rho_l - \rho_v) g \sin\Psi + \sigma\frac{\partial}{\partial x}\left(\frac{1}{r_c}\right)\right]\delta^3 \tag{18}$$

$$m_z = \int_0^\delta \rho_l v dy = \frac{\tau_i}{2\nu_l}\delta^2 - \frac{1}{3\nu_l}\left(\frac{dP_v}{dz}\right)\delta^3 \tag{19}$$

where ν_l is the kinematic viscosity of the condensate.

The temperature drop at the vapor-liquid interface (generally unimportant but could be significant due to high condensation rate where the film is very thin) may readily be included. Equation (20) below, for the interface temperature drop $\Delta T_i\ (T_s - T_i)$, is thought to be the most reliable (see Rose [36]) and takes the "condensation coefficient" as unity

$$\Delta T_i = \zeta q \tag{20}$$

where

$$\zeta = \frac{1}{4\xi}\frac{(\gamma+1)}{(\gamma-1)} T_s \sqrt{RT_s}/(\nu_{fg}/h_{fg}^2) \tag{21}$$

with $\xi = 0.665 \pm 0.003$, q is the local heat flux, γ is the ratio of the principal specific heat capacities, T_s is the saturation temperature of vapor, R is the specific ideal gas constant, v_{fg} is the difference between the vapor and liquid specific volumes, and h_{fg} is the specific enthalpy of evaporation.

The local heat flux q is then given by

$$q = \frac{1}{1 + \zeta\lambda_l/\delta}\frac{\lambda_l (T_s - T_w)}{\delta}$$

for $0 \leqslant x \leqslant x_a$, $x_b \leqslant x \leqslant x_c$,

and $x_d \leqslant x \leqslant x_m$ for square section

for $x_a \leqslant x \leqslant x_b$ and $x_c \leqslant x \leqslant x_m$ for triangular section (22)

where λ_l is the thermal conductivity of condensate, T_w is the temperature of channel surface.

Energy conservation gives

$$q = m h_{fg} \tag{23}$$

The condensing mass flux m is given by

$$m = \rho_l\left(\frac{\partial}{\partial x}\int_0^\delta u dy + \frac{\partial}{\partial z}\int_0^\delta v dy\right) = \frac{\partial m_x}{\partial x} + \frac{\partial m_z}{\partial z} \tag{24}$$

Substituting Eqs. (18), (19), (22), and (24) into Eq. (23) yields the differential equation for δ

$$\frac{(\rho_l - \rho_v) g}{3\nu_l}\frac{\partial}{\partial x}(\delta^3 \sin\Psi) + \frac{\sigma}{3\nu_l}\frac{\partial}{\partial x}\left\{\delta^3\frac{\partial}{\partial x}\left(\frac{1}{r_c}\right)\right\} + \frac{1}{2\nu_l}\frac{\partial(\tau_i\delta^2)}{\partial z} - \frac{1}{3\nu_l}\frac{\partial}{\partial z}\left(\delta^3\frac{dP_v}{dz}\right) = \frac{1}{(1+\zeta\lambda_l/\delta)}\frac{\lambda_l (T_s - T_w)}{h_{fg}\delta} \tag{25}$$

Condensation Towards the Corners. Near the corners of the channel ($x_a \leqslant x \leqslant x_b$ and $x_c \leqslant x \leqslant x_d$ for square section; $0 \leqslant x \leqslant x_a$ and $x_b \leqslant x \leqslant x_c$ for triangular section), orthogonal coordinates (x, y) cannot define the condensate film thickness; polar coordinates (r, φ) are therefore used here. The condensate film thickness δ is taken in the r direction ($\delta = r_w - r_i$) as shown in Fig. 1. The momentum equation for the condensate film at the corners in the φ direction and in the z direction are, respectively, written as

$$\mu_l\left\{\frac{\partial}{\partial r}\left[\frac{1}{r}\frac{\partial}{\partial r}(ru)\right]\right\} + (\rho_l - \rho_v) g \sin\varphi = \frac{1}{r}\frac{\partial P}{\partial \varphi} \tag{26}$$

$$\mu_l\left[\frac{1}{r}\frac{\partial}{\partial r}\left(r\frac{\partial v}{\partial r}\right)\right] = \frac{\partial P_l}{\partial z} \tag{27}$$

where u and v are the velocity components in the φ-direction and in the z direction, respectively, P is given by Eq. (3) and the radius of the curvature of the condensate surface r_c is given by

$$\frac{1}{r_c} = \frac{r_i^2 + 2(\partial r_i/\partial\varphi)^2 - r_i(\partial^2 r_i/\partial\varphi^2)}{\{r_i^2 + (\partial r_i/\partial\varphi)^2\}^{3/2}}$$

for $x_a \leqslant x \leqslant x_b$ and $x_c \leqslant x \leqslant x_d$ for square section

for $0 \leqslant x \leqslant x_a$ and $x_b \leqslant x \leqslant x_c$ for triangular section (28)

The boundary conditions for Eqs. (26) and (27) are

$$u = v = 0 \quad \text{at} \quad r = r_w \tag{29}$$

$$\partial u/\partial r = 0 \quad \text{at} \quad r = r_i \tag{30}$$

$$-\mu_l \partial v/\partial r = \tau_i \quad \text{at} \quad r = r_i \tag{31}$$

Integrating Eqs. (26) and (27) subject to boundary conditions (29)–(31) across the condensate film in the r direction yields

$$u = -\frac{1}{3\mu_l}\left[(\rho_l - \rho_v) g \sin\varphi + \frac{\sigma}{r}\frac{\partial}{\partial\varphi}\left(\frac{1}{r_c}\right)\right] \times\left\{r^2 - r_i\left[\frac{2 + (r_w/r_i)^3}{1 + (r_w/r_i)^2}\right]r + r_w^2 r_i\frac{2 - (r_w/r_i)}{1 + (r_w/r_i)^2}\frac{1}{r}\right\} \tag{32}$$

$$v = -\tau_i\frac{r_i}{\mu_l}\ln\left(\frac{r}{r_w}\right) + \frac{1}{4\mu_l}\left(\frac{dP_v}{dz}\right)\left[r^2 - 2r_i^2\ln\left(\frac{r}{r_w}\right) - r_w^2\right] \tag{33}$$

The condensate flow rates per length in the x and z directions are given by

$$m_\varphi = \int_{r_i}^{r_w} \rho_l u dr = \frac{1}{3\nu_l}\left[(\rho_l - \rho_v)g\sin\varphi + \frac{\sigma}{r}\frac{\partial}{\partial\varphi}\left(\frac{1}{r_c}\right)\right]\delta f_\varphi(\delta) \tag{34}$$

$$m_z = \int_{r_i}^{r_w} \rho_l v dr = \frac{1}{\nu_l}\tau_i \delta f_\tau(\delta) + \frac{1}{4\nu_l}\left(\frac{dP_v}{dz}\right)\delta f_z(\delta) \tag{35}$$

where

$$f_\varphi(\delta) = -r_w{}^2 + r_w\delta - \frac{\delta^2}{3} + \left(r_w - \frac{\delta}{2}\right)(r_w - \delta)\frac{2 + \left(\frac{r_w}{r_w - \delta}\right)^3}{1 + \left(\frac{r_w}{r_w - \delta}\right)^2}$$
$$- \frac{r_w{}^2(r_w - \delta)}{\delta}\frac{2 - \left(\frac{r_w}{r_w - \delta}\right)}{1 + \left(\frac{r_w}{r_w - \delta}\right)^2}\ln\left(\frac{r_w}{r_w - \delta}\right) \tag{36}$$

$$f_\tau(\delta) = (r_w - \delta)\left[1 + \frac{(r_w - \delta)}{\delta}\ln\left(\frac{r_w - \delta}{r_w}\right)\right] \tag{37}$$

$$f_z(\delta) = -r_w\delta + \frac{\delta^2}{3} + 2(r_w - \delta)^2\left[1 + \frac{(r_w - \delta)}{\delta}\ln\left(\frac{r_w - \delta}{r_w}\right)\right] \tag{38}$$

Conduction across condensate film gives

$$\lambda_l\left[\frac{1}{r}\frac{\partial}{\partial r}\left(r\frac{\partial T}{\partial r}\right)\right] = 0$$
$$\text{for } x_a \leq x \leq x_b$$
$$\text{and } x_c \leq x \leq x_d \text{ for square section}$$
$$\text{for } 0 \leq x \leq x_a$$
$$\text{and } x_b \leq x \leq x_c \text{ for triangular section} \tag{39}$$

The boundary conditions for Eq. (39) are

$$T = T_i \quad \text{at} \quad r = r_i \tag{40}$$

$$T = T_w \quad \text{at} \quad r = r_w \tag{41}$$

Integrating Eq. (39) subject to boundary conditions (40) and (41) using Eq. (20) yields

$$q = \frac{1}{1 + \frac{\zeta\lambda_l}{r_w \ln(r_w/r_i)}}\frac{\lambda_l(T_s - T_w)}{r_w \ln(r_w/r_i)}$$
$$\text{for } x_a \leq x \leq x_b \text{ and } x_c \leq x \leq x_d \text{ for square section}$$
$$\text{for } 0 \leq x \leq x_a \text{ and } x_b \leq x \leq x_c \text{ for triangular section} \tag{42}$$

The condensing mass flux m is given by

$$m = \rho_l\left(\frac{\partial}{r_w\partial\varphi}\int_{r_i}^{r_w} u dr + \frac{\partial}{\partial z}\int_{r_i}^{r_w} v dr\right) = \frac{1}{r_w}\frac{\partial m_\varphi}{\partial\varphi} + \frac{\partial m_z}{\partial z} \tag{43}$$

Substituting Eqs. (34), (35), (42), and (43) into Eq. (23) yields the differential equation for δ in the corner region

$$\frac{(\rho_l - \rho_v)g}{3\nu_l}\frac{\partial}{r_w\partial\varphi}[\delta f_\varphi(\delta)\sin\varphi] + \frac{\sigma}{3\nu_l}\frac{\partial}{r_w\partial\varphi}\left[\delta f_\varphi(\delta)\frac{\partial}{r\partial\varphi}\left(\frac{1}{r_c}\right)\right]$$
$$+ \frac{1}{\nu_l}\frac{\partial}{\partial z}[\delta f_\tau(\delta)\tau_i] + \frac{1}{4\nu_l}\frac{\partial}{\partial z}\left[\delta f_z(\delta)\frac{dP_v}{dz}\right]$$
$$= \frac{1}{1 + \frac{\zeta\lambda_l}{r_w \ln[r_w/(r_w - \delta)]}}\frac{\lambda_l(T_s - T_w)}{h_{fg} r_w \ln[r_w/(r_w - \delta)]} \tag{44}$$

Boundary Conditions on Differential Equations of δ. The differential equations (25) and (44) for δ are fourth order in x and φ, respectively, and first order in z. By symmetry the boundary conditions are

$$\partial\delta/\partial x = 0 \quad \text{at} \quad x = 0 \tag{45}$$

$$\partial^3\delta/\partial x^3 = 0 \quad \text{at} \quad x = 0 \tag{46}$$

for square section channel

$$\partial\delta/\partial\varphi = 0 \quad \text{at} \quad \varphi = 0 \ (x = 0) \tag{47}$$

$$\partial^3\delta/\partial\varphi^3 = 0 \quad \text{at} \quad \varphi = 0 \ (x = 0) \tag{48}$$

for triangular section channel and

$$\partial\delta/\partial x = 0 \quad \text{at} \quad x = x_m \tag{49}$$

$$\partial^3\delta/\partial x^3 = 0 \quad \text{at} \quad x = x_m \tag{50}$$

for both square and triangular section channels.

For the case of saturation conditions at the inlet (considered here) the necessary further boundary condition is

$$\delta = 0 \quad \text{at} \quad z = 0 \tag{51}$$

Heat-Transfer Coefficient. At a given location z along the channel, the local heat-transfer coefficient α_x is defined as

$$\alpha_x = q/(T_s - T_w) = \frac{1}{1 + \zeta\lambda_l/\delta}\frac{\lambda_l}{\delta}$$
$$\text{for } 0 \leq x \leq x_a,\ x_b \leq x \leq x_c,$$
$$\text{and } x_d \leq x \leq x_m \text{ for square section}$$
$$\text{for } x_a \leq x \leq x_b \text{ and } x_c \leq x \leq x_m \text{ for triangular section} \tag{52a}$$

$$\alpha_x = q/(T_s - T_w) = \frac{1}{1 + \frac{\zeta\lambda_l}{r_w \ln[r_w/(r_w - \delta)]}}\frac{\lambda_l}{r_w \ln[r_w/(r_w - \delta)]}$$
$$\text{for } x_a \leq x \leq x_b \text{ and } x_c \leq x \leq x_d \text{ for square section}$$
$$\text{for } 0 \leq x \leq x_a \text{ and } x_b \leq x \leq x_c \text{ for triangular section} \tag{52b}$$

The average heat-transfer coefficient α_z for the channel at this location is defined as

$$\alpha_z = q_z/(T_s - T_w) \tag{53}$$

where

$$q_z = \frac{1}{x_m}\left(\int_0^{x_a} q dx + \int_{\varphi_a}^{\varphi_b} q r_w d\varphi + \int_{x_b}^{x_c} q dx + \int_{\varphi_c}^{\varphi_d} q r_w d\varphi\right.$$
$$\left. + \int_{x_d}^{x_m} q dx\right) \text{for square channel} \tag{54a}$$

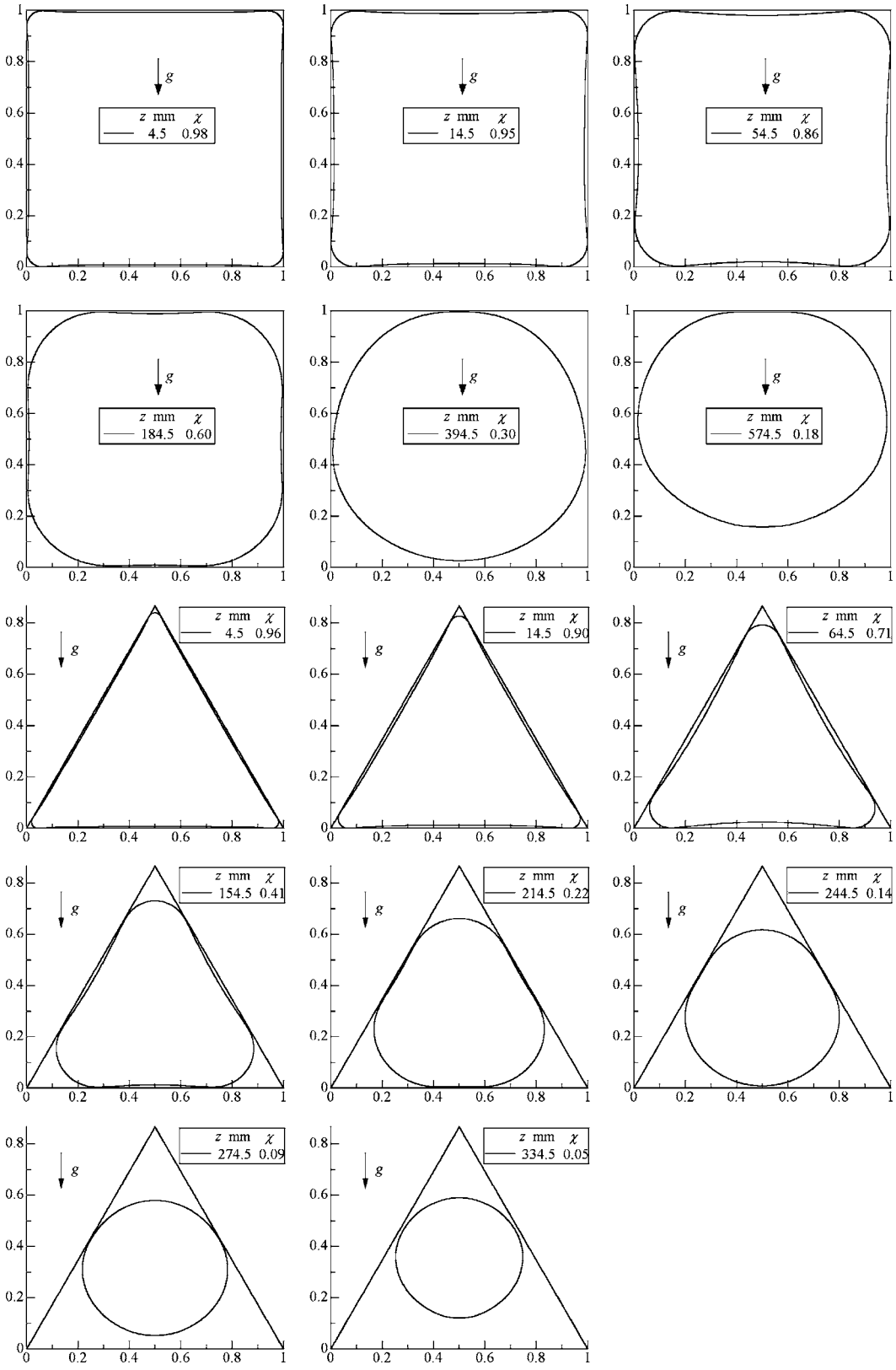

Fig. 2 Condensate film profiles along channel surface at different distances. Effects of interfacial shear stress, surface tension and gravity included. R134a, b=1.0 mm, T_s=50 °C, ΔT=6 K, G =500 kg/m^2 s.

$$q_z = \frac{1}{x_m}\left(\int_0^{\varphi_a} qr_w d\varphi + \int_{x_a}^{x_b} qdx + \int_{\varphi_b}^{\varphi_c} qr_w d\varphi + \int_{x_c}^{x_m} qdx\right) \text{for triangular channel} \quad (54b)$$

It is noted that in the present theory one-dimensional pure conduction is assumed in the direction of the radial polar coordinate at the corners. This is not true when the condensate film becomes thick. However, this will have small effect because where the error is large the heat transfer is very small.

Computation Scheme. Equations (25) and (44), subject to the boundary conditions (45)–(51), are solved numerically by a finite difference scheme. For the purposes of computation the unsteady term $\rho_l \partial\delta/\partial t$ is included on the left side of Eqs. (25) and (44) and the steady state solution subject to an arbitrary initial ($t=0$) distribution of δ is obtained. The computation starts at the inlet of channel with a small step length Δz and proceeds in the direction of vapor flow. For each z, computation is conducted until the convergence criteria $|1-\delta^*_{i,j}/\delta_{i,j}|<10^{-4}$ and $|1-\delta^*_{i,j}/\delta_{i,j}|/\Delta t^* < 0.01$ are satisfied, where $\delta_{i,j}$ and $\delta_{i,j}$ are the old and new values of δ at the grid point (i,j), and Δt^* is the dimensionless time step. The origins O_1 and O_2 are first selected near the corners when the condensate film is thin and moves towards the center of channel cross section as the condensate film becomes thicker. Dependence of numerical results on grid size along x (or φ) and step length Δz were tested. A grid size of 300 grid points along x (or φ) and a value of Δz of 1.0 mm were used.

Results and Discussion

Numerical results are given below for condensation of R134a, R22, and R410A in square and triangular section horizontal microchannels with side in the range of 0.5–5 mm. The physical properties of the refrigerants were obtained from REFPROP [37]. Condensate properties were taken to be uniform at reference temperature

$$T^* = \frac{1}{3}T_s + \frac{2}{3}T_w \quad (55)$$

and σ and h_{fg} were obtained at T_s.

Computations were conducted including and excluding the "interface resistance" (see Eqs. (20)–(22) and (42)). For the fluid and conditions used in the present calculation the terms $\zeta\lambda_l/\delta$ in Eq. (22) and $\zeta\lambda_l/[r_w \ln(r_w/r_i)]$ in Eq. (42) were found to be much less than unity and the effect of "interface resistance" is negligible due to the low refrigerant liquid conductivity as expected. The terms are retained here since they cause no difficulty in the solution and could be significant for fluids such as water and ammonia.

Figure 2 shows specimen calculated condensate film profiles along a channel surface at different distances for R134a with mass velocity 500 kg/m^2 s. Thinning of the film in the vicinity of change in condensate surface curvature may be seen. This is most evident near the inlet. It is interesting to note that, for the case of the square channel, the film remains thin along a significant part of the upper surface at appreciable distances along the channel. As will be seen later this is reflected in values of local mean (around the periphery of the channel) heat-transfer coefficients.

Figure 3 shows the profiles of local film thickness for square and triangular section horizontal microchannels at different distances along channel. It is seen that the film is thick in the corners ($x=0.5$ mm, 1.5 mm for square channel; $x=0$ mm, 1.0 mm for triangular channel). Towards the inlet the film is seen to be very thin near the corners, the thin film region moving towards the centers of the sides at further distances along the channel.

Figure 4 shows the corresponding profiles of local heat-transfer coefficient along the sides of channel surface. These are essentially reciprocals of the curves in Fig. 3. Low values of the heat-transfer coefficient are seen at the corners and high values where the film is very thin. The peaks in the heat-transfer coefficient become smaller and move towards the centre of the sides at larger distances along the channel.

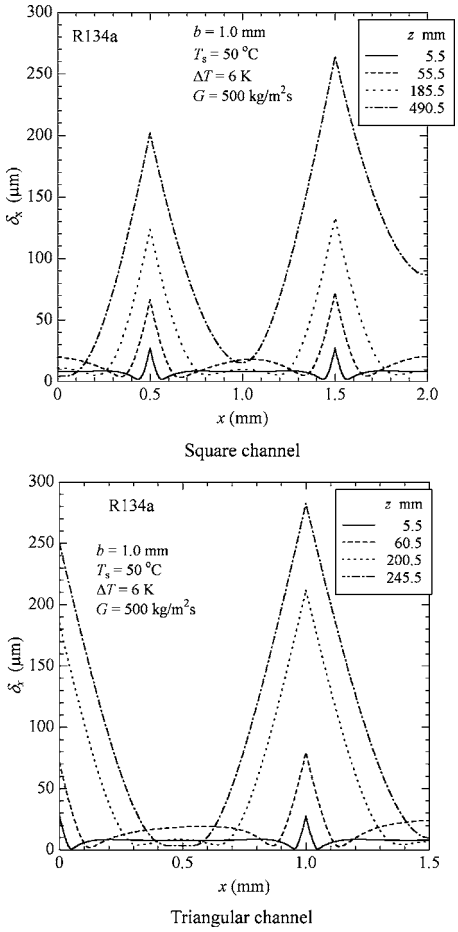

Fig. 3 Local film thickness along channel surface at different distances. Effects of interfacial shear stress, surface tension and gravity included.

Figure 5 shows the dependence of circumferential mean heat-transfer coefficient α_z on distance along the square and triangular channels when all three mechanisms (τ, σ, g) of condensate drainage are included in the calculation (solid line), when gravity is removed (dashed line) and when both surface tension and gravity are removed (chain dot line). The enhancing effect of surface tension over the first 250–350 mm in this case is clearly seen, approximately doubling the heat-transfer coefficient over that part of the channel for both square and triangular channels. The effect of gravity is essentially negligible in this region. The high heat-transfer coefficient at the inlet results from imposing a temperature difference between wall and vapor at the onset of condensation. After the initial high values the coefficient remains almost constant until, when condensate in the corners occupies a substantial part of the channel (see Fig. 2), it falls more steeply, particularly for the triangular channel. The importance of gravity at further distances along the channel is much more significant for the square section channel, approximately doubling the heat-transfer coefficient, due to the thinning of the film on the upper surface mentioned earlier and seen in Fig. 2. For the triangular channel gravity continues to have small effect at further distances along the channel reflecting the condensate profiles seen in Fig. 2.

Figure 6 shows the variation of circumferential mean heat-transfer coefficient with distance along the channel for different mass velocities. It is seen that the enhancing effect of surface

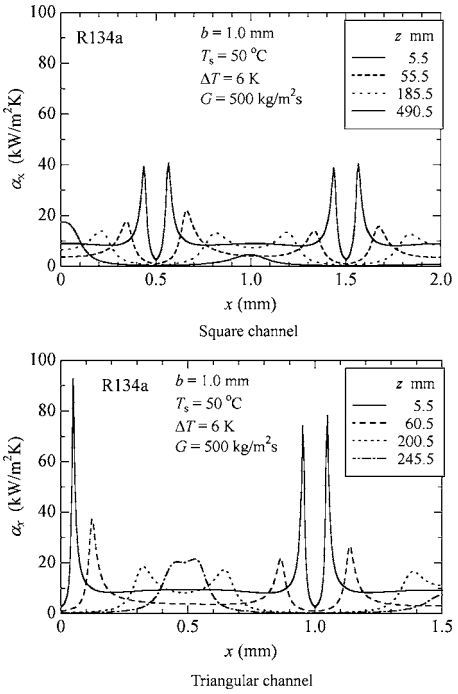

Fig. 4 Local heat-transfer coefficient along channel surface at different distances

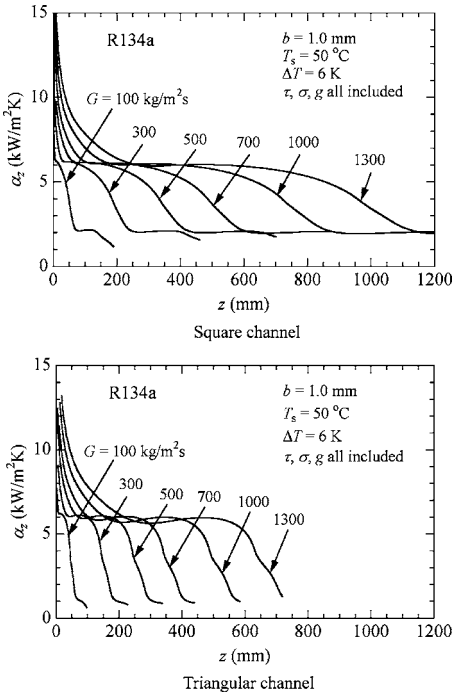

Fig. 6 Variation of mean (over perimeter of channel) heat-transfer coefficient with distance for several fluid mass velocities

tension takes place over a longer distance of the channel for higher mass velocity. It is interesting to note that the values over the horizontal portions of the curves are almost the same for all mass velocities, suggesting perhaps that the effect of surface tension is the dominating mechanism for that part of the channel. It may also be noted that the heat-transfer coefficient is almost the same for the square and triangular channels for the surface tension dominated part of the channel. Figure 7 shows the variation of vapor mass quality χ with distance along the channel for different mass velocities for the two channel geometries.

Figure 8 shows the effect of channel orientation for a triangular section horizontal microchannel. It is seen that the orientation has negligible effect where the surface tension effect dominates.

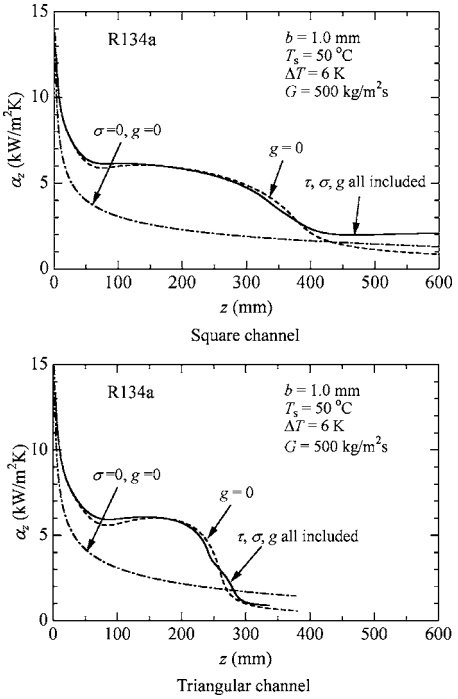

Fig. 5 Variation of mean (over perimeter of channel) heat-transfer coefficient with distance

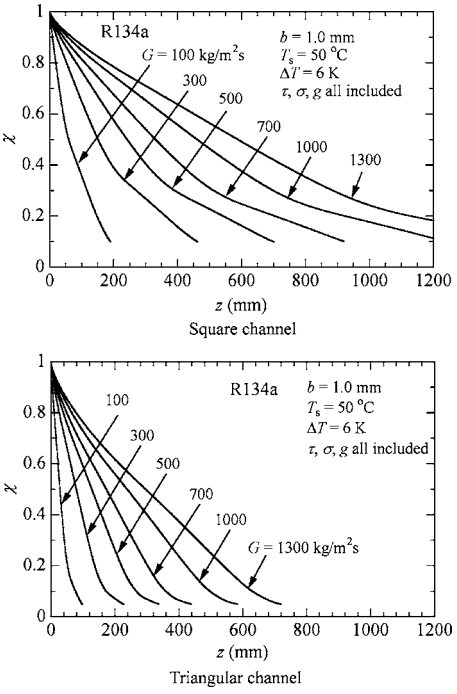

Fig. 7 Variation of vapor mass quality with distance along channels and mass velocity

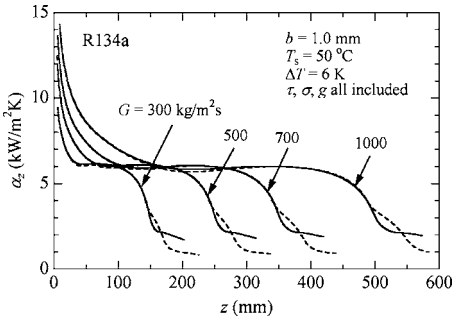

Fig. 8 Effect of orientation for triangular channel. Solid line: inverted triangle; dashed line: upright triangle.

Figure 9 shows the effect of vapor-to-surface temperature difference. It is seen that the heat-transfer coefficient is higher and for a longer distance along the channel for lower vapor-to-surface temperature difference reflecting lower condensation rates and correspondingly thinner condensate films.

Figure 10 shows the effect of channel size for a square section horizontal microchannel. Heat-transfer coefficients are shown for square channels having side of 0.5, 1.0, 2.0, 3.0, and 5.0 mm. The

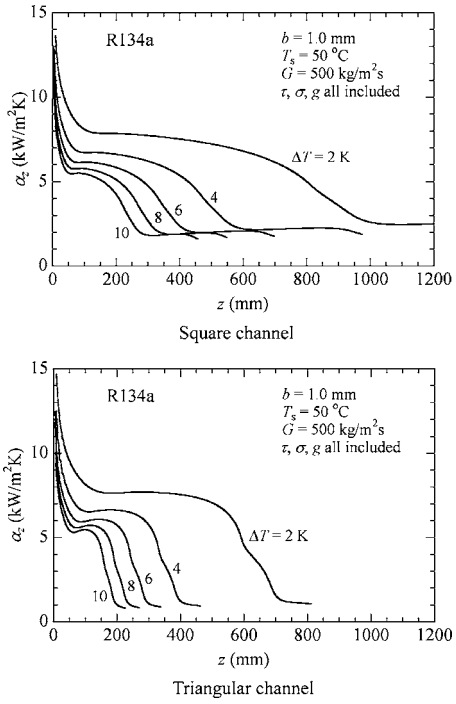

Fig. 9 Effect of vapor-to-surface temperature difference

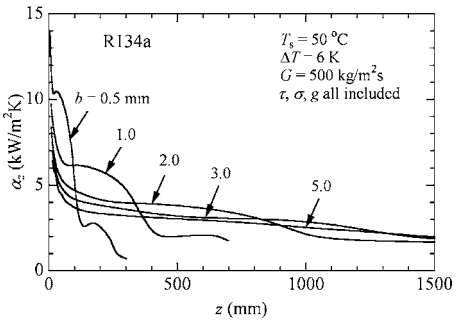

Fig. 10 Effect of channel size for square section channels

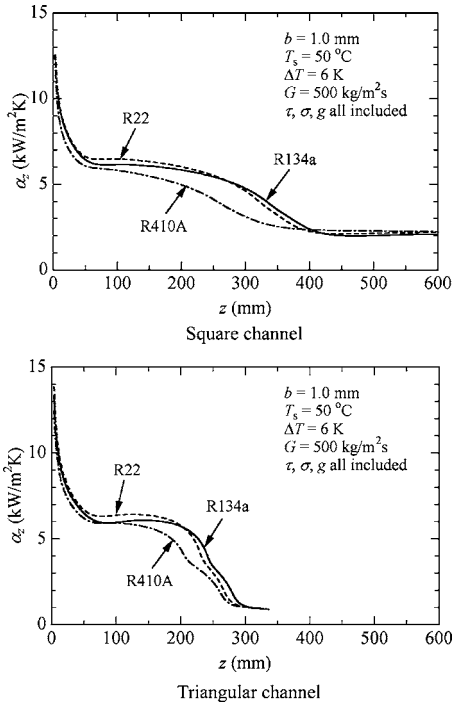

Fig. 11 Effects of fluid properties

enhancing effect of surface tension in the entry part of the channel is higher for the smaller channels but falls off more rapidly along the channel. The smaller channels become more rapidly "flooded" with condensate so that the heat-transfer coefficient further along the channel is significantly lower than for the larger channels. For channels with 3 and 5 mm there is little, if any, discernable effect of surface tension enhancement.

Figure 11 shows the effect of fluid properties on condensation heat-transfer in square and triangular section horizontal microchannels. R410A (50%R32/50%R125) is a near-azeotropic mixture with "glide" temperature difference about 0.2 K and was treated as a pure fluid. For the conditions used the heat-transfer coefficients for R134a and R22 are similar while those for R410A are significantly lower. This may be attributable to the vapor density, vapor-to-liquid density ratio, and surface tension. The higher vapor density and lower surface tension of R410A reduce the interfacial shear stress and surface tension force, respectively.

In order to make detailed comparisons with recent experimental data (Koyama et al. [23], Cavallini et al. [25]) it will be necessary to make calculations with the geometries and conditions used in these investigations. In particular, modification of the calculation procedure to accommodate superheat conditions at the inlet will be necessary. This work is currently in progress and will be reported later. In the meantime it is interesting to make an approximate comparison with the data of Koyama et al. [23] shown in Fig. 12 for the tube illustrated in Fig. 13. Focusing on the heat-transfer coefficient α (diamond symbol), in the lower part of Fig. 12 it may be seen that α is significantly higher over the first 250 mm than for the remainder of the channel with values in the approximate range $5-10\ \mathrm{kW/m^2\,K}$. These may be compared with the calculated values for the square and triangular channels and non-identical conditions shown in Fig. 5. In passing it is noted in Fig. 12 that the small temperature difference on the vapor side ($T_R - T_{wi}$, Koyama et al. notation) compared with that on the coolant side ($T_{wi} - T_s$, Koyama et al. notation) illustrates the problem of obtaining satisfactory vapor-side data from overall measurements (i.e., without surface temperature measurement) in this type of experiment.

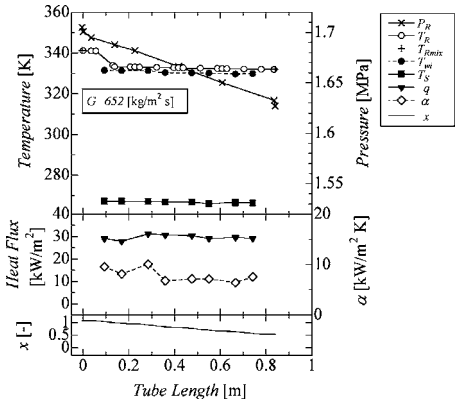

Fig. 12 Data of Koyama et al. (Ref. [23]) for condensation of R134a in tube B (see Fig. 13). P_R is refrigerant pressure, T_R is refrigerant temperature, T_{Rmix} is refrigerant temperature at mixing chamber, T_{wi} is inside wall temperature, T_S is coolant temperature, q is heat flux, α is heat-transfer coefficient, χ is refrigerant vapor mass quality.

Fig. 13 Tube B used by Koyama et el. (Ref. [23]). Hydraulic diameter 0.81 mm.

Concluding Remarks

A theoretical model for heat transfer during condensation in square and triangular section horizontal microchannels has been developed and implemented. The model includes the effects of interfacial shear stress, gravity and transverse surface tension force on the motion of the condensate film. Results are presented for fluids of R134a, R22, and R410A in square and triangular section channels of side in the range of 0.5–5 mm and for mass velocities in the range 100 −1300 kg/m^2 s. The general behavior of the flow pattern (spanwise and streamwise profiles of the condensate film), as well as streamwise variation in local mean (around the channel perimeter) heat-transfer coefficient and vapor mass quality, are qualitatively in accord with trends expected on physical grounds. The results demonstrate significant heat-transfer enhancement by surface tension towards the channel entrance. For smaller channels the initial enhancement is higher but falls off after a shorter distance along the channel; higher mass velocities result in increased length of enhanced heat transfer. For the three fluids tested heat-transfer coefficients for R22 and R134a are almost the same whereas those for R410A are somewhat smaller. The need to use optimum channel dimensions (cross section and length) for given applications (fluid, mass velocity, temperature difference) has been clearly demonstrated.

Acknowledgments

This work was supported by the Engineering and Physical Sciences Research Council (EPSRC) of the UK through Grants Nos. GR/S07209/01 and GR/S20345/01. Dr. Wang would like to thank Professor Hiroshi Honda for his kindness and supervision during the nice time in Kyushu University.

Nomenclature

A_v = vapor flow area
b = side length of square/triangle channel
d_h = hydraulic diameter
d_{hv} = hydraulic diameter of vapor flow area
f_v = friction factor of vapor flow
f_φ, f_τ, f_z = see Eqs. (36)–(38)
g = specific force of gravity
h_{fg} = specific enthalpy of evaporation
m = condensing mass flux
m_x = condensate flow rate per length in x direction, see Eqs. (18) and (34)
m_z = condensing flow rate per length in z direction, see Eqs. (19) and (35)
P = pressure
P_l = liquid pressure
P_v = vapor pressure
q = heat flux
r_c = radius of curvature of the condensate surface in the channel cross section, see Fig. 1
r = radial polar coordinate, see Fig.1
r_i = distance from origins O_1 , O_2 to vapor-liquid interface, see Fig. 1
r_w = radius of curvature of channel surface in the channel cross section, see Fig. 1
R = specific ideal gas constant
Re_v = Reynolds number of vapor flow, $\rho_v U_v d_{hv}/\mu_v$
S_i = perimeter of the vapor-liquid interface in channel cross section
T = temperature
T_s = saturation temperature
T_w = tube wall temperature
T^* = see Eq. (55)
ΔT_i = $T_s - T_i$
t = time
Δt = time step
Δt^* = $\Delta t \lambda_l (T_s - T_w)/\rho_l h_{fg} \delta^2$
u = condensate velocity along channel surface in the x direction or φ direction, see Fig. 1
v = condensate velocity along channel surface in the z direction, see Fig. 1
x,y = coordinates along and normal to channel surface, see Fig. 1
x_a, x_b, x_c, x_d = x coordinates at the foot of the perpendicular from origins O_1 and O_2, see Fig. 1
x_m = x coordinate at the center of the bottom surface, 1.5b for triangle and 2b for square, see Fig. 1
X,Y = fixed coordinates defined in Fig. 1
z = coordinate down stream, see Fig. 1

Greek symbols

α_x = local heat-transfer coefficient
α_z = average heat-transfer coefficient over perimeter of channel at location z
δ = condensate film thickness, defined in Fig. 1
λ = condensate thermal conductivity
ζ = see Eq. (21)
χ = vapor mass quality
ν = kinematic viscosity
ξ = see Eq. (21)
ρ = density
σ = surface tension
τ_i = interfacial shear stress at vapor-liquid interface
φ = angle, polar co-ordinate, see Fig. 1
ϕ = see Eq. (12)
ϕ_a, ϕ_b, ϕ_c, ϕ_d = angles corresponding to x_a, x_b, x_c, x_d, see Fig. 1
Ψ = angle between the normal of channel surface and Y coordinate, see Fig. 1

Subscripts

i = interface
l = condensate
s = saturation
v = vapor
w = wall
x = local
z = average at the location, z direction
φ = φ direction
τ = τ component

References

[1] Palm, B., 2003, "Mini- and Micro-Channel Research in Sweden," *Proc. 1st Int. Conf. on Microchannels and Minichannels*, Rochester, NY April 24–25, ASME, pp. 25–31.

[2] Gregorig, R., 1954, "Hautcondensation an Feingewelten Oberflachen bei Beruksichtigung der Oberflachenspannungen," Z. Angew. Math. Phys., **5**, pp. 36–49.

[3] Rose, J. W., 2004, "Surface Tension Effects and Enhancement of Condensation Heat Transfer," Trans. IChemE, Chem. Eng. Research and Design, **82**(A4), pp. 419–429.

[4] Cavallini, A., Censi, G., Del Col, D., Doretti, L., Longo, A. G., and Rossetto, L., 2002, "Condensation Heat Transfer and Pressure Drop inside Channels for AC/HP Application," *Proc. 12th Int. Heat Transfer Conference*, Grenoble, France, August 18–23, Vol. **1**, pp. 171–186.

[5] Yang, M., and Webb, R. L., 1996, "Condensation of R-12 in Small Hydraulic Diameter Extruded Aluminum Tubes with and without Micro-Fins," Int. J. Heat Mass Transfer, **39**, pp. 791–800.

[6] Vardhan, A., and Dunn, E. E., 1997, "Heat Transfer and Pressure Drop Characteristics of R-22, R-134a and R-407C in Microchannel Tubes," ACRC TR-133, University of Illinois at Urbana-Champaign.

[7] Yan, Y. Y., and Lin, T. F., 1999, "Condensation Heat Transfer and Pressure Drop of Refrigerant R134a in a Small Pipe," Int. J. Heat Mass Transfer, **42**, pp. 697–708.

[8] Kim, N. H., Cho, J. P. and Kim, J. O., 2000, "R-22 Condensation in Flat Aluminum Multi-Channel Tubes," J. Enhanced Heat Transfer, **7**, pp. 427–438.

[9] Zhang, M., and Webb, R. L., 2001, "Correlation of Two-Phase Friction for Refrigerants in Small-Diameter Tubes," Exp. Therm. Fluid Sci., **25**, pp. 131–139.

[10] Webb, R. L., and Ermis, K., 2001, "Effect of Hydraulic Diameter on Condensation of R-134a in Flat, Extruded Aluminum Tubes," J. Enhanced Heat Transfer, **8**, pp. 77–90.

[11] Wang, W. W. W., Radcliff, T. D., and Christensen, R. N., 2002, "A Condensation Heat Transfer Correlation for Millimeter-Scale Tubing with Flow Regime Transition," Exp. Therm. Fluid Sci., **26**, pp. 473–485.

[12] Garimella, S., and Bandhauer, T. M., 2001, "Measurement of Condensation Heat Transfer Coefficients in Microchannel Tubes," *Proc. 2001 Int. Mechanical Engineering Congress and Exposition*, NY, IMECE 2001/ HTD-24221, November, pp. 1–7.

[13] Ermis, K., and Ekmekci, I., 2003, "Condensation Heat Transfer in a Small Hydraulic Diameter Extruded Aluminum Tubes," *Proc. 1st Int. Exergy, Energy and Environment Symp. 13–17 Izmir*, Turkey, July, pp. 201–206.

[14] Kim, N. H., Cho, J. P., Kim, J. O., and Youn, B., 2003, "Condensation Heat Transfer of R-22 and R-410A in Flat Aluminum Multi-Channel Tubes with and without Micro-Fins," Int. J. Refrig., **26**, pp. 830–839.

[15] Kim, M. H., Shin, J. S., Huh, C., Kim, T. J., and Seo, K. W., 2003, "A Study of Condensation Heat Transfer in a Single Mini-Tube and a Review of Korean Micro- and Mini-Channel Studies," *Proc. 1st Int. Conf. on Microchannels and Minichannels*, April 24–25, Rochester, NY, pp. 47–58.

[16] Baird, J. R., Fletcher, D. F., and Haynes, B. S., 2003, "Local Condensation Heat Transfer Rates in Fine Passages," Int. J. Heat Mass Transfer, **46**, pp. 4453–4466.

[17] Rose, J. W., 2004, "Heat-Transfer Coefficients, Wilson Plots and Accuracy of Thermal Measurements," Exp. Therm. Fluid Sci., **28**, pp. 77–86.

[18] Coleman, J. W., 2000, "Flow Visualization and Pressure Drop for Refrigerant Phase Change and Air-Water Flow in Small Hydraulic Diameter Geometries," Ph.D. thesis, Iowa State University.

[19] Coleman, J. W., and Garimella, S., 1999, "Characterization of Two-Phase Flow Patterns in Small Diameter Round and Rectangular Tubes," Int. J. Heat Mass Transfer, **42**, pp. 2869–2881.

[20] Coleman, J. W., and Garimella, S., 2000, "Two-Phase Flow Regime Transitions in Microchannel Tubes: The Effect of Hydraulic Diameter," Proc. ASME Heat Transfer Division, **366-4**, pp. 71–83.

[21] Coleman, J. W., and Garimella, S., 2000, "Visualization of Two-Phase Refrigerant Flow during Phase Change," *Proc. 34th Nat. Heat Transfer Conf.*, NHTC2000-12115, Aug. 20–22, Pittsburgh.

[22] Garimella, S., 2003, "Condensation Flow Mechanisms in Microchannels: Basis for Pressure Drop and Heat Transfer Models," *Proc. 1st Int. Conf. on Microchannels and Minichannels*, ASME, Rochester, NY, April 24–25, pp.181–192

[23] Koyama, S., Kuwahara, K., Nakashita, K., and Yamamoto, K., 2003, "Condensation of Refrigerant R134a in a Multiport Channel," *Proc. 1st Int. Conf. on Microchannels and Minichannels*, ASME, Rochester, NY, April 24–25, pp. 193–205.

[24] Koyama, S., Kuwahara, K., Nakashita, K., and Yamamoto, K., 2003, "An Experimental Study on Condensation of Refrigerant R134a in a Multiport Extruded Tube," Int. J. Refrig., **26**, pp. 425-432.

[25] Cavallini, A., Censi, G., Del Col, D., Doretti, L., Longo, A. G., Rossetto, L., and Zilio, C., 2003, "Experimental Investigation on Condensation Heat Transfer Coefficient Inside Multi-Port Channels," *Proc. 1st Int. Conf. on Microchannels and Minichannels*, ASME, Rochster, NY, April 24–25, pp. 691–698.

[26] Cavallini, A., Del Col, D., Doretti, L., Matkovic, M., Rossetto, L., and Zilio, C., 2004, "Condensation Heat Transfer Inside Multi-Port Minichannels," *Proc. 2nd Int. Conf. on Microchannels and Minichannels*, ASME, Rochester NY, pp. 625–632.

[27] Zhao, T. S., and Liao, Q., 2002, "Theoretical Analysis of Film Condensation Heat Transfer Inside Vertical Mini Triangular Channels," Int. J. Heat Mass Transfer, **45**, pp. 2829–2842.

[28] Wang, H. S., and Rose, J. W., 2004, "Condensation in Microchannels," *Proc. 6th Int. Symp. On Heat Transfer*, Beijing, China, June 15–19, pp. 22–31.

[29] Wang, H. S., Rose, J. W., and Honda, H., 2004, "A Theoretical Model of Film Condensation in Square Section Microchannels," Trans. IChemE, Chem. Eng. Research and Design, **82**(A4), pp. 430–434.

[30] Wang, H. S., and Rose, J. W., 2004, "Film Condensation in Horizontal Triangular Section Microchannels," *Proc. 2nd Int. Conf. on Microchannels and Minichannels*, ASME, Rochester, NY, pp. 661–666.

[31] Honda, H., Wang, H. S., and Nozu, S., 2002, "A Theoretical Study of Film Condensation in Horizontal Microfin Tubes," ASME J. Heat Transfer, **124**(1), pp. 94–101.

[32] Mickley, H. S., Ross, R. C., Squyers, A. L., and Stewart, W. E., 1954, "Heat, Mass and Momentum Transfer for Flow over a Flat Plate with Blowing or Suction," Rep. No. NACA-TN-3208.

[33] Kays, W. M., Crawford, M. E. and Weigand, B., 2005, *Convective Heat and Mass Transfer*, 4th ed., McGraw-Hill, New York, pp. 212–215.

[34] Cavallini, A., Del Col, D., Doretti, L., Longo, G. A., and Rossetto, L., 1999, "A New Computational Procedure for Heat Transfer and Pressure Drop during Refrigerant Condensation inside Enhanced Tubes," J. Enhanced Heat Transfer, **6**, pp. 441–456.

[35] Churchill, S. W., 1977, "Friction-Factor Equation Spans All Fluid-Flow Regimes," Chem. Eng., **84**, pp. 91–92.

[36] Rose, J. W., 1998, "Interphase Matter Transfer, the Condensation Coefficient and Dropwise Condensation," *Proc. 11th Int. Heat Transfer Conf.*, Kyongju, Korea, Aug., Vol. **1**, pp. 89–104.

[37] NIST Thermodynamic and Transport Properties of Refrigerants and Refrigerants Mixtures—REFPROP, Version 6.0.

Reduced Pressure Boiling Heat Transfer in Rectangular Microchannels With Interconnected Reentrant Cavities

Ali Koşar

Chih-Jung Kuo

Yoav Peles[1]
e-mail: pelesy@rpi.edu

Department of Mechanical, Aerospace and Nuclear Engineering,
Rensselaer Polytechnic Institute,
Troy, NY 12180

Boiling flow of deionized water through 227 μm *hydraulic diameter microchannels with* 7.5 μm *wide interconnected reentrant cavities at 47 kPa exit pressure has been investigated. Average two-phase heat transfer coefficients have been obtained over effective heat fluxes ranging from 28 to* 445 W/cm^2 *and mass fluxes from 41 to* 302 kg/m^2 s. *A map is developed that divides the data into two regions where the heat transfer mechanisms are nucleation or convective boiling dominant. The map is compared to similar atmospheric exit pressure data developed in a previous study. A boiling mechanism transition criterion based on the Reynolds number and the Kandlikar* k_1 *number is proposed.* [DOI: 10.1115/1.2035107]

Keywords: Reduced pressure, Microchannels, Nucleate Boiling, Convective Boiling

1 Introduction

Forced-convection boiling in microchannels is among the most effective engineering system known for heat removal and might be the cooling mechanism of choice for many ultra-high heat flux applications. As a direct result, tremendous research efforts to unravel the boiling characteristics in microchannels have been undertaken by various research groups [1–7]. Mehendale et al. [8], Kandlikar [3], Bergles et al. [9], Qu and Mudawar [4], and Thome [10] reviewed previous work on boiling flow in small channels and described both similarities and differences between boiling in microchannels and in their macroscale counterparts. A relatively large number of these studies is devoted to boiling characteristics of atmospheric pressure water. This focus on one atmosphere water is perhaps because extensive literature and knowledge exist for boiling water in conventional-scale channels, the relative ease of experimenting with water at atmospheric pressure, and the superior thermal properties of water (e.g., high latent heat of vaporization and thermal conductivity). Since the corresponding temperature of boiling water at atmospheric conditions (100 °C) is above maximum acceptable values for many applications (e.g., electronic chip cooling), it may be desirable to operate microchannel boiling systems either with water at a reduced pressure (i.e., lower boiling temperature) or utilize a coolant with a low vaporization temperature. Since most commercially available coolants possess significantly lower latent heat of vaporization than water ($\sim$10–20 times lower), the maximum attainable heat fluxes (i.e., the critical heat flux condition) are low compared to the requirements imposed by future ultra-high heat flux electronic chips. It follows that boiling water in microchannels at reduced pressures is a potentially preferable cooling mode of operation.

System pressure is an important parameter affecting flow boiling, and studies of its effects have been performed for conventional channels. According to the results of Klimenko [11], Liu and Winterton [12], and Steiner and Taborek [13], heat transfer coefficients increase with system pressure in conventional channels. Few studies [14–16] investigating the effects of system pressure on boiling heat transfer coefficients in small channels are present in the literature. The experimental study of Tran et al. [14] on circular channels with d_h=2.4 mm using R-12 showed a dependency on the system pressure, and it was observed that an increase in system pressure raised the heat flux-wall superheat temperature curve, while the slope was not altered. Bao et al. [15] studied saturated boiling flow inside a circular copper tube with an inner diameter of 1.95 mm and observed a moderate increase in the boiling heat transfer coefficient with increasing pressure for both R-11 and HCFC123 in the saturated boiling region, while system pressure apparently did not affect the subcooled boiling region. Huo et al. [16] used 2.01 mm and 4.26 mm tubes with R-134a as working fluid and showed that heat transfer coefficients (h_{tp}) increased with system pressure without a significant change in the h_{tp}—vapor quality slope. Owhaib et al. [17] used minichannels and demonstrated that boiling heat transfer coefficients are strongly increased by the system pressure.

A logical extension of conventional-scale knowledge implies that system pressure can alter boiling heat transfer characteristics in microscale systems; however, very limited data are available to test this hypothesis. Thus, the objective of this paper is to study boiling heat transfer at subatmospheric pressures in microchannels having re-entrant surface cavities as shown in Fig. 1. Results obtained in this study are compared with atmospheric pressure data given by Koşar et al. [18]. The effects of system pressure in microchannels are discussed, and a general map is developed to distinguish two regions in which nucleation or convective boiling is the dominant mechanism.

2 Experimental Device, Apparatus, and Procedures

Figure 1(*a*) depicts the microchannel device consisting of five 1 cm long, 200 μm wide, and 264 μm deep, parallel microchannels, spaced 200 μm apart. On each channel wall, the array of 100 interconnected reentrant cavities [Figs. 1(*b*) and 1(*c*)] are 100 μm apart. An acute angle connects the 7.5 μm mouth to the re-entrant body [Fig. 1(*e*)] and ensures its stability [19]. In order to minimize ambient heat losses, an air gap is formed on the two ends of the side walls, and an inlet and exit plenum are etched on the thin silicon substrate ($\sim$150 μm). A heater is deposited on the back side to deliver the heating power and also to serve as a thermistor for temperature measurements. A Pyrex substrate seals the device

[1]To whom correspondence should be addressed.

Contributed by the Heat Transfer Division of ASME for publication in the JOURNAL OF HEAT TRANSFER. Manuscript receieved: February 19, 2005; final manuscript received: May 5, 2005. Review conducted by: Satish G. Kandlikar.

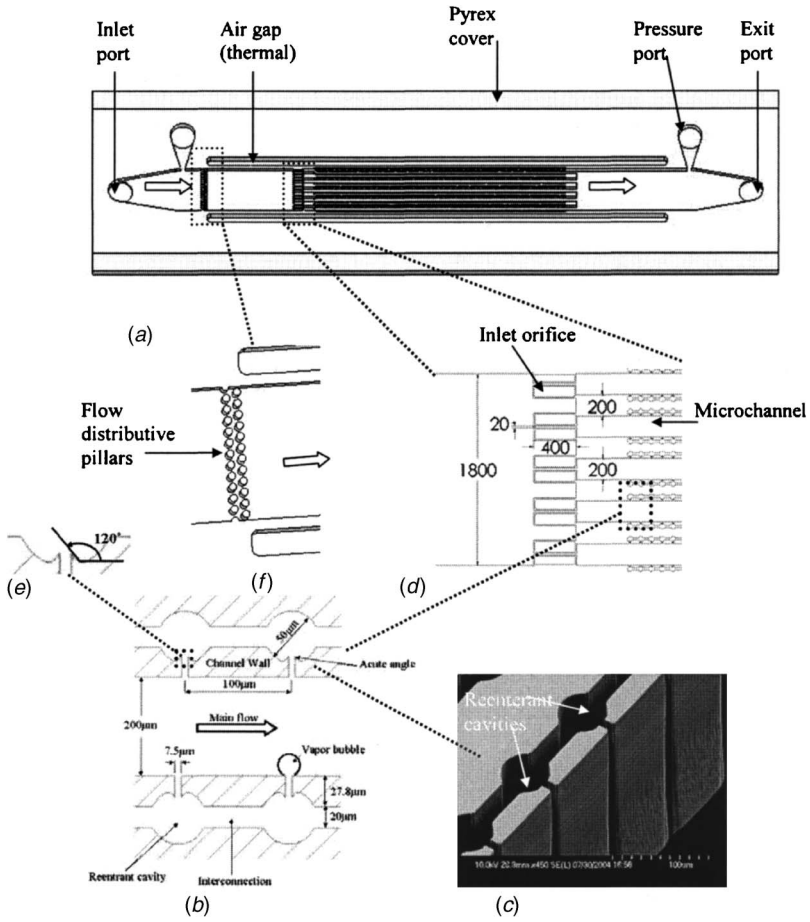

Fig. 1 (a) Computer-aided design model of the microchannel device, (b) dimensions of reentrant cavities, (c) SEM image of re-entrant cavities, (d) geometry of the inlet region, (e) geometry of the re-entrant cavity, and (f) flow distributive pillars

from the top and allows flow visualization. Five 20 μm wide orifices are installed [Fig. 1(*d*)] at the entrance of each channel to suppress flow instabilities. Flow distributive pillars have been employed to provide homogeneous distribution of flow in the inlet [Fig. 1(*f*)]. They are arranged in 2 columns of 12 circular pillars having a diameter of 100 μm. The transverse pitch between the pillars is 150 μm and equal to the longitudinal pitch.

2.1 Microchannel Fabrication Method. The Microelectromechanical systems (MEMS) device is micromachined on a polished double-sided *n*-type ⟨100⟩ single-crystal silicon wafer employing techniques adapted from integrated circuit manufacturing. It is equipped with pressure ports at the inlet and the exit to obtain accurate static pressures measurements.

A 1 μm thick high-quality oxide film is deposited on both sides of the silicon wafer to shield the bare wafer surface during processing, and serves as an electrical insulator. The heater and the vias are formed on the back side of the wafer (on top of the thermistors) by sputtering. A 70 Å thick layer of titanium is initially deposited to enhance adhesion characteristics and is followed by sputtering a 1 μm thick layer of aluminum containing 1% silicon and 4% copper. Subsequent photolithography and concomitant wet bench processing create the heater on the back side of the wafer. A 1 μm thick plasma-enhanced chemical vapor deposition oxide is deposited to protect the heater during further processing.

Next, the microchannels are formed on the top side of the wafer. The wafer is taken through a photolithography step and an reactive ion etching (RIE) oxide removal process to mask certain areas on the wafer, which are not to be etched during the deep RIE (DRIE) process. The wafer is consequently etched in a DRIE process, and silicon is removed from places not protected by the photoresist/oxide mask. The DRIE process forms deep vertical trenches on the silicon wafer with a characteristic scalloped sidewall possessing a peak-to-peak roughness of ~0.3 μm. A profilometer and scanning electron microscope (SEM) are employed to measure and record various dimensions of the device.

The wafer is flipped and the back side is then processed to create an inlet, outlet, side air gap, and pressure port taps for the transducers. A photolithography followed by a buffer oxide etching (BOE) (6:1) oxide removal process is carried out to create a pattern mask. The wafer is then etched through in a DRIE process to create the fluidic ports. Thereafter, electrical contacts/pads are opened on the back side of the wafer by performing another round of photolithography and RIE processing. Finally, the processed wafer is stripped of any remaining resist or oxide layers and anodically bonded to a 1 mm thick polished Pyrex (glass) wafer to form a sealed device. After successful completion of the bonding process, the processed stack is die-sawed to separate the devices from the parent wafer.

The MEMS device is packaged by sandwiching it between two plates. The fluidic seals are forged using miniature "O-rings," while the external electrical connections to the heater are achieved from beneath through spring-loaded pins, which connect the heater and thermistors to electrical pads residing away from the main microchannel body.

2.2 Experimental Test Rig. The setup, shown in Fig. 2, con-

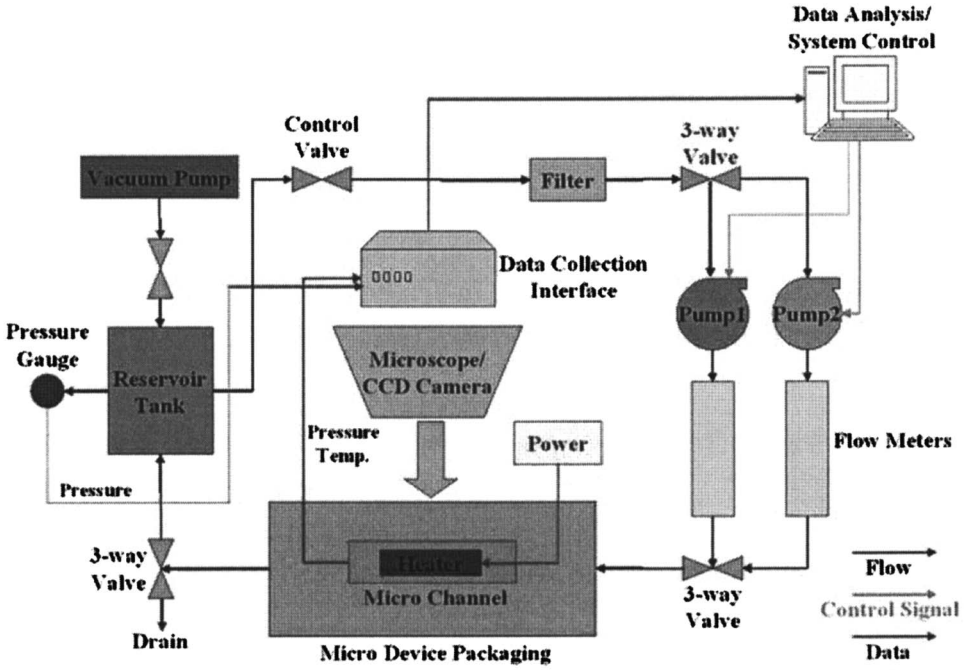

Fig. 2 Experimental setup

sists of three primary subsystems: The flow loop section, instrumentation, and a data acquisition system. The test section houses the MEMS-based microchannel devices and its fluidic and thermal packaging module. The microchannel device is mounted on the fluidic packaging module through O-rings to ensure a complete leak free system. The fluidic packaging delivers the working fluid and allows access to the pressure transducers. The heater, which is fabricated on the device back side, is wired (through electric pads) to the power supply.

The main flow loop includes the microchannel device, a pulseless gear pump, a reservoir which consists of a deaerator unit and a heating element to control the inlet temperature, flow meter, and dissolved oxygen meter (for use with water). The microheater is connected to a power supply with an adjustable dc current to provide power to the device. The temperature sensors output signals are recorded by a data acquisition system. Simultaneously, the inlet pressure and test section pressure drop are collected, and the boiling process in the microchannels are recorded by a Phantom V4.2 high-speed camera (maximum frame rate of 90,000 frames/s, and 2 μs exposure time) mounted over a Leica DMLM microscope. Calibration of the temperature sensors is performed prior to the experiment by placing the device in an oven and establishing the resistance-temperature curve for each individual sensor.

2.3 Experimental Procedures and Data Reduction. The deionized water flow rate was fixed at the desired value, and experiments were conducted after steady flow conditions were reached with an exit pressure of 47 kPa and ambient room temperature. First, the electrical resistance of the device was measured at room temperature. Thereafter, voltage was applied in 1 V increments to the heater, and the current/voltage data were recorded once steady state was reached. In an impeding dryout condition, a meager increase in the applied power causes an abrupt surge in the wall temperature. Once a large temperature increase (more than 10 °C) is observed with an incremental increase in the applied voltage, the power was hastily switched off to prevent burnout. Flow visualization through the high-speed camera and microscope complements the measured data. The procedure is repeated for different flow rates.

To estimate heat losses, electrical power was applied to the test section after evacuating the water from the test loop. Once the temperature of the test section became steady, the temperature difference between the ambient and test section was recorded with the corresponding power. The plot of power versus temperature difference was used to calculate the heat loss ($\dot{Q}_{\text{loss}}$) associated with each experimental data point. The heat losses are found in light of power versus temperature difference curve. The average heat losses for $G=41$, 83, 166, and 302 kg/m^2 s are 25.4, 9.44, 7.5, and 5.5 %, respectively. Heat loss curve for $G=302$ kg/m^2 s is included in Fig. 3.

Prior to the experiments, an identical device to the one tested without a flow restrictor has been hydrodynamically tested to obtain pressure drops across microchannels. Pressure drop measurements of the orificeless device have yielded 0.4, 0.9, 1.9, and 3.5 kPa for $G=41$, 83, 166, and 302 kg/m^2 s, respectively.

Data obtained from the voltage, current, and pressure measurements were used to calculate the average single- and two-phase temperatures, heat transfer coefficients, and critical heat flux (CHF) conditions. The electrical input power and heater resistance, respectively, were determined with:

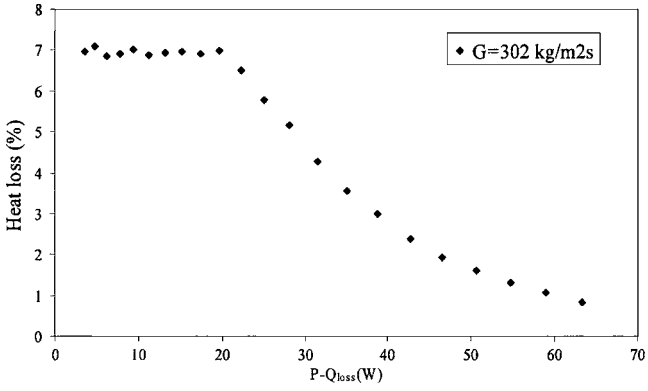

Fig. 3 Heat losses for $G=302$ kg/m^2 s

$$P = V \times I \tag{1}$$

and

$$R = V/I \tag{2}$$

The heater electrical resistance-temperature calibration curve is used for determining the heater temperature. The surface temperature at the base of the microchannels is then calculated as:

$$\overline{T} = \overline{T}_{\text{heater}} - \frac{(P - \dot{Q}_{\text{loss}})t}{k_s A_p} \tag{3}$$

The exit single-phase fluid temperature was calculated with a calorimetric balance, and the average fluid temperature is expressed as:

$$\overline{T}_F = \frac{T_i + T_e}{2} \tag{4}$$

Assuming that the walls of the channels behaved as one-dimensional fins, the power input was related to the average heat transfer coefficient in the channel:

$$P - \dot{Q}_{\text{loss}} = \eta_o A_t \overline{h}(\overline{T} - \overline{T}_F) \tag{5}$$

where η_o is the overall surface effectiveness of the microchannel configuration:

$$\eta_o = \frac{N\eta_f A_f + (A_t - NA_f)}{A_t} \tag{6}$$

where

$$\eta_f = \frac{\tanh(mH)}{mH} \quad m = \sqrt{\frac{\overline{h}2(L+W)}{k_s WL}} \quad A_f = 2HL \tag{7}$$

Equations (5)–(7) were employed to evaluate $\overline{h}$ with an iterative scheme. Thermal entrance length was evaluated according to the following equation [20]:

$$L_{\text{th}}/d_h = 0.05\ \text{Re Pr} \tag{8}$$

To account for the entrance effects, the average single phase heat transfer coefficient was multiplied with the following correction factor:

$$F = \frac{0.775[24(1 - 1.355\beta + 1.947\beta^2 - 1.701\beta^3 + 0.953\beta^4 - 0.254\beta^5)]^{1/3}[L_{th}/(d_h Re\ \text{Pr})]^{-1/3}}{8.235(1 - 2.042\beta + 3.085\beta^2 - 2.477\beta^3 + 1.058\beta^4 - 0.186\beta^5)} \tag{9}$$

The nominator of Eq. (9) is an average Nusselt number correlation of hyrodynamically developed and thermally developing laminar flows for noncircular ducts recommended by Shah and London [21], while the denominator is the Nusselt number recommended for thermally and hydrodynamically fully developed laminar flow [22].

Under boiling conditions, the length of the microchannels is divided into two parts: A single-phase (L_{sp}), and two-phase (L_{tp}) length. L_{tp} and L_{sp} are obtained by flow visualization. Again, assuming a one-dimensional fin for the channel walls, $\overline{h}_{\text{tp}}$ *can* be expressed as follows:

$$\overline{h}_{\text{tp}}(\overline{T}_{\text{tp}} - T_{\text{sat}})(W + A_f\eta_f)L = \frac{(P - \dot{Q}_{\text{loss}})(W + W_b)L}{A_p} \tag{10}$$

The inlet and the exit surface temperatures are given as:

$$T_{\text{si,sp}} = T_i + \frac{(P - \dot{Q}_{\text{loss}})}{\overline{h}A_s} \tag{11}$$

$$T_{\text{se,sp}} = T_{\text{sat}} + \frac{(P - \dot{Q}_{\text{loss}})}{\overline{h}A_s} \tag{12}$$

The average wall temperature in the single-phase region is the mean surface temperature:

$$\overline{T}_{\text{sp}} = \frac{T_{\text{si,sp}} + T_{\text{se,sp}}}{2} \tag{13}$$

With $\overline{T}_{\text{sp}}$ known, $\overline{T}_{\text{tp}}$ is obtained from a weighted average of the single and two-phase regions wall temperatures:

$$\overline{T}_{\text{tp}} = \frac{\overline{T}L - \overline{T}_{\text{sp}}L_{\text{sp}}}{L_{\text{tp}}} \tag{14}$$

Finally, the exit quality can be calculated with the known mass flow rate and net power supplied to the device as:

$$x_e = \frac{(P - \dot{Q}_{\text{loss}}) - \dot{m}c_p(T_{\text{sat}} - T_i)}{\dot{m}h_{FG}} \tag{15}$$

Uncertainties in the measured values were obtained from the manufacturer's specification sheets, while the uncertainties of the derived parameters are calculated using the method developed by Kline and McClintock [23]. Uncertainty in the two-phase convective heat transfer coefficient is estimated to be ±9%.

3 Results and Discussion

3.1 Boiling Curve. Figure 4 depicts the heat flux as a function of the average surface temperature for four mass fluxes. During single-phase flow ($\overline{T} < 80$ °C) the curves exhibit no change in the heat flux-temperature slope for each mass flux. Once boiling begins, an abrupt change occurs in the slope at temperatures nearly 80 °C and nucleate bubbles are visualized as shown in Fig. 5 (The saturation temperature at 47 kPa is 79.8 °C). Initially, the surface temperature remains relatively constant as the heat flux is increased for $G = 83$, 166, and 302 kg/m^2 s. At sufficiently high heat fluxes, the temperature increases with heat flux, however, a

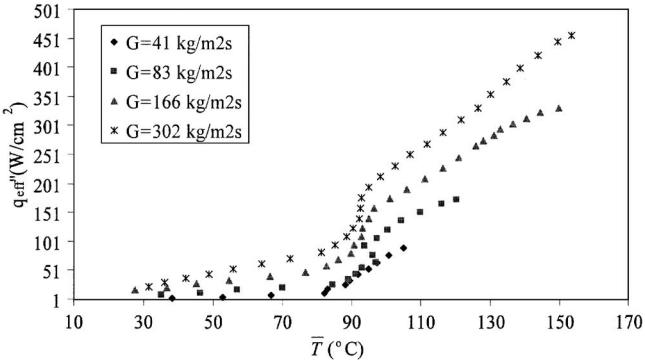

Fig. 4 Boiling curves for water at 47 kPa (q''_{eff} versus $\overline{T}$)

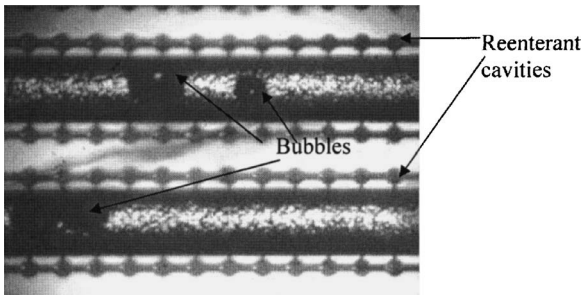

Fig. 5 Nucleation from reentrant cavities (q''=77.4 W/cm^2, G =166 kg/m^2 s)

steeper slope in comparison to single-phase flow characterizes this region. For G=41 kg/m^2 s, this transition is not observed, and the curve maintains a constant slope (higher than single phase) while boiling is present until the critical heat flux condition is reached.

3.2 Two-Phase Heat Transfer Coefficients. Figure 6 shows two-phase heat transfer coefficients as a function of heat flux. For G=41 kg/m^2 s, there is initially a sharp increase in the two-phase heat transfer coefficient which is followed by a more moderate increase; for $q''>46$ W/cm^2, the heat transfer coefficient drops indicating the CHF condition as a result of complete dryout (x_e ~1). The heat transfer coefficients for G=41 kg/m^{2}s and G =83 kg/m^{2}s appear to follow the same trend qualitatively as well as quantitatively for heat fluxes 25 to 36 W/cm^2. For G =41 kg/m^2 s at higher heat fluxes h_{tp} decreases due to the impending CHF condition. The heat transfer coefficient for G =166 kg/m^2 s and $q''>96$ W/cm^2 declines with heat flux, while it increases at lower heat fluxes ($q''<87$ W/cm^2). For G =302 kg/m^2 s, the heat transfer coefficient initially increases and then monotonically decreases throughout the boiling flow until CHF condition is reached.

Figure 7 shows the variation in two-phase heat transfer coefficients with exit quality for different mass fluxes. For G =41 kg/m^2 s, a slight increase in h_{tp} with exit quality is notable. With the dryout condition looming, heat transfer coefficient tends to decrease. For G=83 kg/m^2 s, an increase in heat transfer coefficient is observed at low qualities ($x_e<0.3$), whereas for higher qualities, h_{tp} gradually decreases with x_e. A similar trend is observed for G=166 kg/m^2 s. At G=302 kg/m^2 s after a peak is reached in the heat transfer coefficient at a quality of about 18%, h_{tp} monotonically decreases with exit quality. An interesting feature of Fig. 7 is that the data for $x_e>0.35$ and $G\geqslant 83$ kg/m^2 s follow the same trend, and the magnitude of heat transfer coefficients is comparable for all mass fluxes.

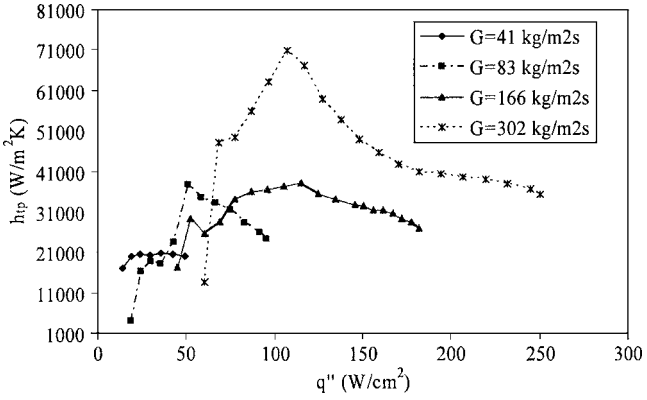

Fig. 6 Two-phase heat transfer coefficients for water at 47 kPa (h_{tp} versus q'')

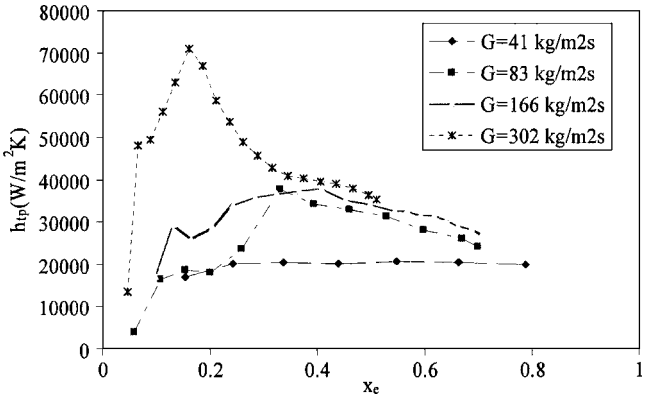

Fig. 7 Two-phase heat transfer coefficients for water at 47 kPa (h_{tp} versus x_e):(a) G=41 kg/m^2 s, (b) G=83 kg/m^2 s, (c) G =166 kg/m^2 s, and (d) G=302 kg/m^2 s

3.3 Comparison of Atmospheric and Subatmospheric Pressure Two-Phase Heat Transfer Data. A comparison of the two-phase heat transfer coefficients obtained in the current study with the atmospheric exit pressure data given in [18,24] are shown in Fig. 8. For the most part, qualitatively the data for the atmospheric and reduced pressure follow the same trend, whereas quantitatively h_{tp} is lower for the reduced pressure, which is consistent with conventional size channel behavior. The two-phase heat transfer coefficients for G=41 kg/m^2 s show no notable differences from the atmospheric pressure data. However, the atmospheric data are considerably scattered due to large flow oscillations, whereas the subatmospheric flow is steady. Currently, the reason is not fully understood. Possibly the higher surface tension at the lower saturation temperature might assist in stabilizing the flow. For G=83 kg/m^2 s at subatmospheric conditions, a zone in which heat transfer coefficients decrease with heat flux is apparent, whereas at atmospheric pressures the heat transfer coefficient significantly decreases with heat flux only at impending dryout conditions. The data for the zone in which the heat transfer coefficient increases with the heat flux is approximately similar in magnitude to the atmospheric pressure data, and deviations start to occur thereafter. The profiles for G=166 kg/m^2 s and 302 kg/m^2 s are similar for both exit pressures; however, they are greater at atmospheric exit pressure by an average of ~20%.

Two-phase heat transfer coefficients as a function of exit quality are shown in Fig. 9 for both reduced and atmospheric exit pressures. The profiles have similar trends for both pressures. For G =83, 166 kg/m^2 s, and 302 kg/m^2 s, heat transfer coefficients are larger at the atmospheric exit pressure, which is in agreement with studies performed in minichannels [14–16], while the heat transfer coefficients are similar in magnitude for both atmospheric and reduced pressures at G=41 kg/m^2 s.

3.4 Flow Boiling Mechanisms. Conventional channel flow boiling mechanisms are closely connected with distinctive dependency of the heat transfer coefficient on mass flux, exit quality, heat flux, and subcooled conditions. Two-phase heat transfer coefficients during nucleate boiling typically increase with heat flux and are weakly dependent on liquid subcooling, mass flux, and mass quality. Boiling heat transfer coefficients during convective boiling, on the other hand, increase with quality and mass flux but are weakly dependent on heat flux. Some studies on microchannel boiling (e.g., reference [4]) have used this heat transfer dependency on the thermohydraulic conditions to identify the predominant flow boiling mechanisms. Although it is not fully clear whether the heat transfer mechanisms in microchannels closely follow the same h_{tp} trends as conventional channel do, it is useful to distinguish the conditions corresponding to nucleate and convective boiling based on criteria adopted from conventional scale

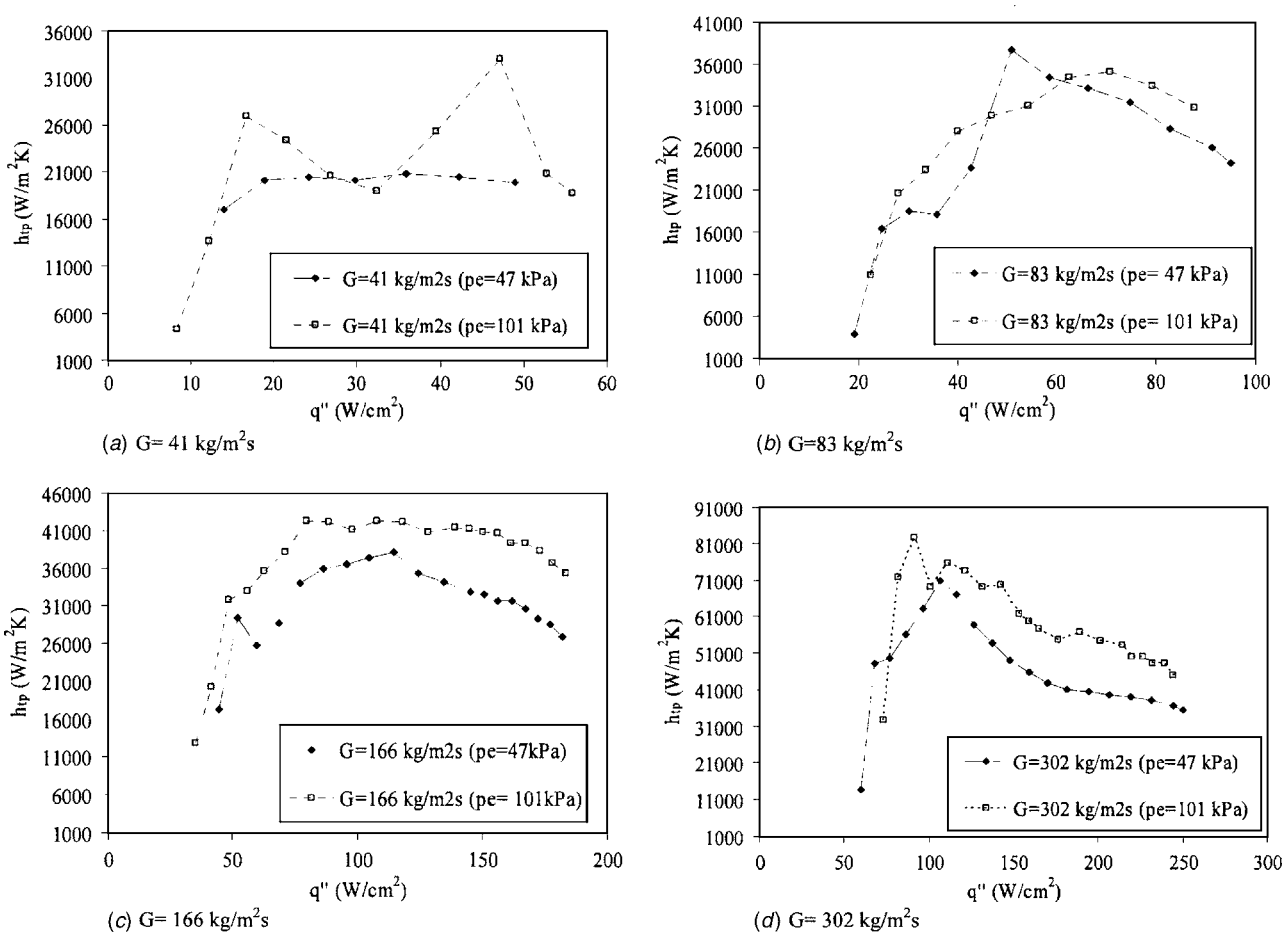

Fig. 8 Comparison of heat transfer coefficients with heat flux at reduced and atmospheric exit pressures: (a) $G=41$ kg/m^2 s, (b) $G=83$ kg/m^2 s, (c) $G=166$ kg/m^2 s, and (d) $G=302$ kg/m^2 s

channels. In accordance to this, Koşar et al. [18] identified both mechanisms in microchannel flow boiling and developed a heat transfer mechanism map separating nucleate and convective dominant regions with a straight line, which relates Boiling number to Reynolds number.

In the present study, the Reynolds number range is between 21 to 167 and the Bo number is between 7.5×10^{-4} to 5.2×10^{-3}. According to reference [18], the experimental data should partly lie within the nucleate boiling regime and partly within the convective boiling regime ($\mathrm{Re}_{cr}=163.59-2.73\times10^{4}\mathrm{Bo}$). The data provided in Fig. 6 can be classified into two regions of heat flux dependency: (i) Increasing h_{tp} with heat flux, and (ii) decreasing h_{tp} with heat flux. For low mass flux ($G=41$ kg/m^2 s), a consistent trend of increasing h_{tp} with heat flux is notable, while the heat transfer coefficient for the high mass flux ($G=302$ kg/m^2 s) monotonically declines with q''. For moderate mass fluxes ($G=83$ and 166 kg/m^2 s), the heat transfer coefficients initially increase with q'', and then continuously decline. The increasing heat transfer coefficients with heat flux at low mass flux and all heat fluxes (up to CHF) and moderate mass fluxes ($G=83$ and 166 kg/m^2 s) under low heat fluxes ($q''<51$ W/cm^2 for $G=83$ kg/m^2 s, $q''<115$ W/cm^2 for $G=166$ kg/m^2 s) are clearly a feature of nucleate boiling mechanism. On the other hand, the dependency of the heat transfer coefficients on heat flux at moderate mass fluxes ($G=83$ and 166 kg/m^{2}s) under high heat fluxes ($q''>115$ W/cm^2) and high mass flux ($G=302$ kg/m^{2}s) under all heat fluxes suggests convective boiling dominance.

The heat transfer coefficients for all heat fluxes at low mass fluxes and moderate mass fluxes under low heat fluxes do not seem to be strongly dependent on the mass flux. However, a significant increase is observed when the mass flux is increased to 302 kg/m^2 s. This supports nucleate boiling dominance at low mass fluxes and convective boiling dominance at high mass fluxes.

From Fig. 7, it is evident that at moderate mass fluxes with high qualities and high mass fluxes for all mass qualities the heat transfer coefficients decrease with x_e. As noted by Qu and Mudawar [4], this is a unique characteristic of microchannel convective flow boiling. It should be noted that the weak dependency of the heat transfer coefficient on mass flux for $x_e>0.35$ does not provide supporting evidence for the convective boiling mechanism.

From the aforementioned discussion, it can be concluded that as mass flux increases the boiling mechanism shifts from nucleate to convective dominant. Furthermore, convective boiling tends to predominate as heat flux increases. Since the Reynolds and Boiling numbers were previously used in reference [18] to determine the boiling mechanisms, a heat transfer mechanism map based on these parameters is shown in Fig. 10. Both the present subatmospheric data and previously obtained data at atmospheric pressure are shown. The identification of the boiling mechanism of each data point was based on the observed trends of h_{tp} in Figs. 6 and 7. Emphasis is given to points where the heat transfer coefficient stops increasing and a continuous or a sudden decrease begins. The data for low mass flux ($G=41$ kg/m^{2}s) are considered to be included in the nucleate dominant region except the last two data points, which apparently correspond to dryout conditions. The data for the moderate mass fluxes ($G=83$ and 166 kg/m^2 s) at low heat flux ($q''<51$ W/cm^2 and $q''<96$ W/cm^2, respectively) are

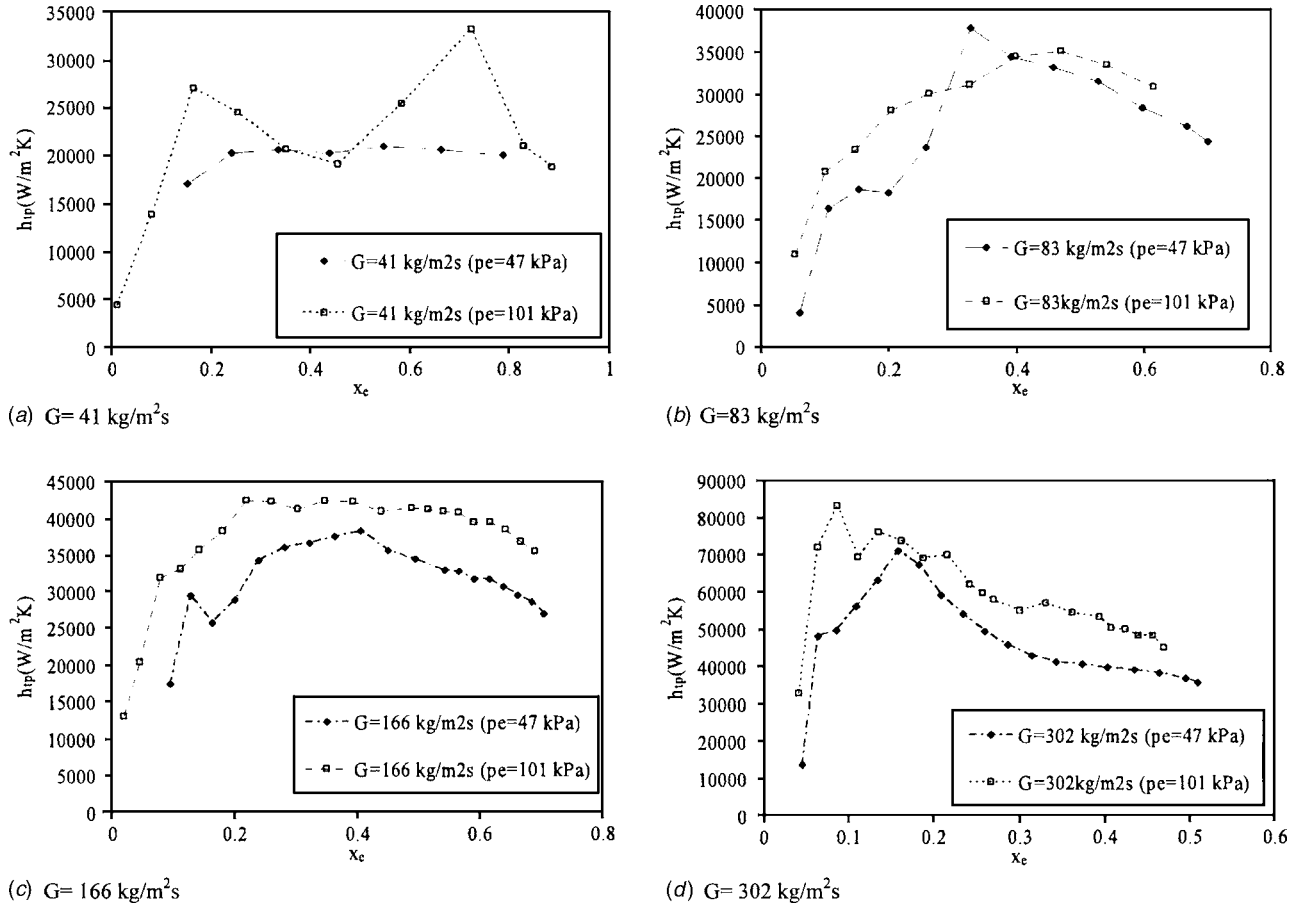

Fig. 9 Comparison of heat transfer coefficients with exit quality at reduced and atmospheric exit pressures

included in the nucleate boiling region, whereas all the remaining data (the remaining data of $G=83$ and 166 $\mathrm{kg/m^2\,s}$, and all the data of $G=302$ $\mathrm{kg/m^2\,s}$) are considered to be convective boiling dominant.

As can clearly be seen in Fig. 10, data from both pressure levels have similar trends. Low Bo and low Re correspond to the nucleate boiling dominant mechanism, while high Bo and high Re are associated with convective boiling. Like the heat transfer mechanism map in reference [18], the transition Reynolds number (transition from nucleate to convective boiling) can be linearly correlated to the Boiling number.

At reduced pressures flow boiling mechanisms transition at lower Boiling numbers than at atmospheric pressure, which implies that the Bo number alone is insufficient to provide a generalized correlation for the two distinct exit pressures. In an attempt to find a commonality between the two sets of data (atmospheric and reduced pressure), the k_1 number suggested by Kandlikar [7] $k_1=\mathrm{Bo}^2(\rho_L/\rho_G)$ is used instead of the Boiling number, and the results are shown in Fig. 11. The k_1 number captures more properly the transition Reynolds number than the Bo number. The transition boundary between the nucleate and convective boiling dominated zones can be expressed with:

$$\mathrm{Re}_{cr}=119-2.2\times10^3 k_1 \tag{16}$$

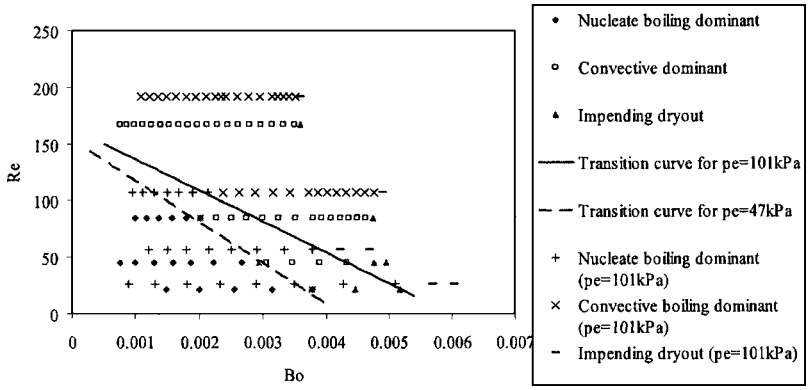

Fig. 10 Comparison of heat transfer mechanism reduced and atmospheric exit pressure data

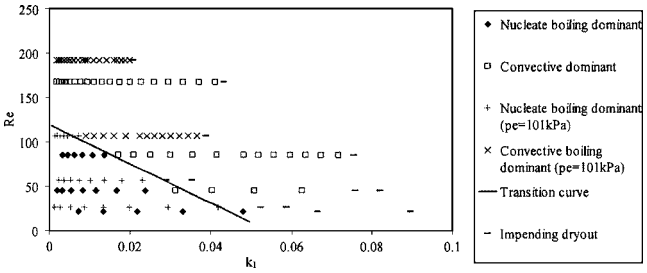

Fig. 11 Heat transfer mechanism map with reduced and atmospheric exit pressure data

3.5 Critical Heat Flux Conditions. The dependence of the heat flux at CHF conditions on the mass velocity and exit quality are shown in Figs. 12 and 13, respectively, along with the data obtained at atmospheric pressures in reference [18]. The exit pressure appears to have no effect on the dependence of CHF on the mass velocity. The increase of critical heat flux with mass velocity in conventional scale apparatus is well documented in the literature and it appears that boiling flow in microchannels exhibits similar dependency. Although it seems that at reduced pressure CHF conditions occur at slightly higher exit quality the data are not sufficient to make any firm conclusions.

4 Conclusions

In this study, boiling heat transfer experiments have been conducted in microchannels with interconnected re-entrant cavities at a reduced pressure (p_e=47 kPa). Governing heat transfer mechanisms are identified and specified for different operating conditions. Two-phase heat transfer coefficients have been compared to results obtained from tests at an atmospheric exit pressure. Moreover, a heat transfer mechanism map containing the data of both atmospheric and reduced exit pressure has been developed based on Re and the dimensionless parameter k_1. The main conclusions drawn from this study are:

- Heat transfer coefficients increase with exit pressure at the same exit quality for moderate and high mass fluxes. This is in agreement with findings in the literature for conventional and minichannels.
- For the most part, heat transfer coefficients displayed similar qualitative trends at reduced and atmospheric pressures.
- Depending on the mass flux and heat flux, both nucleate and convective dominant boiling mechanisms have been detected. A transition between nucleate and convective boiling was quantified. For subatmospheric pressure data, nucleate boiling is dominant for low Re and Bo similar to atmospheric pressure data. However, the transition from the nucleate to convective dominant boiling heat transfer mechanism occurs at a lower Re and Bo than at atmospheric pressure.
- A general heat transfer mechanism map based on the dimensionless parameter k_1 and the Reynolds number was generated, which provides a better prediction of the reduced and atmospheric pressure data than only the Boiling and Reynolds number plot.

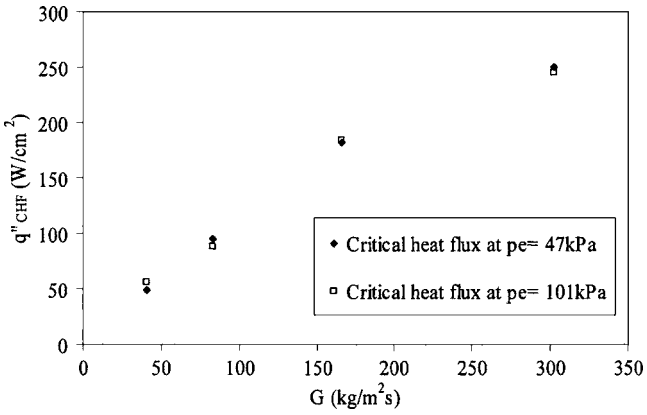

Fig. 12 q''_{CHF} dependence on G

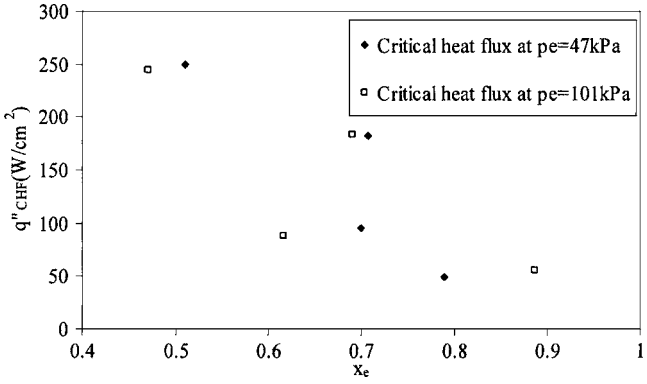

Fig. 13 q''_{CHF} dependence on x_e

Acknowledgment

This work was supported by the Office of Naval Research through the Young Investigator Program, under contract No. N00014-05-1-0582 (Program Officer: Dr. Mark Spector). The authors are indebted to Professor Michael K. Jensen for his constructive and useful guidance. Graduate student support from Rensselaer Polytechnic Institute is also gratefully appreciated. The microfabrication was performed in part at the Cornell NanoScale Facility (a member of the National Nanotechnology Infrastructure Network) which is supported by the National Science Foundation under Grant ECS-0335765, its users, Cornell University and industrial affiliates. The authors are thankful to D. DiGiulio of the RPI Machine shop for his support and insightful recommendations.

Nomenclature

A_f = fin surface area, m^2
A_s = surface area, m^2
A_p = planform area, m^2
A_t = total heat transfer area, m^2
Bo = boiling number, q''_{ch}/Gh_{FG}
c_p = specific heat at constant pressure, kJ/kg K
d_h = hydraulic diameter, m
F = heat transfer coefficient multiplier
G = mass flux, kg/m^2 s
h = heat transfer coefficient, W/m^{2}K
$\overline{h}$ = average single-phase heat transfer coefficient, W/m^{2}K
h_{FG} = latent heat of vaporization, kJ/kg
H = channel height, m
I = electrical current, Amp
k = thermal conductivity, W/m K
k_I = dimensionless parameter, $(q''/Gh_{FG})^2\rho_L/\rho_G$
L = microchannel length, m
L_{th} = thermal enterance length, m
m = defined in Eq. (7)
m = mass flow rate, kg/s
N = number of microchannels
P = power, W
q'' = heat flux, W/cm^2

$\dot{Q}$ = volumetric flow rate, ml/min
R = electrical resistance, Ω
Re = Reynolds number, Gd_h/μ_L
T = temperature, °C
$\overline{T}$ = average temperature, °C
t = thickness between the heater and microchannel base, m
V = voltage, V
W = michrochannel width, m
W_b = fin width, m
x = mass quality

Greek Symbols

β = aspect ratio
η = fin efficiency
μ = viscosity, kg/ms
ρ = density, m^3/s

Subscripts

amb = ambient
CHF = critical heat flux condition
cr = critical
e = exit
eff = effective
exp = experimental
f = fin
F = fluid
G = gas
i = inlet
LO = liquid only
o = overall
s = surface
sat = saturation
se = surface at the exit
si = surface at the inlet
sp = single-phase
tp = two-phase

References

[1] Jiang, L., Wong, M., and Zohar, Y., 2001, "Forced Convection Boiling in Microchannel Heat Sink," J. Microelectromech. Syst., **10**(1), pp. 80–87.
[2] Kandlikar, S. G., 2002, "Fundamental Issues Related to Flow Boiling in Minichannels and Microchannels," Exp. Therm. Fluid Sci., **26**, pp. 389–407.
[3] Kandlikar, S. G., 2002, "Two-Phase Flow Patterns, Pressure Drop, and Heat Transfer during Boiling in Minichannels Flow Passages of Compact Evaporators," Heat Transfer Eng., **23**(1), pp. 5–23.
[4] Qu, W., and Mudawar, I., 2003, "Flow Boiling Heat Transfer in Two-Phase Microchannel Heat Sink. I: Experimental Investigation and Assessment of Correlation Methods," Int. J. Heat Mass Transfer, **46**(15), pp. 2755–2771.
[5] Bowers, M. B., and Mudawar, I., 1994, "High Flux Boiling in Low Flow Rate, Low Pressure Drop Minichannel and Microchannel Heat Sinks," Int. J. Heat Mass Transfer, **37**(2), pp. 321–334.
[6] Steinke, M. E., and Kandlikar, S. G., 2004, "An Experimental Investigation of Flow Boiling Characteristics of Water in Parallel Microchannels," ASME J. Heat Transfer, **126**(4), pp. 518–526.
[7] Kandlikar, S. G., 2004, "Heat Transfer Mechanisms during Flow Boiling in Microchannels," ASME J. Heat Transfer, **126**(1), pp. 8–16.
[8] Mehendale, S. S., Jacobi, A. M., and Shah, R. K., 2000, "Fluid Flow and Heat Transfer at Micro- and Mesoscales with Application to Heat Exchanger Design," Appl. Mech. Rev., **53**(7), pp.175–193.
[9] Bergles, A. E., Lienhard, J. H., Kendall, G. E., and Griffith, P., 2003, "Boiling and Evaporation in Small Diameter Channels," Heat Transfer Eng., **24**(1), pp. 18–40.
[10] Thome, J. R., 2004, "Boiling in Microchannels: A Review of Experiment and Theory," Int. J. Heat Fluid Flow, **25**, pp. 128–139.
[11] Klimenko, V. V., 1990, "A Generalized Correlation for Two-Phase Forced Flow Heat Transfer," Int. J. Heat Mass Transfer, **31**, pp. 541–552.
[12] Liu, Z., and Winterton, R. H. S., 1991, "A General Correlation for Saturated and Subcooled Flow Boiling in Tubes and Annuli, Based on a Nucleate Pool Boiling Equation," Int. J. Heat Mass Transfer, **34**, pp. 2759–2766.
[13] Steiner, D., and Taborek, J., 1992, "Flow Boiling Heat Transfer in Vertical Tubes Correlated by Asymptotic Model," Heat Transfer Eng., **13**, pp. 43–69.
[14] Tran, T. N., Wambsganns, M. W., and France, D. M., 1996, "Small Circular- and Rectangular-Channel Boiling with Two Refrigerants," Int. J. Multiphase Flow, **22**(3), pp. 485–498.
[15] Bao, Z. Y., Fletcher, D. F., and Haynes, B. S., 2000, "Flow Boiling Heat Transfer of Freon R11 and HCFC123 in Narrow Passages," Int. J. Heat Mass Transfer, **43**, pp. 3347–3358.
[16] Huo, X., Chen, L., Tian, Y. S., and Karayiannis, T. G., 2004, "Flow Boiling and Flow Regimes in Small Diameter Tubes," Appl. Therm. Eng., **24**, pp. 1225–1239.
[17] Owhaib, W., Martín-Callizo, C., and Palm, B., 2004, "Evaporative Heat Transfer in Vertical Circular Microchannels," Appl. Therm. Eng., **24**, pp. 1241–1253.
[18] Koşar, A., Kuo, C. J., and Peles, Y., 2005,"Boiling Heat Transfer in Rectangular Microchannels with Reentrant Cavities," Int. J. Heat Mass Transfer, **48**, pp. 3615–3627.
[19] Webb, R. L., 1981, "The Evolution of Enhanced Surface Geometries for Nucleate Boiling," Heat Transfer Eng., **2**(3–4), pp. 46–69.
[20] Incropera, F. P. and DeWitt, D. P., 1996, "Introduction to Heat Transfer," Wiley, NY, pp. 393–394.
[21] Shah, R. K., and London, A. L., 1978, "Laminar Flow Forced Convection in Ducts," *Supplement 1 to Advances in Heat Transfer*, Academic, NY.
[22] Shah, R. K. and Sekuli, D. P., 2003, *Heat Exchanger Design*, Wiley, NY, pp. 477–479.
[23] Kline, S., F. A., and McClintock, F. A., 1953, "Describing Uncertainties in Single-Sample Experiments," Mech. Eng. (Am. Soc. Mech. Eng.), **75**(1), pp. 3–8.
[24] Jensen, M. K., Peles, Y., Srikar, V. T., Koşar, A., and Kuo, C. J., "Enhanced Boiling Heat Transfer in Second Generation Microchannels. Part A. Methods and Preliminary Data," *Proc. 3rd International Conference on Microchannels and Minichannels*, ICMM2005-75195.

Radiative Heat Transfer Using Isotropic Scaling Approximation: Application to Fibrous Medium

Hervé Thierry Kamdem Tagne

Dominique Doermann Baillis[1]
e-mail: dominique.baillis@insa-lyon.fr

Centre de Thermique de Lyon (CETHIL)—UMR 5008 CNRS INSA de Lyon/Université Claude Bernard—Lyon 1 Bât. Sadi Carnot, 69621 Villeurbanne, France

The applicability of the isotropic scaling approximation to heat transfer analysis in fibrous medium is discussed. The isotropic scaling model allows the transformation of an anisotropic scattering problem to an isotropic one. The scaled parameters are derived for general anisotropic scattering and for radiative properties dependent of the incidence radiation. Three different isotropic scaling approaches are considered: Directional isotropic scaling, mean isotropic scaling, and P1 isotropic scaling; corresponding to isotropic scaling parameters function of incident radiation, arithmetic mean over all incident direction of radiative properties, and mean on weighted radiative properties, respectively. The discrete ordinate method is used to solve the radiative transfer equation through fibrous medium. The fibers in the medium are randomly oriented either in space or parallel to the boundaries. Numerical results presented for a pure radiation problem show good accuracy on radiative heat flux between the exact solution and solution obtained with both P1 and directional isotropic scaling while using mean isotropic scaling is unsuitable. Using isotropic scaling approximation to model radiative heat transfer is faster than the exact solution and required few quadratures to converge.
[DOI: 10.1115/1.2035108]

Keywords: Isotropic scaling, Radiative Heat Transfer, Fibrous Medium, Fiber Orientation

Introduction

Radiative heat transfer through semitransparent media has attracted a great deal of interest in several areas, such as thermal insulation, manufacturing and processing materials [1,2]. The radiative behavior of semitransparent media is predicted by solving the radiative transfer equation (RTE). The radiative properties required to solve the RTE are the absorption, the extinction, the scattering coefficients, and the scattering phase function. These properties can be obtained either from analytical models, such as Mie theory or from an inverse method based upon experimental data [3–7].

The exact phase function, such as obtained from Mie theory, may undergo strong angular oscillations and high forward scattering peak at any given single wavelength. These two phenomena enormously complicate the radiative transfer analysis. Thus, different approximate phase functions have been proposed such as the development of the phase function in a series of Legendre polynomials [8], the Henyey–Greenstein function, [9,10] or isotropic function [10–12]. For isotropic phase function, scaling is required to transform an anisotropic scattering problem to an equivalent isotropic problem.

The isotropic scaled parameters, such as optical depth and albedo, can be usually derived from three different approaches: (i) The delta approximation, (ii) the scaling group of the radiative transfer equation, and (iii) the P1 spherical harmonic approach [13–15].

(i) The delta approximation replaces the phase function by the sum of a Dirac-delta function and an isotropic function. The isotropic scaling parameters are then obtained by substituting the delta approximate phase function into the RTE [13,14].

(ii) McKellar and Box [14] derived the conditions under which two solutions to the RTE for two distinct sets of physical conditions will be equivalent. Such transformation forms the scaling group of the radiative transfer equation. In their analysis, the original and the scaled phase functions are expanded in a series of Legendre polynomials and they found a relation between the moments of these two functions. From this approach, the difference of the number of terms in Legendre expansion between the original and the scaled functions must be limited to one. Thus, the isotropic scattering phase function will be obtained only from a linear anisotropic phase function [15].

(iii) In the study of Lee and Buckius [15], the isotropic scaling is obtained from the first order of the spherical harmonic method (P1) of solving the one-dimensional RTE. These authors normalized the RTE and used the P1 approximation to derive the isotropic scaled parameters albedo and optical depth. But this approach requires that the radiative properties are independent of the incident direction.

Earlier analysis of radiative transfer using a scaling model usually considered spherical homogeneous particles with a phase function easily expanded in a series of Legendre polynomials [13–18]. Very few works have been done for nonspherical particles such as fibers. This is probably due to the difficulty to correctly determine the phase function moments for these particles and also because certain anisotropic simplifications introduced for a medium with spherical particles are not as appropriate when the medium is made up of cylindrical fibers [19]. For fibrous randomly oriented in space, Houston [20] assumed that the Mie–Kerker phase function is constant in a set of scattering angle intervals. According to him, to accurately account for the forward peak, the Legendre expansion phase function requires at least 20 terms in the far infrared and 60 terms in the near infrared. To avoid great computer time consuming, he used a delta-*M* scaling

[1]Corresponding author.

Presented as paper IMECE2004-59709 at ASME International Mechanical Engineering Congress and Exposition, November 13–19, 2004. Contributed by the Heat Transfer Division of ASME for publication in the JOURNAL OF HEAT TRANSFER. Manuscript received: December 21, 2004. Final manuscript received: May 12, 2005. Review conducted by: Gang Chen.

approach with $2 \leqslant M \leqslant 5$ for radiative analysis. Recently, Yuen et al. [21] used the Delta-Eddington function to reduce the high anisotropy scattering of randomly oriented in space fibrous medium to a linear anisotropy scattering.

As a result from the above discussion, the three approaches (i,ii,iii) present limitations to derive the isotropic scaling parameters. The delta approximation can be used only for forward scattering, the scaling group of the radiative transfer equation is limited to linear anisotropic scattering, and the P1 scaling must be adapted for cases where the radiative properties depend on the incidence direction. It is also important to note that in most of the previous works using isotropic scaling for radiative analysis, comparisons are made between the isotropic scaling solution and the solution obtained with the Legendre expansion approximate function of spherical particles. The question arises how accurate the result from the exact solution for nonspherical particles would be if using the isotropic scaling. Furthermore, how would the isotropic scaled parameters for non-randomly oriented particles in space be determined?

The objectives of this study are twofold. One is to present a methodology to transform an anisotropic scattering problem to isotropic scattering for general anisotropic scattering and for radiative properties depending or not of the incidence direction such as for fibrous medium. The other objective is to examine the accuracy of the isotropic scaling when using the discrete ordinate method to solve the RTE in one-dimensional fibrous medium. This is achieved by a systematic analysis of the radiative heat flux predicted by the isotropic scaling method and the exact solution for various quadratures. The fibers in the medium are assumed to be circular, infinitely long, and randomly oriented either in space or parallel to the diffuse boundaries.

Models and Analysis

In this paper, the one-dimensional heat transfer is considered. The medium is assumed to be gray and in radiative equilibrium. The boundary surfaces are black; the top and the bottom walls are maintained respectively at temperatures T_1 and T_2. The governing equations for radiative transfer in absorbing/emitting/scattering medium are the radiative transfer and the energy conservative equations. By simultaneously solving these two-coupled equations, the temperature distribution and the heat flux in the medium can be obtained.

Radiative Transfer and Energy Equations. The RTE in one-dimensional gray medium is [6]

$$\mu\frac{\partial I(y,\Omega)}{\partial y} = -\sigma_e(\Omega)I(y,\Omega) + [\sigma_e(\Omega) - \sigma_s(\Omega)]I_b + \frac{1}{4\pi}\int_{4\pi}\sigma_s(\Omega')P(\Omega',\Theta)I(y,\Omega')d\Omega' \quad (1)$$

$\sigma_e - \sigma_s = \sigma_a$ is the absorption coefficient, P is the scattering phase function normalized according to the relation

$$\frac{1}{4\pi}\int_{4\pi}P(\Omega,\Theta)d\Omega_s = 1 \quad (2)$$

with $d\Omega_s = \sin\Theta d\Theta d\psi$ the scattering solid angle. The angles Θ and ψ are regarded as the spherical polar angles of the scattered radiation relative to the incident direction, and ψ the azimuthal angle on the plane normal to the incident direction. The scattering angle Θ between in-coming direction Ω and scattering direction Ω' is

$$\cos\Theta = \mu\mu' + \sqrt{(1-\mu^2)(1-\mu'^2)}\cos(\varphi - \varphi') \quad (3)$$

The radiative energy conservation equation is

$$\frac{dq}{dy} = \int_{4\pi}[\sigma_e(\Omega) - \sigma_s(\Omega)][4\pi I_b - I(y,\Omega)]d\Omega \quad (4)$$

The radiative heat flux q is defined as

$$q = \int_{4\pi} I(y,\Omega)\mu d\Omega \quad (5)$$

Isotropic Scaling Problems. Isotropic scaling reduces an anisotropic scattering problem to an isotropic scattering problem. In this paper, three different models are proposed to derive the isotropic scaling parameters and will be compared with each other: The directional, the P1, and the mean isotropic scaling models.

The Directional Isotropic Scaling Model. In this section, we extend the scaling group of the RTE [14] in order to determine the isotropic scaled parameters for general anisotropic scattering and for radiative properties dependent or not on the incidence direction. The scaling group of the radiative transfer equation is based on the transformation of a problem of optical thickness τ, albedo ω, and anisotropic phase function P to a problem of optical thickness τ^*, albedo ω^*, and anisotropic phase function P^*. This concept is well explained by McKellar and Box [14]. The RTE Eq. (1) is rewritten in a more convenient form

$$\mu\frac{\partial I(\tau,\Omega)}{\partial\tau} = [1-\omega(\Omega)]I_b + \frac{1}{4\pi}\int_{4\pi}K(\sigma_e,\sigma_s,\Omega',\Omega)I(\tau,\Omega')d\Omega' \quad (6)$$

$\tau = \sigma_e(\Omega)y$ is the optical depth, $\omega(\Omega) = \sigma_s(\Omega)/\sigma_e(\Omega)$ is the albedo and K is the Kernel function defined as

$$K(\sigma_e,\sigma_s,\Omega',\Omega) = \sigma_s(\Omega')P(\Omega',\Theta)/\sigma_e(\Omega) - 4\pi\delta(\Omega-\Omega') \quad (7)$$

For a scaled optical depth τ^*, albedo ω^* and phase function P^*, the radiative transfer equation is

$$\mu\frac{\partial I(\tau^*,\Omega)}{\partial\tau^*} = [1-\omega^*(\Omega)]I_b + \frac{1}{4\pi}\int_{4\pi}K^*(\sigma_e^*,\sigma_s^*,\Omega',\Omega)I(\tau^*,\Omega')d\Omega' \quad (8)$$

with

$$K^*(\sigma_e^*,\sigma_s^*,\Omega',\Omega) = \sigma_s^*(\Omega')P^*(\Omega',\Theta)/\sigma_e^*(\Omega) - 4\pi\delta(\Omega-\Omega') \quad (9)$$

To scale a problem based on τ, σ_e, σ_s, ω, P to a problem based on τ^*, σ_e^*, σ_s^*, ω^*, P^* the following transformation is used

$$\tau = \alpha\tau^* \quad (10)$$

$\alpha = \alpha(\Omega)$ is the scaling transformation parameter. Putting Eq. (10) into Eq. (6) and comparing to Eq. (8) leads to

$$\omega^*(\Omega) = \alpha\omega(\Omega) + 1 - \alpha \quad (11)$$

$$K(\sigma_e,\sigma_s,\Omega',\Omega) = K^*(\sigma_e^*,\sigma_s^*,\Omega',\Omega)/\alpha \quad (12)$$

Using Eq. (7) and Eq. (9), Equation (12) is rewritten as

$$\sigma_s^*(\Omega')P^*(\Omega',\Theta)/\sigma_e^*(\Omega) = \alpha\sigma_s(\Omega')P(\Omega',\Theta)/\sigma_e(\Omega) + 4\pi(1-\alpha)\delta(\Omega'-\Omega) \quad (13)$$

In order to determine the scaled parameters τ^*, σ_e^*, σ_s^*, ω^*, and P^* we suggest to form a system of $(N+1)$ equations based on the evaluation of the N first moment of Eq. (13). The order N is the number of terms in the scaled function P^*. In the case of isotropic scaling transformation $P^*(\Omega,\Theta) = 1$ and $N = 1$. The evaluation of the zeroth and first moments of Eq. (13) by applying the operators $1/4\pi\int_{4\pi}\ldots d\Omega_s$ and $1/4\pi\int_{4\pi}\ldots\cos\Theta d\Omega_s$ gives, respectively,

$$\frac{1}{4\pi}\int_{4\pi}\frac{\sigma_s^*(\Omega')}{\sigma_e^*(\Omega)}d\Omega_s=\frac{1}{4\pi}\int_{4\pi}\frac{\alpha\sigma_s(\Omega')P(\Omega',\Theta)}{\sigma_e(\Omega)}d\Omega_s+\int_{4\pi}(1-\alpha)\delta(\Omega-\Omega')d\Omega_s \tag{14}$$

$$\frac{1}{4\pi}\int_{4\pi}\frac{\sigma_s^*(\Omega')}{\sigma_e^*(\Omega)}\cos\Theta d\Omega_s=\frac{1}{4\pi}\int_{4\pi}\frac{\alpha\sigma_s(\Omega')}{\sigma_e(\Omega)}P(\Omega',\Theta)\cos\Theta d\Omega_s+\int_{4\pi}(1-\alpha)\delta(\Omega'-\Omega)\cos\Theta d\Omega_s \tag{15}$$

Using the following equations

$$\begin{cases}4\pi\delta(\Omega'-\Omega)=2\delta(1-\cos\Theta)\\ \displaystyle\int_{-1}^{1}\delta(\gamma-\cos\Theta)Q(\cos\Theta)d\cos\Theta=Q(\gamma)\end{cases} \tag{16}$$

the bias scattering factor [22] of the exact phase function P

$$g(\Omega')=\frac{1}{4\pi}\int_{4\pi}P(\Omega',\Theta)\cos\Theta d\Omega_s \tag{17}$$

and the normalized scattering phase function condition Eq. (2), Eqs. (14) and (15) are rewritten as

$$\begin{cases}\dfrac{\sigma_s^*(\Omega')}{\sigma_e^*(\Omega)}=\alpha\dfrac{\sigma_s(\Omega')}{\sigma_e(\Omega)}+1-\alpha\\ \alpha\dfrac{\sigma_s(\Omega')}{\sigma_e(\Omega)}g(\Omega')+1-\alpha=0\end{cases} \tag{18}$$

To satisfy Eq. (11), the case $\Omega'=\Omega$ is considered and solving the system (18) yield

$$\alpha=1/[1-\omega(\Omega)g(\Omega)] \tag{19}$$

$$\omega^*(\Omega)=\omega(\Omega)[1-g(\Omega)]/[1-\omega(\Omega)g(\Omega)] \tag{20}$$

From Eq. (10), we deduce

$$\sigma_e^*(\Omega)=[1-\omega(\Omega)g(\Omega)]\sigma_e(\Omega) \tag{21}$$

Thus, Eqs. (20) and (21) are the isotropic scaling parameters applicable for general anisotropic scattering and for situations where the radiative properties depend or not on the incidence direction.

The P1 Isotropic Scaling Model. Since the P1 isotropic scaling parameters for randomly oriented particles in space have been developed by Lee and Buckius [15], we focus our analysis on the extension of the model to randomly oriented particles in plane. The P1 approximation ordinary differential equation for heat flux in a one-dimensional medium with radiative properties dependent of the incidence direction is

$$\frac{d^2q}{dy^2}-3(\sigma_{e,P1}-\langle\sigma_s g\rangle_{P1})\overline{\sigma_a}q=4\pi\overline{\sigma_a}\frac{dI_b}{dy} \tag{22}$$

where

$$\overline{\sigma_a}=\int_0^1\sigma_a(\mu)d\mu \tag{23}$$

$$\sigma_{e,P1}=3\int_0^1\sigma_e(\mu)\mu^2d\mu \tag{24}$$

$$\langle\sigma_s g\rangle_{P1}=3\int_0^1\sigma_s(\mu)g(\mu)\mu^2d\mu \tag{25}$$

As it can be deduced from the Dombrovsky study [23], randomly oriented particles in plane can be assumed as medium with equivalent radiative properties independent of the incident radiation. Thus, the equivalent absorption, extinction and scattering coefficients are defined, respectively, as

$$\sigma_{a,\mathrm{eq}}=\overline{\sigma_a} \tag{26}$$

$$\sigma_{e,\mathrm{eq}}=\sigma_{e,P1} \tag{27}$$

$$\sigma_{s,\mathrm{eq}}=\sigma_{e,\mathrm{eq}}-\sigma_{a,\mathrm{eq}} \tag{28}$$

With the previous equations, Eq. (22) have the same differential equation as for particles randomly oriented in space. Following Lee and Buckius [15] analysis, the P1 isotropic scaling parameters are

$$\omega_{P1}^*=\omega_{\mathrm{eq}}(1-g_{\mathrm{eq}})/(1-\omega_{\mathrm{eq}}g_{\mathrm{eq}}) \tag{29}$$

$$\sigma_{e,P1}^*=\sigma_{e,\mathrm{eq}}(1-\omega_{\mathrm{eq}}g_{\mathrm{eq}}) \tag{30}$$

with

$$\omega_{\mathrm{eq}}=\sigma_{s,\mathrm{eq}}/\sigma_{e,\mathrm{eq}} \tag{31}$$

$$g_{\mathrm{eq}}=\langle\sigma_s g\rangle_{P1}/\sigma_{s,\mathrm{eq}} \tag{32}$$

The Mean Isotropic Scaling Model. We assumed that the medium has mean coefficients and albedo, respectively,

$$\overline{\sigma}_{a,e,s}=\int_{4\pi}\sigma_{a,e,s}(\Omega)d\Omega/4\pi \tag{33}$$

$$\overline{\omega}=\overline{\sigma_s}/\overline{\sigma_e} \tag{34}$$

Following the method described for the directional isotropic scaling model (DIS) with the previous mean coefficients and solving the resulting system obtained by integrating Eq. (18)(b) over the scattered solid angle as $1/4\pi\int_{4\pi}\ldots d\Omega'$ leads to

$$\overline{\alpha}=1/(1-\overline{\omega g}) \tag{35}$$

$$\overline{\sigma_e^*}=(1-\overline{\omega g})\overline{\sigma_e} \tag{36}$$

$$\overline{\omega^*}=\overline{\omega}(1-\overline{g})/(1-\overline{\omega g}) \tag{37}$$

with

$$\overline{g}=\int_{4\pi}g(\Omega)d\Omega/4\pi \tag{38}$$

It is important to note that for particles randomly oriented in space, such as spheres, the radiative properties are independent of the incidence direction and the three isotropic scaling models become equal.

Numerical Solution. The solution of the radiative transfer involves the simultaneous solution of Eqs. (1) and (4). The discrete ordinate method (*S-n*) is used to obtain the dimensional heat flux and temperature within the medium for both exact anisotropic and isotropic problems. In this method, the integral part of the equation is replaced by a finite quadrature sum, thereby transforming the RTE into a system of linear differential equations [24]. The control volume method with the diamond scheme is used to solve the system of linear differential equations obtained by the *S-n*. The space is divided in uniform control volumes and several Gauss quadrature are used. The solution process is iterative and the iteration continues until convergence criteria corresponding to a relative change in I smaller than 10^{-5}%.

To solve the exact anisotropic and isotropic problems, the

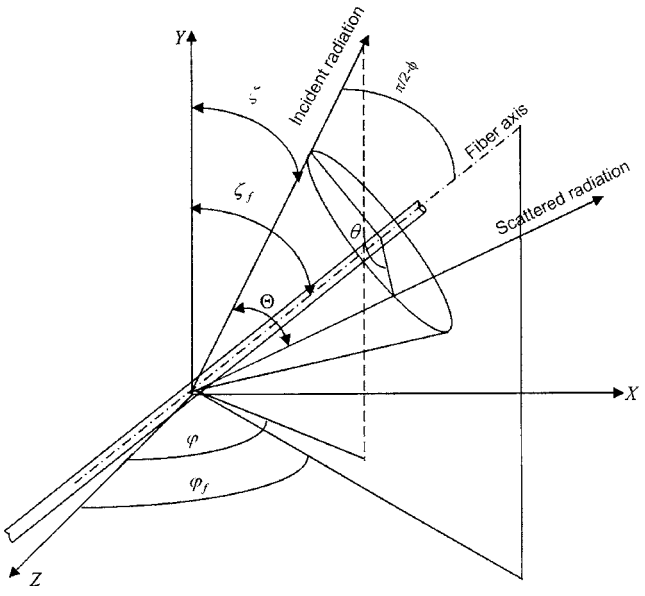

Fig. 1 Geometry of scattering by a fiber at oblique incidence

knowledge of the extinction/scattering coefficients, the phase function and the bias scattering factor of the medium are required. The predictions of these properties are discussed in the next section.

Radiative Properties of the Fibrous Medium. The fibers in the insulation medium are usually several millimeters long and 1 to 15 μm in diameter, and can be assumed as infinitely long circular cylinders because their lengths are far larger than the incident wavelength. Figure 1 presents the geometry of scattering by infinitely long cylinder at oblique incidence. The cylinder of radius r and complex index of refraction m is placed in free space. The incoming incident radiation of wavelength λ and direction defined by angle ϕ, is assumed to be unpolarized for each fiber. The scattered radiation propagates along the conic surface defined by the apex angle of $\pi-2\phi$.

The incident angle ϕ between the incident direction and the fiber axis, the incident direction (μ,φ) and the fiber orientation direction in the medium (μ_f,φ_f) are related by

$$\sin\phi=\mu\mu_f+\sqrt{(1-\mu^2)(1-\mu_f^2)}\cos(\varphi-\varphi_f) \tag{39}$$

The azimuthal angle of the cone, θ (Fig. 1), can be derived from the incident angle ϕ and the scattering angle Θ through the following equality [6,7]

$$\cos\Theta=\sin^2\phi+\cos\theta\cos^2\phi \tag{40}$$

According to Lee [6], the single fiber scattering phase function is given by

$$p(\Omega,\Theta,O_f)=\frac{4\lambda}{\pi^2}\frac{\Gamma(\Theta,\phi)}{C_s(\Omega,O_f)} \tag{41}$$

with

$$\Gamma(\Theta,\phi)=i(\theta,\phi)/\sqrt{(1-\cos\Theta)(1+\cos\Theta-2\sin^2\phi)} \tag{42}$$

The radiative properties: the extinction/scattering coefficients and the scattering phase function of the medium are determined respectively by the following relations

$$\{\sigma_e(\Omega),\sigma_s(\Omega)\}=\int_0^\infty\int_{O_f}\{C_e(\Omega,O_f),C_s(\Omega,O_f)\}dO_f dN_f(r) \tag{43}$$

Table 1 Four gray fibrous medium characteristics

Medium	$\lambda(\mu m)$	m[30]	r(μm)
1	4.00	$1.497-1.69\times10^{-3}i$	1.0
2	4.00	$1.497-1.69\times10^{-3}i$	3.0
3	9.18	$1.05-1.08i$	1.0
4	9.18	$1.05-1.08i$	3.0

$$P(\Omega,\Theta)=\frac{\int_0^\infty\int_{O_f}C_s(\Omega,O_f)p(\Omega,\Theta,O_f)dO_f dN_f(r)}{\int_0^\infty\int_{O_f}C_s(\Omega,O_f)dO_f dN_f(r)} \tag{44}$$

Here $dO_f=d\mu_f d\varphi_f/4\pi$ is the orientation distribution of the fibers and $dN_f(r)=N_f(r)dr$ specifies the total fiber length of radius r in a unit volume. The extinction and scattering cross section per unit length C_e, C_s and the angular distribution of the scattered intensity $i(\theta,\phi)$ are calculated from electromagnetic theory of the scattering of radiation by infinitely long cylinders [25,26]. For monodiameter insulation the integral over $dN_f(r)$ is replaced by $f_v/\pi r^2$ with f_v the volume fraction of a fibrous medium. In the case of fiber randomly oriented in space, the integration over dO_f can be replaced by an integral from 0 to $\pi/2$ over $\cos\phi d\phi$ and relations (43) and (44) become, respectively [27,28]

$$\{\sigma_e,\sigma_s\}=\frac{f_v}{\pi r^2}\int_0^{\pi/2}\{C_e(\phi),C_s(\phi)\}\cos\phi d\phi \tag{45}$$

$$P(\Theta)=\frac{4f_v\lambda}{\pi^3r^2\sigma_s}\int_0^{\pi/2}\Gamma(\Theta,\phi)\cos\phi d\phi \tag{46}$$

For fiber in random azimuthal orientation in the plane parallel to the boundary, the integration over dO_f can be replaced by an integral from 0 to π over $\delta(\mu_f)d\varphi_f/\pi$. By using Eqs. (39), (43), and (44) the integration over $d\varphi_f$ is computed in a manner which removes the incident azimuthal dependence of the radiative properties. The calculation gives, respectively [27,28]

$$\{\sigma_e(\mu),\sigma_s(\mu)\}=\frac{f_v}{\pi^2r^2}\int_{\phi_-}^{\phi_+}\frac{\{C_e(\phi),C_s(\phi)\}\delta(\mu_f)\cos\phi}{\sqrt{(\sin\phi_+-\sin\phi)(\sin\phi-\sin\phi_-)}}d\phi \tag{47}$$

$$P(\mu,\Theta)=\frac{4f_v\lambda}{\pi^4r^2\sigma_s(\mu)}\int_{\phi_-}^{\phi_+}\frac{\Gamma(\Theta,\phi)\delta(\mu_f)\cos\phi}{\sqrt{(\sin\phi_+-\sin\phi)(\sin\phi-\sin\phi_-)}}d\phi \tag{48}$$

where

$$\phi_\pm=\sin^{-1}\left[\mu\mu_f\pm\sqrt{(1-\mu^2)(1-\mu_f^2)}\right] \tag{49}$$

Bias Scattering Factor. Defined by Eq. (17), it can vary from −1 to +1. In general, the negative value corresponds to backward scattering, the zero to isotropic and the positive value to forward scattering. When the radiative properties are independent of the incident direction, such as for particle randomly oriented in space, the bias factor is called the asymmetry scattering factor. Introducing Eq. (44) into Eq. (17) yields

$$g(\Omega) = \frac{\int_0^{\pi}\int_0^{\infty}\int_{O_f} C_s(\Omega,O_f)p(\Omega,\Theta,O_f)\cos\Theta\sin\Theta dO_f dN_f(r)d\Theta}{2\int_0^{\infty}\int_{O_f} C_s(\Omega,O_f)dO_f dN_f(r)} \tag{50}$$

We proposed to carry out the integration over Θ before the integration over the fiber orientation and total length of fiber in a unit volume. Furthermore, for an incident radiation ϕ, the maximum scattering angle on a single fiber is $\Theta=\pi-2\phi$. With these specifications, Eq. (50) becomes

$$g(\Omega) = \frac{\int_0^{\infty}\int_{O_f}\int_0^{\pi-2\phi} C_s(\Omega,O_f)p(\Omega,\Theta,O_f)\cos\Theta\sin\Theta d\Theta dO_f dN_f(r)}{2\int_0^{\infty}\int_{O_f} C_s(\Omega,O_f)dO_f dN_f(r)} \tag{51}$$

Since the scattering cross section per unit length is independent of the scattering angle, the above equation can be rewritten as

$$g(\Omega) = \frac{\int_0^{\infty}\int_{O_f} C_s(\Omega,O_f)\langle\cos\Theta\rangle dO_f dN_f(r)}{\int_0^{\infty}\int_{O_f} C_s(\Omega,O_f)dO_f dN_f(r)} \tag{52}$$

with

$$\langle\cos\Theta\rangle = \frac{1}{2}\int_0^{\pi-2\phi} p(\Omega,\Theta,O_f)\cos\Theta\sin\Theta d\Theta \tag{53}$$

Here, $\langle\cos\Theta\rangle$ is the bias scattering factor of a single fiber defined by Marschall and Milos [29]. By using the previous relation together with relations (40) and (41), one obtains

$$\langle\cos\Theta\rangle = \frac{2\lambda}{\pi^2 C_s(\phi)}\int_0^{\pi} i(\phi,\theta)(\sin^2\phi+\cos^2\phi\cos\theta)d\theta \tag{54}$$

From relation (52), we can conclude that the bias scattering factor of fibrous medium is a function of the bias scattering factor of a single fiber. This conclusion can be easily generalized to calculate fibrous medium scattering phase moments. For mono–diameter insulation with fiber randomly oriented in space or fiber in random azimuthal orientation in the plane parallel to the boundary, the explicit expressions of the bias scattering factor Eq. (52) of the medium is, respectively

$$g = \frac{2\lambda f_v}{\pi^3 r^2\sigma_s}\int_0^{\pi/2}\int_0^{\pi} i(\phi,\theta)(\sin^2\phi+\cos^2\phi\cos\theta)\cos\phi d\theta d\phi \tag{55}$$

$$g(\mu) = \frac{2\lambda f_v}{\pi^4 r^2\sigma_s(\mu)} \times \int_{\phi_-}^{\phi_+}\int_0^{\pi} \frac{i(\phi,\theta)(\sin^2\phi+\cos^2\phi\cos\theta)\delta(\mu_f)\cos\phi}{\sqrt{(\sin\phi_+-\sin\phi)(\sin\phi-\sin\phi_-)}}d\theta d\phi \tag{56}$$

It should be noted that the above equations are simple in form and easy to compute.

Results and Discussion

We assumed that azimuthal symmetry prevails in the medium in radiative equilibrium. We considered four gray fibrous media. The fibers in the medium are randomly oriented either in space or in the plane parallel to the boundary. We also assumed uniform size distribution in the medium with the volume fraction of the fibers $f_v=0.004$. Table 1 lists parameters of the four gray media studied.

The solution of the exact and the isotropic scaling [DIS, P1 isotropic model (P1IS), mean isotropic model (MIS)] is obtained

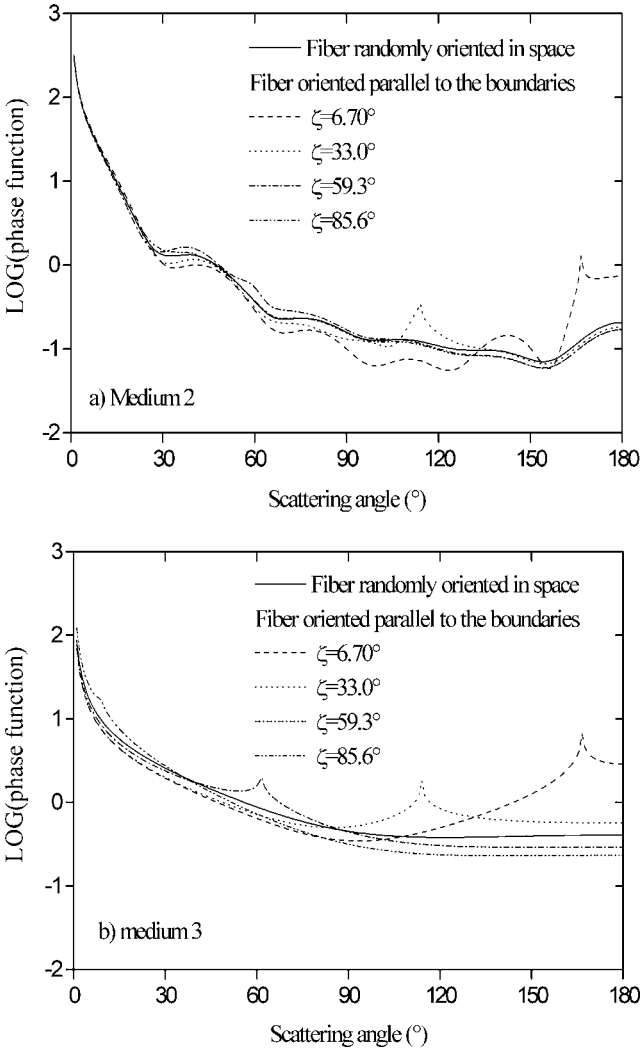

Fig. 2 Scattering phase function versus scattering angle: (*a*) medium 2, (*b*) medium 3

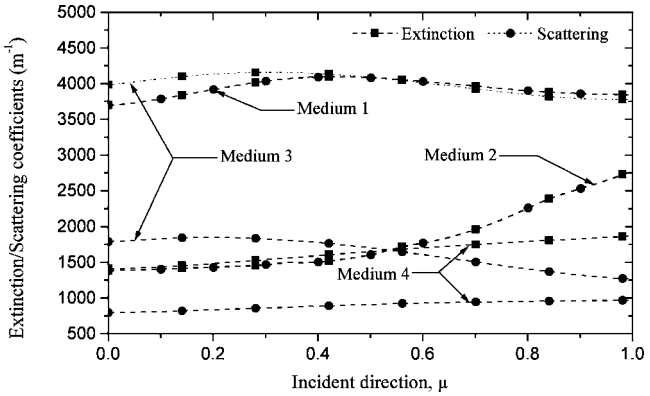

Fig. 3 Extinction/scattering coefficients versus incident direction

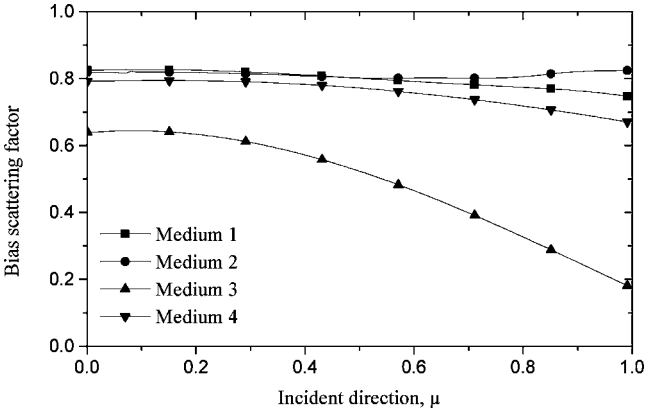

Fig. 4 Bias scattering factor versus incident direction

Table 2 Isotropic parameters

Medium	Fibers randomly oriented in space			
	σ_e	σ_s	ω	g
1	3944.82	3942.17	0.99932	0.79801
2	1800.88	1797.87	0.99833	0.81114
3	4004.00	1636.31	0.40867	0.50118
4	1641.17	896.534	0.54627	0.75504
	Fibers parallel to the boundaries			
	Mean parameters			
	$\overline{\sigma}_e$	$\overline{\sigma}_s$	$\overline{\omega}$	$\overline{g}$
1	3944.80	3942.14	0.99932	0.79798
2	1800.93	1797.88	0.99830	0.81090
3	4003.91	1636.30	0.40867	0.48348
4	1640.88	896.505	0.54635	0.75710
	P1 parameters			
	$\sigma_{e,eq}$	$\sigma_{s,eq}$	ω_{eq}	g_{eq}
1	3932.89	3930.24	0.99932	0.77697
2	2178.47	2175.44	0.99861	0.81227
3	3896.10	1528.53	0.39232	0.35025
4	1763.61	1019.25	0.57793	0.66735

making use of the same solver: the discrete ordinate method. Moreover, the same subroutines DQDAG and DTWODQ from IMSL [30,31] with 30 to 61 points Gauss–Kronrod recommended for oscillatory functions were used to evaluate the single or double integrals of radiative coefficients: absorption, extinction, and the scattering coefficients; bias scattering factor; and scattering phase function. The P1IS and MIS average properties are evaluated using 21-point Gauss–Kronrod of IMSL [31] subroutine DQDAGS. Therefore, it is interesting to see the accuracy and the cost in time that using isotropic scaling implies.

The bias scattering factor of fibrous medium for fiber randomly oriented either in space or parallel to the boundary has been computed from Eq. (50) and from Eqs. (55) and (56). Good agreement was obtained between the two approaches. Furthermore, Eqs. (55) and (56) derived from Eq. (52) requires smallest computation time. Consequently, these equations will be used in the rest of the

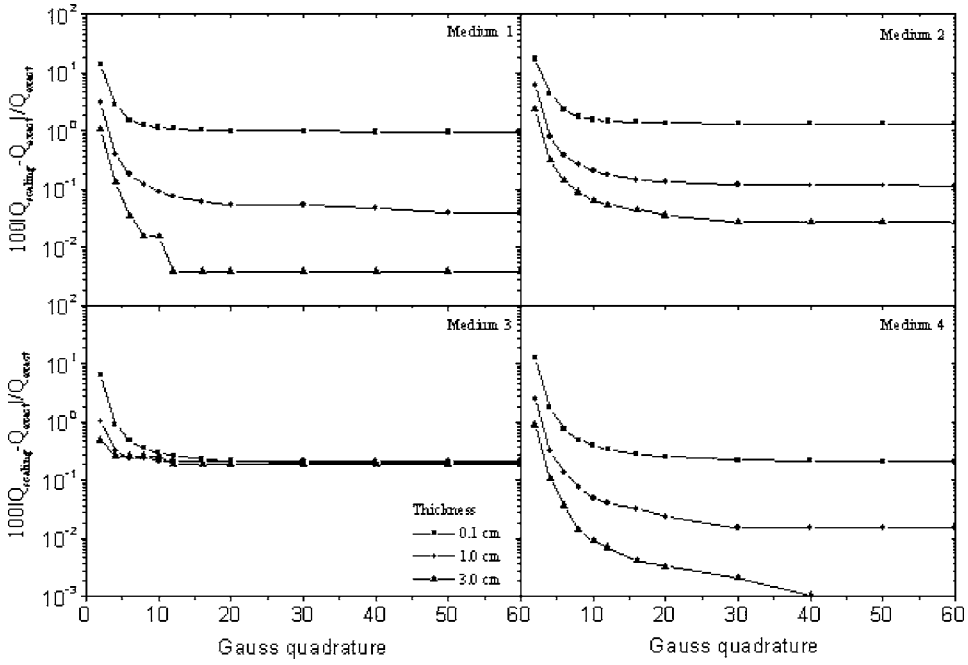

Fig. 5 Relative error versus Gauss quadrature: Fiber randomly oriented in space

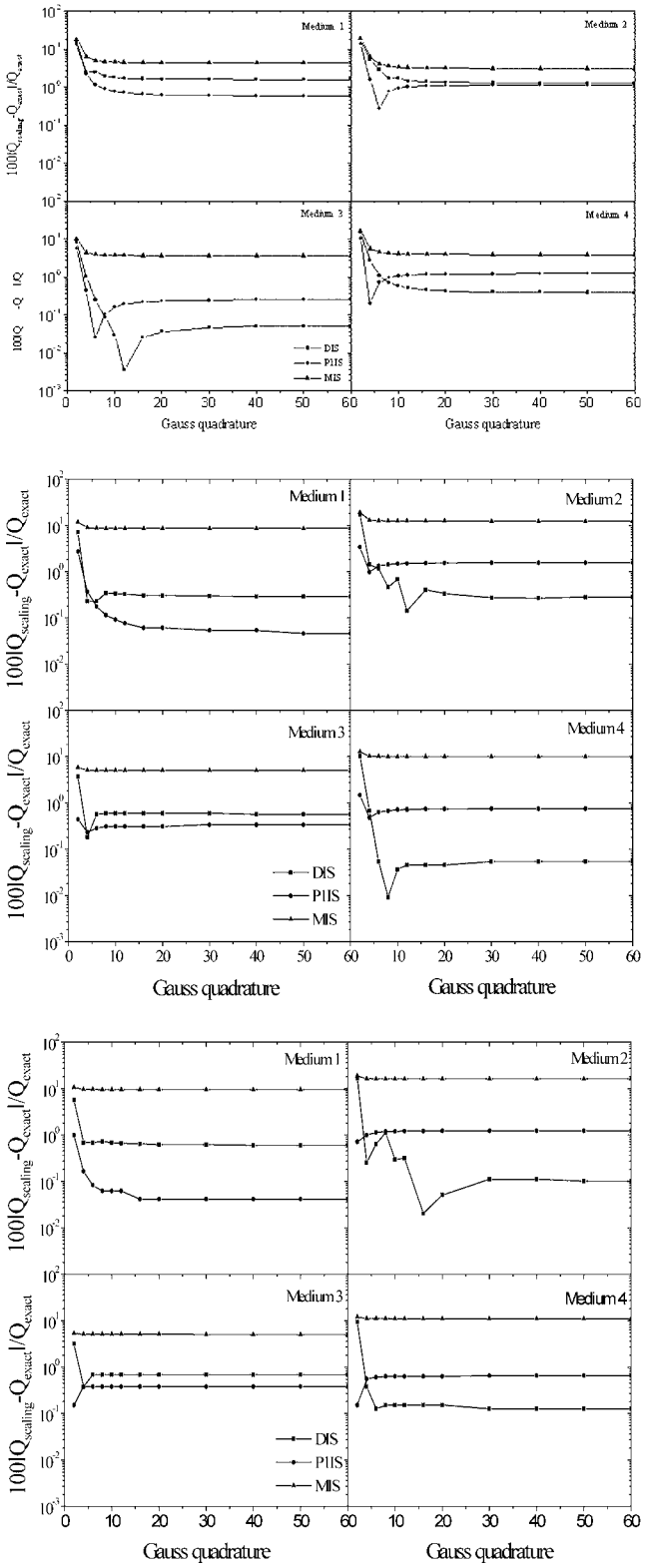

Fig. 6 Relative error versus Gauss quadrature for fiber parallel to the boundaries: (*a*) thickness is 0.1 cm, (*b*) thickness is 1.0 cm, and (*c*) thickness is 3.0 cm

paper to evaluate the bias factor. An analysis of the convergence on the exact problem shows that 60 directions Gauss quadrature is sufficient. Thus, the exact solution is computed with 60 directions Gauss quadrature for all cases. The results obtained using 100 control volumes are the grid independent results for this problem. The dimensionless heat flux Q in the medium is defined as

$$Q = q/\sigma_b(T_1^4 - T_2^4) \tag{57}$$

As an example, the scattering phase function for both fiber randomly oriented in space and parallel to the boundary are shown in Fig. 2 for a nonabsorbing Medium 2 and for an absorbing Medium 3 (Lee [28]). The influence of the incident direction on the scattering phase function can be observed.

For the four media, the variation of the extinction/scattering coefficients and the bias scattering factor with the incident direction for fiber randomly oriented in the plane parallel to the boundary is shown in Figs. 3 and 4, respectively. Figure 4 shows that the bias factor depends weakly on incident direction for nonabsorbing media (Mediums 1 and 2), while this factor varies with the incident direction for absorbing media especially for Medium 3.

Table 2 summarizes the parameters used for the computation of the isotropic scaling models. The mean radiative absorption, extinction, and scattering coefficients and the mean asymmetry factor are very close of radiative properties of fibrous medium randomly oriented in space fibers.

Relative errors between isotropic scaling approximation and exact solution for dimensionless heat fluxes are presented in Fig. 5 for fibers randomly oriented in space. For fibers randomly oriented in space, a good agreement is observed between the isotropic scaling approximation and the exact solution: the relative error is less than 2% for all cases considered and for Gauss quadrature greater than 12. It is also important to note that the error decreases with increasing optical depth for highly scattering medium (Mediums 1, 2, and 4).

Figure 6 shows the relative error between isotropic scaling models and the exact solution for fibers randomly oriented in the plane parallel to the boundary. Figure 6 also presents a comparison between the three different isotropic scaling models: DIS, P1, P1IS and MIS isotropic scaling. For fibers randomly orientatied in the plane parallel to the boundary, a great dispersion appears between the three different isotropic scaling models. The MIS gives a poor accuracy with the exact solution: the relative error is between 3–20%. Thus, this approach is unsuitable for radiative analysis. The DIS and the P1IS predict with accuracy heat flux for all cases studied: telative errors are less than 2%.

Tables 3 and 4 compare the dimensionless isotropic scaling and exact radiative heat fluxes for a medium with fibers randomly oriented in space and in the plane parallel to the boundary, respectively. The isotropic scaling solutions are for a 12 directions Gauss quadrature. These tables also compared the central processing unit (CPU) time (obtain with a processor Celeron-M, FSB 400 MHz) between exact and isotropic scaling solutions. For all cases studied, CPU time of isotropic scaling approximation is much smaller

Table 3 Dimensionless radiative heat flux and CPU time for fiber randomly oriented in space

Thickness (cm)	Medium	Exact		Isotropic Scaling	
		Q	CPU (s)	Q	CPU (s)
0.1	1	0.599459	2366.12	0.60588	0.48
	2	0.762658	3481.78	0.77372	1.23
	3	0.289032	2310.33	0.28978	0.73
	4	0.560779	2839.43	0.56263	0.15
1.0	1	0.141635	2414.51	0.14174	0.99
	2	0.274849	3495.48	0.27532	1.37
	3	0.040005	2460.48	0.04009	6.27
	4	0.120502	2863.85	0.12055	0.89
3.0	1	0.052522	2700.45	0.05252	3.92
	2	0.113960	3563.98	0.11402	2.04
	3	0.013725	3454.47	0.01375	43.35
	4	0.043934	3011.65	0.04394	4.96

Table 4 Dimensionless radiative heat flux and CPU time for fiber parallel to the boundaries

Thickness (cm)	Medium	Exact		DIS		P1IS		MIS	
		Q	CPU (s)	Q	CPU (s)	Q	CPU (s)	Q	CPU (s)
0.1	1	0.57852	4029.81	0.58973	40.92	0.58404	137.55	0.60585	137.09
	2	0.74764	6005.38	0.76012	55.93	0.74198	124.86	0.77348	190.70
	3	0.27913	3523.78	0.27957	36.43	0.27904	124.33	0.28797	123.39
	4	0.54058	5080.64	0.54386	44.99	0.53524	149.19	0.56315	148.10
1.0	1	0.12988	4084.75	0.13006	41.54	0.13059	138.12	0.14172	137.58
	2	0.24302	6021.32	0.24503	56.08	0.24103	125.03	0.27504	190.80
	3	0.03811	3681.78	0.03796	42.40	0.03807	130.44	0.03975	128.90
	4	0.10941	5096.64	0.10957	45.83	0.10882	150.01	0.12078	148.78
3.0	1	0.04770	4414.92	0.04762	44.90	0.04797	141.60	0.05252	140.52
	2	0.09727	6107.45	0.09776	56.91	0.09690	125.96	0.11388	191.50
	3	0.01306	4729.45	0.01300	81.98	0.01304	170.97	0.01363	165.61
	4	0.03948	5191.90	0.03950	50.37	0.03931	155.08	0.04403	152.86

than CPU time of exact solution. The solution of the RTE with isotropic scaling parameters was finished after 0.2–43 s in the case of fibrous randomly oriented in space; 41–81 s for DIS; 125–190 s for P1IS and MIS; while the exact solution required about 2350–5800 s. Therefore, isotropic scaling in the case of medium with randomly oriented fibrous in space is over 80 times faster; in the case of medium with randomly oriented fibrous in plane, the directional isotropic scaling is over 50 times faster, the P1 and the mean isotropic scaling are over 25 times faster than the exact solution.

Conclusions

Three isotropic scaling models have been formulated for radiative analysis in fibrous medium. The discrete ordinate method was used to solve the radiative transfer equation of exact and isotropic problems. This paper tends to show that fibrous medium is equivalent to homogeneous medium with isotropic scattering phase function and radiative properties independent on the incident direction. The results lead to the following conclusions.

- The P1 and the directional isotropic scaling have been proved to model accurately radiative heat transfer in fibrous medium with randomly oriented fiber either in space or parallel to the boundary.
- Arithmetic mean radiative properties cannot be used for radiative analysis in randomly oriented fiber in a plane.
- The isotropic scaling model requires very few quadrature to converge to exact solution than the exact problem.
- The isotropic scaling solution is much faster than the exact solution.

In this paper, fibers randomly oriented either in space or in the plane parallel to the boundary have been considered. The influence of other fiber orientations on the accuracy of the isotropic scaling would be investigated.

Acknowledgment

The first author wishes to thank the French foreign ministry and the CETHIL for co-financing this research.

Nomenclature

f_v = fiber volume fraction
g = asymmetry factor
I = radiative intensity
I_b = blackbody intensity
m = complex index of refraction
P = phase function
q = radiative heat flux
Q = dimensionless radiative heat flux
r = fiber radius
y = thickness

Greek Symbols

δ = delta function
ϕ = incident angle
φ = azimuth angle
μ = direction cosine in y direction
σ = radiative coefficient
σ_b = Stefan-Boltzmann constant
ω = albedo
ζ = polar angle
Ω = ordinate direction
Θ = scattering angle

Superscript

$-$ = mean variables
* = scaled variable
$'$ = scattering direction

Subscript

e = extinction
eq = equivalent
s = scattering
f = fiber
P1 = P1 scaling

References

[1] Baillis, D., and Sacadura, J. F., 2000, "Thermal Radiation Properties of Dispersed Media: Theoretical Prediction and Experimental Characterization," J. Quant. Spectrosc. Radiat. Transf., **67**, pp. 327–363.
[2] Viskanta, R., and Mengüc, M. P., 1989, "Radiative Transfer in Dispersed Media," Appl. Mech. Rev., **42**(9), pp. 241–259.
[3] Petrov, V. A., 1994, "Solution of Inverse Problems of Radiation Transfer in Semitransparent Scattering Materials Based on the Radiation Diffusion Approximation," High Temp. - High Press., **26**, pp. 339–351.
[4] Sacadura, J. F., Uny, G., and Venet, A., 1986, "Models and Experiments for a Radiation Parameter Estimation of Absorbing, Emitting, and Anisotropically Scattering Media," *Int. Heat Transfer*, C. L. Tien, V. P. Carey, and J. K. Farrell, eds. Vol. 2, Hemisphere, New York, pp. 565–569.
[5] Doermann, D., and Sacadura, J. F., 1996, "Heat Transfer in Open Cell Foam Insulation," ASME J. Heat Transfer, **118**, pp. 88–93.
[6] Lee, S. C., 1986, "Radiative Heat Transfer through a Fibrous Medium: Allowance for Fiber Orientation," J. Quant. Spectrosc. Radiat. Transf., **36**(3), pp. 253–263.
[7] Houston, R. L., and Korpela, S. A., 1982, "Heat Transfer Through Fiberglass Insulation," *Proc 7th Int. Heat Transfer Conference*, Vol. 2, pp. 499–504.
[8] Kim, T. K., and Lee, H. S., 1988, "Effect of Anisotropic Scattering on Radiative Heat Transfer in Two-Dimensional Rectangular Enclosures," Int. J. Heat Mass Transfer, **31**(8), pp. 1711–1721.
[9] Hendricks, T. J., and Howell, J. R., 1996, "Absorption Coefficients and Scattering Phase Functions in Reticulated Porous Ceramics," ASME J. Heat Transfer, **118**, pp. 79–87.
[10] Baillis, D., Arduini-Schuster, M., and Sacadura, J. F., 2002, "Identification of Spectral Radiative Properties of Polyurethane Foam from Hemispherical and

Bidirectional Transmittance and Reflectance Measurements," J. Quant. Spectrosc. Radiat. Transf., **73**, pp. 297–306.
[11] Tong, T. W., Sathe, S. B., and Peck, R. E., 1990, "Improving the Performance of Porous Radiant Burners through Use of Submicron Size Fibers," Int. J. Heat Mass Transfer, **33**(6), pp. 1339–1346.
[12] Litovsky, E., Kleiman, J. I., and Menn, N., 2003/2004, "Measurement and Analysis by Different Methods of Apparent, Radiative, and Conductive Thermophysical Properties of Insulation Materials," High Temp. - High Press., **35/36**, pp. 101–108.
[13] Kim, T. K., and Lee, H. S., 1990, "Modified δ-M Scaling Results for Mie-Anisotropic Scattering Media," ASME J. Heat Transfer, **112**, pp. 988–994.
[14] McKellar, H. J., and Box, M. A., 1981, "The Scaling Group of the Radiative Transfer Equation," J. Atmos. Sci., **38**, pp. 1063–1068.
[15] Lee, H., and Buckius, R. O., 1982, "Scaling Anisotropic Scattering in Radiation Heat Transfer for a Planar Medium," ASME J. Heat Transfer, **104**, pp. 68–75.
[16] Joseph, J. H., Wiscombe, W. J., and Weinman, J. A., 1976, "The Delta-Eddington Approximation for Radiative Flux Transfer," J. Atmos. Sci., **33**, pp. 2452–2459.
[17] Modest, M. F., and Azad, F. H., 1980, "The Influence and Treatment of Mie-Anisotropic Scattering in Radiative Heat Transfer," ASME J. Heat Transfer, **102**, pp. 92–98.
[18] Clark, G. C., Chu, C. M., and Churchill, S. W., 1957, "Angular Distribution Coefficients for Radiation Scattered by a Spherical Particle," J. Opt. Soc. Am., **47**(1), pp. 81–84.
[19] Tong, T. W., and Tien, C. L., 1980, "Analytical Models for Thermal Radiation in Fibrous Insulations," J. Therm. Insul., **4**, pp. 27–44.
[20] Houston, R. L., 1980, "Combined Radiation and Conduction in a Nongray Participating Medium that Absorbs, Emits, and Anisotropically Scatters," Ph.D thesis, The Ohio State University.
[21] Yuen, W. W., Takara, E., and Cunnington, G., 2003, "Combined Conductive/Radiative Heat Transfer in High Porosity Fibrous Insulation Materials: Theory and Experiment," *Proc. 6th ASME-JSME Thermal Engineering Joint Conférence*.
[22] Heino, J., Arridge, S., Sikora, J., and Somersalo, E., 2003, "Anisotropic Effects in Highly Scattering Media," Phys. Rev. E, **68**, pp. 031908.
[23] Dombrovsky, L. A., 1996, "Quartz-Fiber Thermal Insulation Infrared Radiative Properties and Calculation of Radiative-Conductive Heat Transfer," ASME J. Heat Transfer, **118**, pp. 409–414.
[24] Siegel, R., and Howell, J. R., 1992, *Thermal Radiation Heat Transfer*, 3rd Ed., Taylor and Francis, London.
[25] Kerker, M., 1969, *The Scattering of Light and other Electromagnetic radiation*, Academic, NY.
[26] Lind, A. C., and Greeenberg, J. M., 1966, "Electromagnetic Scattering for Obliquely Oriented Cylinders," J. Appl. Phys., **37**(8), pp. 3195–3303.
[27] Lee, S. C., and Cunnington, G. R., 2000, "Conduction and Radiation Heat Transfer in High-Porosity Fiber Thermal Insulation," Int. J. Heat Mass Transfer, **14**(2), pp. 121–136.
[28] Lee, S. C., 1990, "Scattering Phase Function for Fibrous Media," Int. J. Heat Mass Transfer, **33**(10), pp. 2183–2190.
[29] Marschall, J., and Milos, F. S., 1997, "The Calculation of Anisotropic Extinction Coefficients for Radiation Diffusion in Rigid Fibrous Ceramics Insulations," Int. J. Heat Mass Transfer, **40**(3), pp. 627–634.
[30] Hsieh, C. K., and Su, K. C., 1979, "Thermal Radiative Properties of Glass From 0.32 to 206 μm," Sol. Energy, **22**, pp. 37–43.
[31] IMSL, IMSL MATH/LiBRARY Users Manual, 2500 Park West Tower One.

Smoothing Monte Carlo Exchange Factors Through Constrained Maximum Likelihood Estimation

K. J. Daun[1]
D. P. Morton
J. R. Howell

Department of Mechanical Engineering,
The University of Texas at Austin

Complex radiant enclosure problems are often best treated by calculating exchange factors through Monte Carlo simulation. Because of its inherent statistical nature, however, these exchange factor estimations contain random errors that cause violations of the reciprocity rule of exchange factors, and consequently the second law of thermodynamics. Heuristically adjusting a set of exchange factors to satisfy reciprocity usually results in a violation of the summation rule of exchange factors and the first law of thermodynamics. This paper presents a method for smoothing exchange factors based on constrained maximum likelihood estimation. This method works by finding the set of exchange factors that maximizes the probability that the observed bundle emissions and absorptions would occur subject to the reciprocity and summation rules of exchange factors as well as a nonnegativity constraint. The technique is validated by using it to smooth the sets of exchange factors corresponding to two three-dimensional radiant enclosure problems. [DOI: 10.1115/1.2035111]

Keywords: Exchange Factor, Monte Carlo, Constrained Maximum Likelihood Estimation

Introduction

The Monte Carlo method is a powerful tool for analyzing radiant enclosures, and is especially well suited for solving problems involving complex geometries and surface properties. In its most common implementation, the Monte Carlo method is used to estimate exchange factors $\mathcal{F}_{ij}$ defined here as the fraction of total radiant energy emitted by the ith surface that is ultimately absorbed by the jth surface. (These estimations are denoted $\hat{\mathcal{F}}_{ij}$.) Once the set of exchange factors has been estimated, an energy balance is written over each surface having the form

$$q_i A_i = \varepsilon_i E_{bi} A_i - \sum_{j=1}^{N} \varepsilon_j E_{bj} A_j \hat{\mathcal{F}}_{ij}. \tag{1}$$

The resulting system of linear equations is solved for the unknown values of emissive power E_{bi} and heat flux, q_i.

Since exchange factors are often analytically intractable, they are instead estimated by performing a large number of statistical experiments. In each experiment, a "photon bundle" representing a quantity of radiant energy is emitted from a random location on the ith surface in a direction chosen at random from a prescribed distribution of emission angles. Each time this bundle is intercepted by another surface it is either absorbed or reflected, depending on the optical properties of the intervening surface relative to the value of a pseudorandom number. Every bundle is ray traced until it is ultimately absorbed by another surface. Once a large number of bundles have been emitted by all the surfaces, the exchange factor between the ith and jth surfaces is estimated by $\hat{\mathcal{F}}_{ij} = N_{bij}/N_{bi}$, where N_{bi} is the total number of bundles emitted by the ith surface and N_{bij} is the number of those bundles ultimately absorbed by the jth surface.

From the definition of an exchange factor, it is clear that in order to satisfy energy conservation over any surface, the subset of exchange factors between a particular enclosure surface and the other surfaces must sum to unity

$$\sum_{j=1}^{N} \mathcal{F}_{ij} = 1. \tag{2}$$

Also, since the second law of thermodynamics requires the net heat transfer between any two surfaces having the same temperature to equal zero, it can be shown that any pair of exchange factors must satisfy the reciprocity rule

$$\varepsilon_i A_i \mathcal{F}_{ij} = \varepsilon_j A_j \mathcal{F}_{ji}. \tag{3}$$

Equation (2) is satisfied when $\hat{\mathcal{F}}_{ij}$ is substituted for $\mathcal{F}_{ij}$ since every emitted bundle is ultimately absorbed. Nevertheless, because $\hat{\mathcal{F}}_{ij}$ contains a statistical error, $\hat{\mathcal{F}}_{ij} = \mathcal{F}_{ij}$ only as N_{bi} approaches infinity, and as a result Eq. (3) is generally not satisfied for $\hat{\mathcal{F}}_{ij}$ and $\hat{\mathcal{F}}_{ji}$. Also, in many problems, pairs of exchange factors that should be equal due to geometric symmetry may not be equal, again due to stochastic errors inherent in the Monte Carlo approach.

When performing a radiant enclosure analysis, it is obviously desirable for the exchange factor set to satisfy the first and second laws of thermodynamics, and also to obey any geometric symmetry. (This is especially important in the inverse design of radiant enclosures, a procedure that is highly sensitive to errors in the exchange factor matrix [1].) Modifying the set of exchange factors so that summation, reciprocity, and symmetry relations are satisfied is very problematic, however, since changing the exchange factor set to satisfy one relationship generally results in a violation of the other two; for example, if the reciprocity relationship were used to modify the initial set of exchange factors in order to enforce Eq. (3), Eq. (2) would no longer be satisfied.

Two main types of algorithms have been developed for heuristically modifying (or "smoothing") exchange factor sets. Algorithms of the first type work by modifying the set of exchange factors so that both reciprocity and summation rules are obeyed, but do not limit the size of the correction. van Leersum [2] presented a technique where the original set of exchange factors is

[1]Present Address: National Research Council, Ottawa, Canada, K1A OR6.

Contributed by the Heat Transfer Division of ASME for publication in the JOURNAL OF HEAT TRANSFER. Manuscript receieved: November 5, 2004; final manuscript received: April 20, 2005. Review conducted by: Stefan Thynell.

modified iteratively by enforcing the summation and reciprocity constraints in succession until the results converged; Lawson [3] modified this technique to account for the relative accuracy of the initial set of exchange factors. (Larger exchange factors are more accurate, since they are estimated using more bundles.) Taylor et al. [4] suggested calculating the elements in the upper triangle of the exchange factor matrix, using reciprocity to solve for those in the lower triangle of the matrix, and finally solving the diagonal of the matrix through the summation relationship. Although these algorithms are simple and easy to implement, there is no guarantee that the modified set of exchange factors will be more accurate than the original unsmoothed set.

The second type of algorithm addresses this shortcoming by finding the smallest vector of correction factors that could be added to the set of exchange factors so that it satisfies both summation and reciprocity relationships. This transforms the smoothing problem into a constrained least-squares minimization problem, where the objective is to minimize the norm of the correction vector subject to the constraints defined in Eqs. (2) and (3). The elements of the correction vector are often weighted when defining the objective function so as to ensure that the smaller, less accurate exchange factors are modified in preference to the larger ones. This technique was pioneered by Vercammen and Froment [5] for smoothing Hottel's exchange areas determined by the Monte Carlo method, and was subsequently adapted and refined by Larsen and Howell [6] and Loehrke et al. [7]. Although these algorithms usually improve the accuracy of the exchange factor set, the analytical solution of the constrained minimization problem is complex. They also occasionally generate negative exchange factors, which are nonphysical; imposing a non-negativity constraint on the exchange factors renders the minimization problem analytically intractable.

This paper presents a method for smoothing exchange factors based on constrained maximum likelihood (CML) estimation. In this approach, each bundle emission is treated as an individual statistical experiment, and $\mathcal{F}_{ij}$ is interpreted as the probability that a bundle emitted by the ith surface will be absorbed by the jth surface. The constrained likelihood maximization procedure then works to find these probabilities by maximizing the likelihood that the results of all the statistical experiments (i.e., the intersection of these results) will be observed subject to equality and inequality constraints on the probabilities that enforce exchange factor summation, reciprocity, non-negativity, and symmetry relations. Although constrained maximum likelihood has been used in many other engineering and operations research applications for parameter estimation, to the best of the authors' knowledge this is the first time this approach has been used to solve for exchange factors. Jamshidian [8] and Schoenberg [9] provide thorough overviews of constrained maximum likelihood estimation and recent applications.

The technique is introduced by demonstrating how unconstrained maximum likelihood estimation can be applied to solve for individual exchange factors between pairs of surfaces. Next, a constrained maximum likelihood estimation procedure for smoothing sets of exchange factors subject to summation, reciprocity, and symmetry relations is presented. Finally, the method is demonstrated by using it to smooth the exchange factor sets of two three-dimensional enclosure problems; the enclosure in the first problem has black surfaces, while the surfaces of the second enclosure have both diffuse and specular optical properties, which is more representative of a problem that might be encountered in an industrial setting. The algorithm described in this paper is for analyzing enclosures containing a nonparticipating medium, although it could be modified to treat more complex problems.

Estimating a Single Exchange Factor Using Maximum Likelihood Estimation

In a Monte Carlo simulation, the exchange factor between the ith and jth surfaces $\mathcal{F}_{ij}$ represents the fraction of energy emitted by the ith surface that is absorbed by the jth surface, which is estimated by

$$\mathcal{F}_{ij} \approx \hat{\mathcal{F}}_{ij} = N_{bij}/N_{bi}, \tag{4}$$

where N_{bi} is the total number of bundles emitted by the ith surface, and N_{bij} is the number of those bundles ultimately absorbed by the jth surface.

In the context of maximum likelihood estimation, each bundle emission from the ith surface is treated as a Bernoulli experiment with a binary outcome; the bundle is either absorbed by the jth surface, or it is not. Furthermore, the exact exchange factor $\mathcal{F}_{ij}$ is interpreted as the probability that a bundle emitted from the ith surface will ultimately be absorbed by the jth surface. Let $\mathbf{X}_{ij}$ represent a vector containing N_{bi} random binary variables used to store the result of each Bernoulli experiment; once the kth experiment is performed, X_{ij}^k is assigned a numerical value x_{ij}^k, where if the kth emitted bundle is absorbed by the jth surface $x_{ij}^k = 1$; otherwise, $x_{ij}^k = 0$. The resulting probability mass function of X_{ij}^k is then

$$f(x_{ij}^k) = \mathcal{F}_{ij}^{x_{ij}^k}(1-\mathcal{F}_{ij})^{1-x_{ij}^k}, \quad x_{ij}^k \in \{0,1\}. \tag{5}$$

Since a total of N_{bi} bundles are emitted from the ith surface, the Bernoulli experiment is performed N_{bi} times and a set of sample data $\{x_{ij}^k, k=1,2,\ldots,N_{bi}\}$ is generated. Furthermore, since each Bernoulli experiment is independent, the probability of the entire solution set occurring, i.e, the probability of outcome $\{x_{ij}^k, k=1,2,\ldots,N_{bi}\}$ is given by

$$L_{ij}(\mathcal{F}_{ij}) = \prod_{k=1}^{N_{bi}} \mathcal{F}_{ij}^{x_{ij}^k}(1-\mathcal{F}_{ij})^{1-x_{ij}^k} = \mathcal{F}_{ij}^{\sum_{k=1}^{N_{bi}} x_{ij}^k}(1-\mathcal{F}_{ij})^{N_{bi}-\sum_{k=1}^{N_{bi}} x_{ij}^k}, \tag{6}$$

where $L_{ij}(\mathcal{F}_{ij})$ is the *likelihood function* of $\mathcal{F}_{ij}$. Because N_{bij} of the results (contained in $\mathbf{X}_{ij}$) equal unity, Eq. (6) simplifies to

$$L_{ij}(\mathcal{F}_{ij}) = \mathcal{F}_{ij}^{N_{bij}}(1-\mathcal{F}_{ij})^{N_{bi}-N_{bij}}. \tag{7}$$

The value of $\mathcal{F}_{ij}$ is estimated by finding the value $\hat{\mathcal{F}}_{ij}$ that maximizes the probability of the experimentally observed results occurring, i.e., $L_{ij}(\hat{\mathcal{F}}_{ij}) = \mathrm{Max}[L_{ij}(\mathcal{F}_{ij})]$. (Note that $\hat{\mathcal{F}}_{ij}$ only estimates the true $\mathcal{F}_{ij}$, since it is determined using the results of a finite number of Bernoulli experiments.) Because the natural log function $\ln(u)$ monotonically increases with increasing u, this is equivalent to finding the value of $\hat{\mathcal{F}}_{ij}$ that maximizes $ln[L_{ij}(\mathcal{F}_{ij})]$, i.e.,

$$\ln[L_{ij}(\hat{\mathcal{F}}_{ij})] = \mathrm{Max}\{\ln[L_{ij}(\mathcal{F}_{ij})]\} = \mathrm{Max}[N_{bij}\ln(\mathcal{F}_{ij}) + (N_{bi} - N_{bij})\ln(1-\mathcal{F}_{ij})]. \tag{8}$$

The value of $\hat{\mathcal{F}}_{ij}$ is solved by writing the first-order necessary conditions at the maximum of $\ln[L_{ij}(\mathcal{F}_{ij})]$, i.e.,

$$\left.\frac{d\{\ln[L_{ij}(\mathcal{F}_{ij})]\}}{d\mathcal{F}_{ij}}\right|_{\mathcal{F}_{ij}=\hat{\mathcal{F}}_{ij}} = \frac{N_{bij}}{\hat{\mathcal{F}}_{ij}} - \frac{N_{bi}-N_{bij}}{1-\hat{\mathcal{F}}_{ij}} = 0, \tag{9}$$

yielding the anticipated result

$$\hat{\mathcal{F}}_{ij} = N_{bij}/N_{bi}. \tag{10}$$

Computing a Set of Exchange Factors Using Constrained Maximum Likelihood Estimation

The technique described above is suitable for estimating a single exchange factor between any pair of surfaces in a radiant

enclosure. In practice, however, Monte Carlo is more often used to calculate a set of exchange factors between all enclosure surfaces. These exchange factors form the $(N\times N)$ matrix $\mathbf{F}$, with elements $\mathcal{F}_{ij}=\mathcal{F}_{ij}$ and where N is the number of enclosure surfaces.

The exchange factor matrix is usually estimated row-by-row; estimates for the ith row are calculated by emitting N_{bi} bundles in random directions from random locations on the ith surface, ray-tracing each bundle until it is absorbed. Each time one of these bundles is absorbed by the jth surface, N_{bij} is incremented. Once all the bundles have been emitted by the ith surface, the ith row of $\mathbf{F}$ is estimated by $\mathcal{F}_{ij}\approx\hat{\mathcal{F}}_{ij}=N_{bij}/N_{bi}, j=1,2,\ldots,N$. Because each bundle is ultimately absorbed by some surface, this procedure produces a set of exchange factors that exactly satisfies the summation rule, Eq. (2), with $\hat{\mathcal{F}}_{ij}$ substituted for $\mathcal{F}_{ij}$. Since each row of $\mathbf{F}$ is estimated independently, however, the reciprocity relation between any pair of surfaces is generally not satisfied.

One alternative is to first estimate $(N^2+N)/2$ exchange factors (say those in the diagonal and upper-triangular portion of $\mathbf{F}$) independently through the Monte Carlo procedure described in the previous section, and then use $\hat{\mathcal{F}}_{ji}=(\varepsilon_i A_i/\varepsilon_j A_j)\hat{\mathcal{F}}_{ij}$ to calculate the remaining $(N^2-N)/2$ exchange factors in the bottom triangle of $\mathbf{F}$. Although this method ensures that the reciprocity relationship now holds between the surfaces, the summation rule is no longer satisfied. This approach is also computationally inefficient, since bundles absorbed by surface elements corresponding to the lower triangle of $\mathbf{F}$ are ignored when calculating exchange factors.

These shortcomings can be avoided by using constrained maximum likelihood estimation to smooth a set of exchange factors. Consider the ith row of $\mathbf{F}$, which contains the exchange factors from the ith surface to every other surface, $\{\hat{\mathcal{F}}_{ij}, j=1,2,\ldots,N\}$, estimated by emitting a total of N_{bi} bundles from the ith surface. For each $j=1,2,\ldots,N$, the random outcome of such an experiment is represented by vector $\mathbf{X}_{ij}$, which contains N_{bi} binary variables. If the kth bundle emitted from the ith surface is absorbed by the jth surface, then $X_{ij}^k=1$; otherwise $X_{ij}^k=0$. Since every bundle emitted by the ith surface is eventually absorbed

$$\sum_{j=1}^{N}\mathcal{F}_{ij}=1 \tag{11}$$

and

$$\sum_{j=1}^{N}N_{bij}=N_{bi}. \tag{12}$$

As shown in the previous section, the probability that all the results contained in $\mathbf{X}_{ij}$ will be observed (i.e., the intersection of these results) is maximized by finding the value of $\hat{\mathcal{F}}_{ij}$ that maximizes $L_{ij}(\mathcal{F}_{ij})$ as defined in Eq. (6). If N_{bi} bundles are emitted for every surface, the intersection of the results contained in all $N\times N$ solution sets corresponds to the probabilities contained in the matrix $\hat{\mathbf{F}}$ that maximizes

$$L(\mathbf{F})=\prod_{i=1}^{N}\prod_{j=1}^{N}\mathcal{F}_{ij}^{N_{bij}}. \tag{13}$$

Again, since the natural logarithm is a monotonically increasing function, $\hat{\mathbf{F}}$ also maximizes.

$$F_{\mathrm{CML}}(\mathbf{F})=\sum_{i=1}^{N}\sum_{j=1}^{N}N_{bij}\ln(\mathcal{F}_{ij}). \tag{14}$$

The set of probabilities that maximizes the likelihood of the results contained in the $N\times N$ solution sets while simultaneously satisfying the summation and reciprocity rules is found by solving the constrained nonlinear programming (NLP) problem

$$\text{Maximize } F_{\mathrm{CML}}(\mathbf{F}) \tag{15}$$

subject to the summation rule,

$$\mathbf{Fe}=\mathbf{e}, \tag{16}$$

where $\mathbf{e}$ is the N vector of ones, and the reciprocity rule,

$$\mathbf{EF}=\mathbf{F}^T\mathbf{E}, \tag{17}$$

where $\mathbf{E}$ is a diagonal matrix with $E_{ii}=\varepsilon_i A_i$. It is also necessary to impose a lower bound on the probabilities

$$\mathcal{F}_{ij}\geqslant 0, \quad i,j=1,2,\ldots,N. \tag{18}$$

The upper bound on the probabilities, $\mathcal{F}_{ij}\leqslant 1$, is redundant due to Eqs. (16) and (18).

Most enclosure geometries also involve pairs of exchange factors that should be equal due to enclosure symmetry. This condition can be enforced by specifying a set of additional equality constraints, or alternatively by inserting perfectly specularly reflecting surfaces along lines of symmetry and then solving for the exchange factors over the reduced computational domain. The latter approach should be used whenever possible, as this both improves the accuracy of a solution obtained by performing a given number of Monte Carlo trials and reduces the size and complexity of the NLP maximization problem.

The NLP problem described above is further simplified by automatically enforcing the reciprocity constraints, which is done by keeping only the exchange factors contained in the diagonal and upper triangle of $\mathbf{F}$ as variables, and substituting $\mathcal{F}_{ij}=(A_j\varepsilon_j)\mathcal{F}_{ji}/(A_i\varepsilon_i)$ for the remaining exchange factors in the lower triangular portion of $\mathbf{F}$. This transforms the original $(N\times N)$ dimensional NLP maximization problem into a $(N^2+N)/2$-dimensional problem, where the objective is to maximize

$$F_{\mathrm{CML}}(\mathbf{F})=\sum_{i=1}^{N}N_{bii}\ln(\mathcal{F}_{ii})+\sum_{i=1}^{N}\sum_{j=i+1}^{N}(N_{bij}+N_{bji})\ln(\mathcal{F}_{ij}), \tag{19}$$

subject to

$$\sum_{j=1}^{i-1}\frac{A_j\varepsilon_j}{A_i\varepsilon_i}\mathcal{F}_{ji}+\sum_{j=i}^{N}\mathcal{F}_{ij}=1, \quad i=1,2,\ldots,N, \tag{20}$$

and

$$0\leqslant\mathcal{F}_{ij}, \quad i=1,2,\ldots,N, \quad j=i, \quad i+1,\ldots,N. \tag{21}$$

Implementation and Demonstration

The constrained maximum likelihood approach described above is demonstrated by using it to smooth exchange factor sets from two enclosure problems. In both cases, the unsmoothed exchange factors were first calculated by ray tracing, and then smoothed by solving the NLP problem defined by Eqs. (19)–(21). Optimization was carried out using GAMS/CONOPT [10,11], an algorithm specifically developed for solving nonlinear programming problems involving large systems of constraints. In order to validate the smoothing procedure, the accuracies of the exchange factor sets obtained using different numbers of bundles were measured by

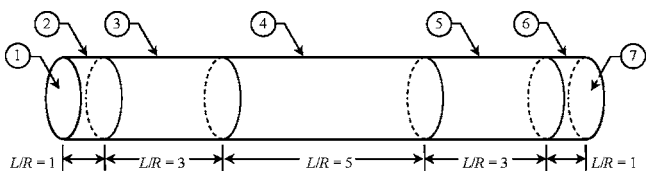

Fig. 1 Enclosure geometry for the first test problem [7]. (Surface numbers are circled.)

Table 1 Comparison of constrained maximum likelihood (CML) and least squares (LS) optimization problems

	CML	LS
Number of variables	$(N^2+N)/2$	N^2
Number of linear equality constraints	N	$(N^2-N)/2$
Number of linear inequality constraints	$(N^2+N)/2$	N

$$\varepsilon_{\text{rms}} = \left[\frac{1}{N} \sum_{i=1}^{N} \sum_{j=1}^{N} (\hat{\mathcal{F}}_{ij} - \mathcal{F}_{ij}^{\text{exact}})^2 \right]^{1/2}, \tag{22}$$

where $\mathcal{F}_{ij}^{\text{exact}}$ is either the analytical solution if it is available, or an estimate of the analytical solution obtained using a large number of bundles relative to the number used to calculate $\hat{\mathcal{F}}_{ij}$.

The constrained maximum likelihood algorithm was also assessed by comparing its performance to that of a least-squares (LS) smoothing algorithm, which works by minimizing

$$F_{\text{LS}}(\mathbf{F}) = \sum_{i=1}^{N} \sum_{j=1}^{N} \frac{(\mathcal{F}_{ij} - \hat{\mathcal{F}}_{ij}^{0})^2}{2w_{ij}}, \tag{23}$$

subject to reciprocity, summation, and nonnegativity constraints. The $\hat{\mathcal{F}}_{ij}^{0}$ values belong to a set of unsmoothed exchange factors estimated using the specified number of bundles, and w_{ij} was set equal to $\hat{\mathcal{F}}_{ij}^{0}$ as recommended in [7] so as to favor modification of the smaller, less accurate exchange factors. This minimization problem was again solved using GAMS/CONOPT [10,11] in contrast with prior implementations of the least-squares smoothing methods [5–7], which carried out the minimization using more complex analytical techniques that could not guarantee a non-negative exchange factor set. It should also be noted that the optimization problem associated with least-squares smoothing is roughly twice as large as that corresponding to the constrained maximum likelihood technique, since the former method must smooth the full set of exchange factors while the latter makes use of reciprocity relations to reduce the number of problem variables. The relative size of the optimization problems associated with the two smoothing techniques is summarized in Table 1.

The first problem, shown in Fig. 1, is the one Loehrke et al. [7] used to evaluate their least-squares smoothing technique. It consists of a right-circular cylinder with a length/radius ratio of 13:1 divided into seven surfaces, each surface having an emissivity of one. This results in a set of 49 exchange factors to be solved. [Although very simple, this example problem was selected because the $\mathcal{F}_{ij}^{\text{exact}}$ values in Eq. (22) equal the view factors between the surfaces, which in turn are solved analytically.] The constrained maximum likelihood and least-squares techniques were applied to exchange factor sets generated by emitting between $N_b = 10^2$ and $N_b = 10^6$ bundles per surface element. Twenty different trials were performed using each different number of bundles, and the average accuracies of the exchange factor sets generated using the two smoothing techniques are plotted in Fig. 2 along with the accuracies of the initial unsmoothed sets. In each case, the exchange factor sets were smoothed in under a minute of CPU time on a 1.8 GHz workstation.

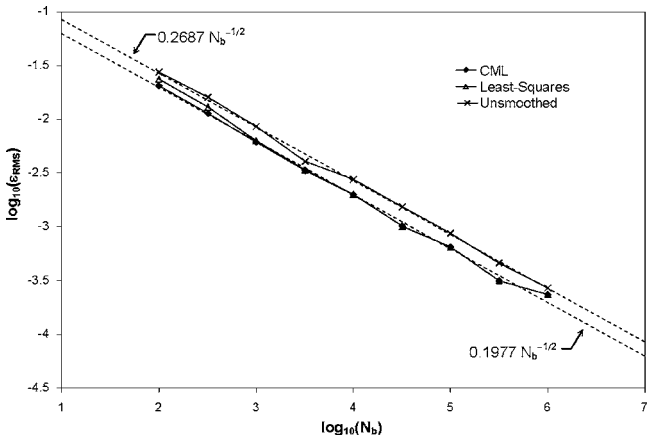

Fig. 2 RMS error in exchange factor sets for the first test problem

Table 2 Surface properties for second test problem

Surface	1	2	3	4	5	6
ε	0.3	0.3	0.3	0.3	0.9	0.6
ρ_d	0.2	0.2	0.2	0.2	0.1	0.3
ρ_s	0.5	0.5	0.5	0.5	0.0	0.1

The root-mean square error of the unsmoothed set decreases according to $\varepsilon_{\text{rms}} \alpha N_b^{-0.502}$ for $10^2 \leq N_b \leq 10^6$, which is consistent with the $1/\sqrt{N_b}$ trend predicted by the central limit theorem. The performance of the two smoothing techniques were quantified by fitting curves of the form

$$\varepsilon_{\text{rms}}(N_b) = C/\sqrt{N_b} \tag{24}$$

to the data. As shown in Fig. 2, when large numbers of bundles are used ($N_b > 1 \times 10^3$) both smoothing techniques produce exchange factor sets that are approximately 25% more accurate than the unsmoothed sets estimated using a specified number of bundles, which is consistent with the results of Loehrke et al. [7]. Equivalently, the number of bundles required to achieve a specified accuracy level is reduced by almost half when smoothing is used.

The second enclosure shown in Fig. 3(*a*) is more representative of a problem that might arise in an industrial setting, as the optical properties of the enclosure surfaces have both diffuse and specular components; these properties are summarized in Table 2. The computational domain was formed by replacing lines of symmetry with perfectly specular reflecting surfaces, as shown in Fig. 3(*b*). Surfaces 3′, 4′, 5′, and 6′ were then discretized into 28 uniformly spaced surface elements, resulting in a set of 784 exchange factors. The CML and least-squares smoothing techniques are again assessed by following the procedure defined above; in this case, however, the $\mathcal{F}_{ij}^{\text{exact}}$ values in Eq. (22) are analytically intractable and instead were estimated by emitting 10^8 bundles per surface. The standard error of these values is less than 5×10^{-4}, as estimated using the replication procedure described in [12]. As shown in Fig. 4, both the CML and least-squares smoothing techniques produce exchange factor sets that are approximately 25% more accurate than the corresponding unsmoothed set.

It should again be noted, however, that the NLP problem solved when performing CML smoothing is roughly half the size of the

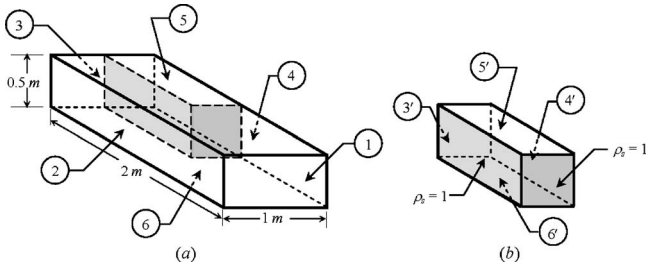

Fig. 3 (*a*) Enclosure geometry, and (*b*) computational domain for the second test problem. (Perfectly specular reflecting surfaces are shaded.)

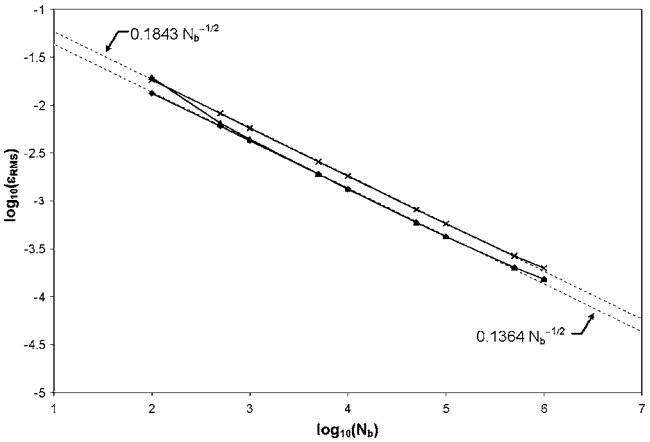

Fig. 4 RMS error in exchange factor sets for the second test problem

one solved during least-squares smoothing. Furthermore, the CML method is more accurate than the least-squares method when relatively few bundles are used ($N_b < 1 \times 10^3$), which shows that CML smoothing would be a powerful tool for solving enclosure problems involving many surface elements, and where computational resources are limited.

Conclusions

This paper presented a constrained maximum likelihood estimation technique for smoothing exchange factor sets containing stochastic errors, with the objective of generating a more accurate set that also satisfies summation and reciprocity conditions. The method works by finding the exchange factor set that maximizes the probability that the results of a large number of statistical experiments (bundle emissions and absorptions) would be observed, subject to the summation, reciprocity, and nonnegativity constraints. Maximization is carried out using GAMS/CONOPT, a much simpler and faster way to solve the optimization problems associated with exchange factor smoothing compared to the analytical techniques employed in previous approaches.

The constrained maximum likelihood method was demonstrated by using it to smooth the exchange factor set corresponding to two three-dimensional radiant enclosure problems. Exchange factor sets smoothed using the CML method were shown to be approximately 25% more accurate than the corresponding unsmoothed sets. The CML-smoothed sets were also more accurate than those smoothed using the least-squares technique in cases where relatively few bundles were used to estimate the exchange factors.

Although the algorithm presented here can only be applied to radiant enclosures containing diffuse-specular surfaces and a nonparticipating medium, it will soon be extended to treat more complicated problems.

Nomenclature

A_i = Area of ith surface element, m^2
C = Coefficient in Eq. (24)
E_{bi} = Blackbody emissive power of ith surface element, W/m^2
$\mathbf{E}$ = Diagonal matrix with $E_{ii} = \varepsilon_i A_i$
$\mathbf{F}$ = Exchange factor matrix
$F_{CML}(\mathbf{F})$ = Constrained maximum likelihood objective function
$F_{LS}(\mathbf{F})$ = Least-squares minimization objective function
$\mathcal{F}_{ij}$ = Exchange factor between ith and jth exchange factors and element of $\mathbf{F}$
$f_{ij}(\mathcal{F}_{ij})$ = Probability density function of $\mathcal{F}_{ij}$
$L_{ij}(\mathcal{F}_{ij})$ = Likelihood function of $\mathcal{F}_{ij}$
N = Number of surface elements
N_b = Total number of bundles used to estimate a set of exchange factors
N_{bi} = Number of bundles emitted by the ith surface element
N_{bij} = Number of bundles emitted by the ith surface element that are absorbed by the jth surface element
q_i = Net radiative heat flux leaving ith surface element, W/m^2
w_{ij} = Weight used in least-squares method, Eq. (23)
$\mathbf{X}_{ij}$ = Boolean solution space for Bernoulli experiments used to estimate $\mathcal{F}_{ij}$
x_{ij}^k = Result of kth Bernoulli experiment used to estimate $\mathcal{F}_{ij}$
ε_i = Emissivity of ith surface element
ε_{RMS} = Error between reduced set of exchange factors and exact solution, Eq. (22)
ρ_{di} = Diffuse reflectivity of ith surface element
ρ_{si} = Specular reflectivity of ith surface element

Subscripts and Superscripts

i, j = Surface element indices
k = Bundle emission index
$\wedge$ = Estimated quantity

References

[1] Ertürk, H, Ezekoye, O. A., and Howell, J. R., 2001, "Inverse Transient Boundary Estimation Problem in a Radiating Enclosure," *Proc. of the 31st ASME National Heat Transfer Conference*, Anaheim, CA, June, pp. 10-12.
[2] van Leersum, J., 1989, "A Method for Determining a Consistent Set of Radiation View Factors from a Set Generated by a Nonexact Method," Int. J. Heat Fluid Flow, **10**, pp. 83–85.
[3] Lawson, D. A., 1995, "An Improved Method for Smoothing Approximate Exchange Areas," Int. J. Heat Mass Transfer, **38**, pp. 3109–3110.
[4] Taylor, R. P., Luck, R., Hodge, B. K., and Steel, W. G., 1995, "Uncertainty Analysis of Diffuse-Grey Radiation Enclosure Problems," J. Thermophys. Heat Transfer, **9**, pp. 63–69.
[5] Vercammen, H. A. J., and Froment, G. F., 1980, "An Improved Zone Method Using Monte Carlo Techniques for the Simulation of Radiation in Industrial Furnaces," Int. J. Heat Mass Transfer, **23**, pp. 329–337.
[6] Larsen, M. E., and Howell, J. R., 1986, "Least-Squares Smoothing of Direct Exchange Areas in Zonal Analysis," ASME J. Heat Transfer, **108**, pp. 239–242.
[7] Loehrke, R. I., Dolagham, J. S., and Burns, P. J., 1995, "Smoothing Monte Carlo Exchange Factors," ASME J. Heat Transfer, **117**, pp. 524–526.
[8] Jamshidian, M., 2004, "On Algorithms for Restricted Maximum Likelihood Estimation," Comput. Stat. Data Anal., **45**, pp. 137–157.
[9] Schoenberg, R. 1997, "Constrained Maximum Likelihood," Comput. Econ., **10**, pp. 251–266.
[10] Brooke, A., Kendrick, D., Meeraus, A., Raman, R., 1998, "GAMS: A User's Guide," GAMS Development Corporation, WA, DC, http://www.gams.com
[11] Drud, A., 1985, "CONOPT: A GRG Code for Large Sparse Dynamic Nonlinear Optimization Problems," Math. Program., **31**, pp. 153–191.
[12] Daun, K. J., Morton, D. P., and Howell, J. R., 2003, "Geometric Optimization of Radiant Enclosures Containing Specular Surfaces", ASME J. Heat Transfer, **125**, pp. 845–851.

Yunfei Chen[1]
Department of Mechanical Engineering and China Education Council Key Laboratory of MEMS, Southeast University, Nanjing, 210096, People's Republic of China

Deyu Li
Department of Mechanical Engineering, Vanderbilt University, Nashville, TN, 37235-1592

Jennifer R. Lukes
Department of Mechanical Engineering and Applied Mechanics, University of Pennsylvania, Philadelphia, PA 19104-6315

Arun Majumdar
Department of Mechanical Engineering, University of CA, Berkeley, California, 94720
Materials Science Division, Lawrence Berkeley National Lab, Berkeley, CA, 94720

Monte Carlo Simulation of Silicon Nanowire Thermal Conductivity

Monte Carlo simulation is applied to investigate phonon transport in single crystalline Si nanowires. Phonon-phonon normal (N) and Umklapp (U) scattering processes are modeled with a genetic algorithm to satisfy energy and momentum conservation. The scattering rates of N and U scattering processes are found from first-order perturbation theory. The thermal conductivity of Si nanowires is simulated and good agreement is achieved with recent experimental data. In order to study the confinement effects on phonon transport in nanowires, two different phonon dispersions, one from experimental measurements on bulk Si and the other solved from elastic wave theory, are adopted in the simulation. The discrepancy between simulations using different phonon dispersions increases as the nanowire diameter decreases, which suggests that the confinement effect is significant when the nanowire diameter approaches tens of nanometers. It is found that the U scattering probability in Si nanowires is higher than that in bulk Si due to the decrease of the frequency gap between different modes and the reduced phonon group velocity. Simulation results suggest that the dispersion relation for nanowires obtained from elasticity theory should be used to evaluate nanowire thermal conductivity as the nanowire diameter is reduced to the sub-100 nm scale. [DOI: 10.1115/1.2035114]

Keywords: Nanowire, Monte Carlo Simulation, Thermal Conductivity, Dispersion Relations, Phonon Scattering, Genetic Algorithm

1 Introduction

An accurate numerical prediction of the thermal transport in nanoscale crystalline structures is very important for both fundamental physics and engineering applications. A comprehensive analysis of thermal conductivities of nanostructures can lead to a deeper understanding of phonon scattering mechanisms, which is of fundamental theoretical significance. In addition, aggressive miniaturization of microelectronic devices leads to substantially increased power dissipation. Thermal management is problematic in such devices because at sub-100 nm length scales, thermal conductivity deviates significantly from bulk values and accurate values are often not known. In theoretical analysis of phonon transport, the Boltzmann transport equation (BTE) is often the starting point. Based on the lifetime assumption and with some simplifications, it is possible to achieve a closed form analytical solution of the BTE [1–6]. However, since many assumptions must be introduced to reach a closed form solution, the results may deviate significantly from experimental observations.

In 1966, two numerical techniques were proposed to solve the BTE for electron transport: the Monte Carlo (MC) method [7] and an iterative technique [8]. Since then, MC simulations have found wide application in investigations of electron distribution, average energy, drift velocity, diffusion coefficients, and band structure for carrier transport in semiconductors [9]. In MC simulation, self-consistent calculation must be guaranteed, in which an assumed distribution function $f(k)$ is used to evaluate scattering probabilities and the same $f(k)$ must be obtained as the solution. Since electron-electron interactions do not significantly affect electron transport in semiconductors, they are often neglected in the traditional MC simulation. Several efforts [10–12] to account for electron-electron interactions showed only partial success and these interactions remain a difficult problem to treat. The MC method cannot be directly implemented to solve the BTE for phonon transport since phonon-phonon interactions must be included in the simulation of phonon transport. Phonon-phonon scattering processes and phonon relaxation times or lifetimes are essential for phonon transport modeling. Only at extremely low temperature, where ballistic transport dominates, is the phonon-phonon interaction unimportant. In 1988, Klitsner et al. [13] applied the MC method to study ballistic phonon transport and found good agreement with a theoretical analysis. Later Peterson [14] simulated phonon transport using a MC method based on the Debye model, in which all phonons were assumed to have the same propagating speed, and interactions between phonons were accounted for by assuming an average lifetime. With these assumptions, heat transfer in a one-dimensional cell array was simulated and the time evolution of the temperature profile was predicted. In 2002, Mazumder and Majumdar [15] reported MC simulation for phonon transport in thin Si films. In their work, phonon polarization and phonon dispersion were taken into account by considering the dependence of phonon lifetime on frequency, polarization, and temperature. Their simulation results agreed well with the experimental data for temperatures lower than room temperature. However, for higher temperature, the three-phonon scattering probability increases and the phonon transition rates between different polarization and different frequency phonons increase. Simple models assuming that the phonon transition process is based on an averaged phonon lifetime lead to unconverged results for phonon transport. Hence for MC simulation at high temperature, self-consistent calculations must be performed to ensure convergence of the simulations.

In the present work, we first modify the MC technique to study phonon transport in bulk Si at temperatures both below and above room temperature (up to 500 K), and then apply the method to model phonon transport in Si nanowires. All important phonon scattering processes in semiconductors, such as three-phonon scattering, boundary scattering, and impurity scattering are taken into account. A genetic algorithm is adopted to guarantee both energy and momentum conservation for normal (N) scattering and energy conservation for Umklapp (U) scattering. The simulation results for the thermal conductivity of bulk Si fit the experimental results very well in the temperature range from 40 K to 500 K. Below 40 K, since no boundary scattering is included in the simulation for

[1]Electronic mail: yunfeichen@yahoo.com

Contributed by the Heat Transfer Division of ASME for publication in the JOURNAL OF HEAT TRANSFER. Manuscript received: September 28, 2004; final manuscript received: May 18, 2005. Review conducted by: Gang Chen.

bulk Si, the simulation results deviate from the experimental value. For the thermal conductivity of Si nanowires, the simulation results agree reasonably well with recent experimental results [16,17].

2 Transport Model and Monte Carlo Method

The Boltzmann equation for phonon transport in the presence of a temperature gradient is written as

$$\vec{V}_g \bullet \nabla T \frac{dn}{dT} = \left(\frac{\partial n}{\partial t}\right)_c \tag{1}$$

where $\vec{V}_g$ is the group velocity

$$\vec{V}_g = \nabla_{\vec{q}} \omega \tag{2}$$

n is the distribution function, q is the phonon wave vector, T is the local temperature, ω is the phonon frequency, and $(\partial n/\partial t)_c$ is the rate of change of n due to collisions. On the left side of Eq. (1), n can be replaced by n_0, the equilibrium Planck distribution. Consequently Eq. (1) can be read as

$$\vec{V}_g \bullet \nabla T \frac{dn_0}{dT} = \sum_{K'} [\Phi(q,q')n(q') - \Phi(q',q)n(q)] \tag{3}$$

where

$$n_0 = \frac{1}{\exp(\hbar\omega/k_B T) - 1} \tag{4}$$

Here $\hbar$ is the Planck's constant divided by 2π, k_B is the Boltzmann's constant, and $\Phi(q,q')$ is the function describing the scattering rate from state q' to state q, which depends on the phonon frequency and polarization.

Equation (3) is a nonlinear integrodifferential equation. The transition rate $\Phi(q,q')$ on the right side of Eq. (3) is very complicated, and without simplification the formulation is difficult to solve. This difficulty can be avoided by using MC. To calculate thermal transport, MC does not try to solve Eq. (3) directly, but instead, follows a large number of phonons in a three-dimensional space subjected to a temperature gradient. The simulation domain is divided into many cells and initial local temperature is imposed on each cell according to the temperature gradient. The initial velocity, polarization, and frequency of each phonon are based on the local temperature. More details on the initial conditions can be found in Ref. [15]. The number of phonons in each cell depends on the local temperature and the cell volume. For silicon, the frequency range between zero and the maximum cut-off frequency of the longitudinal acoustic branch is divided into 1000 spectral intervals. The number of phonons per unit volume in the ith spectral interval is calculated from the equilibrium Planck distribution

$$N_i = \langle n(\omega_{0,i},\mathrm{LA})\rangle D(\omega_{0,i},\mathrm{LA})\Delta\omega_i + 2\langle n(\omega_{0,i},\mathrm{TA})\rangle D(\omega_{0,i},\mathrm{TA})\Delta\omega_i \tag{5}$$

where n $(\omega_{0,i}$, LA) and n $(\omega_{0,i}$, TA) are the Bose-Einstein distribution for the longitudinal and transverse acoustic branches, respectively. $D(\omega_{0,i})$ is the density of states, and $\Delta\omega = \omega_{\max,\mathrm{LA}}/N_b$, in which N_b is the number of intervals from zero to the maximum cutoff frequency of the longitudinal acoustic branch. In Eq. (5), three acoustic branches in the phonon dispersion relation are taken into account, i.e., one longitudinal acoustic branch and two transverse acoustic branches. Optical phonons are not considered because they contribute little to thermal conductivity due to their small group velocity. In this paper N_b is selected to be 1000. The total number of phonons can be obtained by summing up the phonons in the 1000 spectral intervals

$$N = \sum_{i=1}^{N_b} N_i \tag{6}$$

The actual number of phonons per unit volume calculated from Eq. (6) is usually a very large number. With the current computational power, it is impossible to simulate the movements of such a large number of phonons in each cell. In order to save computation time, a prescribed number of phonons are used to represent the actual phonons in each cell by introducing a scaling factor

$$W = \frac{N_{\mathrm{actual}}}{N_{\mathrm{prescribed}}} \tag{7}$$

Equation (7) indicates that one phonon in the simulation code stands for W actual phonons.

Once the phonons are produced, the simulation starts with all of the phonons in given initial conditions with appropriate sampled frequencies, group velocities, wave vectors, and polarizations. A duration of free flight is set and all of the phonons move linearly from initial positions to new positions such that

$$\vec{r}_i = \vec{r}_{0,i} + \vec{V}_{g,i}\Delta t \tag{8}$$

where $\vec{r}$, $\vec{r}_{0,i}$ are the new and initial positions of the ith phonon, respectively, and Δt is the free flight time. The free flight time is kept constant during the simulation and its value is set as small as possible in order to not miss any scattering events. However, smaller Δt increases computation expense. To avoid undue computational burden, the time step in our simulation was set as one half of the smallest phonon scattering time. It was found that this time step gave stable simulation results. If the phonon encounters a boundary during free flight, it is reflected as described in Sec. 3.1. If it does not, the phonon lifetime is calculated according to Matthiessen's rule

$$\frac{1}{\tau_T} = \frac{1}{\tau_i} + \frac{1}{\tau_U} + \frac{1}{\tau_N} \tag{9}$$

where the total phonon lifetime τ_T depends on the lifetime for impurity scattering τ_i, the lifetime for U processes τ_U, and the lifetime for N processes τ_N. Each phonon has its own unique lifetime based on its frequency, polarization, impurity scattering time scale, and local temperature [3]. The calculation of these lifetimes is discussed in more detail in the following sections and in Table 1. $P(t)$, the probability that a phonon has already existed for a free flight time Δt without being scattered, decreases with time such that

$$\frac{\partial P}{\partial t} = -\frac{P}{\tau_T} \tag{10}$$

The probability that the phonon is scattered after the free flight time is

$$\overline{P} = 1 - P = 1 - \exp(-\Delta t/\tau_T) \tag{11}$$

To impose a statistical scattering mechanism on the phonon, a random number R_1, is generated. If $R_1 < \overline{P}$, the phonon will be scattered and replaced by a new phonon at a different state. Then the new phonon begins its new free flight. If $R > \overline{P}$, the phonon will continue its free flight with its state unchanged. If the simulation time is long enough, the system equilibrates, and the final results can be extracted through averaging over a fixed time step [15].

When $R_1 < \overline{P}$, a scattered phonon is found, then, the following procedure is used to determine which scattering process the phonon engages in. As described in Eq. (9), three scattering processes constitute the transition rate. However, the phonon can only engage in one of them. In order to distinguish which process the phonon engages in, the phonon lifetime is divided into two parts

$$\frac{1}{\tau_T} = \frac{1}{\tau_1} + \frac{1}{\tau_2} \tag{12}$$

where

Table 1 Parameters used in Monte Carlo simulation

Scattering process	Inverse relaxation time	parameter	
Boundary scattering		d	0.5
Impurity scattering	$\tau_i^{-1} = B_i\omega^4 \quad (s^{-1})$	B_i	$5.32\times10^{-44}\ (s^3)$
Three phonon			
N process			
Transverse	$\tau_N^{-1} = B_{TN}\omega T^4 \quad (s^{-1})$	B_T	$9.3\times10^{-13}\ (\mathrm{deg}^{-4})$
Longitudinal	$\tau_N^{-1} = B_L\omega^2 T^3 \quad (s^{-1})$	B_L	$1.0\times10^{-30}\ (\mathrm{deg}^{-3}\,s)$
U process			
Transverse	$\tau_{TU}^{-1} = \begin{cases} 0 & (\omega < \omega_{12}) \\ B_{TU}\omega^2/\sinh(\frac{\hbar\omega}{k_B T}) & (\omega \geq \omega_{12}) \end{cases} \quad (s^{-1})$	B_{TU}	$5.50\times10^{-18}\ (s)$
Longitudinal	$\tau_{LU}^{-1} = B_L\omega^2 T^3 \quad (s^{-1})$	B_L	$1.0\times10^{-30}\ (\mathrm{deg}^{-3}\,s)$

$$\frac{1}{\tau_1} = \frac{1}{\tau_i} \tag{13}$$

and

$$\frac{1}{\tau_2} = \frac{1}{\tau_N} + \frac{1}{\tau_U} \tag{14}$$

The probability that the phonon engages in impurity scattering process can be expressed as

$$P_i = \frac{1/\tau_1}{1/\tau_T} \tag{15}$$

A random number R_2 is generated. If $R_2 < P_i$, the phonon will be scattered by impurities. Otherwise, it engages in three phonon scattering process. The same approach is used to determine if the phonon engages in N or U scattering processes.

3 Scattering Mechanisms and their Realization in MC Simulations

3.1 Boundary Scattering. During phonon transport, the primary phonon scattering processes are phonon-boundary collisions, impurity scattering, and three-phonon inelastic interactions. Boundary collisions play an important role in thermal resistance as the structure size decreases to nanoscale. When a phonon strikes the structure wall, a random number is first drawn. If this random number is less than a prescribed specularity parameter d, the phonon is specularly reflected using the following equation as in Ref. [15]:

$$\vec{s}_r = \vec{s}_i + |\vec{s}_i \cdot \vec{n}|\vec{n} \tag{16}$$

where $\vec{s}_i$, $\vec{s}_r$ are the direction vectors of the incident and reflected phonons and $\vec{n}$ is the unit surface normal. In this case the phonon incident angle is equal to the reflected angle. If the random number is larger than d, the phonon is reflected diffusely at the surface. Its direction is selected according to the following relation:

$$\vec{s}_r = \sin\theta\cos\varphi\vec{t}_1 + \sin\theta\sin\varphi\vec{t}_2 + \cos\theta\vec{n} \tag{17}$$

where $\varphi = 2\pi R_3$, $\cos\theta = 2R_4 - 1$, R_3, R_4 are random numbers, $\vec{t}_1$, $\vec{t}_2$ are unit surface tangents, which must be perpendicular to each other such that

$$\vec{t}_1 \times \vec{t}_2 = \vec{n} \tag{18}$$

If d is set to 1, the boundary is perfectly smooth and all phonons will be specularly reflected. In this case, the boundary scattering process does not contribute to thermal resistance.

3.2 Impurity Scattering. Impurity scattering can be the dominant phonon scattering mechanism at low temperatures. The time scale for scattering by impurities is expressed using a simple model by Vincenti and Kruger [18]

$$\tau_i^{-1} = \alpha\sigma\rho|\vec{V}_g| \tag{19}$$

where α is a constant of the order of unity, ρ is the defect density per unit volume, and σ is the scattering cross section expressed as [19]

$$\sigma = \pi r^2\left(\frac{\chi^4}{\chi^4 + 1}\right) \tag{20}$$

Here r is the atomic radius of the impurity and $\chi = r|\vec{q}|$, and $\vec{q}$ stands for the phonon wave vector. If only the isotope scattering is taken into account, Eq. (19) can be simplified as

$$\tau_i^{-1} = B_i\omega^4 \tag{21}$$

If a phonon is scattered by an impurity or a defect, its wave vector will be perturbed and its flight direction will be changed. In order to simulate the impurity scattering process, a new wave vector and a new velocity direction will be generated based on the phonon's frequency. The phonon frequency and polarization keep their original values.

3.3 Three-Phonon Scattering. Three-phonon interactions include both normal and Umklapp scattering processes. Peierls [20]

showed that N processes contribute to thermal resistance by transferring momentum from one group of modes, where resistance (R) processes (Umklapp or impurity processes) are weak, to other modes where R processes are strong. This effect is particularly important for point defect scattering, since the scattering probability is strongly frequency dependent. Callaway [2] assumed that N processes relax toward a quasiequilibrium distribution, i.e., one shifted in momentum space, while R processes tend to restore true equilibrium. The shift of the quasiequilibrium distribution is chosen so that N processes conserve momentum in the aggregate. The displaced Planck distribution can be written as [2]

$$n(\vec{\lambda}) = \left[\exp\left(\frac{\hbar\omega - \vec{\lambda}\cdot\vec{q}}{k_B T} \right) \right]^{-1} = n_0 + \frac{\vec{\lambda}\cdot\vec{q}}{k_B T} \frac{e^{\hbar\omega/k_B T}}{(e^{\hbar\omega/k_B T} - 1)^2} \quad (22)$$

where $\vec{\lambda}$ is a constant vector in the direction of the temperature gradient. From Eq. (22) the departure of the phonon occupation number from that at thermal equilibrium for a small vector interval can be written as

$$\Delta N = \iiint_{\Delta q} [n(\vec{\lambda}) - n_0] d^3 q = \sum_{q_x}^{q_x+\Delta q_x} \sum_{q_y}^{q_y+\Delta q_y} \sum_{q_z}^{q_z+\Delta q_z} [n(\vec{\lambda}) - n_0] \Delta q_x \Delta q_y \Delta q_z \quad (23)$$

The three-phonon interactions obey the energy conservation and momentum conservation laws

$$\vec{q}_1 + \vec{q}_2 \leftrightarrow \vec{q}_3 \quad (24)$$

$$\vec{q}_1 + \vec{q}_2 \leftrightarrow \vec{q}_3 + \vec{G} \quad (25)$$

$$\omega_1 + \omega_2 = \omega_3 \quad (26)$$

where $\vec{G}$ is the reciprocal lattice vector.

4 Genetic Algorithm for Three-Phonon Scattering

In three-phonon scattering processes, if an initial phonon produces two phonons, both of the two new phonons will be followed. If an initial phonon is absorbed along with another to create a third phonon in the scattering process, the state of one of the initial phonons will be set as the created phonon and the other one will be destroyed by setting its energy as zero. Then all the scattered phonons will be treated by a genetic algorithm to satisfy momentum and energy conservation.

In order to satisfy Eqs. (24)–(26) simultaneously, a genetic algorithm [21] is introduced to determine the "fitness" of an ensemble of phonons. Fitness is an indication of how well the ensemble satisfies momentum and energy conservations and is reflected by two parameters D_1 and D_2, which are residuals of the wave vector and frequency, respectively

$$D_1 = \frac{(\sum_{i=1}^{N_p} q'_{x,i} - \sum_{i=1}^{N_c} q_{x,i})^2}{(\sum_{i=1}^{N_c} q_{x,i})^2} + \frac{(\sum_{i=1}^{N_p} q'_{y,i} - \sum_{i=1}^{N_c} q_{y,i})^2}{(\sum_{i=1}^{N_c} q_{y,i})^2} + \frac{(\sum_{i=1}^{N_p} q'_{z,i} - \sum_{i=1}^{N_c} q_{z,i})^2}{(\sum_{i=1}^{N_c} q_{z,i})^2} \quad (27)$$

$$D_2 = \left(\sum_{i=1}^{N_p} \omega'_i - \sum_{i=1}^{N_c} \omega_i \right)^2 \Big/ \left(\sum_{i=1}^{N_c} \omega_i \right)^2 \quad (28)$$

Here N_c is the number of phonons involved in a scattering event, $q'_{x,i}$, $q'_{y,i}$, $q'_{z,i}$, ω'_i are the new phonon wave vectors along the x, y, z directions and frequencies, $q_{x,i}$, $q_{y,i}$, $q_{z,i}$, ω_i are the corresponding phonon parameters before scattering. N_p is the number of phonons to be created. In the simulation, the initial value of N_p is set to equal N_c to simplify the optimization process. However, because of the three-phonon scattering process, the total number of phonons may change and it is possible that N_p does not equal N_c. The genetic algorithm operates as follows:

1. Initialization: Create a father generation $F=\{f_j | j=1,\ldots,n\}$ of phonon ensembles according to local temperature. Each ensemble f_j is defined as $f_j=\{p_i | i=1,\ldots,N_c\}$, so there are N_c phonons per ensemble. Each individual phonon p_i is coded as a 12 digit binary number, so the total number of digits in f_j is $12N_c$. The first digit of each p_i represents the phonon polarization, with 1 standing for LA and 0 for TA. The second digit is a placeholder only, and is always set to 0. The remaining ten digits represent the average phonon frequency. This frequency is the average value in each of the 1000 spectral intervals described above. For example, if a phonon frequency falls in the 600th interval and its polarization is LA, its average frequency is $\omega_{600}=600/1000 \times \omega_{\max,\mathrm{LA}}$ and it is coded as $p_i=[1010\ 0101\ 1000]$. It can be seen that the last ten digits represent the value of 600 in binary notation.
2. Reproduction: Create an offspring generation from the father generation using the crossover operation. In this operation, two ensembles from the father generation are randomly selected and some digits (out of the total $12N_c$ digits for each ensemble) are also randomly selected. One offspring ensemble s_i is produced from the first selected father ensemble by exchanging the selected digits with the second selected father ensemble. For example if f_1 and f_2 are the first and second randomly selected ensembles from the father generation as
$$\begin{cases} f_1 = [0,0,1,0,\ldots,1,\underline{1},\underline{0},\underline{1}] \\ f_2 = [1,0,1,0,\ldots,0,\underline{0},\underline{0},\underline{1}] \end{cases}$$
and the underlined digits represent the randomly selected digits, the offspring ensemble is generated as $s_i=[0,0,1,0,\ldots,1,0,0,1]$. The number of crossover operations performed, m, is also selected randomly, yielding an offspring ensemble set $S=\{s_1,s_2,\ldots,s_m\}$.
3. Initial evaluation: Evaluate all ensembles in F and S and use Eqs. (27) and (28) to calculate the residuals D_1 and D_2 for each ensemble.
4. Selection: Choose the best ensemble from the union of F and S: $f_{\mathrm{best}} \in F \cup S$ by selecting the ensemble with minimum D_1 and D_2.
5. Mutation: From the best ensemble generate a set of $l/2$ mutants: $M=\{s'_i := \mathrm{mut}(s_{\mathrm{best}}) | i=1,2,\ldots,l/2\}$. The selection of l is arbitrary; in this paper, it is set as six, which means three ensembles will be produced from the best ensemble through the mutation operation. Mutation means that selected digits become 0 if their initial values are 1, and vice versa. For example, if $s_i=[0,0,1,0,\ldots,\underline{1},\underline{1},\underline{0},0]$, after the mutation operation, $s'_i=[0,0,1,0,\ldots,0,0,1,0]$ will be produced as one ensemble of the mutant set. k digits are randomly selected in each ensemble to mutate. If k is set too large, it will take a long time for the system to converge due to the algorithm oscillation. The best value of k is set as two or three for the algorithm to be stable. In our simulation k is set to be three.
6. Create a new father generation: Calculate the residuals of all ensembles in M, S, and F, select the na ensembles with the lowest residuals, and create a new father generation F from these. The number na depends on the total number of en-

sembles. If *na* is set too large, it takes a long time for the genetic algorithm to converge. In this paper, it is set as two in each generation step.

7. Terminate check: If at least one of the ensembles has achieved a predefined fitness, stop and return the best individual. Otherwise, continue with the reproduction step (step 2).

N-type scattering processes should satisfy both momentum and energy conservation, while a *U* processes only need to satisfy energy conservation. Using a fitness criterion of 0.001, the algorithm optimization target is thus to satisfy $D_2 < 0.001$ for U scattering processes and $D_1 + D_2 < 0.001$ for *N* scattering processes. The *N* and *U* scattering processes are treated in two different groups. Phonons engaged in *N* scattering processes are considered together to satisfy the energy conservation and momentum conservation and phonons engaged in *U* scattering processes are put together to satisfy the energy conservation. The momentum conservation is not enforced in the calculation for *U* scattering process, similar to that in Refs. [13–15]. However, simulation results for bulk silicon suggest that neglecting momentum conservation for *U* process does not significantly affect the simulation result in the temperature range considered in the paper.

As discussed in Ref. [15], in principle, the three-phonon scattering process can be treated by regarding each phonon as a potential candidate for scattering and exploring the possibility of its interaction with every other phonon in its vicinity following the selection rules. That way, the momentum and energy conservations can be met rigorously. However, the computation would be immensely expensive and impossible for most cases. The genetic algorithm provides a way to meet the momentum and energy conservations for *N* processes and energy conservations for *U* processes. Compared to the more fundamental approach mentioned above, the genetic algorithm significantly reduces computational time and makes the computation expense acceptable; nevertheless, it is still quite time consuming.

5 *N* and *U* Scattering Rates of Phonons

Different expressions for three-phonon scattering rates have been adopted in the literature. Here we choose to use the expressions given by Holland [3]. Even though the phonon scattering rates given by Holland may not be the most physically sound, as discussed in Ref. [22], we choose them here because for bulk Si, extremely good fitting has been achieved with these expressions. In addition, since the most important improvement in the modeling process here from Ref. [15] is the introduction of the genetic algorithm, it is reasonable to keep the Holland scattering rates to see the effect of the genetic algorithm. The *N* and *U* scattering rates for transverse and longitudinal acoustic phonons are given as

$$\tau_L^{-1} = B_L \omega^2 T^3 \tag{29}$$

$$\tau_{\mathrm{TN}}^{-1} = B_{\mathrm{TN}} \omega T^4 \tag{30}$$

$$\tau_{TU}^{-1} = \begin{cases} 0 & (\omega < \omega_{12}) \\ B_{TU}\omega^2/\sinh\left(\frac{\hbar\omega}{k_B T}\right) & (\omega \geqslant \omega_{12}) \end{cases} \tag{31}$$

Equation (31) gives the inverse lifetime for longitudinal phonons engaged in the *N* and *U* scattering processes. For transverse phonons the *U* scattering processes do not begin until $\omega \geqslant \omega_{12}$, where ω_{12} is the transverse branch phonon frequency corresponding to $q/q_{\max} = 0.5$. $q_{\max}$ is the wave vector corresponding to the maximum cutoff frequency of longitudinal phonons in the first Brilliouin zone. For bulk Silicon, the maximum cutoff frequency in the longitudinal acoustical branch is 12.3 THz, following the experimental dispersion curve given by Brockhouse [23]. The parameters B_L, B_{TN}, B_{TU} in these equations are listed in Table 1.

When the structure dimension is reduced to the nanoscale, the *N* and *U* scattering rates of phonons will be different from that in bulk Si due to confinement effects. The *N* and *U* scattering rates in nanowires must be evaluated from first-order perturbation theory based on the phonon dispersion relation for nanowires. The phonon modes in Si nanowires include longitudinal, torsional, and flexural modes. Following the approach used in Ref. [24] to treat cylindrical acoustic waveguides with stress-free boundaries, dispersion relations for these three modes can be obtained from the following equations:

$$(q^2 - q_t^2)^2 \frac{(q_d R) J_0(q_d R)}{J_1(q_d R)} - 2q_d^2(q^2 + q_t^2) + 4q^2 q_d^2 \frac{(q_t R) J_0(q_t R)}{J_1(q_t R)} = 0 \tag{32}$$

$$q_t R J_0(q_t R) = 2 J_1(q_t R) \tag{33}$$

$$J_1(q_d R) J_1^2(q_t R) \phi(q_d, q_t, q, R) = 0 \tag{34}$$

Equation (32) applies to the longitudinal modes, Eq. (33) to the torsional modes, and Eq. (34) to the flexural modes. In all equations q is the z (axial) component of the phonon wave vector, J_0, J_1 are the ordinary Bessel functions, q_d, q_t are the transverse wave-vector components of dilational and shear waves, and R is radius of the nanowire. Relations between q_d, q_t, and q are

$$q_{q,t}^2 = \frac{\omega^2}{\nu_{d,t}^2} - q^2 \tag{35}$$

where ν_d, ν_t are the sound velocities for longitudinal and transverse acoustic waves in bulk Si, respectively. These are given by

$$\nu_d^2 = (\lambda + 2\mu)/\rho$$

$$\nu_t^2 = \mu/\rho \tag{36}$$

in which λ, μ are the Lame constants, and ρ is the density. For bulk Si, the sound velocities are $\nu_d = 8.47 \times 10^3$ m/s and $\nu_t = 5.34 \times 10^3$ m/s, respectively. In Eq. (34) the function $\phi = \phi(q_d, q_t, q, R)$ is defined as

$$\phi = f_1 \Psi_\beta^2 + f_2 \Psi_\alpha \Psi_\beta + f_3 \Psi_\beta + f_4 \psi_\alpha + f_5 \tag{37}$$

where

$$f_1 = 2(\beta^2 - \xi^2)^2$$

$$f_2 = 2\beta^2(5\xi^2 + \beta^2)$$

$$f_3 = \beta^6 - 10\beta^4 - 2\beta^4\xi^2 + 2\beta^2\xi^2 + \beta^2\xi^4 + 4\xi^4$$

$$f_4 = 2\beta^2(2\beta^2\xi^2 - \beta^2 - 9\xi^2) \tag{38}$$

$$f_5 = \beta^2(-\beta^4 + 8\beta^2 - 2\beta^2\xi^2 + 8\xi^2 - \xi^4)$$

$$\psi_\alpha = \alpha J_0(\alpha)/J_1(\alpha)$$

$$\psi_\beta = \beta J_0(\beta)/J_1(\beta)$$

and

$$\alpha = q_d * R$$

$$\beta = q_t * R \tag{39}$$

$$\xi = q * R$$

For each value of q, the allowed q_t and q_d are found for each phonon branch by selecting the applicable equation from Eqs. (32)–(34) and simultaneously solving with Eq. (35) numerically. The phonon dispersion relations for Si nanowires are then obtained from

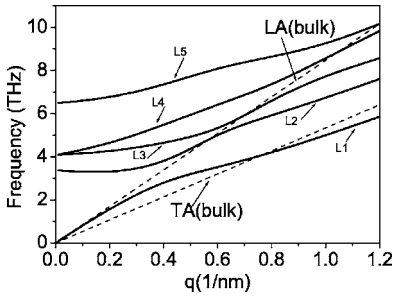

Fig. 1 Longitudinal phonon dispersion relations for 10 nm diameter Si nanowire

$$\omega_n = \nu_{d,t}\sqrt{q^2 + q_{d,tn}^2} \tag{40}$$

where the index n indicates the different allowed branches for a given phonon mode and ω_n is the phonon frequency for the nth branch of that mode.

The calculated dispersion relations for the three phonon modes (longitudinal, flexural, and torsional) are shown in Figs. 1–3, respectively, for a 10 nm diameter Si nanowire. In each mode, the first five branches are given. In Fig. 1, the phonon group velocity of the first longitudinal branch is between the phonon group velocities of longitudinal and transverse acoustic phonons for bulk Si. For small wave vector, the dispersion relation of the first branch of the longitudinal phonon is the same as that of the longitudinal acoustic phonon for bulk Si. As the wave vector increases, the phonon group velocity becomes smaller than that of bulk LA phonon. The first torsional branch is the same as the transverse acoustic phonon for bulk Si. However, the group velocities for other torsional branches and flexural branches are all below the TA mode for bulk Si, which will lead to reduced thermal conductivity. Once the dispersion relation is obtained, the phonon scattering rates can be evaluated according to N and U scattering processes as described below.

It is well known that the momentum of phonons involved in the N process is conserved. The N-scattering process redistributes the momentum and energy, and prevents strong deviation of each phonon mode from the equilibrium distribution. For N scattering process, there are two mechanisms known as the Herring [25] and Simons mechanisms [26]. The Herring mechanism suggests that the relaxation frequency of the transverse phonons is determined by the three-phonon scattering process involving one transverse and two longitudinal phonons, i.e.,

$$T + L \leftrightarrow L \tag{41}$$

Similar to formula (41), the three-phonon scattering process engaged in nanowire involving the torsional mode (or flexural mode) and two longitudinal modes

$$T + L \leftrightarrow L \tag{42}$$

Equation (42) means that one torsional phonon plus one longitudinal phonons produces one longitudinal phonon or one longitudinal phonon can decay into one transverse phonon and one longitudinal phonon. The scattering rate can be described as

$$\tau_{TN}^{-1} = B_{TN}T^4\omega_T \tag{43}$$

The relaxation frequency of the longitudinal phonons in the anisotropic continuum system is determined by the three-phonon process according to Simons mechanism [26], whereby either a longitudinal phonon decays into two torsional (flexural) phonons or two torsional phonons combine to form a longitudinal phonon

$$L \leftrightarrow T + T \tag{44}$$

The N scattering rate of the longitudinal phonons can be written as

$$\tau_{NL}^{-1} = B_L T^3 \omega_L^2 \tag{45}$$

The Umklapp process leads to thermal resistance. From the first-order perturbation theory, Klemens [1] gives the relaxation rate for the U process for a thermal or intermediate-frequency state q as

$$\tau_U^{-1} = \frac{2\gamma^2\hbar}{3\pi^2\rho v^2 v_g}\omega_i\omega_j(\omega_i + \omega_j)[n(\omega_i) - n(\omega_i + \omega_j)]\int_{q_j} dS' \tag{46}$$

where γ is the Grüneisen parameter, v is the sound velocity, $n(\omega_i), n(\omega_i + \omega_j)$ are the equilibrium occupation of states q_i, $q_i + q_j$. For Si nanowires, the dispersion relations are depicted as in Figs. 1–3. The relaxation rate of U process (46) can be approximated as

$$\tau_U^{-1} = \sum_q \frac{8\gamma^2\hbar}{3\rho v^2}\omega_i\omega_j(\omega_i + \omega_j)\pi\delta[\Delta\omega]^*[n(\omega_i) - n(\omega_i + \omega_j)] \tag{47}$$

where $\delta(\Delta\omega)$ guarantees that the energy conservation conditions be satisfied, i.e.,

$$\Delta\omega = \omega_i + \omega_j - \omega'' = 0 \tag{48}$$

Eq. (47) describes the relaxation rate of a combining U process, i.e.,

$$\vec{q}_i + \vec{q}_j = \vec{q}'' + \vec{G} \tag{49}$$

where $\vec{G}$ is the shortest reciprocal-lattice vector. q_i, q_j are the interacting states with high frequency near the zone boundary. $v_g = \|\partial\omega(q'')/\partial q''\|$ is the group velocity at $\omega'' = \omega_i + \omega_j$ in the longitudinal mode in the principal direction. The factor $\int_{q_j} dS'$ is the area of the momentum space of the interacting state q_j with the reference state q_i. In order to obtain the scattering rate for the U process at state of q_i, all of the possible interacting channels must be taken into account, then sum those scattering rates together. However, at temperatures lower than the Debye temperature, the lowest order branches are the most important branches. In order to

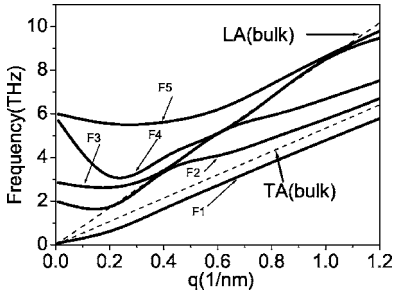

Fig. 2 Flexural phonon dispersion relations for 10 nm diameter Si nanowire

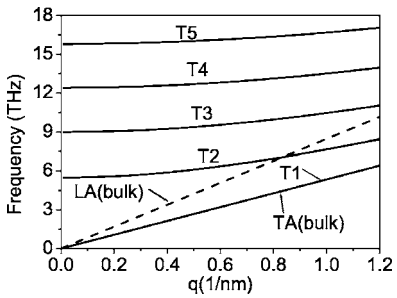

Fig. 3 Torsional phonon dispersion relations for 10 nm diameter Si nanowire

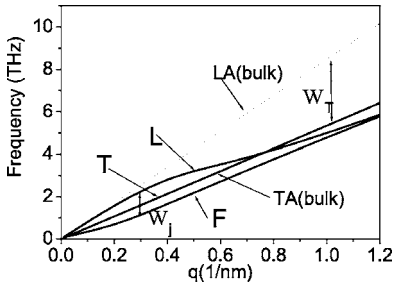

Fig. 4 Dispersion relation for the lowest longitudinal, flexural, and torsional branches of a 10 nm diameter Si nanowire

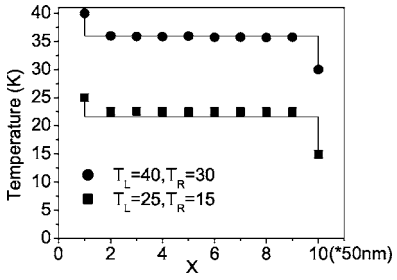

Fig. 5 "Temperature" distribution along the Si nanowire under ballistic transport condition. T_L, T_R correspond to the temperatures on the left and right ends of the nanowire.

demonstrate the calculation procedure, only the first branches for each of the three modes are taken into account as shown in Fig. 4. This approximation neglects the populated phonons at higher energy level in the quasioptical branches. However, as shown in Figs. 1–3, the lowest branches in each mode have the highest phonon group velocities. Compared with previous work [27,31], this approximation will overestimate the energy transport at low temperatures. Based on the Klemens two-step model [28], Eq. (46) can be simplified as [31]

$$\tau_U^{-1} = \frac{2\gamma^2\hbar}{3\pi\rho v^2 v_g}\omega_i\omega_j(\omega_i+\omega_j)r_c^2\exp(-\hbar\omega_j/k_BT) \tag{50}$$

where

$$\int_{q_j} dS' = \pi r_c^2, r_c = R_C[G/2 - q_i]/(G/2), R_c = \pi/(\sqrt{2}a) \tag{51}$$

Here ω_j is the frequency gap between the two different modes as shown in Fig. 4. The relaxation rate for bulk Si can be obtained in the same procedure and the ratio between the two time scales can be obtained approximately as

$$\frac{\tau_U^{-1,\text{nano}}}{\tau_U^{-1,\text{bulk}}} \propto \frac{v_g^{\text{bulk}}}{v_g^{\text{nano}}}\exp[\hbar(\omega_T-\omega_j)/k_BT] \tag{52}$$

where ω_T is the frequency gap between the longitudinal and transverse modes in bulk Si phonon dispersions as shown in Fig. 4. The superscripts bulk and nano stand for bulk material and nanowires in Eq. (52). Equation (52) demonstrates that the Umklapp scattering rate of nanowires is inversely proportional to the phonon group velocity and the frequency gap between different branches in the nanowire. With decreasing phonon group velocity and frequency gap between different modes, the Umklapp scattering rate increases greatly compared with the phonons scattering rate in bulk material.

6 Numerical Results

The phonon transport in single Si nanowires was simulated using MC. Impurity scattering was neglected in the current simulation since our primary interest in this paper is thermal conductivity at high temperatures, where impurity scattering is not as significant. Additionally, in nanowires the boundary scattering is usually strong enough to mask the impurity scattering. The cross section of the nanowires is square with side length a. It is assumed that the dispersion relations developed above for cylindrical waveguides are applicable here when $2R=a$. The main reason for this is that we have a closed form expression for the dispersion of round wires, which is easier to be included in the simulation. We believe that this is acceptable because if we do not consider the dispersion relation modification due to confinement, the boundary simply provides boundary scattering, which limits the phonon mean free path to be on the order of the wire diameter depending on the selection of the specularity parameter. The real shape of the nanowire in our simulation does not affect the simulation results. In order to verify that the MC model correctly predicts phonon transport, we first chose a simple problem: ballistic phonon transport between the two ends of the nanowire. Ballistic transport becomes important at low temperatures, where U processes are frozen out and impurity and boundary scattering are negligible. In this situation there is no thermal resistance and the "temperature" remains constant along the sample length [13]

$$T^4 = (T_L^4 + T_R^4)/2 \tag{53}$$

Here T_L, T_R stand for the temperatures at the two ends of the nanowire. The ballistic condition was realized in the MC simulations by neglecting all scattering processes. The results from both theoretical solution, Eq. (53), and the simulations of a Si nanowire with a total length of 500 nm and $a=50$ nm are shown in Fig. 5 for two different temperatures. The nanowire was divided into ten cells along its length and the local "temperature" in each cell was obtained by fitting the distribution to the Bose-Einstein distribution. Strictly speaking, temperature can only be defined in each cell when local thermodynamic equilibrium is reached, which is clearly not true for the ballistic case. For long enough simulations, however, the hot and cold phonons traveling in opposite directions are sufficiently averaged so that the numerical results in Fig. 5 (symbols) agree well with the theory (line).

Bulk Si was also simulated to further verify the model. This was done by setting the specularity parameter $d=1$, which means that the nanowire surfaces are perfectly smooth and all the phonons are specularly reflected. Since boundary scattering does not contribute to thermal resistance in this case, the nanowire MC model using the bulk Si phonon dispersion relation should yield thermal conductivity values close to that of bulk Si at high temperatures. However, at low temperature, the simulation results deviate from the experimental value due to the lack of boundary and impurity scattering.

Figure 6 illustrates that this is indeed the case: The MC numerical results circles for a nanowire with $d=1$ agree well with the experimental results for bulk Si [3] for temperatures greater than 25 K. The simulation results also agree well with recently reported experimental data on enriched isotope silicon [22,29]. For tem-

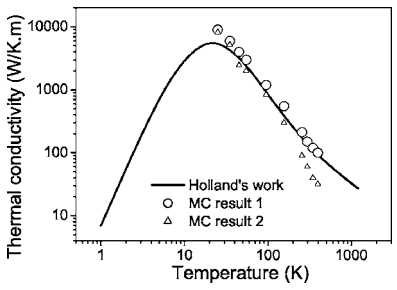

Fig. 6 Temperature dependence of bulk Si thermal conductivity from MC simulation results

peratures below 25 K, the thermal conductivity of bulk Si is dominated by phonon-boundary scattering, and the numerical results (not shown) approach infinity.

In order to demonstrate the advantage of the generic algorithm, we applied the MC code to bulk Si without the genetic algorithm. In this case, the momentum conservation of the *N* scattering processes is removed, and the MC code is the same as that in Ref. [15]. The simulation results are also shown in Fig. 6 as the triangle marks. It is clear that without the conservation of momentum for *N* processes, the simulation results give much lower values at high temperature. This is because without conservation of momentum, the *N* process directly poses resistance to thermal transport since only energy conservation is satisfied. It is well known that the *N* process only contributes to the thermal resistance indirectly by redistributing the phonons and restoring the equilibrium distribution. So without a physically sound modeling of the *N* process, the results deviate from the experimental value for bulk Si.

During the simulation process, it is observed that the length scale of the simulation domain may have an artificial effect on the final simulation results over the temperature range from 25 K to 500 K. Especially at low temperatures, since the scale of the simulation domain may be smaller than the phonon mean free path, temperature jumps appear between the ends of the simulation cell and the boundary walls. At high temperatures, the size of the simulation domain is usually larger than the phonon mean path. In this case, a nonlinear temperature profile arises due to the temperature dependence of thermal conductivity. In order to get precise simulation results, two criteria should be satisfied: The effective thermal flux in each simulation cell should be nearly the same, and the temperature profiles should be reasonably close to linear. The profiles should not be expected to be completely linear, since the thermal conductivity is temperature dependent. In order to satisfy the two criteria, computation time should be selected to be as long as possible for the system to reach steady state. In this paper, to avoid undue computational burden, values roughly 20 times of the characteristic diffusion time were found sufficient to satisfy the criteria. Time step is another factor affecting the simulation results. It should be smaller than the smallest scattering time scale to avoid missing a scattering process. Considering that different simulation cell sizes and different temperatures are used, the time step can be chosen based on the approximation that during each time step, the distance traveled by the fastest phonons is about one fourth the simulation cell. The choice of the simulation domain size at different temperatures is also a formidable task. The length of the simulation domain should be larger than the longest phonon free path to completely remove the temperature jump at the two ends. However, it is difficult to determine the mean free path for each phonon. A trial-and-error process was thus used to find the length scale of the simulation domain. For a certain simulated temperature, the length of the simulated nanowire should meet the demands that the temperature profile remains linear and no temperature jumps appear in the two ends. For the thermal conductivity simulations reported here, the values of the effective thermal flux in each cell were all within ten percent of the averaged flux and the temperature profiles were essentially linear. Finally, in order to further reduce noise effects on the final simulation results, three different simulation runs were averaged that differed only by the seed value used in the simulation's random number generator. Error analysis shows the difference between the three simulation runs are within five percent.

Figure 7 shows calculated and experimental thermal conductivities of Si nanowires of diameters 115 nm, 37 nm, and 22 nm. The three solid lines represent MC simulation results calculated using the dispersion relation for bulk Si, and the symbols represent experimental results from Ref. [16]. In the MC simulation procedure, the impurity scattering and the boundary scattering are all considered. The specularity parameter was calibrated to fit the simulation result to the experimental data [16]. Its value was set to

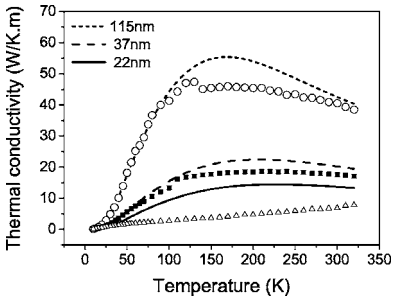

Fig. 7 Thermal conductivity of Si nanowires with different diameters: MC simulation with bulk dispersion relation (lines) and experiment (symbols)

0.5 based on several round tried simulations. The impurity scattering parameter B_i, as shown in Table 1, was obtained using a similar procedure. The parameters B_N and B_U were assumed the same as those for bulk silicon. The MC simulation results agree reasonably well with the experimental results for nanowires with diameters 37 nm and 115 nm. The position for the peak value of thermal conductivity for Si nanowires is displaced to higher temperature compared with that for bulk Si, which is 25 K. This is because for nanowires, boundary scattering is the dominant phonon scattering mechanism up to much higher temperatures.

Quite a few theoretical studies on the thermal transport in nanowires have been reported [30–37]. Several of them [30–34] are theoretical investigations working on hypothetical model system without comparison to experimental results. Those studies are trying to disclose the effects of diffuse/specular boundary reflections, ballistic/diffuse transport and scattering rate change due to phonon dispersion changes in nanowires. More recent theoretical studies [35–37] compared their modeling results with the experimental data [16]. The theoretical results from those studies match the experimental data reasonably well, similar to the present work, for nanowires with diameters larger than 37 nm. Most of the studies in the literature are based on closed form integration, which is not as computationally expensive as the present study. However, Monte Carlo simulation provides a more rigorous approach to the phonon transport and has the potential to be applied to complex geometry.

For the 22 nm diameter wire, the difference between the MC simulation and the experimental results is significant. As discussed above, the phonon dispersion relation at this length scale can differ significantly from that of the bulk and may be the reason for the difference. In order to see if this is the case, the nanowire phonon dispersion relations were used instead of bulk phonon dispersion relations in the MC model. Phonon transport in different diameter nanowires was simulated with different dispersion relations at 300 K (Fig. 8). In Fig. 8, model 1 refers to results obtained using nanowire phonon dispersion and model 2 refers to results obtained using bulk silicon phonon dispersion relations. It

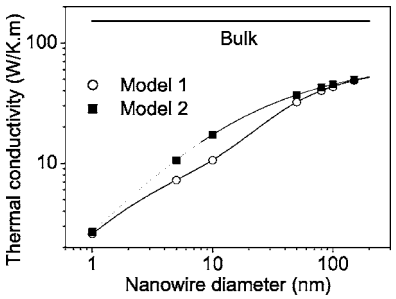

Fig. 8 Nanowire thermal conductivity versus diameter at $T = 300$ K

can be seen from the figure that for large diameter nanowires, the results from different dispersion relations are nearly the same. However, as the nanowire diameter decreases, the difference gets larger and can be observed clearly. The thermal conductivity evaluated from nanowire dispersion relations become significantly smaller than that from the dispersion relation for bulk Si. The maximum difference occurs for nanowires with a diameter between 10 nm to 20 nm. For even smaller diameter nanowires, the difference gets smaller. The reason for this is not fully understood. However, we believe that in this case the strong boundary scattering will prohibit phonon transport and dominate over any other scattering events. This reduces thermal conductivities calculated using both bulk and nanowire dispersion relations to nearly the same value. The reason for smaller thermal conductivity from nanowire dispersion relations may be from two sources. One is that the phonon group velocity in nanowires is smaller than that in bulk material. The other is that the phonon lifetime evaluated from Eq. (47) is smaller than that obtained from the formula for bulk material. With decreasing nanowire diameter, the frequency gap between different branches decreases, which in turn causes the increase of phonon Umklapp scattering rate, and hence reduces the lattice thermal conductivity. Since simulations using nanowire dispersion relations are very time consuming, a detailed calculation for the thermal conductivity of different diameter nanowires spanning a broad temperature range has not yet been carried out.

7 Conclusion

A Monte Carlo method has been developed to simulate phonon transport in nanowires. A genetic algorithm, which meets both momentum and energy conservation requirements for the simulation system, was adopted to model the phonon-phonon scattering process. Phonon dispersion relations for bulk Si and Si nanowires were employed to simulate nanowire thermal conductivity. Simulation results using the bulk Si dispersion relation agree reasonably well with our experimental results for nanowires with a diameter larger than 37 nm. Simulation results using the nanowire dispersions show significant differences compared with those using the bulk dispersions for nanowires with a diameter between 10 nm and 20 nm. These differences were attributed to the phonon group velocity reduction and the phonon lifetime reduction due to strong phonon-phonon scattering derived from nanowire dispersion relations.

Acknowledgments

Y. Chen would like to acknowledge the financial support from the National Natural Science Foundation of China (5027601, 50275026) and the 863 High Technology Program (2003AA404160). The authors would also like to thank Dr. Sandip Mazumder of CFD Research Corporation for the helpful discussions about the MC algorithm.

References

[1] Klemens, P. G., 1958, *Solid State Physics*, Academic Press, NY.
[2] Callaway, J., 1959, "Model of Lattice Thermal Conductivity at Low Temperatures," Phys. Rev., **113**, pp. 1046–1051.
[3] Holland, M. G., 1963, "Analysis of Lattice Thermal Conductivity," Phys. Rev., **132**, pp. 2461–2471.
[4] Armstrong, B. H., 1985, "N Processes, the Relaxation-Time Approximation, and the Thermal Conductivity," Phys. Rev. B, **32**, pp. 3381–3390.
[5] Chen, G., 2001, "Ballistic-Diffusive Heat-Conduction Equations," Phys. Rev. Lett., **86**, pp. 2297–2230.
[6] Ju, Y. S., and Goodson, K. E., 1999, "Phonon Scattering in Silicon Thin Films with Thickness of Order 100 nm," Appl. Phys. Lett., **14**, pp. 3005–3007.
[7] Kurosawa, T., 1966, "Monte Carlo simulation of hot electron problems," *Proceedings of the International Conference on the Physics of Semiconductor*, Kyoto, J. Phys. Soc. Jpn. **21**, pp. 424–427.
[8] Budd, H., 1967, "Path Variable Formulation of the Hot Carrier Problem," Phys. Rev., **158**, pp. 798–804.
[9] Jacoboni, C., and Reggiani, L., 1983, "The Monte Carlo Method for the Solution of Charge Transport in Semiconductors with Applications to Covalent Materials," Rev. Mod. Phys., **55**, pp. 645–705.
[10] Bachelli, L., and Jacoboni, C., 1972, "Electron-Electron Interactions in Monte Carlo Transport Calculations," Solid State Commun., **10**, pp. 71–74.
[11] Matulionis, A., Pozela, J., and Reklaitis, A., 1975, "Monte Carlo Treatment of Electron-Electron Collisions," Solid State Commun., **16**, pp. 1133–1137.
[12] Jacoboni, C., 1978, "Noise and Diffusion of Hot Holes in Si," Solid-State Electron., **21**, pp. 315–318.
[13] Klitsner, T., VanCleve, J. E., Fisher, H. E., and Pohl, R. O., 1988, "Phonon Radiative Heat Transfer and Surface Scattering," Phys. Rev. B, **38**, pp. 7576–7594.
[14] Peterson, R. B., 1994, "Direct Simulation of Phonon-Mediate Heat Transfer in A Debye Crystal," ASME J. Heat Transfer, **116**, pp. 815–822.
[15] Mazumder, S., and Majumdar, A., 2001, "Monte Carlo Study of Phonon Transport in Solid Thin Films including Dispersion and Polarization," ASME J. Heat Transfer, **123**, pp. 749–759.
[16] Li, D., Wu, Y., Kim, P., Shi, L., Yang, P., and Majumdar, A., 2003, "Thermal Conductivity of Individual Silicon Nanowires," Appl. Phys. Lett., **83**, pp. 2934–2936.
[17] Li, D., Wu, Y., Fan, R., Yang, P., and Majumdar, A., 2003, "Thermal Conductivity of Si/SiGe Superlattice Nanowires," Appl. Phys. Lett., **83**, pp. 3186–3188.
[18] Vincenti, W. G., and Kruger, C. H., 1977, *Introduction to Physical Gas Dynamics*, Robert Krieger Publication, New York.
[19] Majumdar, A., 1993, "Microscale Heat Conduction in Dielectric Thin Films," ASME J. Heat Transfer, **115**, pp. 7–16.
[20] Peierls, R. E., 1955, *Quantum Theory of Solids*, Oxford University Press, Oxford.
[21] Goldberg, D. E., 1982, *Genetic Algorithms in Search, Optimization, and Machine Learning*, Addison-Wesley Publishing Company.
[22] Asen-Palmer, M., Bartkowski, K., Gmelin, E., Cardona, M., Zhernov, A. P., Inyushkin, A. V., Taldenkov, A., Ozhogin, V. I., Itoh, K. M., and Haller, E. E., 1997, "Thermal Conductivity of Germanium Crystals with Different Isotopic Compositions," Phys. Rev. B, **56**, pp. 9431–9447.
[23] Brockhouse, B. N., 1959, "Lattice Vibrations in Silicon and Germanium," Phys. Rev. Lett., **2**, pp. 256–258.
[24] Auld, B. A., 1973, *Acoustic Fields and Waves in Solids*, Wiley, NY.
[25] Herring, C., 1954, "Role of Low Energy Phonons in Thermal Conduction," Phys. Rev., **95**, pp. 954–965.
[26] Simons, S., 1963, Proc. Phys. Soc. London, **82**, pp. 401–405.
[27] Blencowe, M. P., 1999, "Quantum Energy Flow in Mesoscopic Dielectric Structures," Phys. Rev. B, **59**, pp. 4992–4998.
[28] Han, Y.-J., and Klemens, P. G., 1993, "Anharmonic Thermal Resistivity of Dielectric Crystals at Low Temperatures," Phys. Rev. B, **48**, pp. 6033–6042.
[29] Kremer, R. K., Graf, K., Cardona, M., Devyatykh, G. G., Gusev, A. V., Gibin, A. M., Inyushkin, A. V., Taldenkov, A. N., and Pohl, H.-J., 2004, "Thermal Conductivity of Isotopically Enriched 28Si: Revisited," Solid State Commun., **131**, pp. 499–503.
[30] Zou, J., and Alexander, B., 2001, "Phonon Heat Conduction in A Semiconductor Nanowire," J. Appl. Phys., **89**, pp. 2932–2938.
[31] Khitun, A., and Wang, K. L., 2001, "Modification of the Three-Phonon Umklapp Process in A Quantum Wire," Appl. Phys. Lett., **79**, pp. 851–853.
[32] Volz, S., Lemonnier, D., and Saulnier, J.-B., 2001, "Clamped Nanowire Thermal Conductivity Based on Phonon Transport Equation," Microscale Thermophys. Eng., **5**, pp. 191–207.
[33] Lü, X., Chu, J. H., and Shen, W. Z., 2003, "Modification of the Lattice Thermal Conductivity in Semiconductor Rectangular Nanowires," J. Appl. Phys., **93**, pp. 1219–1229.
[34] Volz, S., and Chen, G., 1999, "Molecular Dynamics Simulation of Thermal Conductivity of Silicon Nanowires," Appl. Phys. Lett., **75**, pp. 2056–2058.
[35] Dames, C., and Chen, G., 2004, "Theoretical Phonon Thermal Conductivity of SI/Ge Superlattice Nanowires," J. Appl. Phys., **95**, pp. 682–693.
[36] Mingo, N., 2003, "Calculation of Si Nanowire Thermal Conductivity using Complete Phonon Dispersion Relations," Phys. Rev. B, **68**, pp. 113308-1–113308-4.
[37] Mingo, N., Yang, L., Li., D., and Majumdar, A., 2003, "Predicting the Thermal Conductivity of Si and Ge Nanowires," Nano Lett., **3**, pp. 1713–1716.

Accurate Boundary Element Solutions for Highly Convective Unsteady Heat Flows

M. M. Grigoriev[1]

G. F. Dargush

Department of Civil Engineering, State University of New York at Buffalo, Buffalo, NY 14260

Several recently developed boundary element formulations for time-dependent convective heat diffusion appear to provide very efficient computational tools for transient linear heat flows. More importantly, these new approaches hold much promise for the numerical solution of related nonlinear problems, e.g., Navier–Stokes flows. However, the robustness of these methods has not been examined, particularly for high Peclet number regimes. Here, we focus on these regimes for two-dimensional problems and develop the necessary temporal and spatial integration strategies. The algorithm takes advantage of the nature of the time-dependent convective kernels, and combines analytic integration over the singular portion of the time interval with numerical integration over the remaining nonsingular portion. Furthermore, the character of the kernels lets us define an influence domain and then localize the surface and volume integrations only within this domain. We show that the localization of the convective kernels becomes more prominent as the Peclet number of the flow increases. This leads to increasing sparsity and in most cases improved conditioning of the global matrix. Thus, iterative solvers become the primary choice. We consider two representative example problems of heat propagation, and perform numerical investigations of the accuracy and stability of the proposed higher-order boundary element formulations for Peclet numbers up to 10^5.
[DOI: 10.1115/1.2035109]

Introduction

Development of efficient solvers for Navier–Stokes flows at high Reynolds numbers has been an area of constant interest for the past half century. Great progress has been made toward this objective, especially during the last two decades. Well-established and sophisticated codes based upon finite difference methods (FDM), finite volume methods, and finite element methods (FEM) are now routinely used to solve complex flows governed by the nonlinear Navier–Stokes equations in two and three dimensions. As is observed in the literature, the progress in the area of computational fluid dynamics comes from two primary sources: The growth of computational power due to progress in hardware, and the development of novel solution algorithms. If the computational fluid dynamicists were to rely solely on the former source, a straightforward extrapolation of the growth of the computational resources with the current rate would reveal that it would take many years or even decades before the direct numerical simulations (DNS) of turbulent flows of any practical importance would be feasible using existing computational methods. Therefore, the development of novel efficient computational algorithms for the Navier–Stokes equations has been and will be imperative in the foreseen future.

It is well known that the major difficulty in numerical simulations of Navier–Stokes flows arises due to the non-linear convective term. This issue becomes of paramount importance for highly convective flows, when the Reynolds number exceeds 10^4. These flows are subject to formation of zones with very sharp gradients, e.g., boundary layers, that are extremely difficult to resolve. The difficulties are even more prominent when these zones are moving in space. The use of standard central differences or Galerkin formulations for FDM and FEM, respectively, results in nonphysical oscillatory numerical solutions when the local mesh-based Reynolds number exceeds 2, i.e., $\mathrm{Re}_h \geqslant 2$. Consequently, it is mandatory to introduce an upwinding for the convective term. Although this alleviates the appearance of wiggly solutions, the upwinding may lead to excessive numerical diffusion and/or dispersion. The numerical error due to large artificial diffusion and dispersion should, of course, be avoided by all means when modeling turbulent flows using DNS. There, the numerical diffusion may simply overwhelm the turbulent nature of the flow.

In order to reduce numerical diffusion and dispersion, many upwinding methods have been proposed. Among them, the higher-order upwinding methods (QUICK, SUPG, GLS, etc.) are of primary interest owing to low intrinsic numerical error [1–4]. Developed primarily using one-dimensional or velocity-mesh orthogonality assumptions, these algorithms perform well only either for one-dimensional problems or when the flow velocity is aligned with the mesh. Unfortunately, extensions to the multidimensional cases are not straightforward and the performance of the higher-order upwind methods in multidimensions is usually much less than in one-dimensional problems. Moreover, the accuracy degrades significantly if irregular meshes are introduced for complex geometries, or the meshes are not streamlined with the flow [3].

Owing to recent studies [5–19], it has become quite apparent that the use of convective fundamental solutions within the boundary element framework provides an automatic upwinding in the most natural way for the entire range of Reynolds (or, Peclet) number, from zero to infinity. Thus, no artificial upwinding is required, even when the boundary element mesh is not aligned with the flow direction. Despite the obvious attractiveness of the convective boundary element methods, a proper numerical implementation of the convective fundamental solutions appears extremely difficult, even for a scalar problem.

Currently, most of the numerical implementations of the convective boundary element method (BEM) algorithms are for steady-state problems [5–12]. We note that the BEM formulations for steady-state convective diffusion with uniform flow velocity

[1]Author to whom correspondence should be addressed: M. M. Grigoriev, Department of Civil Engineering, 212 Ketter Hall, State University of New York at Buffalo, Buffalo, NY 14260.

Contributed by the Heat Transfer Division of ASME for publication in teh JOURNAL OF HEAT TRANSFER. Manuscript received August 8, 2004. Final manuscript received May 10, 2005. Review conducted by: Surya Pratap Vanka.

involve no volume integration, and, based on our personal experience, are significantly easier to implement than for unsteady problems using time-dependent kernels. Of course, straightforward extensions of the steady-state formulations to unsteady problems are possible if one considers a finite-difference approximation for the time derivative. However, the combination of BEM with the finite differences leads to a time-marching algorithm of the same order of convergence with respect to time step sizes as the order of finite differences. Meanwhile, the use of time-integrated kernels results in an algorithm which is one order higher than the underlying time functions. For example, linear time functions result in second-order convergence in time [20], while a two-level finite differencing in time provides only the first-order algorithm. Therefore, the combination of BEM with temporal finite differences appears less accurate than the use of time-dependent kernels implemented within the BEM framework.

Accurate numerical implementations of the time-dependent convective kernels benefit from closed-form time integrations over the finite time interval. However, due to singularity of the kernels, closed-form integrations are possible only for odd-dimensional problems, i.e., in one and three dimensions. For two-dimensional formulations, these integrals are not available in closed form due to the complexity of the kernels. Owing to the inherent difficulties in the numerical implementations of the time-dependent convective kernels, there have been only a few boundary element studies on unsteady convective diffusion problems using time-dependent convective kernels [13–19]. Grigor'ev [14] presented a linear time step BEM formulation for transient convection diffusion and Burgers' equations, and provided some closed-form time integrals for the one-dimensional case. Shi and Banerjee [13] presented time-integrated two-dimensional kernels in series form. Subsequently, Lim et al. [15] reported a numerical implementation of these time-integrated kernels for Peclet numbers as high as Pe=2000. However, the data presented in Ref. [15] suggest that a more thorough numerical implementation is needed.

Recently, the current authors developed BEM [16–18] for unsteady convective diffusion problems using the time-dependent convective kernels by Carslaw and Jaeger [21]. The authors utilized linear, quadratic, and quartic time interpolation functions [20] for a temporal discretization of the boundary integral equation both in one and two dimensions. For the one-dimensional formulation, the transient convective kernels $g(x-\xi)$ and $f(x-\xi)$ were integrated analytically over the finite time intervals for all time interpolation functions and complete sets of time-integrated kernels were presented. For two dimensions, a series representation for the time-dependent kernels was introduced in Ref. [17]. The authors provided time-integrated formulae for linear, quadratic, and quartic time interpolation functions. Although the implicit time-marching formulation utilized in Refs. [17,18] did not impose any restrictions on the time step size Δt, the applicability of the numerical algorithm was restricted to the following time step sizes:

$$\Delta t \leqslant \Delta t_c = \frac{4\kappa}{V^2} \tag{1}$$

where V is the characteristic velocity of the flow, and κ is the diffusivity. The use of time steps less than the critical time step size Δt_c ensured fast convergence of the series introduced for the time-dependent convective diffusion kernels. Although larger time steps $\Delta t \geqslant \Delta t_c$ were possible, these computations required more terms in the series to attain the desired level of accuracy. Consequently, the efficiency of the BEM deteriorated and, oftentimes, the numerical algorithm failed to converge if the time steps were too large. In a brief communication [19], this boundary element formulation was extended to the higher Peclet number by alleviating the constraint Eq. (1) through a combination of analytical and numerical integration over time. Here, we provide further enhancements relating to spatial integration of time-integrated convective kernels by refining the definition of domains of influence. This enables us to perform detailed numerical investigations of the accuracy and stability of the proposed method. To the best of our knowledge, this is the first contribution in the literature to study these issues within the context of BEM formulations for unsteady convective flows. Although the problems considered in this paper are limited to constant flow velocities, all of the methodology developed here is directly applicable within boundary element formulations for variable velocity transport problems using, for example, a poly-region approach [12].

In the following section of the paper, we present the time-recurring boundary element formulation using the convective fundamental solutions. Temporal discretization is examined in the next section, where we introduce linear, quadratic, and quartic time interpolation functions and discuss the algorithms for time integration of the kernel-temporal shape function products. Then, we consider linear, quadratic, and quartic boundary elements as well as bilinear, biquadratic, and biquartic volume cells for the spatial discretization of the semidiscrete boundary integral equation. In that section, we also discuss a very efficient algorithm to numerically evaluate the coefficients of the discrete boundary integral equation. Our approach involves the definition of the domains of kernel influence associated with surface and volume integrals. Thus, we restrict integration of the time-integrated and instantaneous kernels only over the parts of boundary elements and volume cells, respectively, that are influenced by the kernels. This facilitates a robust and accurate boundary element integration procedure and dramatically improves the efficiency of the convective time-dependent BEM formulations especially for high Peclet number flows. Here, we note that the definitions for the influence domain due to time-integrated kernels presented in this paper are different from those adopted in Ref. [17]. We emphasize that the influence domains tend to the steady-state counterpart [22] as $\Delta t \to \infty$.

In order to investigate the performance of these new higher-order unsteady boundary element formulations, we consider two example problems in the final section. The first problem involves propagation of a thermal disturbance in a square domain, while the second investigates the time and space propagation of temperature fronts. Although analytical solutions are available for both problems, the problems appear to be extremely challenging owing to very sharp variations of the temperature in both time and space.

Governing Equation and Boundary Integral Formulation

We consider the time-dependent transport of heat due to convective diffusion as governed by the following equation:

$$\frac{\partial T}{\partial t} + v_i \frac{\partial T}{\partial x_i} = \kappa \frac{\partial^2 T}{\partial x_i \partial x_i} \tag{2}$$

In Eq. (2), t is time, x_i is the Eulerian coordinate, v_i is the velocity of the flow, T is the temperature, and κ is the diffusivity. Let us introduce nondimensional temperature

$$\tilde{T} = \frac{T - T_{\mathrm{ref}_1}}{T_{\mathrm{ref}_2} - T_{\mathrm{ref}_1}}$$

velocity $\tilde{v}_i = v_i/U$, time $\tilde{t} = Ut/L$, and coordinate $\tilde{x}_i = x_i/L$. Here, U is the characteristic velocity of the flow, L is the specific length of the domain, while T_{ref_1} and T_{ref_2} are lower and upper reference temperatures of the media, respectively. Now, we rewrite Eq. (2) to the following form:

$$\frac{\partial \tilde{T}}{\partial t} + \tilde{v}_i \frac{\partial \tilde{T}}{\partial \tilde{x}_i} = \frac{1}{\mathrm{Pe}} \frac{\partial^2 \tilde{T}}{\partial \tilde{x}_i \partial \tilde{x}_i} \tag{3}$$

where $\mathrm{Pe} = UL/\kappa$ is the global Peclet number. We shall utilize only nondimensional variables in this study, however we shall omit the tilde in the notations for the sake of brevity.

Equation (3) governs transient convective heat diffusion for time $t \geq 0$ in domain Ω bounded by the surface Γ. Both temperatures $\overline{T}(x,t)$ on $x \in \Gamma_T$ and normal fluxes $\overline{Q}(x,t)$ on $x \in \Gamma_Q$ may be specified as Dirichlet and Neumann boundary conditions, respectively. Note that $\Gamma_T \cap \Gamma_Q = 0$ and $\Gamma_T \cup \Gamma_Q = \Gamma$, where the surface Γ bounds the computational domain Ω. In addition to the boundary conditions, initial conditions must be specified as $T_0(x) = T(x,0)$ at $t=0$ for $x \in \Omega$.

The corresponding integral form of the boundary value problem can be written as follows:

$$c(\xi)T(\xi,\tau) = \int_\Omega T(x,0)g(x-\xi,\tau)d\Omega(x) + \int_0^\tau \int_\Gamma \{T(x,t)f(x-\xi,\tau-t) + Q(x,t) \times g(x-\xi,\tau-t) + T(x,t)g(x-\xi,\tau-t)v_n\}d\Gamma(x)dt \tag{4}$$

In Eq. (4), τ is time when the solution is desired, $v_n = v_i n_i(x)$ is the velocity normal to the boundary, $n_i(x)$ is the unit outward normal to the surface $\Gamma(x)$,

$$Q(x,t) = -\frac{1}{\mathrm{Pe}}\frac{\partial T(x,t)}{\partial n}$$

is the normal heat flux due to diffusion, ξ stands for the collocation point $\xi \in \Omega(x)$, and

$$g(x-\xi,\tau-t) = \frac{H(\tau-t)\mathrm{Pe}}{4\pi(\tau-t)} \exp\left[-\frac{s_i s_i}{4(\tau-t)}\mathrm{Pe}\right] \tag{5}$$

is the free-space single-layer kernel obtained by Carslaw and Jaeger [21] for two-dimensional problems. The double-layer kernel can then be given as follows:

$$f(x-\xi,\tau-t) = \frac{1}{\mathrm{Pe}}\frac{\partial g(x-\xi,\tau-t)}{\partial n} = -\frac{s_i n_i}{2(\tau-t)}g(x-\xi,\tau-t) \tag{6}$$

Now in Eqs. (5) and (6), $s_i = x_i - \xi_i + v_i(\tau - t)$ is the convected distance between field and source points, and $H(\tau-t)$ is the Heaviside step function. The geometric function $c(\xi)=0.5$ when ξ is on a smooth portion of the boundary and $c(\xi)=1$ when ξ lies inside the domain Ω.

Equation (4) is an integral representation of the governing time-dependent convective diffusion Eq. (3) that provides the temperature of the media at any point at any time $\tau \geq 0$. The surface integral in Eq. (4) involves Riemann convolutions for boundary temperatures and normal fluxes. The volume integral in Eq. (4) represents an effect of the initial temperature distribution in the domain Ω.

In this paper, we consider a time-stepping procedure based upon recurring initial conditions [20]. This approach is more appropriate for further extension to the nonlinear problems of fluid dynamics than the time convolution approach presented by Dargush and Banerjee [23] which allows one to consider only surface integrals in the boundary integral equation (4) for any initial temperature distributions satisfying the steady convective diffusion equation.

Temporal Discretization

Time-Discrete Integral Equation. Solutions to integral Eq. (4) are sought for the time domain $t \in [0, t_{\max}]$ at any point in space $x \in \Omega$. Consequently, the time domain is subsegmented into N equal increments of size Δt

$$t_m = \frac{m}{N}t_{\max} = m\Delta t, \quad m = 0,1,\ldots,N$$

This facilitates the recurring initial condition formulation. Then, each increment $[t_{m-1}, t_m]$ is subdivided into p_t equal-sized subincrements. We note that p_t is the order of time interpolation functions utilized in this paper, i.e., $p_t=1$ for linear, $p_t=2$ for quadratic, and $p_t=4$ for quartic functions. The boundary integral Eq. (4) may then be written for any time $\hat{t} \in [t_{m-1}, t_m]$ in the form:

$$c(\xi)T(\xi,\hat{t}) = \int_\Omega T(x,t_{m-1})g(y,\hat{t}-t_{m-1})d\Omega(x) + \int_{t_{m-1}}^{\hat{t}} \int_\Gamma \{T(x,t)f(y,\hat{t}-t) + Q(x,t)g(y,\hat{t}-t) + T(x,t)g(y,\hat{t}-t)v_n\}d\Gamma(x)dt \tag{7}$$

for $m=1,2,\ldots,N$. In Eq. (7), $y = x-\xi$. Since the initial condition is known at t_0, we advance to the time level t_1, and obtain a BEM solution at any point $\xi \in \Omega$ at time t_1. Now we use $T(x,t_1)$ as an initial condition in Eq. (7) to advance to the next time level t_2 and so on, until we reach time $t_N = t_{\max}$.

Now we approximate a time variation of boundary temperature $T(x,t)$ and heat flux $Q(x,t)$ via linear, quadratic and quartic interpolation functions presented in Ref. [20]. A general time interpolation can be given as follows:

$$\varphi(x,\overline{t}) = \theta_\alpha(\overline{t})\varphi^{(\alpha)}(x) \tag{8}$$

Here, relative backward time is defined as $\overline{t} = (t_m - t)/\Delta t$, and summation over index $\alpha = 0, 1/4, 1/2, 3/4, 1$ is performed. Linear, quadratic, and quartic time interpolation functions $\theta_\alpha(\overline{t})$ can be found in Ref. [20]. In Eq. (8), $\varphi^{(\alpha)}(x)$ with $\alpha = 0, 1/4, 1/2, 3/4, 1$ stands for either temperature $T^{(\alpha)}$ or flux $Q^{(\alpha)}$ at time $t = t_{m-1} + \alpha\Delta t$.

We substitute Eq. (8) into boundary integral Eq. (7) and then write the generalized integral form of convective diffusion transport as follows:

$$\mathbf{T}\mathbf{A}_{(k)} \cdot \boldsymbol{\Delta} \cdot \mathbf{R}^T_{(k)} + (\mathbf{Q} + \mathbf{T}\mathbf{v}_n)\mathbf{A}_{(k)} \cdot \boldsymbol{\Delta} \cdot \mathbf{P}^T_{(k)} = \mathbf{T}^{(0)}\mathbf{g}^{(0)} \tag{9}$$

Here, $\mathbf{T}$ and $\mathbf{Q}$ are temperature and heat flux vectors, subscript $k = 0, 1/4, 1/2, 3/4, 1$ represents the collocation time level, and matrices $\mathbf{A}_{(k)}$ and $\boldsymbol{\Delta}$ are defined as in Ref. [20]. Components of the vectors $\mathbf{P}^T_{(k)}$ and $\mathbf{R}^T_{(k)}$ in Eq. (9) are given by

$$P_i(y,\lambda) = \frac{\mathrm{Pe}}{4\pi}\exp\left(-\frac{rV\cos\vartheta}{2}\mathrm{Pe}\right)\hat{P}_i(y,\lambda) \quad \text{for } i = -1,0,1,2,3,4 \tag{10}$$

and

$$R_i(y,\lambda) = -\frac{y_j n_j}{2}P_{i-1}(y,\lambda) - \frac{V_j n_j}{2}P_i(y,\lambda), \quad \text{for } i = 0,1,2,3,4 \tag{11}$$

In Eq. (10), $r^2 = y_i y_i$, $V^2 = v_i v_i$, ϑ is the angle between the radius vector y_i and the velocity of the media v_i, and

$$\hat{P}_i(y,\lambda) = \left(\frac{a}{b}\right)^i \int_0^{\lambda/t_m} t^{i-1}\Phi(d,t)dt \tag{12}$$

Here, $\lambda = k\Delta t$ stands for the different time levels, $a^2 = r^2\mathrm{Pe}/4$, $b^2 = V^2\mathrm{Pe}/4$, $t_m = a/b$, and the integrand is given by

$$\Phi(d,t) = \exp\left(-\frac{d}{t} - td\right) \tag{13}$$

with $d = ab$.

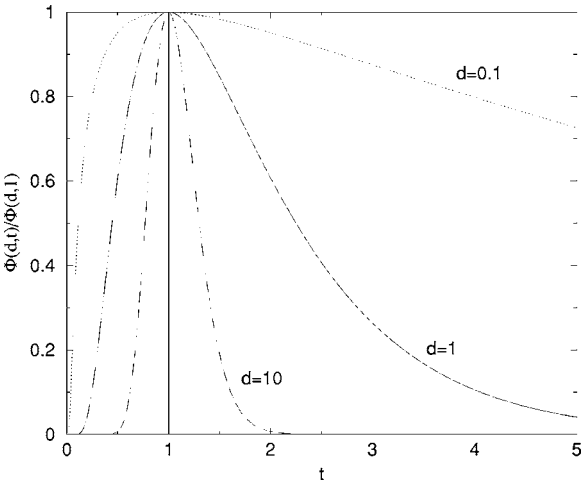

Fig. 1 Variation of the kernel $\Phi(d,t)$ with respect to time

Time-Integrated Kernels. Unfortunately, the closed-form integration of $P_i(y,\lambda)$ has not been possible for the two-dimensional formulation. We should note that, due to singularity of the time-dependent kernels in Eq. (10) as $t\to 0$, the analytical time integration is mandatory in order to develop efficient and accurate time-dependent BEM formulations.

Analysis of the kernel $\Phi(d,t)$ reveals that the function is always non-negative, and it involves only a single maximum

$$\Phi_m(d,1) = \exp(-2ab) \tag{14}$$

at $t=1$.

Figure 1 shows the variation of the kernel $\Phi(d,t)$ for different values of d. For small d, notice that the function changes dramatically at $t\to 0$. As the distance r from the source point to the current field point increases, the kernel response becomes more concentrated at the time $t=1$. We should note that although function $\Phi(d,t)$ itself involves no singularity with respect to time t, the integrand $t^{i-1}\Phi(d,t)$ in Eq. (12) results in singular behavior at $t\to 0$ for $i=-1$ and $i=0$ due to multiplier t^{i-1}.

Let us now split the integral (12) into two parts to integrate $t^{i-1}\Phi(d,t)$ over the time interval $t\in[0,\lambda/t_m]$:

$$\hat{P}_i(y,\lambda) = \hat{P}_i^s(y,t_s) + \hat{P}_i^n(y,\lambda) \tag{15}$$

In Eq. (15), the singular and nonsingular parts are given by

$$\hat{P}_i^s(y,t_s) = \left(\frac{a}{b}\right)^i \int_0^{t_s/t_m} t^{i-1}\Phi(d,t)dt \tag{16}$$

$$\hat{P}_i^n(y,\lambda) = \left(\frac{a}{b}\right)^i \int_{t_s/t_m}^{\lambda/t_m} t^{i-1}\Phi(d,t)dt \tag{17}$$

respectively. In Eqs. (16) and (17), time t_s will be a smaller value between the actual time step λ and the critical time step Δt_c defined by Eq. (1), i.e.

$$t_s = \min[\lambda, \Delta t_c] \tag{18}$$

Notice that the time-integration algorithm presented in Ref. [17] can readily be employed for integral (16). Meantime, for the nonsingular part of the time integral $\hat{P}_i^n(y,\lambda)$, we introduce an adaptive algorithm for numerical integration and perform evaluation of the time integrals with any desired level of accuracy.

In order to accomplish the integration of integral (17) to any desired level of accuracy for a wide range of parameters d, including $d\ll 1$ and $d\gg 1$, we first split the numerical integration into two time intervals $t\in[t_s/t_m,1]$ and $t\in[1,\lambda/t_m]$ as follows:

$$\hat{P}_i^n(y,\lambda) = \left(\frac{a}{b}\right)^i \left[\int_{t_s/t_m}^{1} t^{i-1}\Phi(d,t)dt + \int_{1}^{\lambda/t_m} t^{i-1}\Phi(d,t)dt\right] \tag{19}$$

The integral over the first nonsingular time interval in Eq. (19) can further be subsegmented into $\overline{K}$ nonuniform subintervals

$$\tilde{\tau}_k \overset{\text{def}}{=} [\tilde{t}_{k-1}, \tilde{t}_k], \quad k=1,2,\ldots,\overline{K} \tag{20}$$

Here, $\tilde{t}_0 = t_s/t_m$, $\tilde{t}_{\overline{K}} = 1$, and $\tilde{t}_{k-1} < \tilde{t}_k$ for all $k=1,2,\ldots,\overline{K}$. The values of $\tilde{t}_k$ are directly evaluated from a set of predefined ratios

$$\tilde{\Phi}_k = \frac{\Phi(d,\tilde{t}_k)}{\Phi(d,1)}, \quad k=1,2,\ldots,\overline{K} \tag{21}$$

using the following

$$\tilde{t}_k = 1 - \frac{\ln\tilde{\Phi}_k + \sqrt{\ln\tilde{\Phi}_k(\ln\tilde{\Phi}_k - 4d)}}{2d} \tag{22}$$

We should note that the predefined values $\tilde{\Phi}_k$ are distributed nonuniformly to accurately capture the variation of the first integral in Eq. (19) via the sum of integrals over each time interval $\tilde{\tau}_k$:

$$\int_{t_s/t_m}^{1} t^{i-1}\Phi(d,t)dt = \sum_{k=1}^{\overline{K}} \int_{\tilde{t}_{k-1}}^{\tilde{t}_k} t^{i-1}\Phi(d,t)dt \tag{23}$$

Integrals over time intervals $\tilde{\tau}_k$ are nonsingular and can be evaluated accurately using the standard Gauss quadrature.

The second integral in Eq. (19) can be evaluated in a similar way considering that $\tilde{t}_0 = 1$, $\tilde{t}_{\overline{K}} = \lambda/t_m$, and $\tilde{t}_{k-1} < \tilde{t}_k$.

The algorithm presented above allows evaluation of integral (19) with any desired level of accuracy for all Peclet numbers considered in this paper. We note that the number of Gauss points in the quadrature formula, as well as the number of time intervals $\overline{K}$, may vary depending on the Peclet number as well as the parameter d.

Spatial Discretization

We divide the boundary Γ into a number of boundary elements Γ_l and introduce linear, quadratic, and quartic interpolation functions [20] to represent a spatial variation of the temperatures and normal fluxes over boundary elements at any time level k. Since the boundary integral equation (9) involves a volume integral due to an initial condition, we segment the domain of interest $\Omega(x)$ into a number of volume cells $\Omega_e(x)$ and introduce bi-linear, bi-quadratic and bi-quartic interpolation functions [17] to represent a variation of the initial temperature over the volume cells.

Boundary Element Integration. The following surface integrals over the boundary element Γ_l [16,17]

$$\Phi_\beta^{(\alpha)}(\xi,t) = \int_{\Gamma_l} P_\alpha(y,t) N_\beta(\eta) d\Gamma(x) \tag{24}$$

and

$$\Psi_\beta^{(\alpha)}(\xi,t) = \int_{\Gamma_l} R_\alpha(y,t) N_\beta(\eta) d\Gamma(x) \tag{25}$$

are needed for $\alpha=0,1,2,3,4$ and $\beta=1,2,3,4,5$. We notice that the time-integrated kernels $P_\alpha(y,t)$ and $R_\alpha(y,t)$ are significant only at the proximity of the convected (or, fictitious) source point $\xi_i^{(c)} = \xi_i - v_i t$. Meanwhile, the response due to the concentrated point source propagates upstream and remains significant for very large distances r. For large time steps $t\to\infty$, the time-integrated kernel responses coincide with the steady-state kernels [22]:

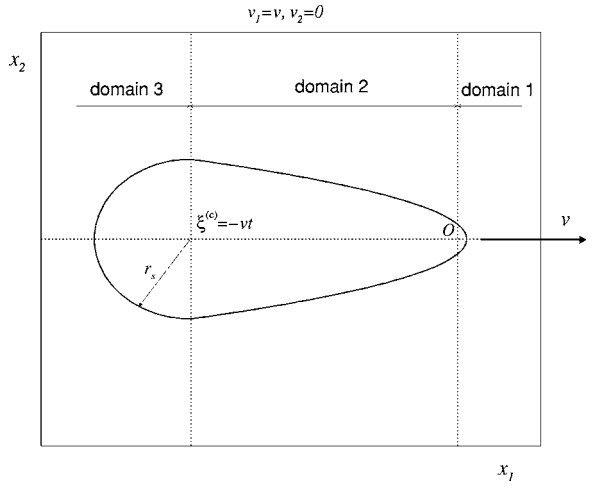

Fig. 2 Domain of influence due to time-integrated kernel originated at point *O*

$$g^{\mathrm{st}}(x-\xi)=\frac{1}{2\pi\kappa}\exp\left(-\frac{y_i v_i}{2\kappa}\right)K_0\left(\frac{rv}{2\kappa}\right) \tag{26}$$

and

$$f^{\mathrm{st}}(x-\xi)=-\frac{1}{4\pi\kappa}\left\{n_i v_i K_0\left(\frac{rv}{2\kappa}\right)+y_i n_i\frac{v}{r}K_1\left(\frac{rv}{2\kappa}\right)\right\}\exp\left(-\frac{y_i v_i}{2\kappa}\right) \tag{27}$$

In Eqs. (26) and (27), $K_0(\cdot)$ and $K_1(\cdot)$ are modified Bessel functions of the second kind of order zero and one, respectively.

Next, we establish the domain of influence for $P_\alpha(y,t)$, $R_\alpha(y,t)$, and perform integration only within that domain. As the responses due to time-integrated kernels propagate upstream with the speed v_i, it is advantageous to utilize the steady-state kernels to track the responses of the time-integrated kernels in time. First, we introduce a local coordinate system aligned with the convective velocity vector as shown in Fig. 2. Then we assume, for the sake of simplicity, that the time-integrated kernels have no effect on the downstream part of the influence domain beyond the current location of the convected source point $\xi_i^{(c)}$ for $t>0$. Thus, the entire influence due to the time-integrated kernels for $x>\xi^{(c)}$ can be described by the domain of influence due to the steady-state kernels $g^{\mathrm{st}}(x-\xi)$ and $f^{\mathrm{st}}(x-\xi)$.

According to Fig. 2, we distinguish three domains of influences owing to time-integrated kernels. Domain 1 represents a downstream influence for $x_1\geqslant 0$ due to the steady-state kernel and will not change as the time progresses $t>0$. Domain 2 is also controlled by the steady-state kernel, and its size in the streamwise direction is limited within $x\in[\xi^{(c)},0]$. Following the approach presented in Ref. [22], for the Domains 1 and 2 governed by the steady-state kernels, let us denote

$$\overline{\alpha}=\frac{rv}{2\kappa} \tag{28}$$

We intend to limit the domain of influence $\Sigma_s(y)$ bounded by the contour $\sigma_s(y)$ to the values $g^{\mathrm{st}}(x-\xi)\geqslant\epsilon_s$ and $f^{\mathrm{st}}(x-\xi)\geqslant\epsilon_s$, where ϵ_s represents a small tolerance for surface integrals, e.g., $\epsilon_s=10^{-10}$, to ensure the contribution of the convective kernels from outside the domain of influence is negligible. This requires consideration of very large values of $\overline{\alpha}\gg 1$ for the points $x\in\Sigma_s(y)$, where

$$\lim_{\overline{\alpha}\to\infty}\frac{K_0(\overline{\alpha})}{K_1(\overline{\alpha})}=1 \tag{29}$$

Moreover, the evaluation of contour $\sigma_s(y)$ does not require a precise evaluation of the kernel functions. Thus, the contour of the kernel influence $\sigma_s(y)$ can be estimated as follows:

$$\exp(-\overline{\alpha}\theta)K_0(\overline{\alpha})=\sigma_s(y) \tag{30}$$

Influence Domains 1 and 2 are then bounded by the curve

$$\sigma_s(y)=\epsilon_s \tag{31}$$

Finally, Domain 3 of the kernel influence shown in Fig. 2 is governed by the instantaneous kernels $g(y,t)$ and $f(y,t)$. Using a frame of reference $\xi^{(c)}$ translating upstream with the kernel $g(y,t)$, we can show that contours of constant values of

$$\overline{g}(y,t)=\frac{g(y,t)}{g(-vt,t)}=\exp\left\{-\frac{(x_1-\xi_1^{(c)})^2+(x_2-\xi_2^{(c)})^2}{4t}\mathrm{Pe}\right\} \tag{32}$$

are concentric circles of radius r_s

$$r_s^2=-\frac{4t}{\mathrm{Pe}}\ln(\overline{g}(y,t)) \tag{33}$$

Thus, Domain 3 will be a semicircle with the center at $(\xi_1^{(c)},\xi_2^{(c)})$ and radius $r_s=\epsilon_s$. Domains 1, 2, and 3 will then form a domain of influence with the closed contour $\Sigma_s(y)$.

The integrations over the boundary elements in Eqs. (24) and (25) are then performed only within the domain $\Sigma_s(y)$ associated with the source point ξ. No integration is needed if boundary element $\Gamma_l(x)$ lies outside the domain $\Sigma_s(y)$, i.e., $\Gamma_l(x)\cap\Sigma_s(x-\xi)=0$.

Notice that when the collocation point ξ does not lie on the boundary element $\Gamma_l(x)$, the time-integrated kernels $P_\alpha(y,t)$ and $R_\alpha(y,t)$ involve no singularity and hence can be evaluated using a standard Gaussian quadrature. However, to perform the integration in a more efficient way, we introduce N_s contours of preset levels

$$\sigma_s^{(i)}\geqslant\epsilon_s^{(i)},\quad i=1,2,\ldots,N_s\quad\text{and}\quad\sigma_s^{(N_s)}=\epsilon_s \tag{34}$$

and segment the boundary element $\Gamma_l(x)$ via these contours. Or, alternatively, the contours can be evaluated directly from the outer-level contour via the following nonuniform scaling

$$r^{(i)}(\vartheta)=\Theta_i r^{(N_s)}(\vartheta),\quad i=1,2,\ldots,N_s-1 \tag{35}$$

where $0<\Theta_i<1$, and $r^{(N_s)}(\vartheta)$ is the distance from the source point ξ to the outer-level contour $\sigma_s^{(N_s)}$. In the former approach, difficulties arise in specifying the preset level contours to attain a desired clustering of the segments for different combinations of t and Pe as

$$\lim_{y\to 0}\sigma_s(y)\to\infty \tag{36}$$

Thus, we utilize the latter approach throughout the study. Note that the parameter Θ_i is much less sensitive to the Peclet number than the preset levels in the former approach. For both approaches considered above, the nonuniform clustering of the segments allows very efficient and accurate integration over the nonsingular boundary element Γ_l influenced by the transient kernel. A variable-order Gaussian quadrature is utilized for every segment of interest to ensure a high level of accuracy.

However, when the collocation point ξ lies on the straight boundary element Γ_l, the evaluation of the boundary integrals (24) and (25) involves a singularity as $y\to 0$. Notice that the contribution due to kernel $P_{-1}(y,t)$ vanishes since $y_i n_i=0$ for the singular boundary element segment. Thus, the only log-type singularity is due to time-integrated kernel $P_0(y,t)$, and all other terms in Eqs. (24) and (25) for $\alpha\geqslant 1$ result in nonsingular integrals. Moreover, a boundary element integral involving $P_0(y,t)$ is singular only

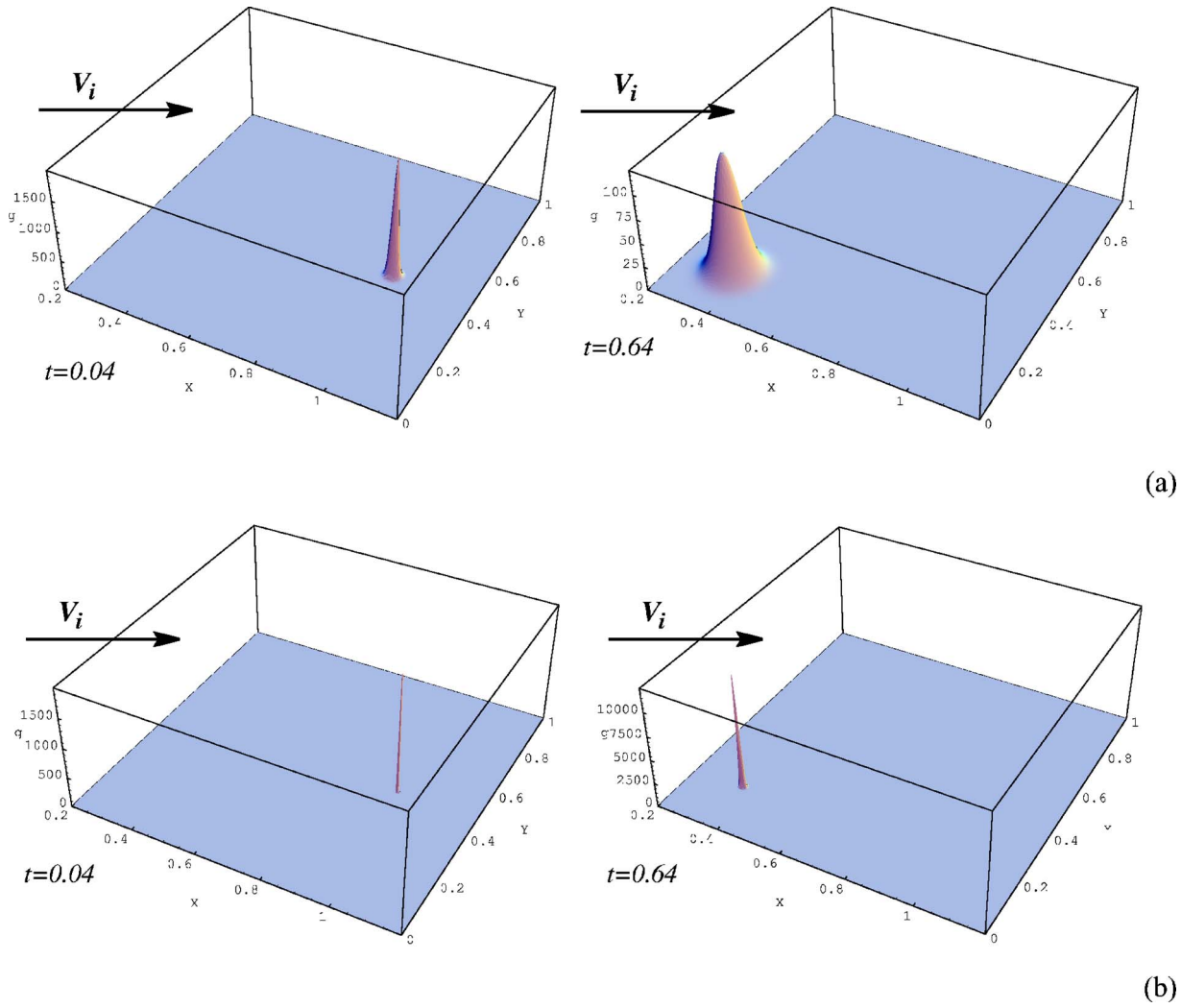

Fig. 3 Surface plots of the instantaneous convective diffusion *g* kernel: (*a*) $\kappa=10^{-3}$; (*b*) $\kappa=10^{-5}$. Source point located at $\xi_i=(1,0.5)$, velocity of the media $v_i=(1,0.5)$.

when the shape function $N_\beta(\eta)$ coincides with the local number of the collocation node γ. Otherwise, the integral is non-singular due to the following property of the shape function

$$N_\beta(\eta(y^{(\gamma)})) = \begin{cases} 1, & \text{if } \gamma=\beta \\ 0, & \text{otherwise} \end{cases} \tag{37}$$

The evaluation of the nonsingular integrals is similar to the algorithm described above.

In order to remove the singularity from the integral $\Phi_\beta^{(\alpha)}(\xi,t)$, we rewrite integral (24) to the following form:

$$\int_{\Gamma_l} P_0(y^{(\beta)},t)N_\beta(\eta)d\Gamma(x) = \int_{\Gamma_l} P_0(y^{(\beta)},t)\{N_\beta(\eta)-1\}d\Gamma(x) + \int_{\Gamma_l} P_0(y^{(\beta)},t)d\Gamma(x) \tag{38}$$

Notice that the first integral on the right-hand side of Eq. (38) is no longer singular and can be integrated using the approach outlined above. The second integral in Eq. (38) can be split into singular and nonsingular parts using Eqs. (10) and (12) as follows:

$$\int_{\Gamma_l} P_0(y^{(\beta)},t)d\Gamma(x) = \frac{\mathrm{Pe}}{4\pi}\left[\int_{\Gamma_l} \exp\left(-\frac{rV\cos\vartheta}{2}\mathrm{Pe}\right)\hat{P}_0^s(y,t_s)d\Gamma(x) + \int_{\Gamma_l} \exp\left(-\frac{rV\cos\vartheta}{2}\mathrm{Pe}\right)\hat{P}_0^n(y,t_s)d\Gamma(x)\right] \tag{39}$$

We notice that the nonsingular time-integrated kernel $\hat{P}_0^n(y,t_s)$ involves no singularity, and thus the second boundary element integral in Eq. (39) can be evaluated in a standard way using a Gaussian quadrature with subsegmentation. Evaluation of the first integral in Eq. (39) can be performed in a way outlined in Ref. [17].

Volume Cell Integration. Although integration of the instantaneous convective kernel over the volume cells involves no singularity, this step also requires careful attention for moderate and high Peclet numbers due to the nature of the *g* kernel. Figures 3(*a*) and 3(*b*) show an upstream propagation of the convective kernel $g(y,t)$ for the diffusivity $\kappa=10^{-3}$ and $\kappa=10^{-5}$, respectively. Here, the source is located at the point $\xi_1=1$ and $\xi_2=1/2$. The convective velocity of the media is not aligned with the Cartesian coordinates and is defined as follows: $v_1=1$, $v_2=1/2$. Notice that the

bell-shaped response is symmetric with respect to the rotated axis of symmetry translating upstream with the speed $-v_i$. When the diffusivity of the media is relatively large [Fig. 3(*a*)], the kernel decays quickly due to large diffusion. As the diffusivity κ reduces, the response becomes extremely localized around the axis of symmetry owing to the dominance of convection over the diffusion processes [Fig. 3(*b*)]. Thus, it becomes mandatory to develop an integration algorithm that tracks the propagation of the transient convective kernel. Obviously, a straightforward integration of the kernel over volume cells would be extremely inefficient, especially for high Peclet numbers [Fig. 3(*b*)].

Here, we introduce the domain of influence $\Sigma_v(y)$ for the instantaneous convective kernel $g(y,t)$ at the current time level t. The contribution of the kernel $g(y,t)$ is significant only within the domain of influence $\Sigma_v(y)$, whereas the kernel is negligible outside of it. The domain of influence is bounded by the contour satisfying the following

$$\overline{g}(y,t) = \epsilon_v \tag{40}$$

Here, $\epsilon_v = 10^{-10}$ is a small parameter to ensure the kernel is significant only within the domain of influence, and the transient convective kernel is scaled using Eq. (32) to provide $0 < \overline{g}(y,t) \leqslant 1$. Recall that the contours of constant values of the instantaneous g kernels are concentric circles of radius r_s defined by Eq. (33). Therefore, the influence domains due to the $g(y,t)$ kernel will be a set of circles propagating upstream from the source point ξ_i with the speed $-v_i$ as shown in Ref. [17]. Notice that the center of these circles coincides with the axis of symmetry.

It must be emphasized that the integration over a volume cell Ω_e is performed if any part of the volume cell is inside the domain of influence $\Sigma_v(y)$:

$$\Omega_e \cap \Sigma_v(y) \neq 0 \tag{41}$$

Otherwise, no integration over Ω_e is needed. If the volume cell is influenced by the instantaneous g kernel, we introduce a grid in polar coordinates (r,θ) so that the point of origin coincides with the axis of symmetry [17]. Angular segmentation is uniform with the increment $\Delta\theta$. For the radial segmentation, we introduce N_v preset levels for the scaled kernel $\overline{g_i}(y,t)$

$$\epsilon_v^{(i)} \leqslant g_i(y,t) < 1, \quad i = 1,2,\ldots,N_v \quad \text{and } \overline{g}_{N_v}(y,t) = \epsilon_v \tag{42}$$

Here, the radius of each circular level $\overline{g_i}(y,t)$ is evaluated directly from Eq. (42). Note that the outer-level circle $\overline{g}_{N_v}(y,t)$ is the boundary of the kernel influence.

Generally, the volume cell Ω_e is not aligned with the segmentation grid and, thus, some of the grid segments generated in the polar coordinate system (r,θ) require a volume integration only over the parts that belong to the volume cell. For the sake of simplicity in evaluating the intersections between the influence domain and volume cells, the circular domains are replaced with polygons [17]. Note that the volume integrals are evaluated using a standard Gaussian quadrature. Similar to the boundary element integration, we utilize a variable order of Gaussian quadrature for every volume segment of interest to ensure a high level of accuracy.

Assembly and a Matrix Solution. The BEM presented in this paper leads to the following set of linear equations

$$\mathbf{A}\mathbf{x} = \mathbf{b} \tag{43}$$

In Eq. (43), $\mathbf{x}$ is the generalized vector of unknown boundary temperatures and heat fluxes, $\mathbf{b}$ is the vector due to known boundary temperatures and heat fluxes, and $\mathbf{A}$ is a global matrix which is sparse due to the nature of the convective kernels. The size of the global matrix for the two dimensional problem considered here can be as large as 25,000 resulting in over 10 million nonzero entries.

As shown in the following section, the sparsity of the global matrix increases dramatically with an increase of the Peclet number. The nonzero elements of the matrix are clustered around the main diagonal, while off-diagonal elements decay rapidly or are virtually zero for the entire matrix. In this paper, we utilize the preconditioned biconjugate gradient method (BCGM) for sparse linear systems presented by Press et al. [24]. We should note that the use of the main diagonal as a preconditioner results in a stable, accurate, and efficient solution algorithm for Peclet numbers $\mathrm{Pe} < 10^5$. However, when the Peclet number exceeds 10^5, the BCGM sparse solver has been unable to converge for some particular combinations of mesh discretizations and physical time t_i. This problem will be discussed in the next section in more detail. Here, we merely state that, for these particular cases of the iterative solver failure, we have utilized a direct sparse solver developed by Ø sterby and Zlatev [25].

Numerical Results

The numerical algorithm described above has been implemented as a C++ code for the UNIX environment. We investigate the performance (accuracy and robustness) of the proposed BEM for linear, quadratic, and quartic functions in time and space. Here, we consider two time-dependent problems of heat propagation in a steady uniform ambient flow. Both problems under consideration possess exact solutions, thus making it possible to obtain numerical errors at any point $x \in \Omega$ at any time $t \in [0, t_{\max}]$. Note that, in these problems, the velocity of the flow is not aligned with the coordinate system to allow more thorough tests for the BEM formulation. We emphasize that both examples lead to very steep thermal fronts at high Peclet numbers considered in this study and, thus, offer great challenges for any computational methodology.

Example Problem 1. Let us first consider the unsteady convective heat diffusion in the unit square $(x_1,x_2) \in (0,1)\times(0,1)$ with the following exact solution:

$$T_{\mathrm{ex}}(x_1,x_2,t) = \frac{1}{1+t}\exp\left[-\frac{(x_1 - t + 1/4)^2 + (x_2 - t/2)^2}{4\kappa(1+t)}\right] \tag{44}$$

The example problem represents a time propagation of a thermal disturbance in a unidirectional flow with the velocity $v_1 = 1$ and $v_2 = 1/2$ not aligned with the coordinate system. The disturbance originates outside of the computational domain at the point $x_1 = -1/4$, $x_2 = 0$ with the following initial temperature distribution

$$T_0(x_1,x_2) = T_{\mathrm{ex}}(x_1,x_2,0) = \exp\left[-\frac{(x_1 + 1/4)^2 + x_2^2}{4\kappa}\right] \tag{45}$$

As time progresses, the thermal disturbance diffuses and convects by the ambient flow to interact first with the left-hand boundary of the computational domain. Then, it propagates through the domain of interest with virtually no interaction with the boundaries, and hits the outflow boundary to leave the computational domain. We continue the numerical solution until the center of the thermal disturbance reaches point $x_1 = 5/4$, $x_2 = 3/4$ outside the domain at $t_{\max} = 1.5$.

For the initial boundary value problem (IBVP), we specify initial conditions for the temperature using Eq. (45). For the Peclet numbers considered in this example problem, the computational domain is virtually unaffected by the initial temperature $T_0(x_1,x_2)$ owing to localization of the thermal fronts. However, as time advances, the contribution due to the volume integral in Eq. (9) will not be insignificant since we employ the recurring initial time formulation. To create a well-defined IBVP, we specify temperatures on the vertical boundaries at $x_1 = 0$, $x_1 = 1$ directly from Eq. (44). Meanwhile, the normal heat fluxes on the horizontal boundaries at $x_2 = 0$ and $x_2 = 1$ are also specified corresponding to exact

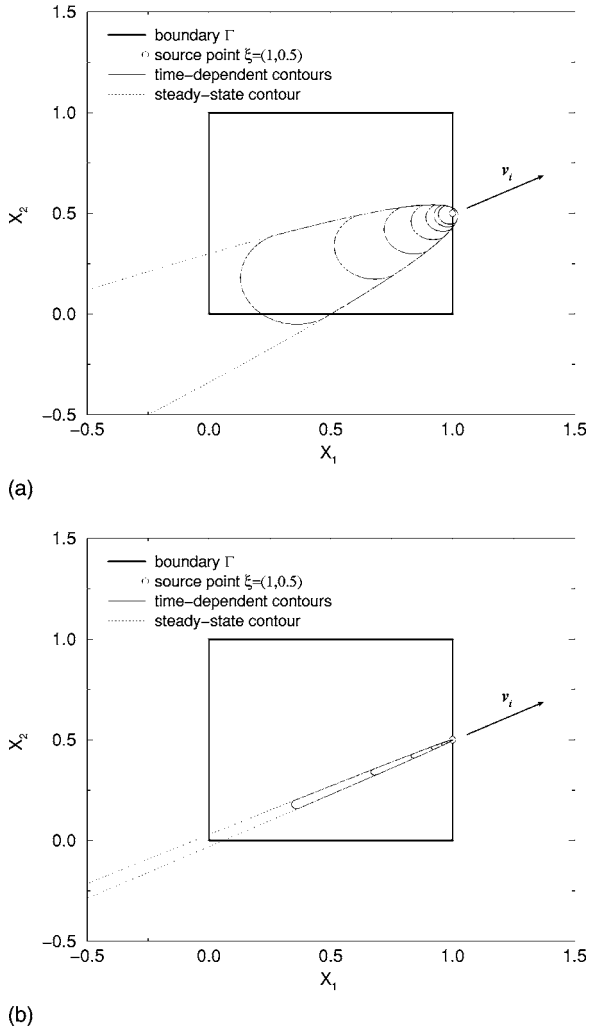

Fig. 4 Influence domains due to time-integrated kernel: (*a*) Pe=1250 and (*b*) Pe=125,000. Time *t* varies from 0.01 to 0.64 with increments in factors of 2; $\epsilon_s=10^{-10}$.

temperature distribution Eq. (44). An L_∞ error norm $\|T\|_t$ is used to monitor the numerical solution error throughout the paper for any time $t \in [0, t_{\max}]$. Thus,

$$\|T\|_t = \max|T_{\text{num}}(x_1,x_2,t) - T_{\text{ex}}(x_1,x_2,t)| \quad \text{for all } x \in \Omega \quad (46)$$

Accordingly, we evaluate the largest numerical error for the entire time and space domains as follows

$$\|T\|_{\max} = \max\|T\|_t| \quad \text{for } t \in [0, t_{\max}] \quad (47)$$

In this paper, we consider three values of the diffusivity κ, namely, $\kappa=10^{-3}$, 10^{-4}, and 10^{-5}. In all cases, a corresponding Peclet number is defined as $\text{Pe}=UL/\kappa$ with velocity magnitude $U=\sqrt{5}/2$ and characteristic length $L=\sqrt{5}/2$. Thus, numerical results discussed in this paper encompass the range of Peclet numbers from 1250 to 125,000.

Typical influence domains due to the time-integrated kernels $\Sigma_s(y)$ with boundary contours $\sigma_s(y)=10^{-10}$ associated with the source point $\xi_1=1$, $\xi_2=0.5$ are shown in Fig. 4. Here, the inner contour corresponds to time $t=0.01$ and each subsequent contour represents a doubling of the time level. Notice the upstream propagation of the response due to the concentrated instantaneous point source. The domain of influence becomes very localized as the Peclet number increases. The localization of the time-integrated kernel response facilitates a diagonal dominance of the global matrix as shown in Fig. 5, where all nonzero entries are

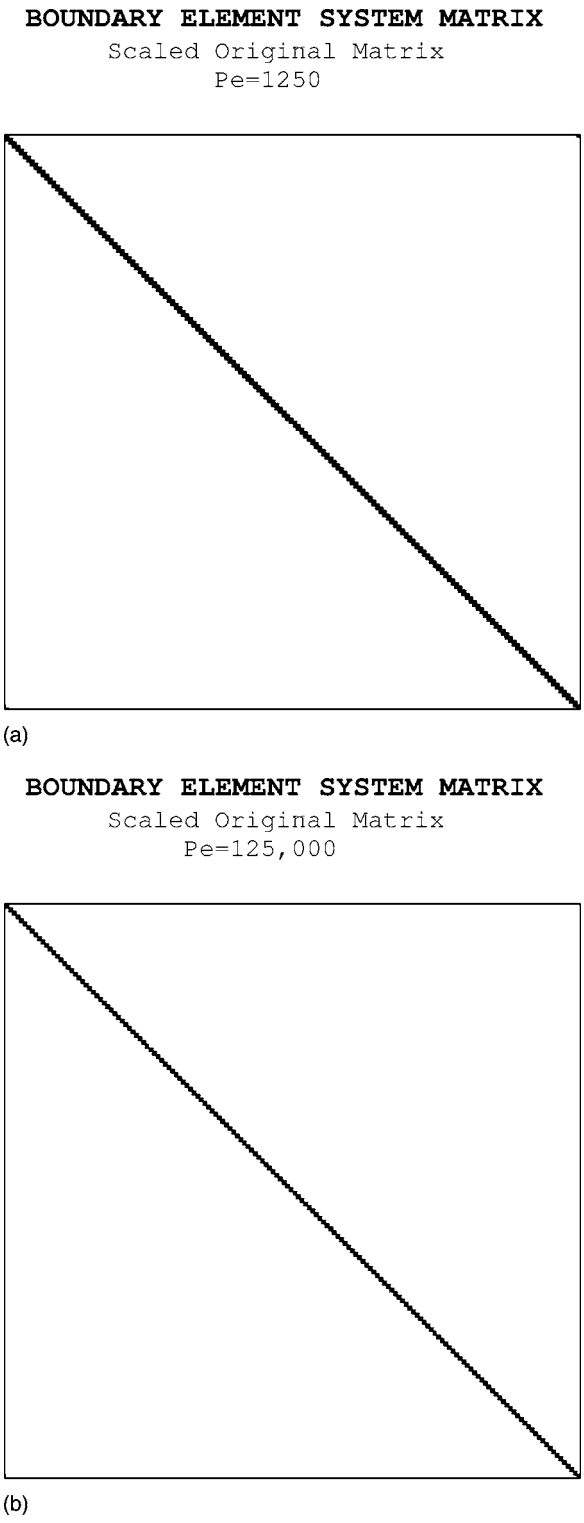

Fig. 5 Global sparse matrix A for Problem 1, boundary element mesh 40×40, $p_t=4$, $p_h=4$; (*a*) Pe=1250, density of the matrix 0.01755; (*b*) Pe=125,000, density of the matrix 0.00934

represented by black dots. Thus the use of the main diagonal as the simplest preconditioner in the BCGM [24] can be extremely efficient. We should emphasize that the iterative algorithm has been robust for almost all runs considered in this study. However, for Peclet number Pe=125,000, the convergence of the iterative solutions was poor or the iterations even diverged for time step sizes $0.003 > \Delta t > 0.0015$ when the thermal interacts with the in-

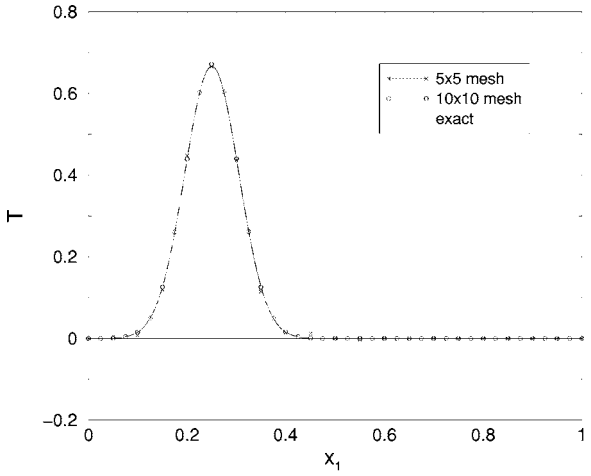

(a)

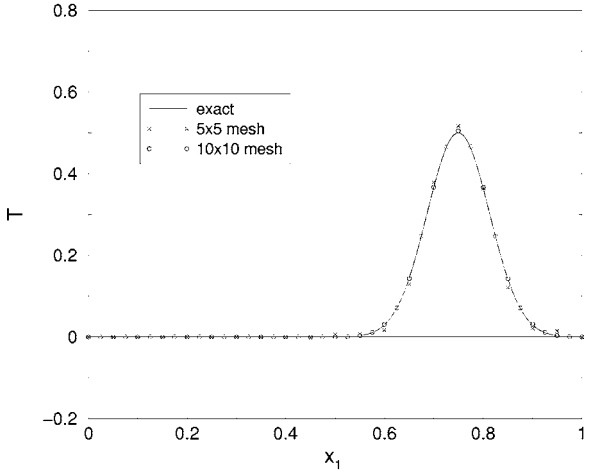

(b)

Fig. 6 Temperature profiles for Problem 1 at Pe=1250; Δt =0.05 Lines—exact solutions; Symbols—BEM solutions for p_t =4, p_h=4; (*a*) x_2=0.25, t=0.5; (*b*) x_2=0.5, t=1, Pe_h=62.5 for mesh 5×5, and Pe_h=31.25 for mesh 10×10

flow boundary of the computational domain. As mentioned above, we utilized a direct sparse solver [25] whenever the sparse BCGM solver fails to converge.

Figure 6 presents the temperature profiles along two cross sections $x_2=0.25$ and $x_2=0.5$ for the Peclet number $\mathrm{Pe}=1250$. Here, we consider coarse meshes $n_{x_1}\times n_{x_2}=5\times 5$ and 10×10 of quartic boundary elements and biquartic volume cells. Notice very smooth and accurate numerical solutions even for the coarser BEM mesh, although the local (mesh-based) Peclet number

$$\mathrm{Pe}_h=\frac{h}{p_h}\mathrm{Pe} \tag{48}$$

significantly exceeds the critical value $\mathrm{Pe}_{\mathrm{cr}}=2$ beyond which upwinding-free methods exhibit nonphysical instabilities [2,3]. In Eq. (48), h is the characteristic size of the boundary element mesh, and p_h is the order of the boundary elements and volume cells. Note that $p_h=1$, $p_h=2$, and $p_h=4$ for linear, quadratic, and quartic boundary elements, respectively. We emphasize that uniform boundary element discretizations of the computational domain are utilized throughout this paper, thus, the mesh size is as follows

$$h=\Delta x_1=\Delta x_2=\frac{1}{n_{x_1}}=\frac{1}{n_{x_2}}$$

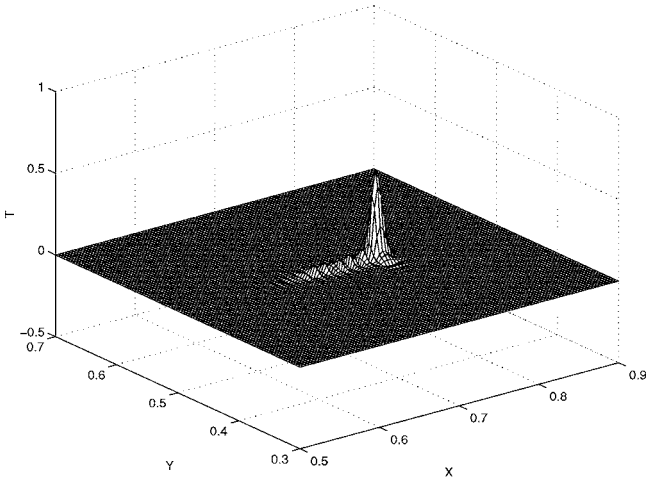

(a)

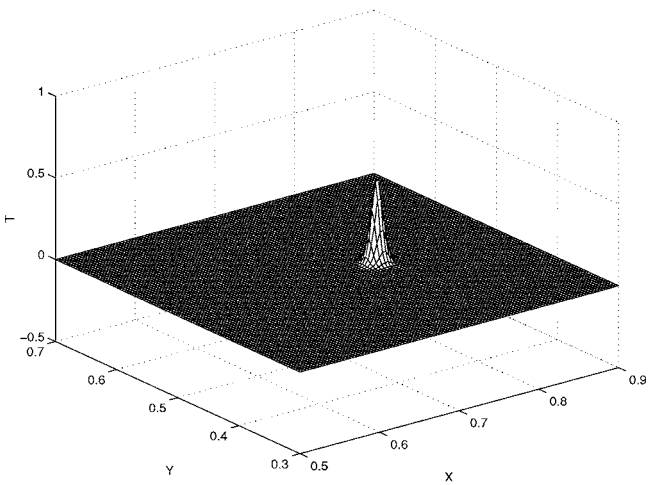

(b)

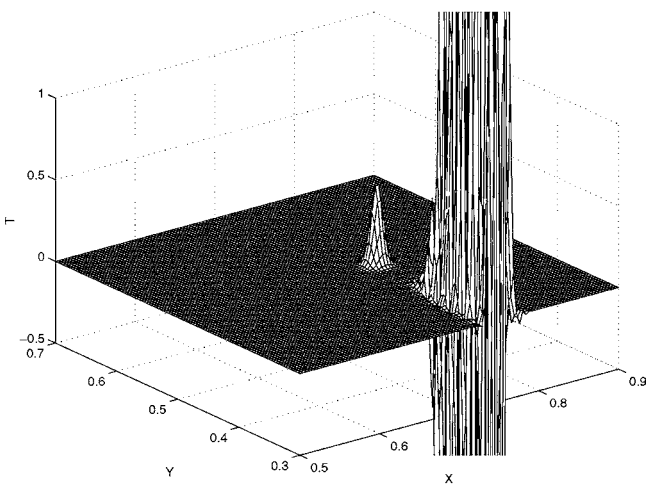

(c)

Fig. 7 Surface plots of the thermal temperatures for Pe =125,000; Δt=0.005, p_t=4, p_h=4, t=1.0. Problem 1: (*a*) Mesh 90×90, Pe_h=347.2; (*b*) mesh 100×100, Pe_h=312.5; (*c*) mesh 154×154, Pe_h=202.9.

As we increase the Peclet number to $\mathrm{Pe}=125{,}000$, the thermal disturbance becomes very concentrated around its center. The problem leads to dramatic variations of the temperature in time

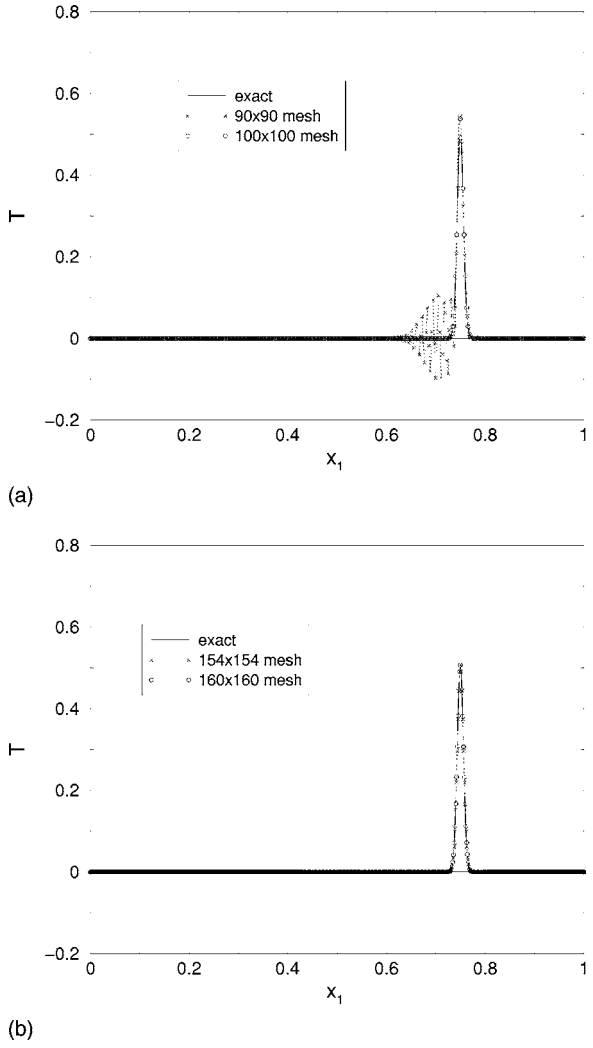

Fig. 8 Temperature profiles for Problem 1 at Pe=125,000; Δt =0.005; x_2=0.5; t=1; Line—exact solution; Symbols—BEM solutions for p_t=4, p_h=4 (*a*) Pe_h=347.2 for mesh 90×90 and Pe_h =312.5 for mesh 100×100; (*b*) Pe_h=202.9 for mesh 154×154 and Pe_h=195.3 for mesh 160×160

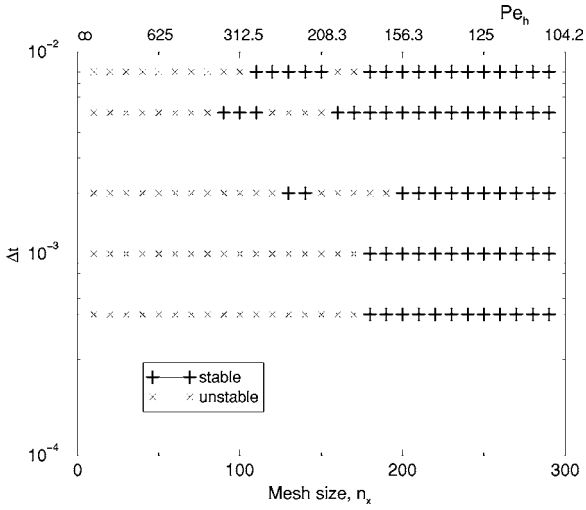

Fig. 9 BEM solution stability chart for Pe=125,000; p_t=4, p_h =4; Problem 1

and space. Thus, extremely fine boundary element meshes as well as time step sizes are needed to resolve very sharp temperature fronts. Figures 7(*a*) and 7(*b*) present surface plots of the thermal propagation through the computational domain for meshes 90 ×90 and 100×100, respectively, with the time step size Δt =0.005. Due to an improper resolution in space for mesh 90 ×90, the numerical solution exhibits nonphysical oscillations in Fig. 7(*a*). The wiggles propagate mostly upstream from the thermal disturbance with slight oscillations noticeable in the x_2 direction. When we slightly refine the boundary element mesh to 100 ×100 in Fig. 7(*b*), the solution becomes very smooth and accurate as shown in Fig. 8(*a*). Here, we present temperature profiles along the cross sections x_2=0.25 and x_2=0.5 for t=0.5 and t=1, respectively.

We should like to note for this particular Peclet number Pe =125,000 and quartic time functions p_t=4 that the numerical solutions become extremely unstable when boundary element meshes coarser than 90×90 are utilized. Thus, no solutions are possible for these coarse boundary element meshes. Interestingly, for this time step size, the numerical solutions using quartic time functions and quartic boundary elements also become unstable when we refine the mesh beyond 110×110. The instabilities persist until we utilize a mesh finer than 160×160. Figure 7(*c*) shows the temperature surface plots for mesh 154×154 using the time step size Δt=0.005. Notice the occurrence of oscillations in the x_2 directions that grow rapidly in time to completely contaminate the numerical solution at $t \geqslant 1$ [Fig. 7(*c*)].

Here, we should like to note two additional observations. First, the shape of the thermal disturbance is not impacted by the nonphysical oscillations. Second, no oscillations are present in the streamwise directions. The temperature profiles for mesh 154 ×154 in the x_1 directions presented in Fig. 8(*b*) demonstrate oscillation-free numerical solutions. We emphasize here that the numerical solutions remain stable and accurate for all BEM meshes beyond 160×160 for Δt=0.005. This mesh corresponds to the local Peclet number Pe_h=195.3.

In Fig. 9, we further investigate the intermittent stability pattern that persists for the Peclet number Pe=125,000 using quartic time functions. Here, we utilize quartic boundary elements p_h=4 and consider the following time step sizes: Δt=0.008, 0.005, 0.002, 0.001, and 0.0005. (Additional research is needed in the evaluation of the kernels $P_i(y,\lambda)$ and $R_i(y,\lambda)$ to permit time step sizes beyond Δt=0.008.) For cases with $\Delta t > 0.001$, there are two regions of instability. The first region corresponds to very coarse meshes. As the mesh gets refined, the numerical solution becomes stable and accurate even on a relatively coarse mesh (Fig. 9). Then, however, the solution becomes unstable again as we refine the mesh further. Finally, when the local Peclet number becomes smaller than 170, the solution regains the stability and accuracy. Any further mesh refinement up to 340×340 shows no signs of instabilities. The intermittent nature of the instability phenomena also disappears completely when we utilize time step sizes $\Delta t \leqslant 0.001$ (Fig. 9). Here notice that the numerical solutions are unstable only when the local Peclet number $Pe_h \geqslant 175$. Conversely, one must consider using boundary element meshes finer than 170×170 to obtain stable and accurate numerical solutions for this very high Peclet number. We note that no oscillations have been observed for any other combination of the Peclet number, and p_t and p_h for the boundary element discretizations up to 340×340 volume cells. We would like to emphasize that the surface and volume integrations were performed for different thresholding parameters ϵ_s and ϵ_v, respectively, to ensure that the insufficient integration accuracy was not a reason for numerical instabilities arising at certain levels of mesh refinement. Interestingly, no stability issues arose in Ref. [17] when modeling other smooth problems, even for Pe=10^6. Thus, we believe that theoretical stability analyses of the BEM are mandatory to address these instability issues for certain convective flow regimes.

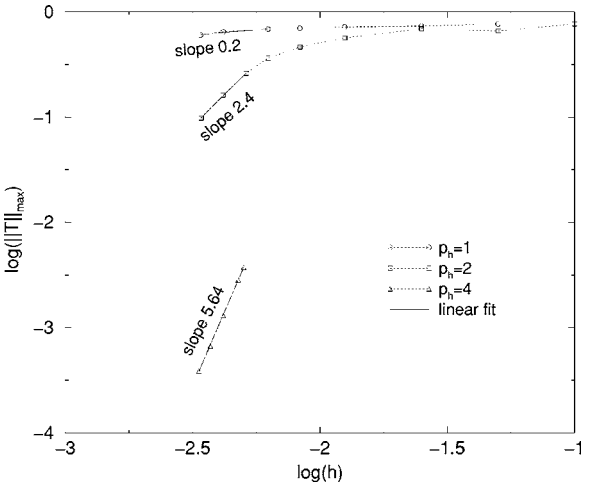

Fig. 10 Convergence of the BEM solution error with respect to the mesh size h; p_t=4 Problem 1: Pe=125,000, Δt=0.002

Next, we concentrate on a quantitative assessment of the numerical errors by performing convergence studies of the boundary element solutions for different mesh sizes h. To present the numerical results in a more compact form, we utilize the nodal-based error $\|T\|_t$ defined by Eq. (46). Figure 10 shows the investigation of the convergence rates of the BEM solution errors with respect to the mesh size h for Pe=125,000. Note that we utilize p_t=4 and consider small time step sizes Δt to ensure that the numerical error due to time discretization is negligible. The rates of convergence approach p_h+2 for quartic boundary elements and volume cells (p_h=4). Due to stability issues discussed above, no results are presented for coarse and moderate mesh refinements at Pe=125,000 and p_h=4 in Fig. 10.

Example Problem 2. The next unsteady convective heat diffusion problem under consideration is again defined in the unit square $(x_1,x_2) \in (0,1)\times(0,1)$. The exact solution for this example problem is given by:

$$T_{ex}(x_1,x_2,t) = \frac{1}{2}\,\mathrm{erfc}\left[\frac{x_1 - t + 0.05}{\sqrt{4\kappa(t+1)}}\right] + \frac{1}{2}\,\mathrm{erfc}\left[\frac{x_2 - t - 0.1}{\sqrt{4\kappa(t+1)}}\right] \tag{49}$$

The problem represents a time propagation of two sharp temperature fronts in a unidirectional flow with the velocity v_1=1 and v_2=1 not aligned with the coordinate system. Two temperature fronts originate outside the computational domain at x_1=−0.05 and x_2=0.1, respectively, and are aligned with the coordinates axes. As time progresses, the fronts propagate by the ambient flow to interact with the computational domain at an angle of 45°. We obtain numerical solutions until the temperature fronts completely leave the computational domain.

Again for the IBVP, we specify initial conditions for the temperature using Eq. (49). Temperature boundary conditions on the vertical boundaries at x_1=0, x_1=1 and normal heat fluxes on the horizontal boundaries at x_2=0 and x_2=1 are directly set from Eq. (49). For this example problem, we consider a single value of the diffusivity $\kappa = 10^{-4}$. With $L=\sqrt{2}$ and $U=\sqrt{2}$, the corresponding Peclet number is then 20,000. The temperature fronts are sharp for this large Peclet number flow, and due to small dissipation, the sharp fronts remain virtually unaffected for the entire space and time domains. In order to properly resolve dramatic variations of the temperature in time and space, extremely fine boundary element meshes together with small time step sizes are needed. Figures 11(*a*) and 11(*b*) present surface plots of the temperatures for t=0.25 and t=1.0, respectively. The BEM solutions are obtained

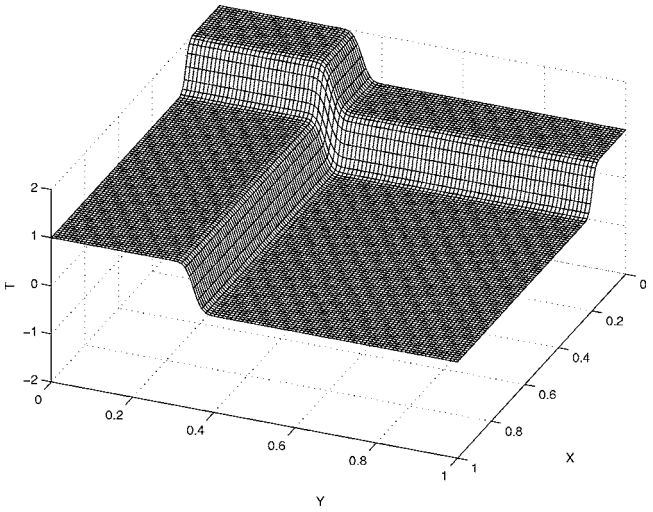

(a)

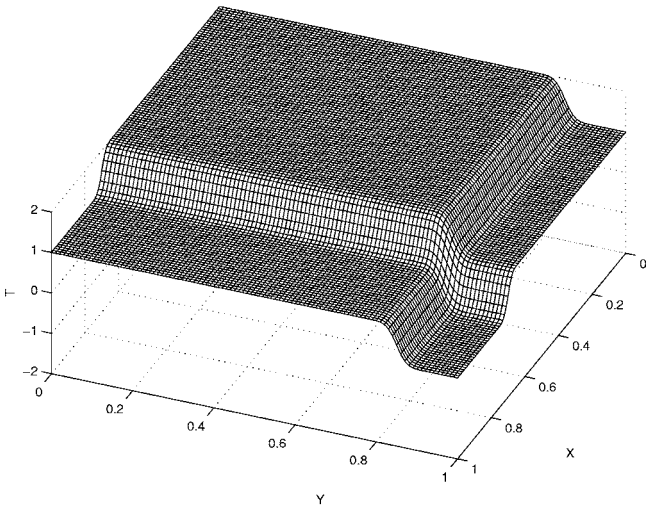

(b)

Fig. 11 Surface plots of the temperatures for Pe=20,000; Δt =0.005, p_t=4, p_h=4 Problem 2, mesh 80×80, Pe$_h$=62.5: (*a*) t =0.25; (*b*) t=1.0

for mesh 80×80 using Δt=0.005. Notice that the solutions are very smooth and accurate as shown in Fig. 11. Here, we present temperature profiles for different time levels along the cross sections x_2=0.2 and x_2=0.8.

Figures 12(*a*) and 12(*b*) show the time evolution of the BEM error $\|T\|_t$ for various mesh and time step sizes, respectively. Here, we use quartic time interpolation functions, quartic boundary elements, and biquartic volume cells to ensure the highest level resolution both in time and space. Notice in Fig. 12 that the numerical error is large when a boundary element discretization of insufficient resolution is utilized. However, $\|T\|_t$ decreases rapidly as either the boundary element mesh or time step size is refined. For the boundary element mesh 100×100, a reduction of time step sizes below Δt=0.005 does not improve the BEM solution [Fig. 12(*a*)]. In order to further reduce the numerical error $\|T\|_t$, finer boundary element meshes are required. In Fig. 12(*b*) notice that the uniform 200×200 rectangular mesh using the fourth-order spatial functions ensures mesh-independent solutions for Δt =0.0025. Again, much finer boundary element meshes are needed to obtain mesh-independent solutions for smaller time step sizes Δt.

Figure 13 presents the investigation of the convergence rates of

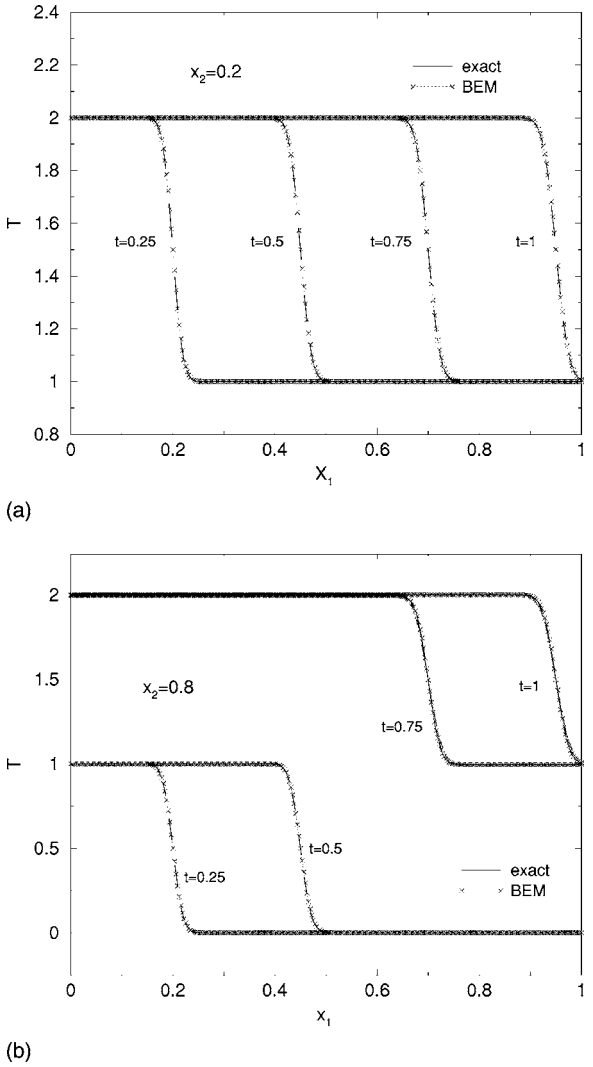

Fig. 12 Temperature profiles for Problem 2 at Pe=20,000; mesh 80×80, $\Delta t=0.005$. Lines—exact solutions; Symbols—BEM solutions for $p_t=4$, $p_h=4$ (*a*) $x_2=0.2$; (*b*) $x_2=0.8$.

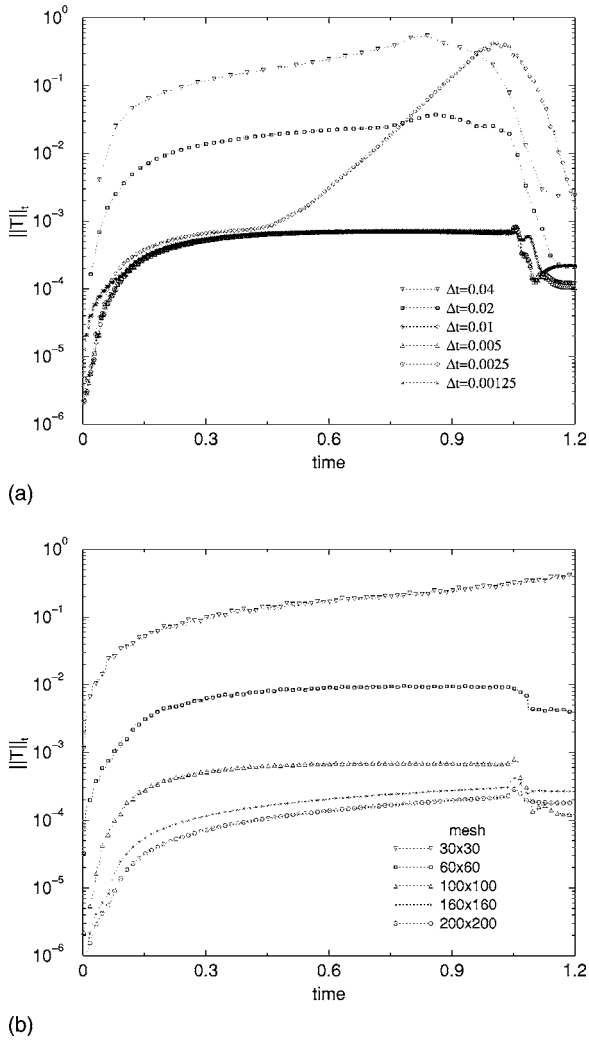

Fig. 13 Time evolution of the BEM solution error for Problem 2: Pe=20,000, $p_t=4$, $p_h=4$ (*a*) variable time step size, mesh 100×100; (*b*) variable mesh size, $\Delta t=0.0025$

the BEM solutions with respect to the mesh size h. Note that we utilize quartic time functions ($p_t=4$) and consider time step sizes $\Delta t=0.0025$ to ensure that the numerical error due to time discretization is negligible for this example problem. Observe in Fig. 13 that, again, the rates of convergence approach p_h+2 for $p_h=4$. For quartic boundary elements and biquartic volume cells, the numerical error continues decreasing until meshes finer than 120×120 are used (Fig. 14). Then, the BEM error remains at the level of approximately $\|T\|_t=0.0003$ with further mesh refinement. This indicates that the time step size must be reduced in order to obtain better accuracy of the BEM solutions.

Conclusions

Higher-order BEM for linear unsteady convective diffusion problems are presented for two dimensions. The time-dependent convective diffusion kernels originally proposed by Carslaw and Jaeger [21] are implemented within the boundary element framework. Higher-order time functions, higher-order boundary elements, and volume cells are utilized to ensure highly accurate numerical solutions for predominantly convective flows. A very efficient and accurate adaptive algorithm has been developed to perform integration of the time-integrated kernels over the boundary elements and evaluation of the volume integrals involving instantaneous convective kernels arising in the boundary integral formulation. This proposed algorithm leads to extremely sparse matrices when convection dominates diffusion. Accordingly, the

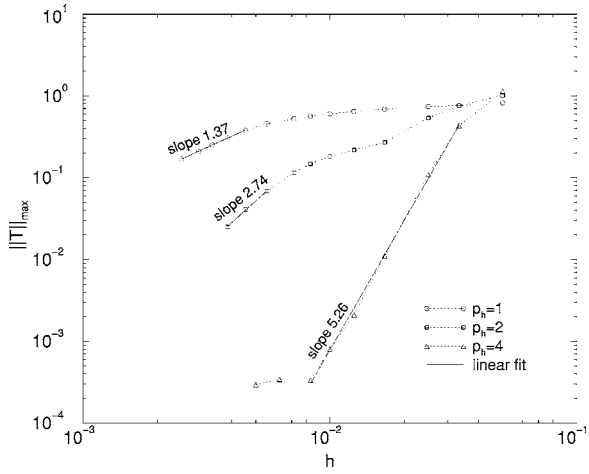

Fig. 14 Convergence of the BEM solution error with respect to the mesh size h. Problem 2: Pe=20,000, $\Delta t=0.0025$; $p_t=4$.

efficiency of the numerical formulation increases as the integrations and, respectively, evaluations are performed only within tiny domains of kernel influence due to the time-integrated and instantaneous kernels.

Accuracy of the higher-order BEM for time-dependent convective diffusion has been examined for two example problems of heat propagation in two dimensions with exact solutions. The problems investigated in this paper involve significant computational challenges for high Peclet numbers due to steep temperature fronts that propagate in space and in time. We have observed numerical instabilities in the proposed boundary element formulation for the first example problem when the global Peclet number is $\mathrm{Pe}=125{,}000$ and the local Peclet number exceeds $\mathrm{Pe}_h \geqslant 170$. Note, however, that the BEM solutions are stable and accurate for smaller local Peclet numbers. For Peclet numbers $\mathrm{Pe}=1250$ and $\mathrm{Pe}=12{,}500$ as well as for the second example problem considered in this study, no numerical instabilities have been observed although the local Peclet number can even exceed a few thousand. Additional research is needed to develop theoretical stability analyses for the current formulation and also to extend the methodology to three dimensions.

Nomenclature

$\mathbf{F}$ and $\mathbf{G}$ = discrete coefficients
$f(y)$ and $g(y)$ = convective kernels
h = mesh size
N = time increments
Pe = global Peclet number
Pe_h = local Peclet number
p_h = space order
p_t = time order
$Q(x,t)$ = normal heat flux
r = radius vector
s_i = convected distance
$T(x,t)$ = temperature
$\|T\|$ = solution error
t = time
U,V = characteristic velocities
v_i = velocity of the flow
x_i = Eulerian co-ordinate
$y_i=x_i-\xi_i$ = relative distance
Δt = time step size
Γ = boundary of the domain
κ = diffusivity
ξ_i = source point
τ = relative time
Ω = domain

References

[1] Brooks, A., and Hughes, T. J. R., 1982, "Streamline Upwind/Petrov-Galerkin Formulation for Convection Dominated Flows with Particular Emphasis on the Incompressible Navier–Stokes Equations," Comput. Methods Appl. Mech. Eng., **32**, pp. 199–259.

[2] Peyret, R., and Taylor, T. D., 1983, *Computational Methods for Fluid Flow*, Springer, New York.

[3] Gresho, P. M., and Sani, R. L., 1998, *Incompressible Flow and the Finite Element Method: Advection-Diffusion and Isothermal Laminar Flow*, Wiley, Chichester.

[4] de Sampaio, P. A. B., and Coutinho, A. L. G. A., 2001, "A Natural Derivation of Discontinuity Capturing Operator for Convection-Diffusion Problems," Comput. Methods Appl. Mech. Eng., **190**, pp. 6291–6308.

[5] Tanaka, Y., Honma, T., and Kaji, I., 1988, "Boundary Element Solution of a Three-Dimensional Convective Diffusion Equation for Large Peclet Numbers," Boundary Element Methods in Applied Mechanics, M. Tanaka and T. A. Cruse, eds., Pergamon, Oxford, pp. 295–304.

[6] Okamoto, N., 1988, "Analysis of Convective Diffusion Problem With First-Order Chemical Reaction by Boundary Element Method," Int. J. Numer. Methods Fluids, **8**, pp. 55–64.

[7] Enokizono, M., and Nagata, S., 1992, "Convection-Diffusion Analysis at High Peclet Number by the Boundary Element Method," IEEE Trans. Magn., **28**, pp. 1653–1654.

[8] Dargush, G. F., Banerjee, P. K., and Shi, Y., 1991, "Development of an Integrated BEM Approach for Hot Fluid Structure Interaction," NASA CR-187236, NASA Lewis Research Center, Cleveland, OH.

[9] Grigoriev, M. M., and Fafurin, A. V., 1997, "A Boundary Element Method for Steady Viscous Flow Using Penalty Function Formulation," Int. J. Numer. Methods Fluids, **25**, pp. 907–929.

[10] Qiu, Z. H., Wrobel, L. C., and Power, H., 1998, "Numerical Solution of Convection-Diffusion Problems at High Peclet Number Using Boundary Elements," Int. J. Numer. Methods Eng., **41**, pp. 899–914.

[11] Ramsak, M., and Skerget, L., 1999, "Mixed Boundary Elements for Laminar Flows," Int. J. Numer. Methods Fluids, **31**, pp. 861–877.

[12] Dargush, G. F., and Grigoriev, M. M., 2000, "A Poly-Region Boundary Element Method for Boussinesq Flows," Comput. Methods Appl. Mech. Eng., **190**, pp. 1261–1287.

[13] Shi, Y., and Banerjee, P. K., 1993, "Boundary Element Methods for Convective Heat Transfer," Comput. Methods Appl. Mech. Eng., **105**, pp. 261–284.

[14] Grigor'ev, M. M., 1994, "A Boundary Element Method for the Solution of Convective Diffusion and Burgers' Equations," Int. J. Numer. Methods Heat Fluid Flow, **4**, pp. 527–552.

[15] Lim, J., Chan, C. L., and Chandra, A., 1994, "A BEM Analysis for Transient Conduction-Convection Problems," Int. J. Numer. Methods Heat Fluid Flow, **4**, pp. 31–45.

[16] Grigoriev, M. M., and Dargush, G. F., 2003, "Boundary Element Methods for Transient Convective Diffusion. Part I: General Formulation and 1D Implementation," Comput. Methods Appl. Mech. Eng., **192**, pp. 4281–4298.

[17] Grigoriev, M. M., and Dargush, G. F., 2003, "Boundary Element Methods for Transient Convective Diffusion. Part II: 2D Implementation," Comput. Methods Appl. Mech. Eng., **192**, pp. 4299–4312.

[18] Grigoriev, M. M., and Dargush, G. F., 2003, "Boundary Element Methods for Transient Convective Diffusion. Part III: Numerical Examples," Comput. Methods Appl. Mech. Eng., **192**, pp. 4313–4335.

[19] Grigoriev, M. M., and Dargush, G. F., 2005, "Efficiency of Boundary Element Methods for Time-Dependent Convective Heat Diffusion at High Peclet Numbers," Commun. Numer. Methods Eng., **21**, pp. 149–161.

[20] Grigoriev, M. M., and Dargush, G. F., 2002, "Higher-Order Boundary Element Methods for Transient Diffusion Problems. Part I: Bounded Flux Formulation," Comput. Methods Appl. Mech. Eng., **55**, pp. 1–40.

[21] Carslaw, H. S., and Jaeger, J. C., 1959, *Conduction of Heat in Solids*, 2nd Ed., Claredon, Oxford.

[22] Grigoriev, M. M., and Dargush, G. F., 2004, "Efficiency and Accuracy of Higher-Order Boundary Element Methods for Steady Convective Heat Diffusion," Numer. Heat Transfer, Part A, **45**, pp. 109–133.

[23] Dargush, G. F., and Banerjee, P. K., 1991, "A Time-Dependent Incompressible Viscous BEM for Moderate Reynolds Numbers," Int. J. Numer. Methods Eng., **31**, pp. 1627–1648.

[24] Press, W. H., Teukolsky, S. A., Vetterling, W. T., and Flannery, B. P., 1992, *Numerical Recipes in C. The Art of Scientific Computing*, Cambridge University Press, Cambridge, UK.

[25] Østerby, O., and Zlatev, Z., 1983, "Direct Methods for Sparse Matrices," *Lecture Notes in Computer Science*, Springer, Berlin, Vol. 157.

Turbulent Three-Dimensional Air Flow and Heat Transfer in a Cross-Corrugated Triangular Duct

Li-Zhi Zhang
Mem. ASME
e-mail: lzzhang@scut.edu.cn
Key Laboratory of Enhanced Heat Transfer and Energy Conservation of the Ministry of Education,
School of Chemical and Energy Engineering,
South China University of Technology,
Guangzhou 510640,
People's Republic of China

Turbulent complex three-dimensional air flow and heat transfer inside a cross-corrugated triangular duct is numerically investigated. Four turbulence models, the standard k-ε (SKE), the renormalized group k-ε, the low Reynolds k-ω (LKW), and the Reynolds stress models (RSM) are selected, with nonequilibrium wall functions approach (if applicable). The periodic mean values of the friction factor and the wall Nusselt numbers in the hydro and thermally developing entrance region are studied, with the determination of the distribution of time-averaged temperature and velocity profiles in the complex topology. The results are compared with the available experimental Nusselt numbers for cross-corrugated membrane modules. Among the various turbulence models, generally speaking, the RSM model gives the best prediction for $2000 \leqslant \mathrm{Re} \leqslant 20{,}000$. *However, for* $2000 \leqslant \mathrm{Re} \leqslant 6000$, *the LKW model agrees the best with experimental data, while for* $6000 < \mathrm{Re} \leqslant 20{,}000$, *the SKE predicts the best. Two correlations are proposed to predict the fully developed periodic mean values of Nusselt numbers and friction factors for Reynolds numbers ranging from 2000 to 20,000. The results are that compared to parallel flat plates, the corrugated ducts could enhance heat transfer by 40 to 60%, but with a 2 times more pressure drop penalty. The velocity, temperature, and turbulence fields in the flow passages are investigated to give some insight into the mechanisms for heat transfer enhancement.* [DOI: 10.1115/1.2035110]

Keywords: Turbulence, Heat transfer, Cross corrugated ducts, Friction factor

Introduction

Heat and moisture transfer through hydrophilic membranes, which is not frequently reported, has great advantages for the air conditioning industry for the recovery of energy from exhaust air. The concept is usually called the fresh air preconditioner. The standard methods for exhaust air waste heat recovery are metal heat exchangers and energy wheels. The metal heat exchangers cannot recover latent heat and the energy wheels have cross-over problems.

The development of membrane technologies has most recently embodied applications in the exhaust air waste heat recovery [1–3]. In these studies, parallel flat plates configurations are used, mainly due to their simplicity in construction. However, since heat mass transfer coefficients are relatively low, performances are quite limited [4]. To intensify the heat and moisture transfer in a membrane exchanger, turbulence promoters of various configurations have been considered including volume displacement rods in tubular membranes, static mixers in tubular membranes, fluidized beds in tubular membranes and mesh screens in flat and spiral-wound membranes. However, flux enhancement is still not satisfactory [5].

Most recently, attention has been drawn toward using corrugated membranes as turbulence promoters. This is analogous to the use of corrugated plates in plate heat exchangers, which has been proven to increase the mechanical strength of the plates as well as the heat transfer rate. The configuration is shown in Fig. 1, where two cross flows exchange heat through corrugated plates. To get such an arrangement, flat membrane sheets are corrugated to form a series of parallel triangular ducts. Sheets of the corrugated plates are then stacked together to form a 90° orientation angle between the neighboring plates, which guarantees the same flow pattern for both fluids. The membranes are very thin and soft. With a predesigned plastic frame, triangular shaped duct walls are formed to construct the required geometry.

Metal plate heat exchangers usually have corrugated sinusoidal ducts. There have been many reports on heat transfer and friction characteristics on cross-corrugated sinusoidal ducts, which provided the basis for the performance evaluation of compact heat exchangers. Focke [6] experimentally investigated the performance of plate heat exchangers with sinusoidal corrugations. The author and co-workers studied the effect of corrugation angle between the neighboring plates on the flow behavior in passages. They found that a 90° orientation angle produces the largest driving force that generates swirl in the furrows [7]. Ciofalo et al. [8] reported numerical investigations for periodic boundary conditions and entry flows. They used the commercial code Flow3D to solve steady laminar and turbulent flow equations in the Reynolds number range between 1000 and 10,000. Biomerius et al. [9] numerically investigated the flow and heat transfer behavior in the laminar and transitional flow regime between $\mathrm{Re} = 170$ and 2000. They found that transition to turbulence takes place at a smaller Re than conventional regular ducts. Very recently, Mehrabian and Poulter [10] modeled the fully developed laminar flow and heat transfer in a cross-corrugated sinusoidal duct with commercial code AEA-CFX4. They found that the inclination angle between the corrugations and the overall flow direction is a major parameter in the thermohydraulic performance of plate heat exchangers. The objectives of these studies are to model the fully developed flow in a repeated segment. Insights of the heat transfer and flow phenomena in the entrance region are very scarce.

Heat transfer and friction performance in the cross-corrugated triangular membranes, proposed for air conditioning and some separation industries, are of great importance for system design. Studies on this topic are still quite limited. Nevertheless, mass transfer in the configuration, an analogy to heat transfer, is tentatively studied by several authors. Scott et al. [5] found that mass flux across the corrugated membrane increases substantially in

Contributed by the Heat Transfer Division of ASME for publication in the JOURNAL OF HEAT TRANSFER. Manuscript received: November 23, 2004; Final manuscript received: April 26, 2005. Review conducted by: Surya Pratap Vanka.

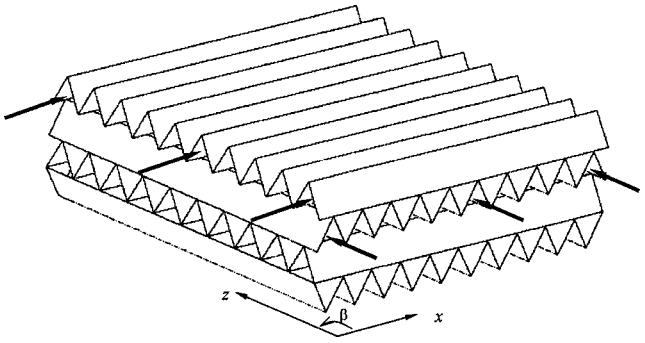

Fig. 1 The flow channel geometry

comparison with flat membranes. Scott and Lobato [11] provided some correlations for predicting Sherwood numbers from Reynolds and Schmidt numbers, using electrochemically measured mass flux data. These studies are very interesting. However, the problem of detailed description of the local heat transfer and friction factor, and flow characteristics, in the complex geometry, is still not addressed.

The aforementioned reasons have motivated the current investigation to numerically predict the local heat transfer and friction factors along the flow in the entrance region of a cross-corrugated triangular duct. The study is confined to turbulent flow for Re $=2000-20{,}000$. Heat transfer and friction performance for laminar flow for $\mathrm{Re}<2000$ will be studied in another separate study.

Methods and Models

Computational Grids. The flow in a cross-corrugated duct is complex [12]. For a corrugation angle of 90° between two neighboring plates, the fluid flows predominantly along the furrows, i.e., between the corrugation on each of the plates [7]. Due to symmetry, the computational domain is selected as a repeated block in the exchanger, as shown in Fig. 2. It is composed of two walls: The upper wall is a corrugated triangular straight duct, and the lower wall is ten parallel ducts of the same geometry with the upper wall, but orient 90 ° to the former one. Consequently, the whole computational domain can be considered as ten repeated segments, or ten cycles.

Three-dimensional numerical simulations of fluid flow and heat transfer in the computational domain are conducted. The solution technique is based on a finite difference/finite volume representation, while allowing for general body-fitted grids. The SIMPLEC pressure-velocity coupling algorithm is used.

Due to the triangular nature of the block, the computational domain is meshed with tetrahedral grids. The meshes on the outside walls are shown in Fig. 3. The graph depicts the meshes only for the first three and one-half cycles, to get an amplified view of the mesh structure. Grid independence tests are done to optimize and balance the solution precision and convergence time. Since "wall function" simulations are conducted, the grid-generation procedure is based on the following rules: The wall-adjacent layer

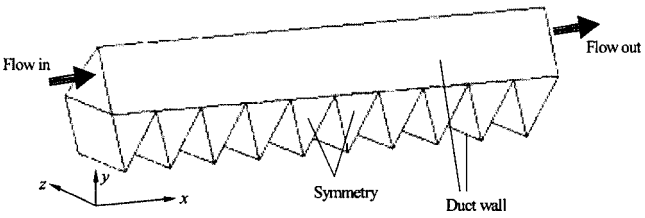

Fig. 2 The single cross-corrugated channel segment for computation

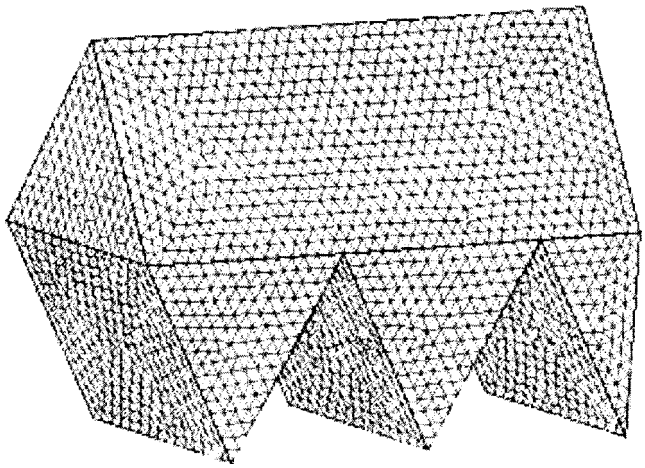

Fig. 3 The grid distribution for the computation domain, showing two and one-half cycles

of control volumes is generated algebraically so that it has an (approximately) uniform thickness, while the iterative algorithm is restricted to the inner control volumes. The reason behind this scheme is that, the wall function technique requires that the near-wall grid points (control volume central points) lie well outside of the viscous layer (say, $y+=30$).

Governing Equations. The equations describing the fluid flow and heat transfer are transport equations for the continuity, momentum, and energy, which are developed from conservation laws of physics. The fluid flow is described by conservation of mass (the continuity equation), momentum (Navier–Stokes equations), and energy (the temperature equation for the fluid). The velocities and temperatures are time-averaged and divided into a mean and a fluctuating value, $u_j=U_j+u_j'$ and $T=T+T'$. Together with the boundary conditions, they form the steady-state governing equations for incompressible flow with negligible external and viscous forces:

$$\frac{\partial(\rho U_j)}{\partial x_j}=0 \tag{1}$$

$$\frac{\partial}{\partial x_j}(\rho U_i U_j)=-\frac{\partial P}{\partial x_i}+\frac{\partial}{\partial x_j}(\tau_{ij}+\tau_{ij}^t) \tag{2}$$

$$\tau_{ij}=\mu\left(\frac{\partial U_i}{\partial x_j}+\frac{\partial U_j}{\partial x_i}\right);\quad \tau_{ij}^t=-\rho\overline{u_i'u_j'} \tag{3}$$

$$\frac{\partial}{\partial x_j}(\rho c_p U_j T)=\frac{\partial}{\partial x_j}(q_j+q_j') \tag{4}$$

$$q_j=\frac{\mu c_p}{\mathrm{Pr}}\frac{\partial T}{\partial x_j};\quad q_j^t=-\rho c_p\overline{u_j'T'} \tag{5}$$

where ρ, μ, and c_p are density, viscosity, specific heat, respectively. It would be impossible to solve these equations analytically because of nonlinearity and the stochastic nature of turbulence. The extra terms that appear due to averaging the velocity and temperature are the Reynolds stress and the turbulent heat flux. Modeling these is known as the closure problem of turbulence. Various turbulence models have been proposed and in total four models are considered.

The hydraulic diameter of the channel is defined as

$$D_h=\frac{4V_{\mathrm{cyc}}}{A_{\mathrm{cyc}}} \tag{6}$$

where V_{cyc} and A_{cyc} are the volume and the surface area of the

channel, respectively.

The Reynolds number, Re, is defined as

$$\mathrm{Re} = \frac{\rho U_m D_h}{\mu} \tag{7}$$

where U_m is the area-weighted mean velocity through a cross section (m/s).

The cycle-average heat transfer coefficient is evaluated from the temperature difference between the inlet and the outlet of a cycle

$$h_m = \frac{\rho U_m c_p A_{ci}(T_i - T_o)}{A_{\mathrm{cyc}} \Delta T} \tag{8}$$

where A_{ci} is the cross-sectional area at inlet or outlet of a cycle (m^2); T_i and T_o are fluid temperature at inlet and outlet of a cycle, respectively (K); ΔT is the logarithmic temperature difference between the wall and the fluid, which is calculated by

$$\Delta T = \frac{(T_i - T_w) - (T_o - T_w)}{\ln \dfrac{T_i - T_w}{T_o - T_w}} \tag{9}$$

where T_w is the wall temperature (K).

The cycle-average Nusselt number, Nu_m, is defined as

$$\mathrm{Nu}_m = \frac{h_m D_h}{\lambda} \tag{10}$$

The cycle-average friction factor is calculated by

$$f_m = \frac{\dfrac{P_i - P_o}{L_{\mathrm{cyc}}} D_h}{\dfrac{1}{2}\rho U_m^2} \tag{11}$$

where L_{cyc} is the length of a cycle (m); P_i and P_o are pressure at inlet and outlet of a cycle, respectively (Pa).

Dimensionless coordinates

$$x^* = \frac{x}{L_{\mathrm{cyc}}} \tag{12}$$

$$y^* = \frac{y}{y_0} \tag{13}$$

$$z^* = \frac{z}{z_0} \tag{14}$$

where y_0, z_0 are the pitch and width of the repeated segment of the duct (m), respectively.

Turbulence Models

Standard k-ε Model. The k-ε model is the most popular of the two-equation models and has produced qualitatively satisfactory results for a number of complex flows. According to this concept, the turbulent shear stress in Eq. (2) is determined by

$$\tau_{ij}^t = \mu_t \left(\frac{\partial U_i}{\partial x_j} + \frac{\partial U_j}{\partial x_i} \right) - \frac{2}{3}\delta_{ij} k \rho \tag{15}$$

where δ_{ij} is the Kronecker delta function, $\delta_{ij}=1$ when $i=j$ and zero when $i \neq j$. The turbulent viscosity μ_t is determined by the Prandtl–Kolmogorov equation [13]

$$\mu_t = C_\mu \rho k^2 / \varepsilon \tag{16}$$

where the turbulence kinetic energy k and dissipation rate ε are calculated by

$$U_j \frac{\partial k}{\partial x_j} = \frac{1}{\rho}\frac{\partial}{\partial x_j}\left(\frac{\mu_t}{\sigma_k}\frac{\partial k}{\partial x_j} \right) + \frac{\mu_t}{\rho}\frac{\partial U_i}{\partial x_j}\left(\frac{\partial U_i}{\partial x_j} + \frac{\partial U_j}{\partial x_i} \right) - \varepsilon \tag{17}$$

$$U_j \frac{\partial \varepsilon}{\partial x_j} = \frac{1}{\rho}\frac{\partial}{\partial x_j}\left(\frac{\mu_t}{\sigma_\varepsilon}\frac{\partial \varepsilon}{\partial x_j} \right) + C_{\varepsilon 1}\frac{\varepsilon}{k}\frac{\mu_t}{\rho}\frac{\partial U_i}{\partial x_j}\left(\frac{\partial U_i}{\partial x_j} + \frac{\partial U_j}{\partial x_i} \right) - C_{\varepsilon 2}\frac{\varepsilon^2}{k} \tag{18}$$

The turbulent heat transfer term in Eq. (5) is determined by the following equation

$$q' = \frac{\mu_t}{\sigma_\theta}\frac{\partial T}{\partial x_j} \tag{19}$$

The constants in the above model take following values [13]:

$$C_\mu = 0.09; \quad C_{\varepsilon 1} = 1.44; \quad C_{\varepsilon 2} = 1.92;$$

$$\sigma_k = 1.3; \quad \sigma_\varepsilon = 1.3; \quad \sigma_\theta = 1.3$$

Renormalized k-ε Model. The renormalization group (RNG)-based k-ε model (RNG KE) follows the same framework as the above two equations model but uses RNG methods [14]. The model is to provide improved predictions of near-wall flows and flows with high streamline curvature. The momentum and energy equations can be rewritten in the following form:

$$\frac{\partial(\rho U_i U_j)}{\partial x_j} = -\frac{\partial P}{\partial x_i} + \frac{\partial}{\partial x_j}\left[\mu_{\mathrm{eff}}\left(\frac{\partial U_i}{\partial x_j} + \frac{\partial U_j}{\partial x_i} \right) - \frac{2}{3}\mu_{\mathrm{eff}}\frac{\partial u_k}{\partial x_k} \right] \tag{20}$$

$$\frac{\partial(U_j \rho c_p T)}{\partial x_j} = \frac{\partial}{\partial x_j}\left[\alpha_T\left(\mu_{\mathrm{eff}}\frac{\partial T}{\partial x_j} \right) \right] + \frac{\partial U_j}{\partial x_i}\left[\mu_{\mathrm{eff}}\left(\frac{\partial U_i}{\partial x_j} + \frac{\partial U_j}{\partial x_i} \right) - \frac{2}{3}\mu_{\mathrm{eff}}\frac{\partial u_k}{\partial x_k} \right] \tag{21}$$

where

$$\mu_{\mathrm{eff}} = \mu\left[1 + \sqrt{\frac{C_\mu}{\mu}}\frac{k}{\sqrt{\varepsilon}} \right]^2 \tag{22}$$

$$U_j \frac{\partial k}{\partial x_j} = \frac{\tau_{ij}^t}{\rho}\frac{\partial U_j}{\partial x_j} - \varepsilon + \frac{\partial}{\partial x_j}\left[(\alpha_k \mu_{\mathrm{eff}})\frac{\partial k}{\partial x_j} \right] \tag{23}$$

$$U_j \frac{\partial \varepsilon}{\partial x_j} = C_{\varepsilon 1}\frac{\varepsilon}{k}\frac{\tau_{ij}^t}{\rho}\frac{\partial U_i}{\partial x_j} - C_{\varepsilon 2}\frac{\varepsilon^2}{k} + \frac{\partial}{\partial x_j}\left(\alpha_\varepsilon \mu_{\mathrm{eff}}\frac{\partial \varepsilon}{\partial x_j} \right) - R \tag{24}$$

where R in the ε equation is given by

$$R = \frac{C_\mu \eta^3 \left(1 - \dfrac{\eta}{\eta_0} \right)}{1 + \beta \eta^3}\frac{\varepsilon^2}{k} \tag{25}$$

with $\eta = Sk/\varepsilon$, and $\eta_0 = 4.38$, $\beta = 0.012$. Other constants are [15]:

$$C_\mu = 0.085; \quad C_{\varepsilon 1} = 1.42; \quad C_{\varepsilon 2} = 1.68$$

The term S is the modulus of the mean rate-of-strain tensor, S_{ij}, which is defined as

$$S = \sqrt{2 S_{ij} S_{ij}} \tag{26}$$

where

$$S_{ij} = \frac{1}{2}\left(\frac{\partial U_i}{\partial x_j} + \frac{\partial U_j}{\partial x_i} \right) \tag{27}$$

The RNG KE model yields an accurate description of how the effective turbulent transport varies with the effective Reynolds number (or eddy scale). The coefficients $\alpha_T, \alpha_k, \alpha_\varepsilon$, in Eqs. (21)–(24) are the inverse effect Prandtl number for T, k, and ε, respectively. They are computed using the following formula:

$$\left| \frac{\alpha - 1.3929}{\alpha_0 - 1.3929} \right|^{0.6321} \left| \frac{\alpha + 2.3929}{\alpha_0 + 2.3929} \right|^{0.3679} = \frac{\mu}{\mu_{\mathrm{eff}}} \tag{28}$$

where α_0 is equal to 1/Pr, 1.0, and 1.0, for the computation of α_T, α_k, α_ε, respectively.

Low Reynolds k-ω Model. Unlike the k-ε model, it is easier to prescribe the boundary conditions in the k-ω model. We know that $k=0$ on solid boundaries, and ω can be specified at the first few grid points away from the wall as $\omega=6\mu/\beta y^2$, (y the distance to wall). The resulting equations for k, ω, and μ_t are:

$$\nu_t = \alpha^* \frac{k}{\omega} \tag{29}$$

The equations for kinetic energy and specific dissipation rate are given as:

$$U_j \frac{\partial k}{\partial x_j} = \tau_{ij} \frac{\partial U_i}{\partial x_j} - \beta^* \omega k + \frac{\partial}{\partial x_j}\left[(\nu + \sigma_k \nu_t) \frac{\partial k}{\partial x_j} \right] \tag{30}$$

$$U_j \frac{\partial \omega}{\partial x_j} = \frac{\sigma}{\nu_t} \tau_{ij} \frac{\partial U_i}{\partial x_j} - \beta_2 \omega^2 + \frac{\partial}{\partial x_j}\left[(\nu + \sigma_\omega \nu_t) \frac{\partial \omega}{\partial x_j} \right] + 2\sigma_{\omega 2} \frac{1}{\omega} \frac{\partial k}{\partial x_j} \frac{\partial \omega}{\partial x_j} \tag{31}$$

The model constants are provided in references [16,17]:

$$\beta^* = \frac{9}{100} \frac{\frac{5}{18} + \left(\frac{\mathrm{Re}_t}{R_\beta}\right)^4}{1 + \left(\frac{\mathrm{Re}_t}{R_\beta}\right)^4} \tag{32}$$

$$\alpha^* = \frac{\alpha_0^* + \frac{\mathrm{Re}_t}{R_k}}{1 + \frac{\mathrm{Re}_t}{R_k}} \tag{33}$$

$$\alpha = \frac{5}{9} \frac{\alpha_0 + \frac{\mathrm{Re}_t}{R_\omega}}{1 + \frac{\mathrm{Re}_t}{R_\omega}} (\alpha^*)^{-1}$$

$$\beta = 0.075, \quad \alpha_0 = 0.1, \quad \sigma_k = 0.1, \quad \sigma_\omega = 0.5, \quad R_\beta = 8, \tag{34}$$

$$R_k = 6, \quad \alpha_0^* = \beta/3, \quad R_\omega = 2.7$$

Full Reynolds Stress Modeling. The Reynolds stress model (RSM) is also considered as a choice. The RSM model equation for the transport of Reynolds stresses is given by the following equation:

$$\begin{aligned} \frac{\partial}{\partial x_k}(\rho U_k \overline{u_i' u_j'}) = &- \frac{\partial}{\partial x_k}[\rho \overline{u_i' u_j' u_k'} + \overline{p(\delta_{kj} u_i' + \delta_{ik} u_j')}] \\ &+ \frac{\partial}{\partial x_k}\left[\mu \frac{\partial}{\partial x_k}(u_i' u_j') \right] - \rho\left(\overline{u_i' u_k'} \frac{\partial U_j}{\partial x_k} + \overline{u_j' u_k'} \frac{\partial U_i}{\partial x_k} \right) \\ &+ \overline{p\left(\frac{\partial u_i'}{\partial x_j} + \frac{\partial u_j'}{\partial x_i} \right)} - 2\mu \overline{\frac{\partial u_i'}{\partial x_k} \frac{\partial u_j'}{\partial x_k}} \end{aligned} \tag{35}$$

The summation convention is used in the above equations. Therefore, there are six equations, in all. In addition to the Reynolds stress transport equations, the dissipation rate is modeled by the dissipation equation as in the standard k-ε model (SKE). A detailed description of the model is given by Moore et al. [18] and Rokni et al. [19]. The default constants supplied by CFD code for simulation are:

$$C_\mu = 0.09; \quad C_{\varepsilon 1} = 1.44; \quad C_{\varepsilon 2} = 1.92; \quad C_{1\mathrm{ps}} = 1.8$$

Boundary Conditions

At the walls, the no-slip condition is used. For k-ε and RSM, the two-layer-based nonequilibrium wall functions methods are also employed. The key elements in the nonequilibrium wall functions are as follows:

(1) The log-law for mean velocity is sensitized to pressure-gradient effects.
(2) The two-layer-based concept is adopted to compute the budget of turbulence kinetic energy in the wall-neighboring cells.
(3) The law of the wall for mean temperature remains the same as in the standard wall function.

The wall-neighboring cells are assumed to consist of a viscous sublayer and a fully turbulent layer, where the logarithmic law of the wall applies. This method requires some consideration of mesh, i.e., the cell adjacent to the wall should be located to ensure that the parameter $y+(\equiv \rho u_\tau y/\mu)$ (u_τ, friction velocity) or $y^*(\equiv \rho C_\mu^{1/4} k_p^{1/2} y/\mu)$ falls into the 30–60 range. In the present study, the $y+$ is adapted into the 35–55 range. In addition, a uniform wall temperature condition is assumed.

At the inlet, all dependent variables are assumed to enter the pipe with uniform profile in the direction parallel to the corrugation of the upper wall, i.e.,

$$u = u_0, \quad T = T_0, \quad k = k_0, \quad \varepsilon = \varepsilon_0 \tag{36}$$

The inlet boundary values of k and ε are computed from an estimated turbulence intensity, I, and turbulent length scale, ℓ, as follows:

$$k_0 = \frac{2}{3}(u_0 I)^2, \quad \varepsilon_0 = C_\mu^{3/4} \frac{k_0^{3/2}}{\ell} \tag{37}$$

The turbulent intensity I, defined as u'/u, is equal to 5%, and the length scale ℓ is set to be $0.07 \cdot D_h$ in the present study, as suggested by Li et al. [15].

The exit boundary condition is treated as an outflow condition, which means that the diffusion flux for all dependent variables are set to zero at the exit and an overall mass balance is obeyed. This outflow boundary condition is true if the flow becomes fully developed at a position far upstream from the exit because the accuracy of the exit boundary condition should not affect the flow and heat transfer fields far upstream from the exit. The results computed afterward indicated that the flow becomes fully developed after three to five cycles after the inlet. Therefore, the assumption is considered valid.

Solution Method

The governing equations are solved by using standard finite difference methods that employ control-volume-based discretization techniques along with a pressure-correction algorithm. The *N-S* equations are solved by SIMPLEC scheme, while the convective term in the energy equation is solved by a first-order upwind implicit approximation, and the diffusive term is by a second-order central difference scheme. The fluid in the study is selected as air.

Because of the intensive nonlinearity and coupling features of this problem, the underrelaxation technique is applied to the iteration process to accelerate convergence. The convergence criterion of

$$\frac{R_\phi^n}{R_\phi^{n-1}} \leqslant 10^{-4} \tag{38}$$

is applied for all equations, where R_ϕ^n refers to the maximum residual value summed over all the computation cells after nth iteration. To test the criterion independence, another convergence criterion of 10^{-5} is applied to a case. The difference of computed

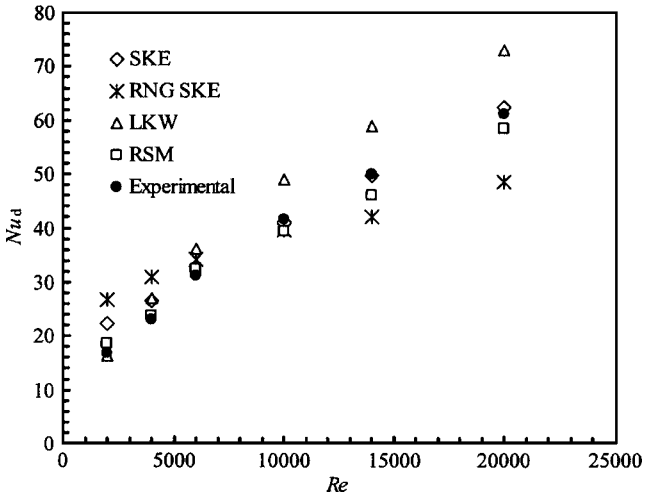

Fig. 4 Predictions of fully developed periodic mean Nusselt numbers with various turbulence models

periodic Nu numbers of the two convergence criterion is within 1%.

The grid independency test has also been done. The calculations were primarily carried out with three different grid densities: 209,985, 104,992, and 419,970 mesh points. The channel fully developed periodic mean pressure drop and temperature change for the two fine grids are almost the same and 10% higher than that for the coarse grid. For the finest grids, 419,970, the solution is too time consuming, which is hard to use practically. Based on the above experience, which establishes the grid independence, the final calculations are performed for the 209,985 grids and the results obtained in this paper refer to the grid geometry mentioned above.

Results and Discussion

Model Validation. Selection of an appropriate turbulence model for numerical simulation requires consideration of computational cost, anticipated flow phenomena, and the variables of primary interest. The Nusselt numbers in the duct are of major concern in this case. Therefore, the agreements of the calculated Nu and experimental data are the main criterion for selecting turbulence models.

For validation and comparison of the four turbulence models used, a cross-corrugated triangular duct with geometric parameters identical to Scott and Lobato [11] is numerically simulated: $z_0=2$ mm; $L_{cyc}=2$ mm; and $y_0=1$ mm. Figure 4 shows the experimentally obtained (the discrete data were obtained from the experimentally obtained Sherwood correlations for a 90° corrugation angle) and the calculated fully developed periodic mean Nusselt numbers. As seen from this figure, of the four turbulence models employed, generally, the RSM fits the experiment the best. The differences are from 5% to 11%, for Re ranging from 2000 to 20,000. At lower Re, the low Reynolds k-ω model (LKW) agrees the best, while the standard k-ε fits poorly. At higher Re, i.e., $Re \geqslant 6000$, the SKE gives the best prediction. As for the RNG KE, it seems inappropriate to use such model for the corrugated triangular duct: The differences found between the calculated and experimentally are substantial. In the low Re range, the model overpredicts the Nusselt number by 58%, while in the high Re range, it underpredicts the Nu by 21%.

In the following analysis, for Re ranging from 2000 to 20,000, the RSM model is employed to investigate the fluid flow and heat transfer. The imperfection with this model is that the computational time is very long [17], due to large memory size required.

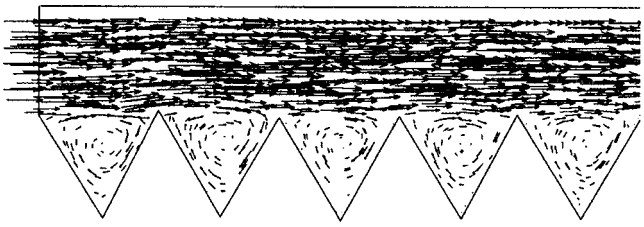

Fig. 5 Velocity vectors in the x-y midplane showing five cycles

Flow Distribution and Friction Factor. Figure 5 shows the vector plot of the velocity in the x-y plane at $z^*=0.5$ (the center in width), for Re=10,000. In the figure, the flow has two distinct patterns: In the corrugation troughs of the upper wall, parallel flow is predominant, while in the troughs of the lower wall, clockwise strong swirls are generated due to the fact that the fluid turns abruptly when facing the trough walls of the lower wall. The shapes of the swirls in the valleys become almost identical to each other, after three to five cycles, indicating a cyclic fully developed manner. These swirls intensify the momentum transfer in the duct.

Figure 6 shows the velocity vectors in the y-z plane at $x^*=4.5$. This plane is perpendicular to the main flow direction, and is located at the center of the fourth cycle. It can be seen that in the corner regions, there exist appreciable secondary flows. These secondary flows all exhibit the same pattern: Departing from one wall, arriving at the other of the same corner, and leaving a small region very close to the corner where the fluid flows are almost retarded. In the central part of the upper wall, the secondary flows are very weak and cannot be observed clearly, while in the lower wall, the secondary flows are relatively strong, even in the central part. There are semiswirls around each corner. The interactions of these semiswirls generate demonstrable secondary flows in the central part of the lower wall valley. These secondary flows gen-

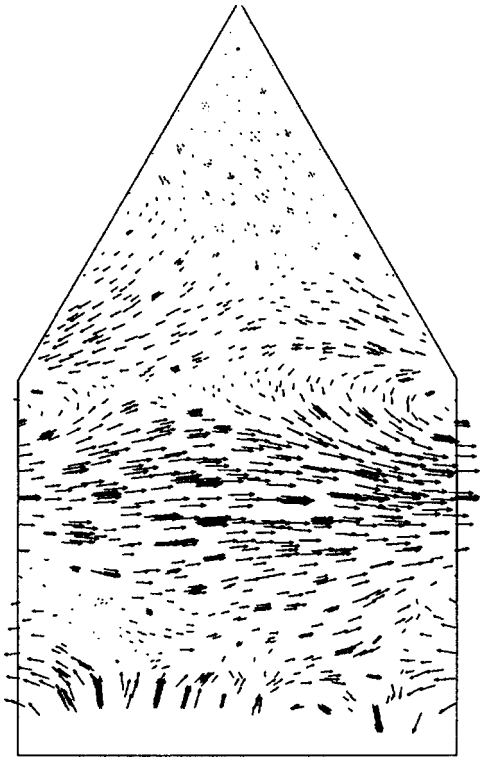

Fig. 6 Velocity vectors in the y-z plane at $x^*=4.5$

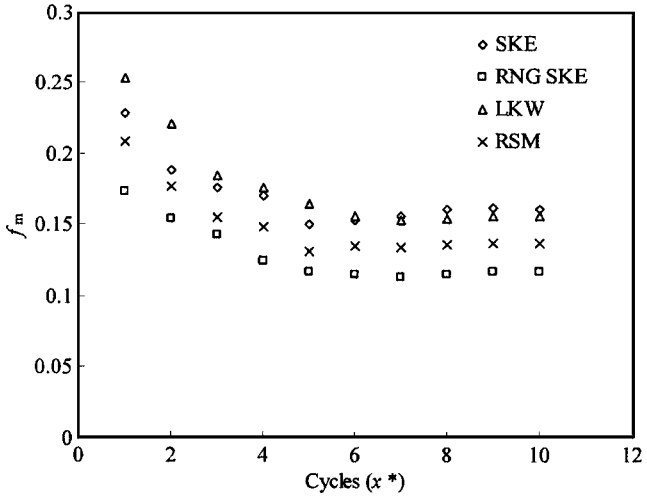

Fig. 7 Distribution of periodic mean friction factor along flow direction

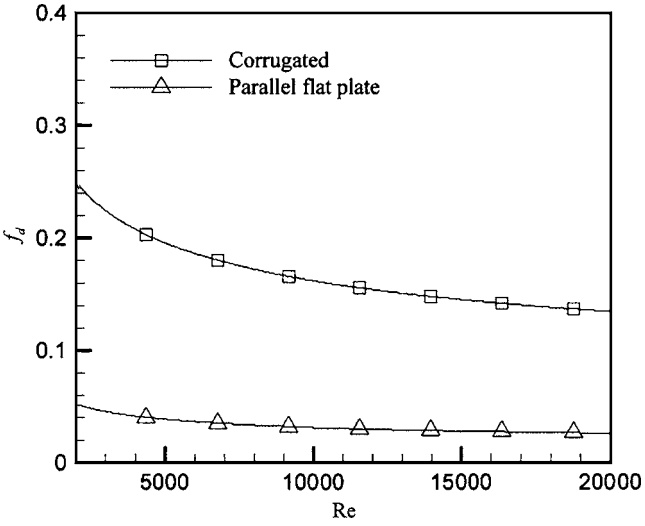

Fig. 9 Comparisons of periodic mean friction factors with Reynolds numbers, cross-corrugated, and parallel flat plates

erated swirls will intensify momentum and heat transfer.

For the cross-corrugated triangular ducts, the cyclic mean friction factor is one of the most important parameters affecting heat exchanger design. Figure 7 shows the calculated periodic mean friction factor along the duct length with four turbulence models. The trend is like most of the developing flows: Near the inlet region, the friction factor is very high; with the flow propagates, after three to five cycles, it decreases gradually to the fully developed value, f_d. At the location near the outlet, the mean friction factor rises somewhat, which may be attributed to the influence of outflow boundary conditions.

The corrugation usually leads to increased pressure drop. Figure 8 shows the calculated fully developed periodic mean friction factor with varying Reynolds numbers. Figure 9 demonstrates comparisons between the friction factors in parallel flat plates passages and in corrugated ducts. Under the same flow rates, the friction factor for the cross-corrugated ducts is three times greater than that for a parallel flat plates duct. Another feature with this figure is that the f_d decreases with an increasing Re.

To summarize the relations between the periodic mean friction factors with Renolds numbers, a correlation has been proposed, with data obtained from the RSM model. The correlation is:

$$f_D = 1.9498\,\mathrm{Re}^{-0.27} \tag{39}$$

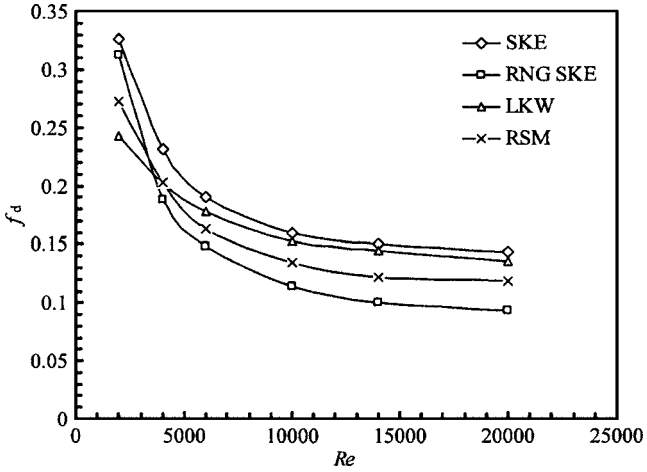

Fig. 8 Calculated fully developed periodic mean friction factor

for $2000 \leqslant \mathrm{Re} \leqslant 10{,}000$

In contrast, friction factor in parallel flat plates is correlated by [20,21]

$$f_D = (0.790 \ln \mathrm{Re} - 1.64)^{-2} \tag{40}$$

Temperature Distribution and Nusselt Number. The isotherms shown in Fig. 10 in an x-y midplane for $\mathrm{Re} = 10{,}000$ clearly show a cyclic manner. After three to five cycles, the thermal flow has become fully developed [22], and the shapes of isotherms in different valleys are similar. It is clear that the isotherms in the last one to two valleys have some distortion, which may also be attributed to the exit flow boundary conditions. The temperature gradients at the walls are very high, indicating an enhanced heat transfer, due to strong turbulence. The temperature profiles in a y-z cross section are shown in Fig. 11. The isotherms at the bottom line are sparsely distributed, indicating poor heat transfer at the sharp edge (in flow direction) of the duct. Contrary to laminar flow, which usually has lower heat transfer on the lower walls, the turbulence flow in this case has high heat transfer both on the upper walls and on the lower walls, as a result from turbulence.

Figure 12 shows the mean Nusselt numbers for each cycle, Nu_m, along the duct length, with four turbulence models. At the entrance, the cyclic mean Nusselt numbers are very high, due to very thin boundary layers at the entrance. Along the flow direction, the cyclic mean Nusselt numbers decrease rapidly in the first three to five cycles, and then arrive gradually at some stable values, which is denoted as the fully developed value, Nu_D. Using the data from RSM model and a least-squares curve fit technique, a correlation has been formulated, which is:

$$\mathrm{Nu}_D = 0.234\,\mathrm{Re}^{0.599}\mathrm{Pr}^{0.333} \tag{41}$$

for $2000 \leqslant \mathrm{Re} \leqslant 20{,}000$.

In contrast, heat transfer of the turbulence flow in parallel flat plates is governed by the Dittus and Boelter equation [20]

$$\mathrm{Nu}_D = 0.023\,\mathrm{Re}^{0.8}\,\mathrm{Pr}^{0.333} \tag{42}$$

Fig. 10 Isotherms in the x-y midplane, $z^* = 0.5$

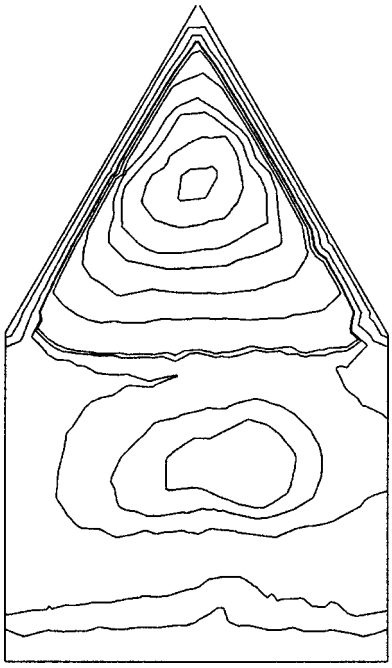

Fig. 11 Isotherms in the *y-z* plane at $x^*=4.5$

The variations of fully developed cyclic mean Nusselt numbers with Re, which is dictated by the above correlation, is depicted in Fig. 13. The Nusselt numbers increase, almost linearly with Re. For comparison, the fully developed Nusselt numbers in parallel flat plates passages [20] are also plotted in Fig. 13. As can be seen, the corrugation results in a 40–60% heat transfer enhancement. This is mainly due to the enhanced momentum transfer in the cross corrugations.

Turbulence. Figure 14 shows the contours of turbulence intensity, u'/u, in the *x-y* plane at $z^*=0.5$ when Re=10,000. The turbulence is almost uniform in the upper corrugation. However, significant variations of turbulence happen near the walls and in the valleys of the lower corrugation, especially on the crests of the valleys. The largest turbulence occurs near the crests of the lower wall, in Zone A, where the lower wall faces the fluid. The second largest turbulence occurs also near the lower walls' crests, but in Zone B, where the wall locates backward the main flow direction. The amount of heat transfer and momentum is mainly dependent upon the level of turbulence that is produced within the duct. The strong turbulence in the lower corrugations is responsible for the intensification of the heat and momentum transfer.

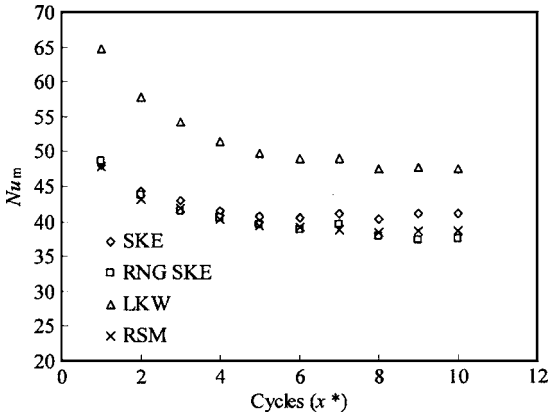

Fig. 12 Distribution of periodic mean Nusselt numbers along flow direction

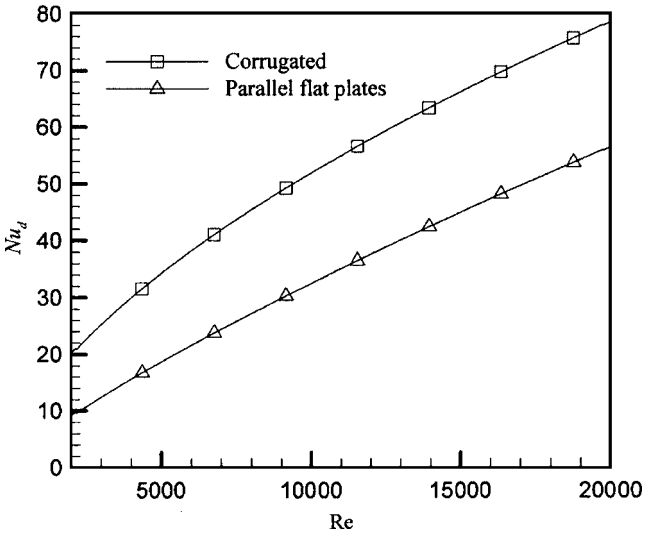

Fig. 13 Comparisons of the fully developed Nusselt numbers for the corrugated duct and parallel flat plates

Conclusions

Three-dimensional turbulence flow and convective heat transfer in the entrance region of a cross corrugated triangular duct which is proposed for a novel membrane module has been studied numerically employing four turbulence models: SKE, RNG-KE, LKW, and RSM. Compared to available experimental data, the RSM seems superior to others during the whole Reynolds range from 2000 to 20,000. The cross-corrugation nature of the duct generates strong turbulence and secondary flows to enhance heat transfer on the duct walls. Compared to a parallel flat plate geometry, the cross-corrugation can obtain a 40 to 60% heat transfer augmentation, however with a penalty of twice the friction pressure drop. In addition, both the friction factor and the heat transfer

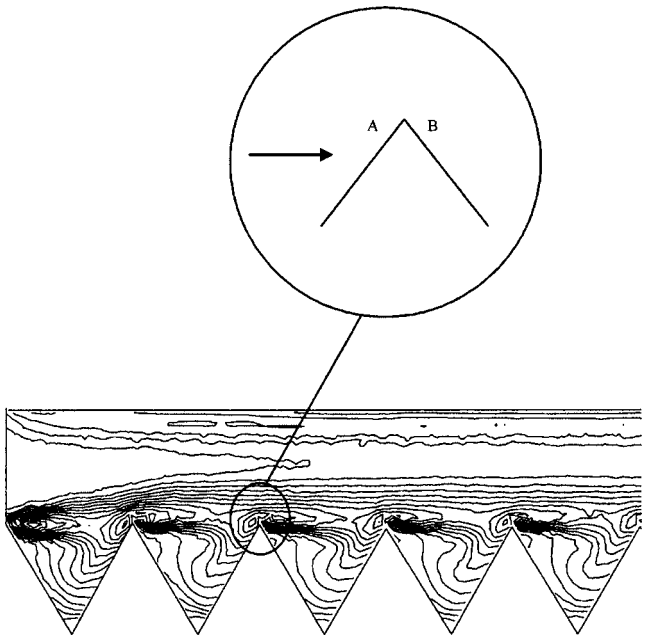

Fig. 14 Contours of turbulence intensity in the *x-y* plane at $z^*=0.5$

exhibit a cyclic manner, and the generated swirls rotate clockwise in the corrugation valleys. The turbulence is almost uniform in the upper corrugation, but has large variations in the lower corrugations and especially near the crests of valleys.

Acknowledgment

This Project 50306005 is supported by National Natural Science Foundation of China.

Nomenclature

A_{ci} = cross-sectional area at inlet or outlet of a cycle, m^2
A_{cyc} = surface area of the channel, m^2
c_p = specific heat, kJ/(kgK)
D_h = hydraulic diameter of the channel, m
f = friction factor
f_D = fully developed cyclic mean friction factor
h = heat transfer coefficient, $kW/(m^2\,K)$
I = turbulent intensity
k = turbulent kinetic energy, m^2/s^2
ℓ = turbulence length scale, m
L_{cyc} = length of a cycle in flow direction, m
Nu = Nusselt number
Nu_D = fully developed cyclic mean Nusselt numbers
p = pressure (Pa)
P = time average pressure (Pa)
Pr = Prandtl Numbers
q = heat flux, W/m^2
Re = Reynolds number,
T = temperature, K
U = time average velocity, m/s
u = velocity, m/s
V_{cyc} = volume of channel, m^3
x, y or z = coordinates, m
y_0 = pitch of the repeated segment of the duct, m
z_0 = width of the repeated segment of the duct, m

Greek Letters

ρ = density, kg/m^3
ν = kinematic viscosity, m^2/s
μ = molecular viscosity, Ns/m^2
τ = shear stress, N/m^2
ω = specific dissipation, s^{-1}
ε = turbulent dissipation rate, m^2/s^3

Superscripts

* = dimensionless
$'$ = fluctuation

Subscripts

0 = inlet
i = inlet
m = mean
o = outlet
t = turbulent
w = wall

References

[1] Zhang, L. Z., and Jiang, Y., 1999, "Heat and Mass Transfer in a Membrane-Based Enthalpy Recovery Ventilator," J. Membr. Sci., **163**, pp. 29–38.
[2] Kistler, K. R., and Cussler, E. L., 2002, "Membrane Modules for Building Ventilation," Chem. Eng. Res. Des., **80**, pp. 53–64.
[3] Zhang, L. Z., and Niu, J. L., 2002, "Effectiveness Correlations for Heat and Moisture Transfer Processes in an Enthalpy Exchanger With Membrane Cores," ASME J. Heat Transfer, **122**, pp. 922–929.
[4] Niu, J. L., and Zhang, L. Z., 2001, "Membrane-Based Enthalpy Exchanger: Material Considerations and Clarification of Moisture Resistance," J. Membr. Sci., **189**, pp. 179–191.
[5] Scott, K., Mahmood, A. J., Jachuck, R. J., and Hu, B., 2000, "Intensified Membrane Filtration With Corrugated Membranes," J. Membr. Sci., **173**, pp. 1–16.
[6] Focke, W. W., 1985, "Asymmetrically Corrugated Plate Heat Exchangers," Int. Commun. Heat Mass Transfer, **12**, pp. 67–77.
[7] Focke, W. W., Zachariades, J., and Olivier, I., 1985, "The Effect of the Corrugation Inclination Angle on the Thermohydraulic Performance of Plate Heat Exchangers," Int. J. Heat Mass Transfer, **28**, pp. 1469–1479.
[8] Ciofalo, M., Stasiek, J., and Collins, M. W., 1996, "Investigation of Flow and Heat Transfer in Corrugated Passages. II. Numerical Simulations," Int. J. Heat Mass Transfer, **39**, pp. 165–192.
[9] Biomerius, H., Hoisken, C., and Mitra, N. K., 1999, "Numerical Investigation of Flow Field and Heat Transfer in Cross-Corrugated Ducts," ASME J. Heat Transfer, **121**, pp. 314–321.
[10] Mehrabian, M. A., and Poulter, R., 2000, "Hydrodynamics and Thermal Characteristics of Corrugated Channels: Computational Approach," Appl. Math. Model., **24**, pp. 343–364.
[11] Scott, K., and Lobato, J., 2003, "Mass Transport in Cross-Corrugated Membranes and the Influence of TiO_2 for Separation Processes," Ind. Eng. Chem. Res., **42**, pp. 5697–5701.
[12] Zimmer, C., Gschwind, P., Gaiser, G., and Kottle, V., 2002, "Comparison of Heat and Mass Transfer in Different Heat Exchanger Geometries with Corrugated Walls," Exp. Therm. Fluid Sci., **26**, pp. 269–273.
[13] Patel, C. V., Rodi, W., and Scheuerer, G., 1984, "Turbulence Models for Near Wall and Low Reynolds Number Flows: A Review," AIAA J., **23**, pp. 1308–1319.
[14] Mompean, G., 1998, "Numerical Simulation of a Turbulent Flow Near a Right-Angled Corner Using the Speziale Nonlinear Model with RNG k-ε Equations," Comput. Fluids, **27**, pp. 847–859.
[15] Li, L. J., Lin, C. X., and Ebadian, M. A., 1998, "Turbulent Mixed Convective Heat Transfer in the Entrance Region of a Curved Pipe with Uniform Wall Temperature," Int. J. Heat Mass Transfer, **41**, pp. 3793–3805.
[16] Jones, R. M., Harvey, A. D., and Acharya, S., 2001, "Two Equation Turbulence Modeling for Impeller Stirred Tanks," ASME J. Fluids Eng., **123**, pp. 640–648.
[17] Song, B., and Amano, R. S., 2000, "Application of Nonlinear k-ω Model to a Turbulent Flow Inside a Sharp U-Bend," Comput. Mech., **26**, pp. 344–351.
[18] Moore, E. M., Shambaugh, R. L., and Papavassiliou, D. V., 2004, "Analysis of Isothermal Annular Jets: Comparison of Computational Fluid Dynamics and Experimental Data," J. Appl. Polym. Sci., **94**, pp. 909–992.
[19] Rokni, M., and Sunden, B., 2003, "Calculation of Turbulent Fluid Flow and Heat Transfer in Ducts by a Full Reynolds Stress Model," Int. J. Numer. Methods Fluids, **42**, pp. 147–162.
[20] Incropera, F. P., and Dewitt, D. P., 1996, *Introduction to Heat Transfer*, Wiley, NY, Chap. 8, p. 392.
[21] Tinaut, F. V., Melgar, A., and Rahman Ali, A. A., 1992, "Correlations for Heat Transfer and Flow Friction Characteristics of Compact Plate-Type Heat Exchangers," Int. J. Heat Mass Transfer, **35**, pp. 1659–1665.
[22] Yuan, Z. X., Tao, W. Q., and Wang, Q. W., 1998, "Numerical Prediction for Laminar Forced Convection Heat Transfer in Parallel-Plate Channels With Stream-Wise-Periodic Rod Disturbances," Int. J. Numer. Methods Fluids, **28**, pp. 1371–1387.

Boundary/Finite Element Modeling of Three-Dimensional Electromagnetic Heating During Microwave Food Processing

Y. Huo
Graduate Research Assistant
ASME Student Member

B. Q. Li[1]
Professor
ASME Fellow

School of Mechanical and Materials Engineering
Washington State University,
Pullman, WA 99164

A three-dimensional 3D finite element-boundary integral formulation is presented for the analysis of the electric and magnetic field distribution, power absorption, and temperature distribution in electrically conductive and dielectric materials. The hybrid finite/boundary method represents an optimal approach for modeling of large-scale electromagnetic-thermal materials processing systems in which the volume ratio of the sample over the entire computational domain is small. To further improve the efficiency, the present formulation also incorporates various efficient solvers designed specifically for the solution of large sparse systems of linear algebraic equations. The resulting algorithm with a compressed storage scheme is considered effective and efficient to meet the demand of 3D large scale electromagnetic/thermal simulations required for processing industries. Examples of 3D electromagnetic and thermal analysis are presented for induction and microwave heating systems. Numerical performance of the computer code is assessed for these systems. Computed results are presented for the electric field distribution, power absorption, and temperature distribution in a food load thermally treated in an industrial pilot scale microwave oven designed for food sterilization. Computed temperature distribution in a food package compares well with experimental measurements taken using an infrared image camera. [DOI: 10.1115/1.2035112]

1 Introduction

Electromagnetic and thermal phenomena occur in processing systems for both electrically conducting and nonconducting materials. For the former, induction heating is often applied. Heating by induction is based on the Faraday principle of induction, by which the joule heating results from the self-interaction of eddy currents, which in turn originate from the free moving electrons. For the latter, however, the heating stems from the excitation of dipoles at their resonant frequency. In the case of microwave heating of dielectric materials such as ceramics or foods, the electromagnetic energy is generated in the materials when the applied field frequency resonates with that of the dipoles.

Many different numerical schemes have been used to predict the electromagnetic fields in microwave systems. These schemes are based on either the time domain (TD) formulation or the frequency domain (FD) formulation. Numerical techniques to solve the time domain Maxwell's equations include the finite difference time-domain (FDTD) method [1], the finite element time-domain (FETD) method [2], and the transmission-line matrix (TLM) method [3]. To obtain the required electromagnetic heating distribution using a time-domain method, time matching is required to reach a time harmonic, quasisteady state. With the frequency domain formulation, however, the solution of the time-harmonic field distribution is obtained at once without time matching. This makes the frequency-domain approach very attractive for electromagnetic heating applications because heating by an oscillating electric field comes from the time-averaged value over a frequency period.

Turning to the study of microwave processing of foods, Zhang et al. [4] have recently presented a finite element model for electromagnetic field distribution and thermal conduction in a food package loaded in a household microwave. For the three-dimensional (3D) electromagnetic field calculations, edge elements are often used to satisfy the requirement that either the electric field or magnetic field is to be divergence-free [5]. For a majority of microwave heating problems, the size ratio of a sample to a microwave cavity is very small, often less than 10%, and thus one efficient algorithm may be developed using a hybrid finite and boundary element method (FE/BE). By this hybrid method, the finite elements are used for the domain of the food package, and the boundary elements for the free space. The usefulness of this strategy has been demonstrated in the case of 2D or axisymmetric induction heating problems where the entire free space (including the radiation boundary condition at infinity) is discretized by the use of boundary elements [6–8]. It is generally recognized that the advantage of a hybrid finite/boundary element method is even more pronounced when employed for 3D applications where the heating absorber occupies a small portion of the entire computational space.

This paper presents a hybrid finite element and boundary element method for the modeling of 3D electromagnetic field distribution and/or power absorption as well as temperature distribution in induction and/or microwave processing systems, with the latter emphasizing the application in microwave thermal food sterilization. The very basic idea of the FE/BE coupling for the microwave field distribution, without heating, was demonstrated by Paulsen et al. [9]. Their algorithm, however, used node-based finite element interpolations, which are now well known to produce spurious results, owing to the failure to enforce the divergence-free constraint [8]. While various approaches may be applied to alleviate the problem, our present approach uses the edge elements to satisfy the divergence-free condition so as to eliminate the spurious solution. Consequently, both the finite element and boundary element interpolations are edge based to ensure the FE/BE compatibility. While possible in theory, the numerical implementation of an edge-based FE/BE method does not appear

[1]Email: li@mme.wsu.edu

Paper presented at the National Heat Transfer Conference, 2004. Contributed by the Heat Transfer Division of ASME for publication in the JOURNAL OF HEAT TRANSFER. Manuscript received: November 24, 2004; final manuscript received: May 16, 2005. Review conducted by: Surya Pratap Vanka.

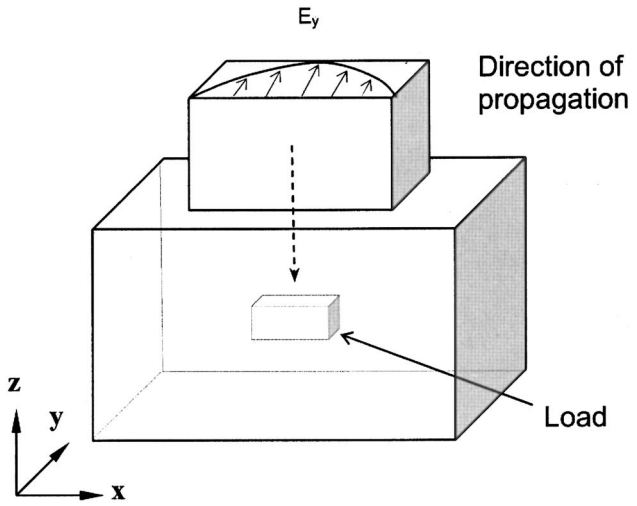

Fig. 1 Schematic representation of MW Applicator System

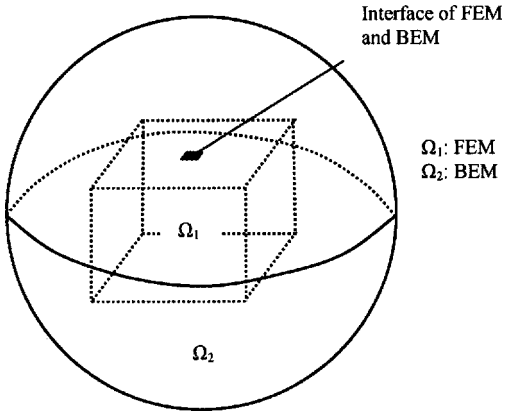

Fig. 2 Schematic representation of the coupling of the finite element and boundary element

to have been attempted for the solution of electromagnetic-heating problems in general 3D geometries. In what follows, the hybrid finite/boundary element formulation of 3D Maxwell equations is presented. Both iterative and direct coupling schemes are discussed, along with their advantages and disadvantages. The mesh distribution for the hybrid finite/boundary simulation of microwave distribution in industrial food processing systems is also discussed, along with the computational performance of the hybrid method and the finite element method. Finally, calculated results are compared with the experimentally measured data in a microwave heating system for food processing.

2 Problem Statement

The microwave (MW) applicator system to be analyzed is an industrial MW food processing unit and is schematically shown in Fig. 1, where two rectangular waveguides (one feed waveguide and one multimode cavity) are coupled to each other. The top part of the MW applicator system is the standard WR-975 waveguide with $a_x=248$ mm and $b_y=124$ mm; the bottom part is the oversized waveguide of $a_x=496$ mm, $b_y=248$ mm, and $c_z=100$ mm. The piece of food load with the dimension $140\times100\times30$ (mm^3) is fixed at the center of the multimode cavity. An electric field of the TE_{10} mode with a frequency 915 MHz is applied at the top of the feed waveguide to produce the dissipated electrical power that is absorbed by the food load, for which the initial and environmental temperatures are set at the room temperature.

The whole simulation procedure can be divided into two steps. First, the electrical and magnetic fields inside the waveguide are simulated by using the finite element method (FEM) or finite/boundary element (FE/BE) method and the dissipated power distribution in the food piece is then derived from the electromagnetic field distribution. Second, the temperature distribution inside the food piece is computed using the FEM by setting the dissipated power as the heating source term and applying the radiation boundary condition to the surface of the food piece. The differential form of Maxwell's equations is the most widely used representation for electromagnetic boundary-value problems. Maxwell's equations are coupled partial differential equations, which have more than one unknown variable. Therefore, the vector wave equation derived from the Maxwell equations combined with the energy equation is taken as the governing equations for the microwave heating problems under consideration

$$\nabla\times\frac{1}{\mu_r}\nabla\times\mathbf{E}-\omega^2\mu\varepsilon_c\mathbf{E}=-j\omega\mu\mathbf{J}_i \tag{1}$$

$$\rho C_p\frac{\partial T}{\partial t}=\nabla\cdot\kappa\nabla T+Q \tag{2}$$

In the above, $\mathbf{J}_i$ is an impressed or source current, and $\varepsilon_c(=\varepsilon-j\sigma/\omega)$ results from the combination of the induced current ($\sigma\mathbf{E}$) and displacement current ($j\omega\mathbf{D}$). It is noted that Eq. (1) is written in phasor notation [10]. With reference to Fig. 1, the appropriate boundary conditions for these governing equations are stated below

$$\hat{\mathbf{n}}\times\mathbf{E}=0 \quad \in \boldsymbol{\Omega}_1\cap\boldsymbol{\Omega}_3 \quad \text{for PEC boundary condition} \tag{3}$$

$$-\frac{1}{\mu_{r1}}\hat{\mathbf{n}}_1\times\nabla\times\mathbf{E}_1=-\mathbf{U}_1=\mathbf{U}_2=\hat{\mathbf{n}}_2\times\nabla\times\mathbf{E}_2 \quad \in \boldsymbol{\Omega}_1\cap\boldsymbol{\Omega}_2 \tag{4}$$

$$-\kappa\hat{\mathbf{n}}\cdot\nabla T=\varepsilon\sigma_s(T^4-T_\infty^4) \quad \in \boldsymbol{\Omega}_4\cap\boldsymbol{\Omega}_5 \tag{5}$$

where Ω_1, Ω_2, and Ω_3 are the FEM domain, (BEM) domain, and the PEC (perfect electrically conducting) domain respectively; Ω_4 and Ω_5 represent the food piece and the environment, respectively. $\hat{\mathbf{n}}_1$ is the outnormal from the FE region, and $\hat{\mathbf{n}}_2$ the outnormal from the BE region.

3 Method of Solution

The 3D electromagnetic field may be solved using the edge finite element method [11]. The edge-based elements are necessary to satisfy the divergence-free constraint, $\nabla\cdot\mathbf{E}=0$ [3]. However, the huge sparse matrix produced by the FEM appears to be a major setback to finding an efficient numerical solution to a large scale problem. Our experience shows that this remains true even with various efficient solvers designed specifically for the solution of a large sparse system of linear algebraic equations to improve the computational efficiency. To alleviate the disadvantage of the finite element method, a hybrid finite element-boundary method is employed instead. Using this approach, finite elements are used in the food package where power density is needed and material properties may be a function of temperature, while boundary elements are used elsewhere. The FEM and the BEM are coupled through the interface boundary conditions. This idea is shown in Fig. 2.

3.1 Finite Element Formulation. To develop a finite element formulation in the food package, the wave equation is integrated with respect to a vector testing function $\delta\mathbf{E}$.

$$\int\int\int_V \delta\mathbf{E}\left(\nabla\times\frac{1}{\mu_r}\nabla\times\mathbf{E}-\omega^2\mu\varepsilon_c\mathbf{E}\right)dV=$$

$$-\int\int\int_V j\omega\mu\mathbf{J}_i\cdot\delta\mathbf{E}dV \tag{6}$$

Integration by parts gives rise to the surface integral term

$$\int\int\int_V\frac{1}{\mu_r}\nabla\times\mathbf{E}\cdot\nabla\times\delta\mathbf{E}dV-\int\int\int_V\omega^2\mu\varepsilon_c\delta\mathbf{E}\cdot\mathbf{E}dV$$

$$=\oiint_S\frac{1}{\mu_r}(\delta\mathbf{E}\times\nabla\times\mathbf{E})\mathbf{n}dS-\int\int\int_V j\omega\mu\delta\mathbf{E}\cdot\mathbf{J}_i dV \tag{7}$$

Making use of the vector identity

$$(\delta\mathbf{E}\times\nabla\times\mathbf{E})\hat{\mathbf{n}}=-(\hat{\mathbf{n}}\times\nabla\times\mathbf{E})\delta\mathbf{E} \tag{8}$$

and also the boundary conditions, the final integral formulation is obtained

$$\int\int\int_V\left(\frac{1}{\mu_r}\nabla\times\mathbf{E}\cdot\nabla\times\delta\mathbf{E}-\omega^2\mu\varepsilon_c\delta\mathbf{E}\cdot\mathbf{E}\right)dV$$

$$=-\oiint_S[\delta\mathbf{E}\cdot\mathbf{U}]dS-\int\int\int_V j\omega\mu\delta\mathbf{E}\cdot\mathbf{J}_r dV \tag{9}$$

With appropriate finite element discretization and necessary elemental calculations followed by assembly, one has the matrix representation of Eq. (9)

$$[\mathbf{K}]\{\mathbf{E}\}+[\mathbf{B}]\{\mathbf{U}\}=\{\mathbf{F}\} \tag{10}$$

where the matrix elements are calculated using the following expressions:

$$K_{ij}=\int\int\int_V\left(\frac{1}{\mu_r}\nabla\times\mathbf{N}_i\cdot\nabla\times\mathbf{N}_j-\omega^2\mu\varepsilon_c\mathbf{N}_i\cdot\mathbf{N}_j\right)dV$$

$$B_{ij}=\oiint_S\mathbf{N}_i\cdot\mathbf{S}_j dS$$

$$F_i=-\int\int\int_V j\varpi\mu\mathbf{N}_\mathbf{i}\cdot\mathbf{J}_\mathbf{i}dV$$

Note that here $\mathbf{N}_i$ and $\mathbf{S}_i$ are edge-based vector shape functions and their derivatives [8].

3.2 Boundary Element Formulation Using the Dyadic Green Function. The basic idea of the hybrid FE/BE method was introduced for the study of electromagnetics by Silvester and Hsieh [12] and McDonald and Wexler [13] for solving exterior or unbounded field problems. Later, the method was applied to solve two- and three-dimensional antenna and scattering problems. Here, it is applied to solving the electromagnetic field in a microwave system, and the formulation is based on Green's theorem involving the dyadic Green's function

$$\int\int\int_V(\mathbf{E}\cdot\nabla\times\nabla\times\bar{\bar{G}}-\bar{\bar{G}}\cdot\nabla\times\nabla\times\mathbf{E})dV$$

$$=\oiint_S(\bar{\bar{G}}\times\nabla\times\mathbf{E}-\mathbf{E}\times\nabla\times\bar{\bar{G}})\hat{\mathbf{n}}dS$$

$$=\oiint_S[(\hat{\mathbf{n}}\times\mathbf{E})\cdot\nabla\times\bar{\bar{G}}+(\hat{\mathbf{n}}\times\nabla\times\mathbf{E})\bar{\bar{G}}]dS \tag{11}$$

Now, substituting into the above equation the following wave equations and the equations for the dyadic Green's function:

$$\nabla\times\nabla\times\mathbf{E}-k_0^2\mathbf{E}=-j\omega\mu\mathbf{J}_i \tag{12}$$

$$\nabla\times\nabla\times\bar{\bar{G}}-k_0^2\bar{\bar{G}}=\bar{\bar{I}}\delta(\mathbf{r}-\mathbf{r}') \tag{13}$$

and carrying out the necessary integration, one has

$$\mathbf{E}(\mathbf{r})=-jk_0Z_0\int\int\int_V\mathbf{J}(\mathbf{r}')\bar{\bar{G}}_0(\mathbf{r},\mathbf{r}')dV'-\oiint_S\{[\hat{\mathbf{n}}'\times\mathbf{E}(\mathbf{r}')]$$

$$\times[\nabla'\bar{\bar{G}}_0(\mathbf{r},\mathbf{r}')]+[\hat{\mathbf{n}}'\times\nabla'\times\mathbf{E}(\mathbf{r}')]\bar{\bar{G}}_0(\mathbf{r},\mathbf{r}')\}dS' \tag{14}$$

The surface's unit normal direction points outward from the region Ω_2. In Eq. (14) the first term on the right-hand side is the field radiated by **J** in the free-space environment, thus denoted as $\mathbf{E}_{\text{inc}}$. With the following relation:

$$\nabla'\times\bar{\bar{G}}=\nabla'G_0(\mathbf{r},\mathbf{r}')\times\bar{\bar{I}} \tag{15}$$

and the surface divergence theorem, Eq. (14) can be further simplified as

$$\mathbf{E}(\mathbf{r})=\mathbf{E}_{\text{inc}}(\mathbf{r})-\oiint_S\{\hat{\mathbf{n}}'\times\mathbf{E}(\mathbf{r}')\times\nabla'G(\mathbf{r},\mathbf{r}')$$

$$+[\hat{\mathbf{n}}'\times\nabla'\times\mathbf{E}(\mathbf{r}')]G(\mathbf{r},\mathbf{r}')\}dS(\mathbf{r}')-\frac{1}{k_0^2}\oiint_S\nabla G(\mathbf{r},\mathbf{r}')$$

$$\times\nabla'[\hat{\mathbf{n}}'\times\nabla\times\mathbf{E}(\mathbf{r}')]dS(\mathbf{r}') \tag{16}$$

Taking the cross product of Eq. (16) with surface normal $\hat{\mathbf{n}}$ yields

$$\hat{\mathbf{n}}\times\mathbf{E}(\mathbf{r})=\hat{\mathbf{n}}\times\mathbf{E}_{\text{inc}}(\mathbf{r})-\hat{\mathbf{n}}\times\oiint_S\{\hat{\mathbf{n}}'\times\mathbf{E}(\mathbf{r}')\times\nabla'G(\mathbf{r},\mathbf{r}')$$

$$+[\hat{\mathbf{n}}'\times\nabla'\times\mathbf{E}(\mathbf{r}')]G(\mathbf{r},\mathbf{r}')\}dS(\mathbf{r}')-\frac{1}{k_0^2}\hat{\mathbf{n}}$$

$$\times\oiint_S\nabla G(\mathbf{r},\mathbf{r}')\nabla'[\hat{\mathbf{n}}'\times\nabla\times\mathbf{E}(\mathbf{r}')]dS(\mathbf{r}') \tag{17}$$

After the BE discretization using edge boundary elements, followed by calculations at the element level, Eq. (17) may be represented in the following matrix form:

$$[\mathbf{B}^{\mathbf{ss}}]\{\mathbf{E}^{\mathbf{s}}\}=\{\mathbf{b}^{\mathbf{s}}\}-\sum_{\mathbf{t}}^{\mathbf{M_t}}[\mathbf{P}^{\mathbf{st}}]\{\mathbf{E}^{\mathbf{t}}\}-\sum_{\mathbf{t}}^{\mathbf{M_t}}[\mathbf{Q}^{\mathbf{st}}]\{\mathbf{U}^{\mathbf{t}}\} \tag{18}$$

where the matrix elements are calculated by

$$[\mathbf{B}^{\mathbf{ss}}]=-\int\int_{S^s}\{\mathbf{N}^s\}\{\mathbf{S}^s\}^T dS(\mathbf{r})$$

$$\{\mathbf{b}^{\mathbf{s}}\}=\int\int_{S^s}\{\mathbf{S}^s\}\mathbf{E}_{\text{inc}}(\mathbf{r})dS(\mathbf{r})$$

$$[\mathbf{P}^{\mathbf{st}}]=\int\int_{S^s}\left[\{\mathbf{S}^s\}\cdot\iint_{S^t}\{\mathbf{S}^t\}^T\times\nabla'G(\mathbf{r},\mathbf{r}')dS(\mathbf{r}')\right]dS(\mathbf{r})$$

$$[\mathbf{Q}^{\mathbf{st}}]=\int\int_{S^s}\left[\{\mathbf{S}^s\}\cdot\int\int_{S^t}\{\mathbf{S}^t\}^T G(\mathbf{r},\mathbf{r}')dS(\mathbf{r}')\right]dS(\mathbf{r})$$

$$-k^{-2}\int\int_{S^s}\left[\{\nabla\cdot\mathbf{S}^s\}\int\int_{S^t}\nabla'\cdot\{\mathbf{S}^t\}^T G(\mathbf{r},\mathbf{r}')dS(\mathbf{r}')\right]dS(\mathbf{r})$$

With some matrix algebra, Eq. (18) is written more conveniently in the following form:

$$[\mathbf{B}_2]\{\mathbf{U}_2\} = \{\mathbf{F}_2\} + [\mathbf{K}_2]\{\mathbf{E}_2\} \tag{19}$$

where $\mathbf{B}_2$ is the boundary element matrix associated with the unknowns.

3.3 Coupling of Boundary and Finite Elements. The boundary and finite element formulations for the solution of electric field distribution are coupled through the interface conditions along the boundary of Ω_1 and the boundary of Ω_2,

$$\frac{1}{\mu_{r1}}\hat{\mathbf{n}} \times \nabla \times \mathbf{E}_1 = \frac{1}{\mu_{r2}}\hat{\mathbf{n}} \times \nabla \times \mathbf{E}_2 \quad \text{and } \hat{\mathbf{n}} \times \mathbf{E}_1 = \hat{\mathbf{n}} \times \mathbf{E}_2$$

There are two ways to obtain a coupled solution of Eqs. (10) and (19) with the use of the above interface conditions. One way is to use direct coupling, by which the entire boundary element region is treated as a macroelement, and the boundary element global matrix is then incorporated into Eq. (10). This approach works efficiently for 2D and moderately sized 3D problems [14]. However, it becomes inefficient for large 3D problems such as the one under consideration because it substantially increases the resultant edge finite element matrix bandwidth and hence the CPU times. Another approach is iterative [10,14]. By this approach, Eq. (19) is solved for $\{\mathbf{U}_2\}$ with an assumed $\{\mathbf{E}_2\}$ on the interface. The standard (LU) decomposition for complex matrix can be used for the solution. Then $\{\mathbf{E}_1\}$ is solved using Eq. (10) with known $\{\mathbf{U}_2\}$. The convergence on $|\{\mathbf{E}_2\}-\{\mathbf{E}_1\}| < \varepsilon$, where ε is the convergence criterion, is checked. If convergence is not achieved, $\{\mathbf{E}_2\}=\{\mathbf{E}_1\}$ along the interface is used to predict an updated $\{\mathbf{U}_2\}$ using Eq. (19) and then $\{\mathbf{E}_1\}$ is updated using Eq. (10). The process is repeated until the convergence is achieved.

It is worth noting here that for either of the two approaches, the matrix $\mathbf{B}_2$ requires a LU decomposition only once and the decomposed matrices are stored in the memory for subsequent back substitutions when needed. In the case of the iterative procedure, this means that subsequent iteration between FE and BE requires only a back substitution procedure, thereby leading to a significant increase in computational speed.

3.4 Finite Element Solution of Temperature Distribution. The energy equation is solved using the Galerkin finite element method. The finite element solution of Eq. (2) is well known and has been documented in some of our publications [1,2]. Here the volumetric heating source $Q(Q=P_d=0.5\sigma_e \mathbf{E}\cdot\mathbf{E}^*)$ is calculated from the hybrid FE/BE element solution described above. Using the Galerkin finite element formulation, the matrix equation for the temperature field takes the following form:

$$\mathbf{N_T}\cdot\dot{\mathbf{T}} + \mathbf{L_T}\cdot\mathbf{T} = \mathbf{G_T} \tag{20}$$

where the coefficients are calculated by

$$\mathbf{N_T} = \int\int\int_v \rho C_p \theta\theta^T dV$$

$$\mathbf{L_T} = \int\int\int_v \kappa \nabla\,\theta\cdot\nabla\theta^T dV$$

$$\mathbf{G_T} = \int\int\int Q\theta dV + \int\int q_T \theta dS$$

It is noted that for the temperature calculations, the standard node-based shape functions are used.

3.5 One-Way Versus Mutual Coupling for Microwave and Thermal Calculations. For electromagnetic-thermal problems, two types of coupling exist, depending upon weather or not the dielectric property is a function of temperature. If the dielectric property is temperature independent, then the electric field needs to be calculated once and the same power density is used for the time-matching solution of the temperature field during heating. On the other hand, if the property is a function of the local temperature, the mutual coupling of the electric and thermal fields is required. In this case, an iterative procedure is required for the electromagnetic and thermal calculations. In the present implementation for mutual coupling, the iterative procedure involves updating the electromagnetic field using the FE/BE and the temperature field using the FEM until convergence on both fields is achieved. This is done at every time step during transient thermal calculations. This is permissible since the relaxation time for electric field is several orders of magnitude shorter than that for the thermal field [10].

4 Numerical Solution of a FE Sparse Matrix

Since a large sparse matrix is formed during the finite element discretization, it is necessary to develop efficient computer methods for solving the sparse systems of linear algebraic equations. A large number of research articles and books have been published in the field [15–18]. The methods may be classified into iterative and direct categories. Although iterative methods have the advantage of saving computer storage, they are difficult to converge to an accurate order and are, in general, slower than the direct methods, which require more memory but no iteration. A rule of thumb is that whenever memory is affordable a direct method should be used. Of course, a blind use of the direct method without carefully accounting for sparseness will lead to a disaster for finite element computations. There are four distinct phases (ordering, storage allocation, factorization, and triangular solution) in the direct method for the solution of a sparse matrix arising from finite element formulations. Ordering is the key, and unfortunately, is theoretically proven to be heuristic. In the present study, available ordering algorithms are compared in order to reduce either computer storage or computer execution time or a combination of the two. First, the band scheme and the skyline scheme are the simplest methods and can be implemented relatively easily, but they are not necessarily efficient. Second, it is attractive to select the general sparse methods that only exploit the nonzero elements in the triangular factor **L** of **A**. Those methods have common characteristics, such as symbolic factorization, general sparse symmetric factorization, and general sparse symmetric solution. Three ordering schemes in this category, quote minimum degree, multiple minimum degree, and nested dissection, are studied. The other ordering methods, quotient tree and one-way methods, are also applied, and their performances are compared with the other three. All these schemes have been incorporated in our code and extensive testing has been made. The comparative numerical study suggests that the multiple minimum degree is the most efficient method for solving the electromagnetic problems presently under consideration.

5 Result and Discussion

The computational algorithm developed above is capable of predicting the electric field distribution, the magnetic field distribution, the energy distribution, and the temperature and fluid flow distribution. For computational electromagnetics, the mesh plays an important role. Thus, it is necessary to study the mesh distribution effect; in particular, it is necessary to study the mesh density along the propagation of the electromagnetic field. Figure 3 shows the electric field distribution corresponding to different cell sizes in the propagation direction, which illustrates that the relative error of the computed results becomes very small when c_z/λ is close to 10%. The above testing suggests that at least ten cells per wavelength (λ) are required to obtain accurate results. Although the rule of selecting the mesh is obtained from the finite element method, it appears to be applicable to the boundary element method as well. The final mesh used for the numerical computations is determined such that any further refinement of the mesh produces an error smaller than 0.1% (relative to the final mesh).

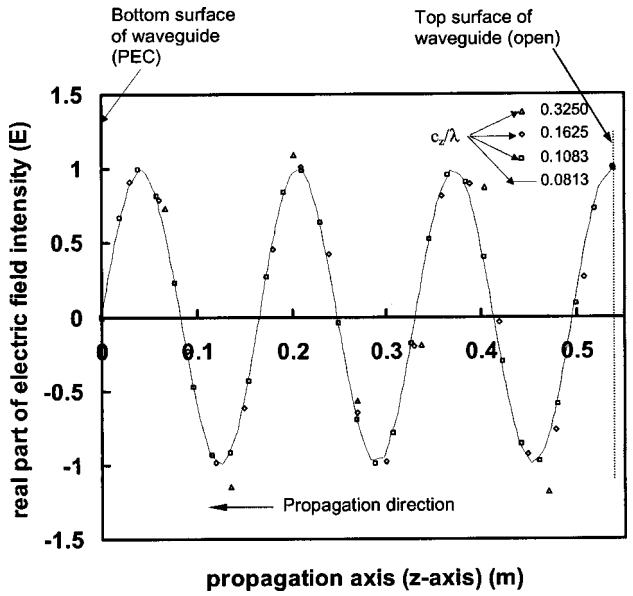

Fig. 3 Electric distribution along the center line of the standard WR-975 waveguide along the propagation direction with dominant mode TE_{10} computed by using meshes of different cell sizes (c_z) in the propagation direction (z direction)

5.1 Validation of the Computer Model. Since computer codes for the temperature calculations have already been validated in the previous papers [7,8], they are omitted here. However, the computer code for the simulation of the electromagnetic fields needs to be checked against the available analytic solution before being applied for the MW applicator. The testing is done for two cases: (1) benchmark testing in a standard waveguide and (2) electromagnetic field distribution in the semi-infinite metallic slab.

First, the electric field distribution in the standard MW-975 waveguide is considered. The waveguide is filled with air, and the length of the waveguide in the propagation direction is $1.25\lambda_z$. The TE_{10} model from a device is launched at the entrance of the waveguide, and then the waves undergo reflection at the bottom surface. The reflected waves interfere with the incident waves to distribute the electrical field within the internal space. The analytical expression for the electric field is written as follows:

$$\mathbf{E}_y = \mathbf{E}_0^+ e^{-jk_z Z} + \mathbf{E}_0^- e^{+jk_z Z} \tag{21}$$

Figure 4 shows the 3D view of the distribution of the electric field ($\mathbf{E}_y$ component) and the module of the electric field $|\mathbf{E}|$ distribution. Figure 5 compares the numerically calculated electric field distribution along the central axis in the propagation direction with the analytic solution given by Eq. (21). The computed result from the FE/BE model is only plotted for the FE region because the surface integral is used in the BE region. Excellent agreement exists between the numerical and analytical solutions, thereby validating the present FE/BE formulation. Though not shown, the same results were obtained using the FEM only.

As another comparison, a semi-infinite metallic slab shown as the inset in Fig. 6 is considered. The analytical equation for the electric and magnetic fields can be easily obtained

$$\mathbf{E}_y = \mathbf{E}_s e^{-\gamma_m y}, \quad \mathbf{H}_y = \mathbf{H}_s e^{-\gamma_m y} \tag{22}$$

The coefficients are calculated by

$$\gamma_m = \alpha(1+j) \text{ and } \delta = \frac{1}{\alpha} = \sqrt{\frac{2}{\sigma_m \omega \mu}}$$

where δ is the skin depth over which the electric and magnetic fields drop to $1/e$ of their value at the surface. Figure 6 depicts that the numerical results from the FE/BE or FEM agree with the analytical results very well, thereby validating once again the FE/BE and/or FE implementations.

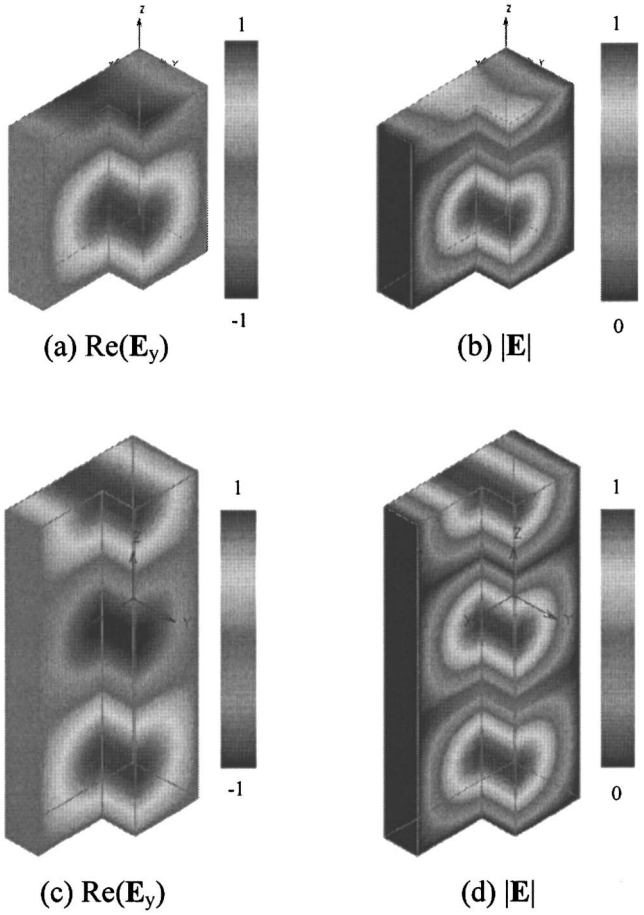

Fig. 4 3D view of the distribution of the dominant electric field ($\mathbf{E}_y$ component) and the module of the electric field ($\mathbf{E}$) in the standard WR-975 waveguide with $c_z = 1.25\lambda_z$ (red color represents the higher normal of the electric field/positive E_y component; blue color represents the lower normal of the electric field/negative E_y component)

5.2 Simulation of Industrial Microwave Food Processing. The computer model, tested above, is now applied to simulate the electromagnetic and thermal phenomena during microwave food processing in an industrial microwave applicator (see Fig. 1). The food package has a permittivity ε' of 47.45 and a loss factor ε'' of 38.55. It is placed at the center of the bottom cavity. The incident dominant mode TE_{10} has a frequency of 915 MHz, and the environmental temperature is 300 K. The materials properties used for the temperature calculations are given in Table 2.

The food load is a dielectric material and thus has no conductive losses. The polarization losses of the electromagnetic field are the main mechanism for heating. For microwave heating problems, the FE/BE model has a decisive advantage in terms of memory storage, as shown in Table 1. Note that here the FEM memory requirement is based on the multiple minimum degree ordering scheme for the direct solver, and the FE/BE memory requirement includes both FE and BE matrices. The calculations show that the solution of the FE/BE method is almost twice as fast as that of FEM. For microwave food processing simulations, the boundary element matrix $\mathbf{B}_2$ is LU decomposed once and the decomposed matrix is saved in the memory. This is because the dielectric property of the air is taken as constant. This feature is of crucial importance for the mutually coupled microwave-thermal problems. Numerical simulations show that for these mutually

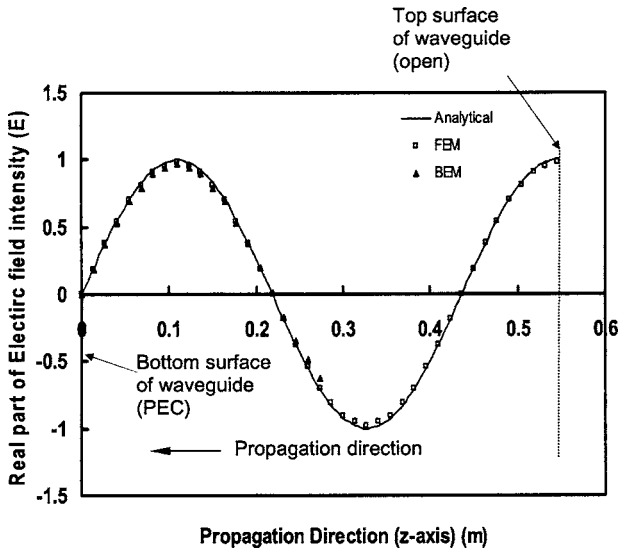

Fig. 5 Dominant electric field (E_y component) distribution along the center line of the standard WR-975 waveguide in the propagation direction (negative *z* direction) obtained from the analytical, FEM and FE/BE solutions. The result by using FE/BE has only the bottom half part which is the FEM part.

coupled problems, the hybrid FE/BE method is significantly more efficient than the FEM, owing to the fact that the matrix $\mathbf{B}_2$ is a constant matrix and needs to be decomposed only once for the entire time matching calculations. Lacking specific data, the test was done by assuming that the dielectric property is a linear function of temperature. In contrast, if the FEM is used for the electromagnetic calculations, the solution of the mutually coupled problems would require the (LD) decomposition of the large FE matrix at every iteration over every time step, which is computationally very expensive.

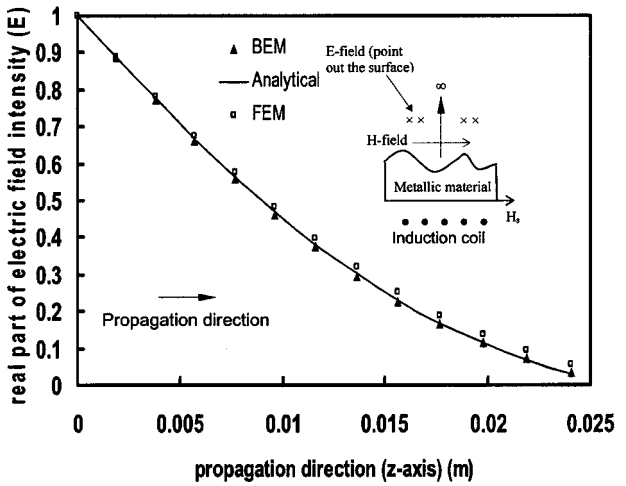

Fig. 6 Electric field distribution (E_y component) for the semi-infinite metallic slab and part of induction heating coil

Table 1 Edge number and memory requirement for solving the same problem by using FEM and FE/BE

Methods	Number of Edges (or unknowns)	Memory requirement
FEM	299619	5.38 GB
FE/BE	22098	2.93 GB

Table 2 Thermophysical properties used for calculations

Parameters of food package	Value
K (W/m-K)	0.631
C_P (J/kg-K)	4200
ρ (kg/m^3)	1000
Emisivity ε_0 (for air case)	0.3
T_∞	300.0 K

Calculations using the FE/BE-FE model described above have been performed for many different cases. One case (see Table 2) is selected here. Figure 7 shows the $|\mathbf{E}|$ distribution in the MW applicator from different angles of view. Figure 7(*b*) shows the view cut through the middle plane (the *y*-*z* plane) in the *x* direction, while Fig. 7(*c*) shows the plane-cut view in the middle plane (the *x*-*z* plane) in the *y* direction. This feature of the electromagnetic field distribution is expected from the principle of electromagnetism [2]. Figure 8 compares the numerical and experimental results for the temperature distribution on the top surface of the food

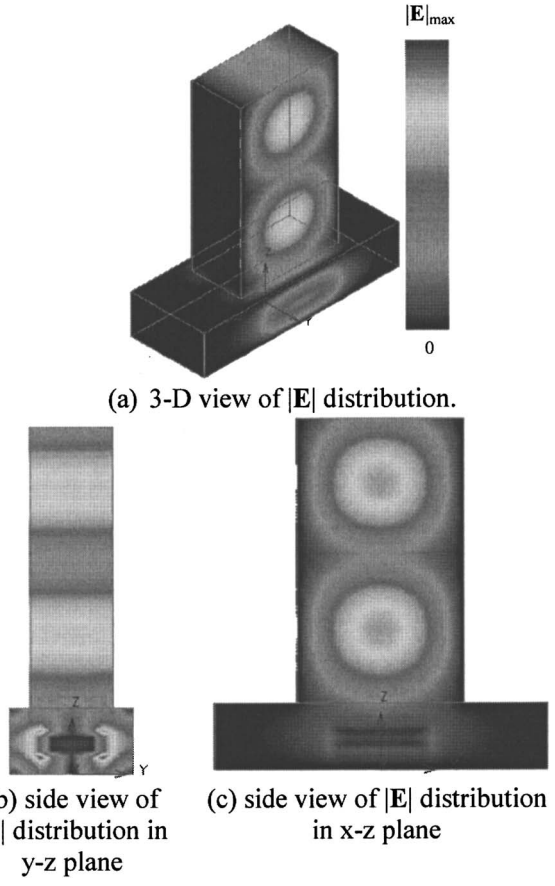

Fig. 7 Electric field ($|\mathbf{E}|$) distribution in the industrial MW applicator loaded with a food package (140×100×30 mm). The top part of the MW applicator is the standard MR-975 feeding waveguide with the height of 522.9 mm and the bottom cavity dimensions (496×192×100 mm^3).

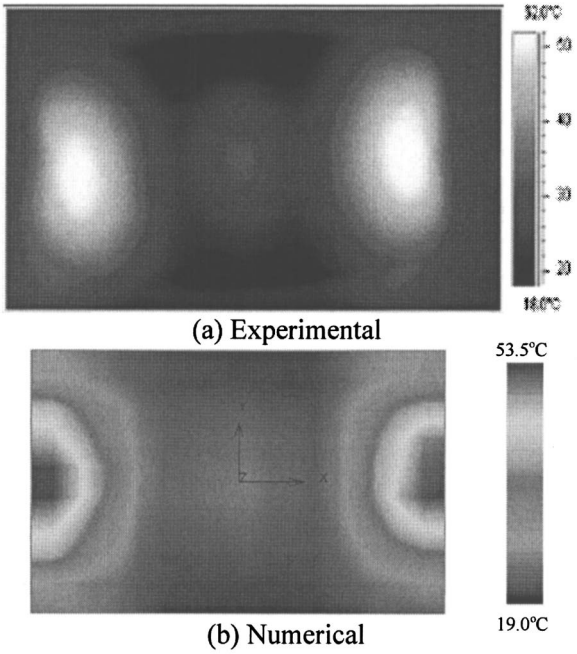

Fig. 8 Temperature distribution over the top surface of a food gel slab package (in open air): (*a*) experimental measurements obtained using the infrared camera and (*b*) numerical data calculated using the coupled FE/BE electromagnetic and FE thermal model

load in the microwave applicator. The temperature measurements were obtained using an infrared camera. Examination of the figure shows that two hotspots appear around two sides of the boundary in the *x* direction and a small lower hotspot appears at the center of *x-y* plane's top surface. It is noted here that the color codes are different because two different types of software are used to plot the experimental and numerical data. The highest and lowest temperatures in the numerical and experimental results are also given in Fig. 8. Clearly, the numerical results agree very well with the experimental measurements. The heating pattern is attributed to the fact that the microwaves undergo multiple reflections on the wall and the food load when the wave is launched into the bottom cavity, which is a multimode applicator. It is thought that this multimode applicator is configured with two major kinds of resonant frequencies. One frequency induces the high hotspots on two sides of the boundary, while the other yielded the lower hotspot at the center of the food package.

6 Conclusion

This paper has presented an integrated 3D model for electromagnetic and thermal analysis of the microwave heating process for packaged foods in a pilot microwave applicator of an industrial scale. The edge-based hybrid finite/boundary element method was used for the solution of the Maxwell equations in frequency domain, while the node-based finite element method is used to model the thermal transport in microwave-heated food packages. The hybrid finite element/boundary element method uses an iterative procedure, which allows a reduction of bandwidth of the resultant matrix. Further testing confirms that about ten elements per wavelength are needed to obtain an accurate solution for microwave processing problems. Numerical simulations were made for food packages under irradiation by microwaves in air. Experiments were conducted in an industrial microwave applicator, and measured temperature distributions compare well with the numerical results obtained from the integrated 3D electromagnetic/thermal model. The hybrid FE/BE method has significant memory and excution time advantages over the more common all FE method for microwave heating calculations. The method is computationally efficient for the electromagnetic-thermal problems during microwave thermal processing.

Acknowledgments

Support of this work is provided by WSU IMPAC. Additional support is provided by NASA (Grant No. NNM04AA17G.

Nomenclature

$\mathbf{D}$ = Electric flux density
$\mathbf{E}$ = Electric field
$\mathbf{H}$ = Magnetic density
f = Frequency
$\mathbf{J}$ = Current density
k = Wave number
T = Temperature
C_p = Specific heat
Q = Heat source
G = Green's function
$\bar{\bar{G}}$ = Dyadic Green's functions

Greek

ρ = Density
δ = Electrical skin depth ($\delta = \sqrt{2/\omega\mu_0\sigma}$)
ω = Angular frequency
σ = Electrical conductivity
Ω = Computational domain
ε_0 = Permittivity of free surface
μ_0 = Magnetic permeability of free space
κ = Thermal conductivity
σ_s = Stefan-Boltzmann constant
ε = Emissivity
$\hat{\mathbf{n}}$ = Outnormal

Subscripts

1 = FEM domain
2 = BEM domain
3 = PEC domain
4 = Food piece
5 = Environment
i = the ith point

Subscripts

* = Complex conjugate

References

[1] Yee, K. S., 1966, "Numerical Solution of Initial Boundary Value Problem Involving Maxwell's Equations in Isotropic Media," IEEE Trans. Antennas Propag., **AP14**, pp. 302–307.
[2] Dibben, D. C., and Metaxas, A. C., 1994, "Finite Element Time Domain Analysis of Multimode Applicators Using Edge Elements," J. Microwave Power Electromagn. Energy **29**, pp. 242–251.
[3] Johns, P. B., and Beurle, R. L., 1971, "Numerical Solution of Two-Dimensional Scattering Problems Using a Transmission Line Matrix," Proc. Inst. Electr. Eng., **118**, pp. 1203–1208.
[4] Zhang, H., Datta, A. K., Taub, I. A., and Doona, C., 2001, "Electromagnetics, Heat Transfer, and Thermokinetics in Microwave Sterilization," AIChE J. **47**, pp. 1957–1968.
[5] Nedelec, J. C., 1980, "Mixed Finite Elements in R^3," Numer. Mech. **35**, pp 315–341.
[6] Song, S. P., and Li, B. Q., 1998, "A Boundary/Finite Element Analysis of Magnetic Levitation Systems in Normal and Micro Gravity: Surface Deformation and Thermal Phenomena," ASME J. Heat Transfer, **120**, pp. 491–503.
[7] Huo, Y., and Li, B. Q., 2004, "Three-Dimensional Marangoni Convection in Electrostatically Positioned Droplets Under Microgravity," Int. J. Heat Mass Transfer, **47**, pp. 3533–3547.
[8] Jin, J., 2002, *The Finite Element Method in Electromagnetics*, Wiley-Interscience, NY.
[9] Paulsen, K. D., Lynch, D. R., and Strohbehn, J. W., 1988, "Three-Dimensional Finite, Boundary and Hybrid Element Solutions of the Maxwell Equations for Lossy Dielectric Media," IEEE Trans. Microwave Theory Tech., **36**(4), pp. 682–693.
[10] Song, S. P., and Li, B. Q., 1999, "Coupled Boundary/Finite Element Computation of Magnetically and Electrostatically Levitated Droplets," Int. J. Numer.

Methods Eng., **44**(8), pp. 1055–1077.
[11] Akrappu, R., Li, B. Q., and Tang, J., 2004, "Finite Element Modeling of Microwave Thermal Processing," in *Multiphase Phenomena and CFD Modeling and Simulation in Materials Processing*, edited by L. Nastec and B. Q. Li, TMS, Warrendale, PA.
[12] Silvester, P. P., and Hsieh, M. S., 1971, "Finite Element Solution of 2-Dimensional Exterior Field Problems," IEE Proc.: Optoelectron. **118**, pp. 1743–1747.
[13] McDonald, B. H., and Wexler, A., 1972, "Finite Element Solution of Unbounded Field Problems," IEEE Trans. Microwave Theory Tech. **MTT-20**, pp. 841–847.
[14] Li, B. Q., Cui, X. and Song, S. P., "A Galerkin Boundary Element Formulation of Surface Radiation Problems," Int. J. Boundary Element Analysis, to be published.
[15] George, A., and Liu, J. W., 1981, "*Computer Solution of Large Sparse Positive Definite Systems*," Prentice-Hall, Englewood, NJ.
[16] Liu, J. W. H., 1992, "The Multifrontal Method for Sparse Matrix Solution: Theory and Practice," SIAM Rev., **34**(1), pp. 82–109.
[17] Ng, E. G., and Raghavan, P., 1999, "Performance of Greedy Ordering Heuristics for Sparse Cholesky Factorization," SIAM J. Matrix Anal. Appl. **20**(4), pp. 902–914.
[18] Davis, T. A., 2004, "A Column Pre-ordering Strategy for the Unsymmetric-Pattern Multifrontal Method," ACM Trans. Math. Softw., **30**(2), pp 165–195.

Improved Two-Temperature Model and Its Application in Ultrashort Laser Heating of Metal Films

Lan Jiang

Hai-Lung Tsai[1]

Laser-Based Manufacturing Laboratory,
Department of Mechanical and Aerospace Engineering,
University of Missouri-Rolla,
Rolla, MO 65409

The two-temperature model has been widely used to predict the electron and phonon temperature distributions in ultrashort laser processing of metals. However, estimations of some important thermal and optical properties in the existing two-temperature model are limited to low laser fluences in which the electron temperatures are much lower than the Fermi temperature. This paper extends the existing two-temperature model to high electron temperatures by using full-run quantum treatments to calculate the significantly varying properties, including the electron heat capacity, electron relaxation time, electron conductivity, reflectivity, and absorption coefficient. The proposed model predicts the damage thresholds more accurately than the existing model for gold films when compared with published experimental results. [DOI: 10.1115/1.2035113]

Keywords: Ultrashort Laser, Quantum Mechanics, Metal Thin Film, Two-Temperature Model

1 Introduction

In the past two decades, the ultrashort (typically <10 ps) laser heating of metals and its nonequilibrium energy transport have been very active research topics [1–12]. Nonequilibrium between electrons and phonons is already significant on the picoscecond time order, in which the electron temperature can be much higher than that of the lattice [1,5,7]. The energy transport process in ultrafast laser heating of thin films consists of two stages [1,5–9]. The first stage is the absorption of the laser energy through photon-electron interactions within the ultrashort pulse duration. It takes a few femtoseconds for electrons to reestablish the Fermi distribution. This characteristic time scale, the mean time for electrons to restore their states, is called the electron relaxation time. In spite of nonequilibrium states of the electrons within this characteristic time, the temperature of the electrons is still numerically valid in the limit when the pulse duration is much longer than the electron relaxation time, which is proved by a model using the full Boltzmann transport theory [1]. Within the duration of a single ultrashort pulse, the change of lattice temperature is generally negligible.

The second stage is the energy distribution to the lattice through electron-phonon interactions, typically on the order of tens of picoseconds. Although the electron-phonon collision time may be comparable to the electron-electron collision time, it takes much longer to transfer energy from free electrons to phonons, because the phonon mass is much greater than the electron mass. The characteristic time for the free electrons and the lattice to reach thermal equilibrium is called the thermalization time. In this process, a phonon temperature is used to characterize the Bose distribution.

This two-temperature concept described above was validated by many experiments [3,7,10–14]. Accordingly, the two-temperature model is widely used for the ultrashort laser processing of metals [5–9,15,16]. Especially, Qiu and Tien [5–7] and Qiu et al. [8] group has made excellent theoretical and experimental contributions in this area. However, in the existing two-temperature model, the estimations of the following important properties are limited to temperatures that are much lower than the Fermi temperature T_F that is measured to be 5.9×10^4K for gold [5–8]

- Electron heat capacity $C_e=\gamma T_e$ [7] where T_e is the electron temperature and γ is the electron heat capacity constant. This estimation is limited to $0<T_e<0.1\ T_F$ [17].
- Electron relaxation time $\tau_e=3m_e/(\pi^2 n_e k_B^2 T_e)/k(T_e)$ where m_e is the nonrelativistic mass of a free electron; n_e is the density of the free electron, which is 5.9×10^{22} cm^{-3} for gold; and k_B is the Boltzmann constant [7]. This estimation is based on $C_e=\gamma T_e$ and therefore limited to $0<T_e<0.1\ T_F$ [5,17,18].
- Electron heat conductivity $k_e=(T_e/T_l)k_{\mathrm{eq}}(T_l)$ where k_{eq} is the electron heat conductivity when the electrons and phonons are in thermal equilibrium; and T_l is the lattice temperature [7]. This estimation can be derived and is limited to $T_D<T_e<0.1\ T_F$ where T_D is the Debye temperature of the phonon [17].
- Reflectivity $\Delta T_e/(\Delta T_e)_{\max}\cong\Delta R/(\Delta R)_{\max}$ [8] where R is the reflectivity. This estimation is limited to $300\ \mathrm{K}<T_e<700\ \mathrm{K}$ [8]. Further, $(\Delta T_e)_{\max}$ and $(\Delta R)_{\max}$ are unknown before the estimation.

The aforementioned estimations are limited to low temperatures relative to the Fermi temperature [17]. However, at a fluence near or above the threshold fluence, the electron temperature in metals heated by an ultrashort laser pulse can be comparable to the Fermi temperature. Hence, the two-temperature model is suitable only for low fluences and cannot be used to correctly predict the damage threshold in which the electron temperatures are much higher than $0.1\ T_F$.

This paper extends the existing estimations of optical and thermal properties to high electron temperatures by the following improvements: (1) using the Fermi distribution, the heat capacity of free electrons is calculated; (2) the free electron relaxation time and electron conductivity are determined by using a quantum model derived from the Boltzmann transport equation for dense

[1]Corresponding author; e-mail address: tsai@umr.edu

Contributed by the Heat Transfer Division of ASME for publication in the JOURNAL OF HEAT TRANSFER. Manuscript received: September 21, 2004; final manuscript received: June 7, 2005. Review conducted by: C. P. Grigoropoulos.

plasma; and (3) the free electron heating and interband transition are both taken into account using a modified Drude model with quantum adjustments to calculate the reflectivity and the absorption coefficient. The proposed two-temperature model is employed to calculate the heating process of thin gold films until melting occurs, which is assumed to be the initiation of damage. The predicted damage threshold fluences for 200 nm gold film using the proposed model are in good agreement with published experimental data. The damage threshold fluence as a function of pulse duration is also studied.

2 Theory

2.1 Two-Temperature Model. This paper considers the laser pulse duration in 140 fs–100 ps that are much longer than the electron relaxation time (a few femtoseconds). Hence, the electron temperature, characterized by the Fermi distribution, can be employed [1]. In this study, the laser beam diameter (tens to hundreds of micrometers) is much greater than the optical penetration depth (tens to hundreds of nanometers) and electron penetration depth (tens to hundreds of nanometers) in the nanoscale-thickness thin films and, hence, a one-dimensional model is accurate enough to describe the physical phenomena. The two-temperature model is given below

$$C_e(T_e)\frac{\partial T_e}{\partial t} = \nabla[k_e(T_e)\,\nabla\,T_e] - G(T_e - T_l) + S(z,t) \tag{1}$$

$$C_l(T_l)\frac{\partial T_l}{\partial t} = G(T_e - T_l) \tag{2}$$

where S represents the laser source term, C_l is the lattice heat capacity, and G is the electron-lattice coupling factor estimated by [5]

$$G = \frac{\pi^2 m_e n_e c_s^2}{6\tau(T_e)T_e} \tag{3}$$

where c_s is the speed of sound in bulk material calculated by

$$c_s = \sqrt{\frac{B}{\rho_m}} \tag{4}$$

where B is the bulk modulus and ρ_m is the density.

2.2 Free Electron Heat Capacity. In a wide range of electron temperatures, the full-run quantum treatment should be used to calculate the free electron heat capacity. The average number of electrons $\langle n_k\rangle$ in energy state ε_k obeys the following Fermi distribution:

$$\langle n_k\rangle = \frac{1}{e^{\beta(T_e)[\varepsilon_k-\mu(T_e)]}+1} \tag{5}$$

where $\beta(T_e)=1/k_BT_e(t,z)$ and μ is the chemical potential. For free electron gas, the chemical potential can be calculated by [17]

$$\mu(n_e,T_e) = \varepsilon_F(n_e)\left[1 - \frac{\pi^2}{12}\left(\frac{k_BT_e(t,z)}{\varepsilon_F(n_e)}\right)^2 + \frac{\pi^2}{80}\left(\frac{k_BT_e(t,z)}{\varepsilon_F(n_e)}\right)^4\right] \tag{6}$$

where the higher order terms are neglected, z is the depth from the thin film surface, and ε_F is the Fermi energy. Strictly speaking, Eq. (6) is valid for free electrons in equilibrium states only. The free electrons could be disturbed from the Fermi-Dirac distribution by a femtosecond laser pulse. However, when the pulse duration is much longer than the free electron relaxation time, Eq. (6) is still a good approximation, which is similar to the treatment for the electron temperature in this condition [1]. The Fermi energy is determined by [17]

$$\varepsilon_F = \left(\frac{(hc)^2}{8m_ec^2}\right)\left(\frac{3}{\pi}\right)^{2/3} n_e^{2/3} \tag{7}$$

where c is the speed of light in vacuum. The average kinetic energy per electron in J, $\langle\varepsilon\rangle$, is calculated by

$$\langle\varepsilon\rangle = \frac{\sum_k \langle n_k\rangle\varepsilon_k}{N_e} = \frac{\int_0^\infty \frac{1}{e^{\beta(T_e)[\varepsilon-\mu(T_e)]}+1}\rho(\varepsilon)\varepsilon d\varepsilon}{\int_0^\infty \frac{1}{e^{\beta(T_e)[\varepsilon-\mu(T_e)]}+1}\rho(\varepsilon)d\varepsilon} \tag{8}$$

where ε is the kinetic energy of a free electron, N_e is the total number of free electrons, and $\rho(\varepsilon)$ is the density of states given by

$$\rho(\varepsilon) = \frac{8\sqrt{2}\pi m_e^{3/2}}{h^3}\sqrt{\varepsilon} \tag{9}$$

where h is the Planck constant. The heat capacity can be determined by

$$C_e(T_e) = n_e\left(\frac{\partial\langle\varepsilon\rangle}{\partial T_e}\right)_V \tag{10}$$

where V is the volume. In $0<T_e<0.1\ T_F$, Eqs. (5)–(10) can be simplified to the following expression [17]:

$$C_e(T_e) = \frac{\pi^2 n_e}{2}\left(\frac{k_BT_e}{\varepsilon_F}\right)k_B \equiv \gamma T_e \tag{11}$$

where γ is the electron heat capacity constant. Equation (11) has been widely employed in the two-temperature model [5–9]. For comparison purpose, the average kinetic energy and specific heat of an ideal electron gas are given below

$$\langle\varepsilon\rangle = \frac{3}{2}k_BT_e, \quad C_e = \frac{3}{2}n_ek_B \tag{12}$$

2.3 Free Electron Heat Conductivity and Relaxation Time. The free electron heat conductivity is expressed by the following Drude theory of metals [17]:

$$k_e(T_e) = \frac{1}{3}\nu_e^2(T_e)\tau_e(T_e)C_e(T_e) \tag{13}$$

where ν_e^2 is the mean square of electron speed. In this study, ν_e^2 and C_e are determined directly by the Fermi distribution based on Eqs. (5)–(10). In Eq. (13), the scattering effects are indirectly considered through the calculation of the free electron relaxation time. In $T_D<T_e<0.1\ T_F$ and using the values of ν_e^2 and C_e for an ideal gas, Eq. (13) can be simplified to $\tau_e=3m_e/(\pi^2n_ek_B^2T_e)k(T_e)$ [17] that is used in Ref. [7].

In this study, by considering metals as dense plasma [1,17,19,21–23], the free electron relaxation time is calculated as follows by a quantum treatment derived from the Boltzmann transport equation [20,21]:

$$\tau_e(t,z) = \frac{3\sqrt{m_e}(k_BT_e(t,z))^{3/2}}{2\sqrt{2}\pi(Z^*)^2n_ee^4\ln\Lambda}\{1+\exp[-\mu(T_e)/k_BT_e(t,z)]\}F_{1/2} \tag{14}$$

where e is the electron charge, Z^* is the ionization state and is one for gold, $F_{1/2}$ is the Fermi integral, and $\ln\Lambda$ is the Coulomb logarithm determined by

$$\ln\Lambda = \frac{1}{2}\ln\left[1+\left(\frac{b_{\max}}{b_{\min}}\right)^2\right] \tag{15}$$

where the maximum ($b_{\max}$) and minimum ($b_{\min}$) collision parameters are given by

$$b_{\max} = \frac{(k_B T/m_e)^{1/2}}{\max(\omega, \omega_p)}, \quad b_{\min} = \max\left(\frac{Z^* e^2}{k_B T}, \frac{\hbar}{(m_e k_B T)^{1/2}}\right) \tag{16}$$

where $\hbar = h/2\pi$ is the reduced Planck constant, ω is the laser frequency, and ω_p is the plasma frequency defined by

$$\omega_p = \sqrt{\frac{n_e e^2}{m_e \epsilon_0}} \tag{17}$$

where ϵ_0 is the electrical permittivity of free space.

2.4 Optical Properties. A critical task is to determine the laser source term in Eq. (1). A general expression for laser intensity (W/cm^2) I inside the bulk material for both nonlinear and linear absorptions is [21,22]

$$I(t,z) = \frac{2}{\sqrt{\pi/\ln 2}} \frac{J}{t_p} [1 - R(t)] \exp\left[- (4 \ln 2)\left(\frac{t}{t_p}\right)^2 - \int_0^z \alpha(t,z) dz \right] \tag{18}$$

where J is the laser fluence in J/cm^2, t_p is the pulse duration, R is the reflectivity, and $\alpha(t,z)$ is the absorption coefficient. If the absorption coefficient is assumed to be a constant, using the definition that optical penetration depth $\delta = 1/\alpha$ the laser source term (W/cm^{-3}) is simplified to the following expression commonly used in the existing model [5–8]:

$$S(t,z) = \frac{0.94J}{t_p \delta} [1 - R(t)] \exp\left[- 2.77\left(\frac{t}{t_p}\right)^2 - \frac{z}{\delta} \right] \tag{19}$$

Rethfeld et al. have demonstrated that the ultrashort laser-metal interaction can be well described by laser-plasma interactions [1]. According to the Drude model for free electrons ϵ the electrical permittivity (dielectric function) of metals modeled as a plasma, is expressed as [23]

$$\mathbf{c}(t,z) = \epsilon_1(t,z) + i\epsilon_2(t,z) = 1 + \left(\frac{n_e e^2}{m_e \epsilon_0}\right)\left(\frac{-\tau_e^2(t,z) + i\tau_e(t,z)/\omega}{1 + \omega^2 \tau_e^2(t,z)}\right)$$

$$= 1 + \omega_p^2 \left(\frac{-\tau_e^2(t,z) + i\tau_e(t,z)/\omega}{1 + \omega^2 \tau_e^2(t,z)}\right) \tag{20}$$

Equation (20) shows how the plasma frequency in Eq. (17) is defined.

The relationship between the complex refractive index $\mathbf{f}$ and the complex electrical permittivity is given by

$$\left(\frac{\mathbf{c}}{\mathbf{v}}\right) = \mathbf{f} = (f_1 + i f_2) = \sqrt{\boldsymbol{\epsilon}} = \sqrt{\epsilon_1 + i\epsilon_2} \tag{21}$$

where $\mathbf{c}$ is the velocity of light in vacuum, $\mathbf{v}$ is the velocity of light in the material, f_1 is the normal refractive index, and f_2 is the extinction coefficient. Thus, the f_1 and f_2 functions can be derived as

$$f_1(t,z) = \sqrt{\frac{\epsilon_1(t,z) + \sqrt{\epsilon_1^2(t,z) + \epsilon_2^2(t,z)}}{2}},$$

$$f_2(t,z) = \sqrt{\frac{-\epsilon_1(t,z) + \sqrt{\epsilon_1^2(t,z) + \epsilon_2^2(t,z)}}{2}} \tag{22}$$

The reflectivity and the absorption coefficient of the metal are determined by the following Fresnel expression:

$$R(t) = \frac{[f_1(t,0) - 1]^2 + f_2^2(t,0)}{[f_1(t,0) + 1]^2 + f_2^2(t,0)}, \quad \alpha(t,z) = \frac{2\omega f_2(t,z)}{c} = \frac{4\pi f_2(t,z)}{\lambda} \tag{23}$$

where λ is the wavelength of the laser.

However, the Drude model for metals, Eq. (20), does not consider the interband transition and the Fermi distribution. For gold, the d-band transition plays a critical role in the optical properties [4,14]. In d-band transition, electrons jump from the top of the d band to the unoccupied states near the Fermi level in the conduction band (p band). For noble metals like gold, the contribution of interband absorption to optical properties can be directly added to the Drude model, Eq. (20), for electrical permittivity [25]. Experiments have shown that the transient reflectivity of gold films is directly related to the change in the occupation number of electrons near the Fermi energy [14]. The change in occupied state distributions near the Fermi level caused by electron heating is called the Fermi distribution smearing [14]. Eesley estimated the distribution of occupied electronic states near the Fermi energy by [14]

$$\rho_F = \frac{1}{1 + \exp\{[h\nu - (\varepsilon_F - \varepsilon_d)]/k_B T_e\}} \tag{24}$$

where ν is the laser frequency; $(\varepsilon_F - \varepsilon_d) = 2.38$ eV for gold [4] is the difference between the Fermi energy and the d-band energy ε_d. It is seen the absorption of photon energy $h\nu$ is directly affected by the d-band transition. The smearing of the electron distribution is given by

$$\Delta\rho_F = \rho_F(h\nu, T_e) - \rho_F(h\nu, T_0) \tag{25}$$

which is linearly proportional to the imaginary component of the electrical permittivity in Eq. (20) [4]

$$\frac{\Delta\epsilon_2}{\epsilon_2} = \frac{\Delta\rho_F}{\rho_F} \tag{26}$$

where T_0 is the room temperature [4]. After adding $\Delta\epsilon_2$ to ϵ_2 in Eq. (20), the reflectivity and the absorption coefficient with the consideration of d-band transition can be determined by Eq. (23).

2.5 Phonon Heat Capacity. The above discussion addresses the temperature dependent properties of electrons. Similarly, the phonon heat capacity in Eq. (2) is also temperature dependent which can be calculated by the well-known quantum treatment, the Debye model [24] in which the average kinetic energy of phonons $\langle \varepsilon_p \rangle$ is calculated by [24]

$$\langle \varepsilon_p \rangle = \int_0^{\nu_{\max}} \frac{6\pi h}{n_a c_s^3} \frac{\nu^3}{e^{h\nu/kT_l} - 1} d\nu \tag{27}$$

where n_a is the phonon number density and $\nu_{\max}$ is the maximum frequency of phonons calculated by

$$\nu_{\max} = \left(\frac{3}{4\pi}\right)^{1/3} \frac{c_s}{a} \tag{28}$$

where a is the average interatomic spacing, $a = (V/N)^{1/3} = (n_a)^{-1/3}$. The molar heat capacity of phonons can be calculated by

$$C_l(T_l) = 2n_a \left(\frac{\partial \langle \varepsilon_p \rangle}{\partial T_l}\right)_V \tag{29}$$

where N_A is the Avogadro constant. The factor of 2 appears in Eq. (29) is used to account for both the kinetic energy and potential energy that are statistically equal in an ideal-lattice metal.

The two equations Eqs. (1) and (2) are solved by a fully implicit schedule with iterations at each time step for temperature-dependent thermal properties until convergence is achieved. Different grid sizes and time step sizes are employed to assure the final results are consistent.

3 Results and Discussion

3.1 Heat Capacity. First, some general discussions are presented about the heat capacities of free electrons and phonons in certain temperature ranges. Figure 1(a) demonstrates the significant differences in average kinetic energy of free electrons between the quantum treatment using Eqs. (5)–(10) and the ideal gas approximation using Eq. (12) for gold. At 300 K, the average kinetic energies of free electrons predicted by the quantum treat-

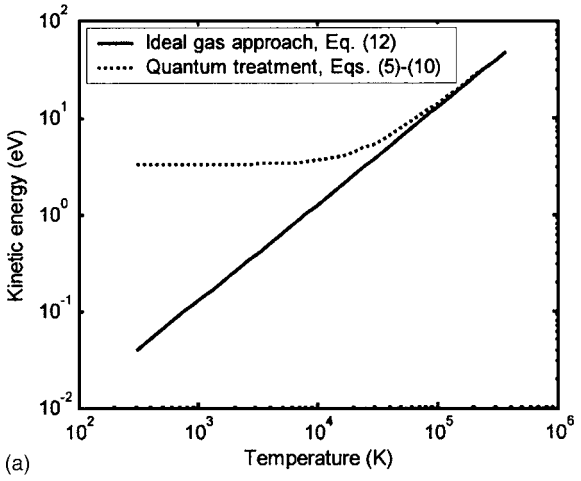

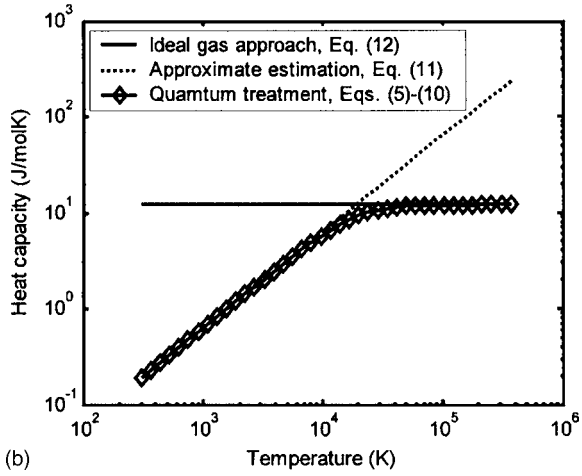

Fig. 1 The differences between different treatments for gold: (*a*) average free electron kinetic energy in electronvolts and (*b*) molar free electron specific heat

ment and classical approach are 3.3 and 0.039 eV, respectively, and they are different by about two orders of magnitude. It is seen only at temperatures much higher than the Fermi temperature (5.9×10^4 K for gold), the classical approach of Eq. (12) is valid. Figure 1(*b*) shows the significant differences between the ideal gas approach using Eq. (12), the approximation using Eq. (11), and the quantum treatment using Eqs. (5)–(10) for electron specific heat per mole. Equation (11) for $T_e \ll T_F$ and Eq. (12) for $T_e \gg T_F$ have been discussed for femtosecond laser ablation of metals [26] and yet the full-run quantum using Eq. (5)–(10) was not used in their work. At temperatures much lower than the Fermi temperature, the results by quantum treatment overlap with the approximations using Eq. (11) that is widely employed in the two-temperature model [5–8]. This implies when $T_e \ll T_F$, Eqs. (5)–(10) can be simplified to Eq. (11). Figure 1 clearly shows the necessity of quantum treatment for free electrons in the ultrashort laser-metal interaction.

On the other hand, the variation of gold phonon heat capacity in [300 K, 1337.33 K] calculated by the Debye model is insignificant, as shown in Fig. 2. In [300 K, 1337.33 K] for gold phonons, the molar phonon heat capacity predicted by the quantum treatment (the Debye model) is similar to that predicted by the classical estimation (the Law of Dulong and Petit) that states the molar heat capacity of metals is about $3R_u$, where R_u is the universal gas constant [24]. In fact, this is expected as the Debye temperature (the quantum characteristic temperature of phonons) of gold is 165 K that is low as compared to the phonon temperature. Hence,

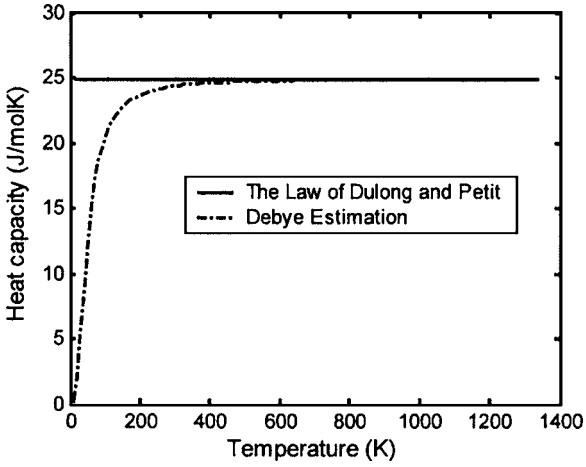

Fig. 2 Molar phonon specific heat predicted by different approaches

the lattice heat capacity of gold in the calculation can be reasonably considered as a constant. Note the gold heat capacity is the sum of the free electron heat capacity and phonon heat capacity.

3.2 Fermi Distribution Smearing. Figure 3 shows the smearing of electron distributions as a function of temperature at

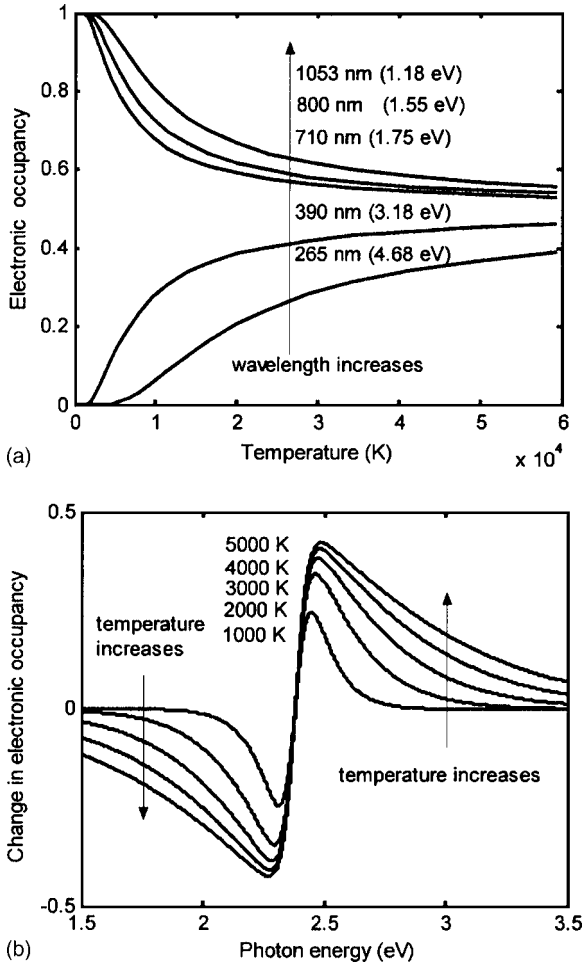

Fig. 3 Distribution of occupied electronic states near the Fermi energy: (*a*) electronic occupy and (*b*) change in electronic occupancy

different laser wavelengths in which T_0 is assumed to be 300 K. When the photon energy for a given wavelength, for example, 1.18 eV (1053 nm), is smaller than the difference between the Fermi energy and the *d*-band energy, $(\varepsilon_F - \varepsilon_d) = 2.38$ eV for gold, Fig. 3(*a*). This is true for all lasers with wavelengths above about 522 nm. On the other hand, when the photon energy, for example, 3.18 eV (390 nm), is higher than $(\varepsilon_F - \varepsilon_d)$, the Fermi distribution of occupied states increases in the heating process, which in turn increases the electron-phonon coupling. For both cases, as the electron temperature increases, the Fermi distribution of occupied states approaches a constant 0.5. Figure 3(*b*) shows the change in electronic occupancy as a function of laser wavelength. The merge of different curves near the 2.38 eV photon energy confirms the discussion given above.

3.3 Damage Threshold Fluence. This study calculates a 140 fs, 1053 nm laser heating of 200 nm gold film by using both the existing two-temperature model [5–8] and our proposed model. For this condition, the experimental threshold fluence is 0.43 ± 0.04 J/cm^2 [27]. By assuming the damage starts when the maximum lattice temperature reaches the melting temperature, 1337.33 K for gold, our model gives 0.45 J/cm^2 for the threshold fluence, while the existing two-temperature model gives 0.75 J/cm^2.

At 0.45 J/cm^2, the temperature distributions of the electrons and the lattice predicted by the proposed model are shown in Fig. 4. As shown in the figure, the electron temperature can reach as high as 2.12×10^4 K which is well beyond the electron temperature range $(0 < T_e < 0.1\ T_F)$. Thus, in the existing model [5–8], the simplified estimations of electron heat capacity, electron heat conductivity, electron relaxation time, and reflectivity, as mentioned earlier, may not be adequate.

3.4 Comparisons Between the Existing Model and the Proposed Model. At 0.05 J/cm^2, a low laser fluence with respect to the threshold fluence, the calculated results for a 200 nm gold film by the existing model and the proposed model are very similar in both the electron temperatures and phonon temperatures, as shown in Fig. 5. It is seen the highest electron temperature 3347 K predicted by the proposed model, is within the low electron temperature range for free electrons. In low fluences, the similarities between results from the existing model and the proposed models are expected, because the full-run quantum treatment can be simplified to the existing model for low electron temperatures. The slight difference between the predictions of the two models is mainly caused by the different treatments in reflectivity. In the existing model, reflectivity estimation $\Delta T_e/(\Delta T_e)_{\max} \cong \Delta R/(\Delta R)_{\max}$ is limited to $300\ \text{K} < T_e < 700$ K that is much lower than the highest electron temperature 3347 K, under 0.05 J/cm^2.

On the other hand, at 0.2 J/cm^2, a fluence comparable to the threshold fluence, significant differences between the two models are observed in Fig. 6. This confirms the need to estimate the thermal and optical properties with quantum treatments for the ultrashort laser heating of metals at fluences comparable to the threshold fluence.

3.5 Effect of Pulse Duration. This study also investigates the effect of pulse duration on the damage threshold. As shown in Fig. 7, the proposed model significantly increases the prediction accuracy of the damage thresholds compared with the existing model. At the wavelength of 1053 nm, the damage thresholds of 200 nm film predicted by the proposed model are almost independent of the pulse duration in 140 fs–100 ps, which is confirmed by the experimental data [27]. As shown in Fig. 7, the predicted trend of the damage thresholds by our proposed model can be roughly divided into two ranges: 140 fs–10 ps and 10 ps–100 ps with the turning point around 10 ps. It is expected for the threshold fluence to increase with the increase of the pulse duration in 10 ps–100 ps. However, the properties of the 200 nm thin film are quite different

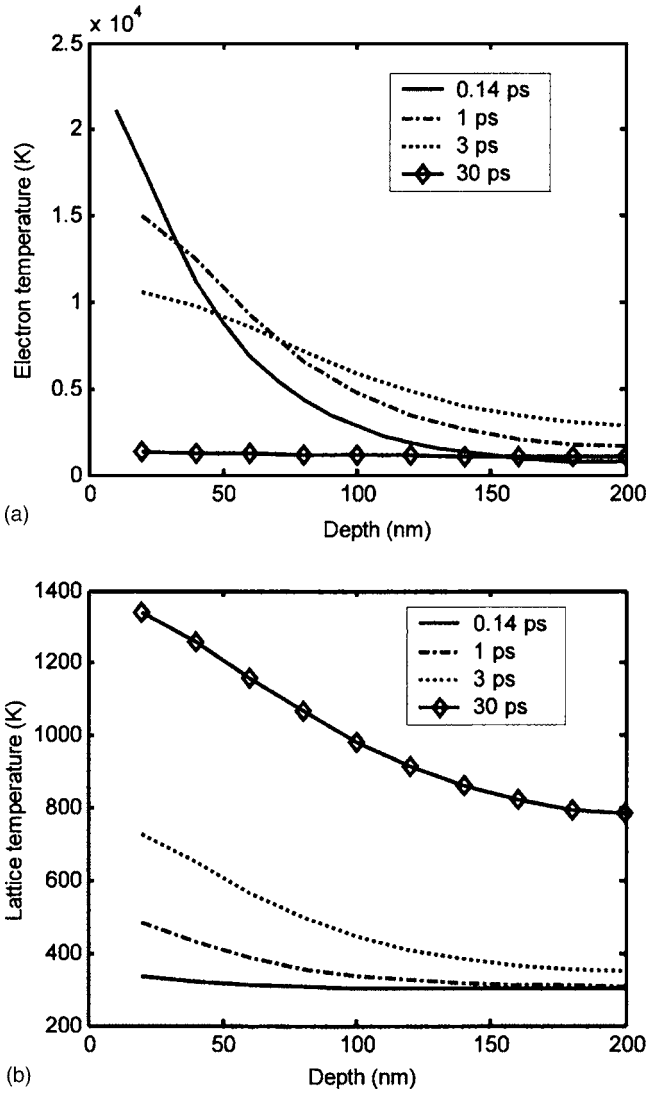

Fig. 4 (*a*) electron temperature distribution and (*b*) lattice temperature distribution at different times predicted by the proposed model for a 200 nm gold film irradiated by a 140 fs, 1053 nm pulse at 0.45 J/cm^2

with its bulk material when the thin film thickness is comparable to the optical penetration depth. In 140 fs–10 ps, for the 200 nm thin film, the shorter pulse duration leads to(1) the higher electron temperature and hence higher heat conductivity, causing a more uniform temperature distribution in the thin film after the thermalization time at which the maximum lattice temperature is expected. This factor tends to increase the threshold fluence; and (2) the stronger transient changes in the reflectivity of gold film during the 1053 nm pulse irradiation that tends to decrease threshold fluence [16]. Hence, roughly speaking, these two factors balance each other, which makes the threshold fluence in 140 fs–10 ps almost independent of pulse duration.

4 Conclusions

This study introduces full-run quantum treatments to the two-temperature model for several critical optical and thermal properties, including the electron heat capacity, electron relaxation time, electron conductivity, reflectivity and absorption coefficient. The proposed model releases the low temperature limitation of the existing estimations on optical and thermal properties and effectively extends the application range to high laser fluences. On the other hand, at low temperature ranges, the proposed full-run quan-

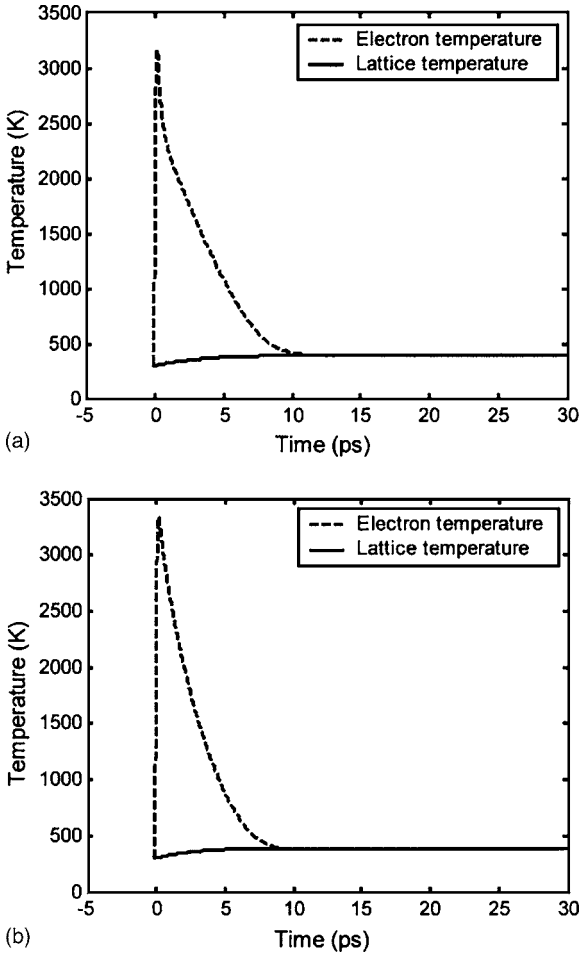

Fig. 5 Surface temperature as a function of time for 200 nm gold film irradiated by a 140 fs, 1053 nm pulse at 0.05 J/cm^2: (*a*) the existing model and (*b*) the proposed model

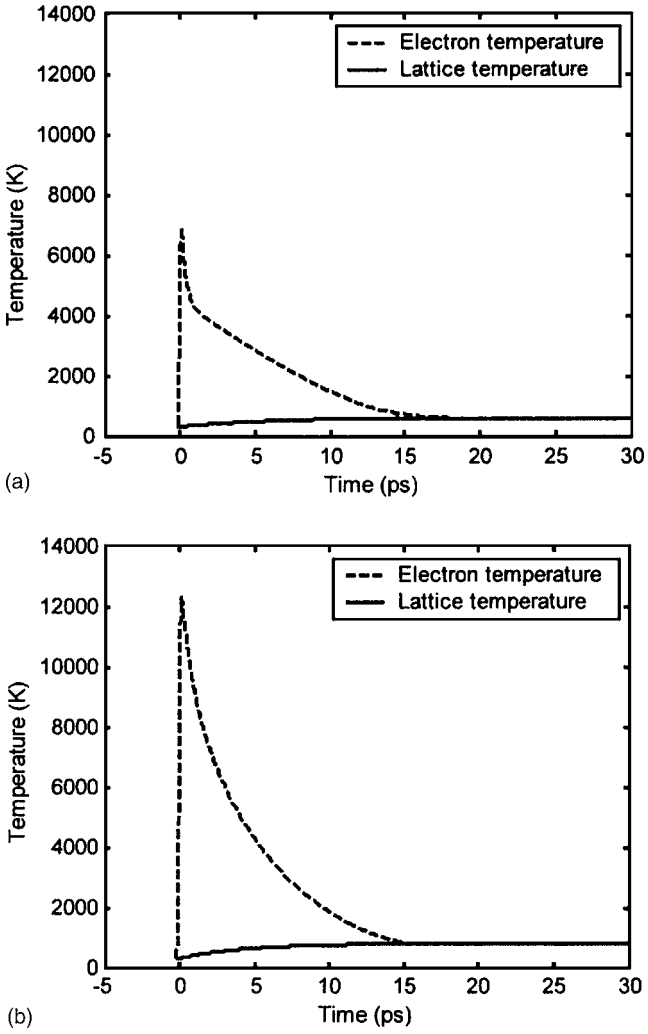

Fig. 6 Surface temperature as a function of time for 200 nm gold film irradiated by a 140 fs, 1053 nm pulse at 0.2 J/cm^2: (*a*) the existing model (*b*) the proposed model

tum treatments can be simplified to those employed by the existing two-temperature model, which is proved by either mathematical derivations or simulation results. The proposed model is employed to calculate the heating process of thin gold films until melting occurs, which is assumed to be the initiation of damage. The predicted damage threshold fluences for 200 nm gold film by the proposed model are in good agreement with published experimental data. The predicted damage thresholds of thin films are almost independent of pulse duration in the ultrashort ($<$10 ps pulse range, as confirmed by experiments.

Acknowledgment

This work was supported by the Air Force Research Laboratory under Contract No. FA8650-04-C-5704 and the National Science Foundation under Grant No. 0423233.

Nomenclature

a = average interatomic spacing
B = bulk modulus
b_{max} = maximum collision parameter in Eq. (15)
b_{min} = minimum collision parameter in Eq. (15)
c = speed of light in vacuum
$\mathbf{c}$ = velocity of light in vacuum
C_e = electron heat capacity
C_l = lattice heat capacity
c_s = speed of sound
e = electron charge

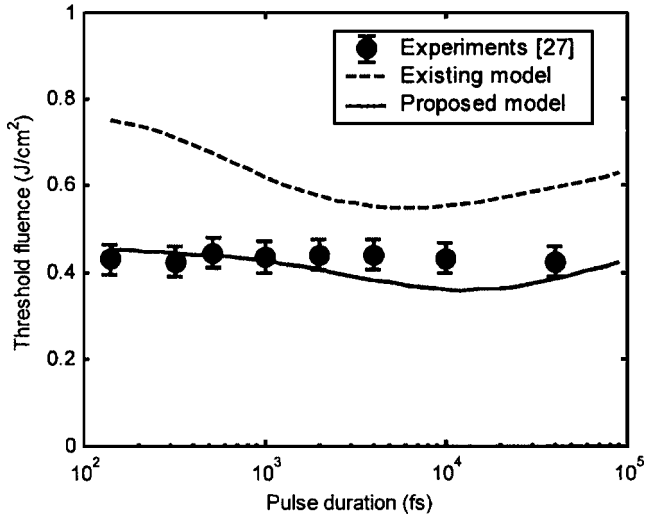

Fig. 7 Damage threshold fluences of 200 nm gold film processed by a 1053 nm laser at different pulse durations

k_B = Boltzmann constant
$\mathbf{f}$ = complex refractive index
f_1 = normal refractive index
f_2 = extinction coefficient
G = electron-lattice coupling factor
h = Planck constant
$\hbar$ = reduced Planck constant
I = laser intensity
J = laser fluence in J/cm^2
k_B = Boltzmann's constant
k_e = electron conductivity
k_{eq} = electron heat conductivity in the electron-phonon thermal equilibrium
m_e = nonrelativistic mass of a free electron
n_a = phonon number density
n_e = density of the free electrons
$\langle n_k \rangle$ = average number of electrons in energy state ε_k
N_A = Avogadro constant
N_e = Total number of free electrons
R = reflectivity
R_u = universal gas constant
S = laser source term
t = time
t_p = pulse duration
T_D = Debye temperature
T_e = electron temperature
T_F = Fermi temperature
T_l = lattice temperature
T_0 = room temperature
V = volume
v_e^2 = mean square of electron speed
v_s = sound speed in the metal
Z^* = ionization state

Greek Symbols

α = absorption coefficient
δ = optical penetration depth
$\boldsymbol{\epsilon}$ = complex dielectric function
ϵ_0 = electrical permittivity of free space
ϵ_1 = real part of the dielectric function
ϵ_2 = imaginary part of the dielectric function
$\langle \varepsilon \rangle$ = average electron kinetic energy
$\langle \varepsilon_p \rangle$ = average phonon kinetic energy
ε_d = d-band energy
ε_F = Fermi energy
ε_k = electron energy state
$\ln \Lambda$ = Coulomb logarithm in Eq. (14)
γ = electron heat capacity constant in Eq. (11)
λ = wavelength of the laser
μ = chemical potential
ν = laser frequency
ν_{max} = maximum frequency of phonons
ρ = density of states
ρ_F = distribution of occupied electronic states
ρ_m = density
τ = electron relaxation time
ω = laser frequency
ω_p = plasma frequency

References

[1] Rethfeld, B., Kaiser, A., Vicanek, M., and Simon, G., 2002, "Ultrafast Dynamics of Nonequilibrium Electrons in Metals under Femtosecond Laser Irradiation," Phys. Rev. B, **65**, pp. 214303–214313.
[2] Del Fatti, N., Voisin, C., Achermann, M., Tzortzakis, S., Christofilos, D., and Vallee, F., 2000, "Nonequilibrium Electron Dynamics in Noble Metals," Phys. Rev. B, **61**, pp. 16956–16966.
[3] Fujimoto, J. G., Liu, J. M., Ippen, E. P., and Bloembergen, N., 1984, "Femtosecond Laser Interaction with Metallic Tungsten and Nonequilibrium Electron and Lattice Temperatures," Phys. Rev. Lett., **53**, pp. 1837–1840.
[4] Schoenlein, R. W., Lin, W. Z., Fujimoto, J. G., and Eesley, G. L., 1987, "Femtosecond Studies of Nonequilibrium Electronic Processes in Metals," Phys. Rev. Lett., **58**, pp. 1680–1683.
[5] Qiu, T. Q., and Tien, C. L., 1992, "Short-Pulse Laser Heating on Metals," Int. J. Heat Mass Transfer, **35**, pp. 719–726.
[6] Qiu, T. Q., and Tien, C. L., 1993, "Heat Transfer Mechanisms during Short-Pulse Laser Heating of Metals," ASME J. Heat Transfer, **115**, pp. 835–841.
[7] Qiu, T. Q., and Tien, C. L., 1994, "Femtosecond Laser Heating of Multi-Layer Metals-I Analysis," Int. J. Heat Mass Transfer, **37**, pp. 2789–2797.
[8] Qiu, T. Q., Juhasz, T., Suarez, C., Bron, W. E., and Tien, C. L., 1994, "Femtosecond Laser Heating of Multi-Layer Metals-II Experiments," Int. J. Heat Mass Transfer, **37**, pp. 2799–2808.
[9] Tzou, D. Y., Chen, J. K., and Beraun, J. E., 2002, "Hot-Electron Blast Induced by Ultrashort-Pulsed Lasers in Layered Media," Int. J. Heat Mass Transfer, **45**, pp. 3369–3382.
[10] Elsayed-Ali, H. E., Norris, T. B., Pessot, M. A., and Mourou, G. A., 1987, "Time-Resolved Observation of Electron-Phonon Relaxation in Copper," Phys. Rev. Lett. **58**, pp. 1212–1215.
[11] Schoenlein, R. W., Lin, W. Z., Fujimoto, J. G., and Eesley, G. L., 1987, "Femtosecond Studies of Nonequilibrium Electronic Processes in Metals," Phys. Rev. Lett., **58**, pp. 1680–1683.
[12] Hertel, T., Knoesel, E., Wolf, M., and Ertl, G., 1996, "Ultrafast Electron Dynamics at Cu(111): Response of an Electron Gas to Optical Excitation," Phys. Rev. Lett., **76**, pp. 535–538.
[13] Brorson, S. D., Kazeroonian, A., Moodera, J. S., Face, D. W., Cheng, T. K., Ippen, E. P., Dresselhaus, M. S., and Dresselhaus, G., 1990, "Femtosecond Room-Temperature Measurement of the Electron-Phonon Coupling Constant Gamma in Metallic Superconductors," Phys. Rev. Lett., **64**, pp. 2172–2175.
[14] Eesley, G. L., 1986, "Generation of Nonequilibrium Electron and Lattice Temperatures in Copper by Picosecond Laser Pulses," Phys. Rev. B, **33**, pp. 2144–2151.
[15] Anisimov, S. I., Kapeliovich, B. L., and Perel'man, T. L., 1974, "Electron Emission from Metal Surfaces Exposed to Ultrashort Laser Pulses," Sov. Phys. JETP, **39**, pp. 375–377.
[16] Wellershoff, S., Hohlfeld, J., Güdde, J., Matthias, E., 1999, "The Role of Electron-Phonon Coupling in Femtosecond Laser Damage of Metals," Appl. Phys. A: Mater. Sci. Process. **69**(Suppl.), pp. 99–107.
[17] Ashcroft, N. W., and Mermin, N. D., 1976, *Solid State Physics*, Holt, Rinehart, and Winston, New York.
[18] Kittel, C., 1986, *Introduction to Solid State Physics*, J Wiley, NY.
[19] Gamaly, E. G., Rode, A. V., Luther-Davies, B., and Tikhonchuk, V. T., 2002, "Ablation of Solids by Femtosecond Lasers: Ablation Mechanism and Ablation Thresholds for Metals and Dielectrics," Phys. Plasmas, **9**, pp. 949–957.
[20] Lee, Y. T., and More, R. M., 1984, "An Electron Conductivity Model for Dense Plasma," Phys. Fluids, **27**(5), pp. 1273–1286.
[21] Jiang, L., and Tsai, H. L., 2004, "Prediction of Crater Shape in Femtosecond Laser Ablation of Dielectrics," J. Phys. D **37**, pp. 1492–1496.
[22] Jiang, L., and Tsai, H. L., 2005, "Energy Transport and Material Removal during Femtosecond Laser Ablation of Wide Bandgap Materials," Int. J. Heat Mass Transfer, **48** (3–4), pp. 487–499.
[23] Fox, M., 2001, *Optical Properties of Solids*, Oxford University Press, Oxford.
[24] Baierlein, R., 1999, *Thermal Physics*, Cambridge University Press, New York.
[25] Palpant, B., Prével, B., Lermé, J., Cottancin, E., and Pellarin, M., 1998, "Optical Properties of Gold Clusters in the Size Range 2-4 nm," Phys. Rev. B, **57**, pp. 1963–1970.
[26] Nolte, S., Momma, C., Jacobs, H., Tunnermann, A., Chichkov, B. N., Wellegehausen, B., and Welling, H., 1997, "Ablation of Metals by Ultrashort Laser Pulses," J. Opt. Soc. Am. B **14**, pp. 2716–2722.
[27] Stuart, B. C., Feit, M. D., Herman, S., Rubenchik, A. M., Shore, B. W., and Perry, M. D., 1996, "Optical Ablation by High-Power Short-Pulse Lasers," J. Opt. Soc. Am. B, **13**, pp. 459–468.

Journal of Heat Transfer

Technical Briefs

Frost-Air Interface Characterization Under Natural Convection

Y. L. Hao[1]

J. Iragorry

Y.-X. Tao

Department of Mechanical and Materials Engineering,
Florida International University, Miami,
FL 33174
e-mail: taoy@fiu.edu

Surface frosting from atmospheric humidity under natural convection is encountered in conventional refrigeration systems, cryogenic surgery, and cryogenic stress relief of die casting metal forming applications. To advance the predictability of frost initiation and formation processes, this study reports a microscopic analysis of frost growth on a flat surface during the onset period of freezing when subcooled droplets are formed and changed to the ice phase. The onset of freezing is quantified by the mean droplet size and ice particle fractions at a critical time (when water droplet freezing point is reached) with the aid of a video microscope. An early-stage frost formation model with effective parameters is demonstrated to provide the important information for the transition to the steady-growth model. The model results are compared with the measured air-frost surface temperatures at different cooling and ambient boundary conditions, using holographic interferometry. The comparison between the model prediction and experimental results demonstrates the sensitivity of effective parameters in simulating the frost thickness and air-frost interface temperature. [DOI: 10.1115/1.2033901]

Introduction

Frost formation is encountered in many engineering applications. Under design and operating conditions of various freezers and refrigeration systems, frost formation on evaporator surfaces (air-refrigerant heat exchanger) occurs inevitably, reducing the heat transfer rate and blocking the air passage. Recent developments in medical research and practice, cryogenic surgery involve formation of frost under natural convection. The quality of the surgery and the performance of the related medical system may be influenced by the uncertainty of the frosting effect [1,2]. Although a wealth of literature has been devoted to the subject [3], there still lacks a satisfactory model that is capable of accurate analysis or simulation of a given frosting process. It is evident that due to the complexity of physical phenomena occurring during a frost formation process, there is a need to provide more reliable information about the critical parameters, serving as indicators of frost formation process, which can then be used to develop a better defrosting strategy, or new devices to aid truly frost-free systems.

The purpose of this brief is to provide frost-air interface parameters, especially the frost "surface" temperature, as a quantitative measure to characterize the frost properties. With the aid of comparison with a numerical simulation, we are to demonstrate the significance of those parameters such that the sensitivity of frost-air interface temperature may be used either as an experimental signal or a simulation predictor. Therefore, it may lead to future studies on defrosting sensors and frost formation model improvement.

Theoretical Background. A frost formation process studied is defined here as starting from when the temperature of the cooling plate decreases from an initial ambient condition (either above or below freezing) and reaches a steady state. The condensing droplets in a subcooling state form, coalesce, and change to ice particles when a critical time, t_c, is reached. The critical time is a function of ambient conditions (temperature, humidity, natural or forced convection) and cold surface temperature and surface roughness. In Fig. 1(*a*), the mean droplet diameter, d, and the mean length scale, ℓ, of the nucleation site are defined at the critical time [4], where $\ell=\sqrt{\pi/\phi}d/2$ and ϕ is the areal fraction of droplets. This moment will be marked as the initial time for the model discussed below.

Once the drop-wise condensation (DWC) period reaches the critical time, t_c, the solidification and tip-growth (STG) period starts and continues until a transitional time, t_t, is reached when a relatively uniform porous layer of frost forms. During the STG period, we propose a simplified model based on [3] to relate the parameters defined at critical time t_c, to the initial conditions for the STG period. Because of the nature of nonuniform tip growth on individual droplets, especially for tiny ones that are still in liquid phases, the average value of ℓ based on the areal droplet fraction is not representative of the actual volumetric fraction of frost, $\phi_i=\rho_f/\rho_i$. Therefore, we choose $\ell_{eff}=\sqrt{\pi/\phi_i}d_{eff}/2$, where ℓ_{eff} and d_{eff} are defined in Fig. 1(*c*) in such a way that the total mass of ice accumulation is equal for both definitions. As an approximation, we adopt the following treatment: $d_{eff}=d$ and ϕ_i is extrapolated from the frost measurement, as will be discussed further. The above-defined STG process and parameters allow us to use the early-growth model developed in [4] to simulate the frost formation during the STG period along with the model that simulates the densification and bulk-growth (DBG) period.

Methods of Investigation

Experiments. Figure 1(*b*) shows the experimental apparatus used to investigate the microscopic characteristics of frost forma-

[1]Present address: Southeast University, Nanjing, 210096, People's Republic of China.

Contributed by the Heat Transfer Division of ASME for publication in the JOURNAL OF HEAT TRANSFER. Manuscript received by the Heat Transfer Division March 16, 2004; revision received April 5, 2005. Review conducted by: C. H. Oh.

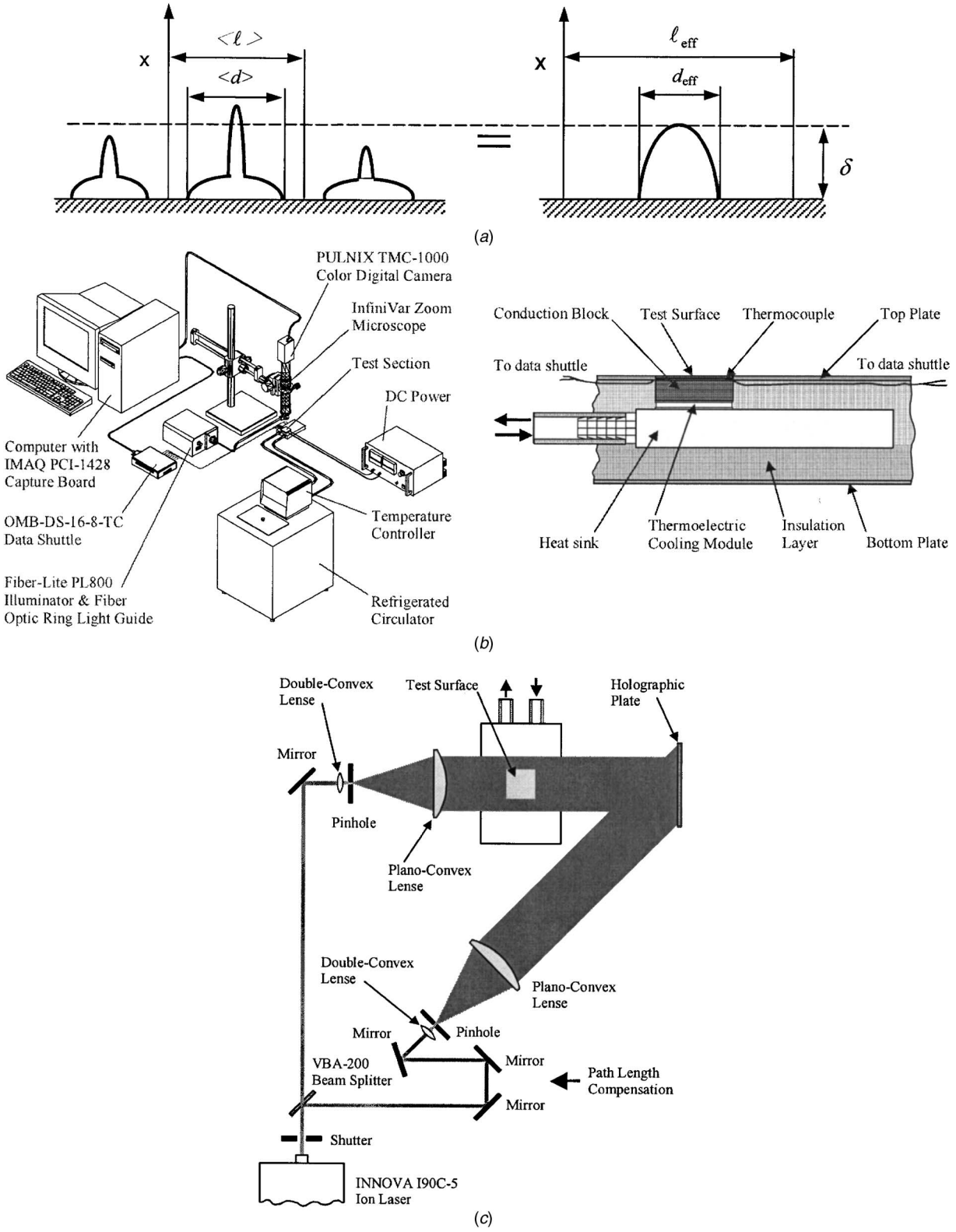

Fig. 1 Schematics of (*a*) the model for the initial conditions for the solidification and tip-growth (STG) period, (*b*) the microscopic video system characterizing microdroplets/particles and the test section, and (*c*) the holographic interferometry system

tion. The test section consists of a test surface, an aluminum block of $40\times40\times1.6$ mm, insulated at sides, a thermoelectric cooling module with the required heat-sink heat exchanger, and the insulation layers, as shown in Fig. 1(*b*). The test surface can be cooled to temperatures as low as $-40°$C, using a thermoelectric cooling module with a heat-sink heat exchanger. The thermoelectric cooling module is mounted on the heat-sink heat exchanger using thermally conductive double-sided adhesive tape. The tempera-

tures of the test surface, heat sinks, and the air temperature above the test surface are measured using thermocouples, which are recorded and monitored by a PC computer. A Fisher Scientific hygrometer is used to measure the ambient temperature and relative humidity.

The OMEGA cement-on style-2 thermocouples installed between the test surface and the aluminum block have the uncertainty of ±0.1°C. All of the other thermocouples used in the present study are OMEGA T-type precision fine wire thermocouples with the uncertainty of ±0.5°C. The uncertainty of the heat flux through the test plate obtained based on the temperature measurement is estimated to be round 3%. The uncertainty of the effective thermal conductivity of frost layer measurement is estimated to be less than 5%. A refrigerated circulator is used to supply the ethylene glycol solution (50%) to the heat-sink heat exchanger and can be controlled with ±0.1°C.

The microscope video system (InfiniVar) is used to measure the condensate droplet sizes and areal fractions, which are recorded digitally [Fig. 1(*b*)] with the system resolution of 0.5625 μm and accuracy of 1.08 μm. A two-exposure, holographic interferometry technique is used to determine the air-frost interface temperature [Fig. 1(*c*)] at a desired time after the test starts. The reference temperature is measured by a pair of thermocouples (within ±0.5°C) mounted at the location of 25.4 mm above the cold plate surface. The overall uncertainty on the temperature determined by holographic interferometry is estimated being less than ±0.6°C. The measurement of the distance, x, of each isotherm to the cold plate surface was done by digitizing the image of a size of 2048 $\times$1536 pixels with an uncertainty of 3.5×10^{-5} m. The pattern of drop-wise condensation and resulting ice particle distribution during the early frosting period is analyzed by applying local fractal dimension concepts [5]. A numerical code is developed to scan the images to arrive at the characteristic diameter.

Table 1 Test conditions

Case No.	T_a °C	RH_a %	$T_{w,0}$ °C	Initial surface condition	T_{ws} °C
1	23.5	49	10	Dry	–4
2	23.7	49	10	Wet	–4
3	23.0	50	10	Dry	–8
4	23.1	49	10	Wet	–8
5	23.1	48	10	Dry	–15
6	23.2	48	10	Wet	–15
7	24.3	46	10	Dry	–18
8	24.1	44	10	Wet	–18
9	24.1	50	10	Dry	–20
10	23.7	48	10	Wet	–20
11	24.8	45	10	Dry	–22
12	24.9	45	10	Wet	–22

T_a=ambient temperature; RH_a=ambient relative humidity; $T_{w,0}$= initial cold surface temperature; T_{ws}= steady-state cold surface temperature

Numerical Model for STG and DBG Periods. The governing equations and major boundary conditions of those two models are similar to the ones in Ref. [6]. The only difference is that the heat transfer coefficient in this study is calculated from the Raleigh number based correlation for natural convection rather than that

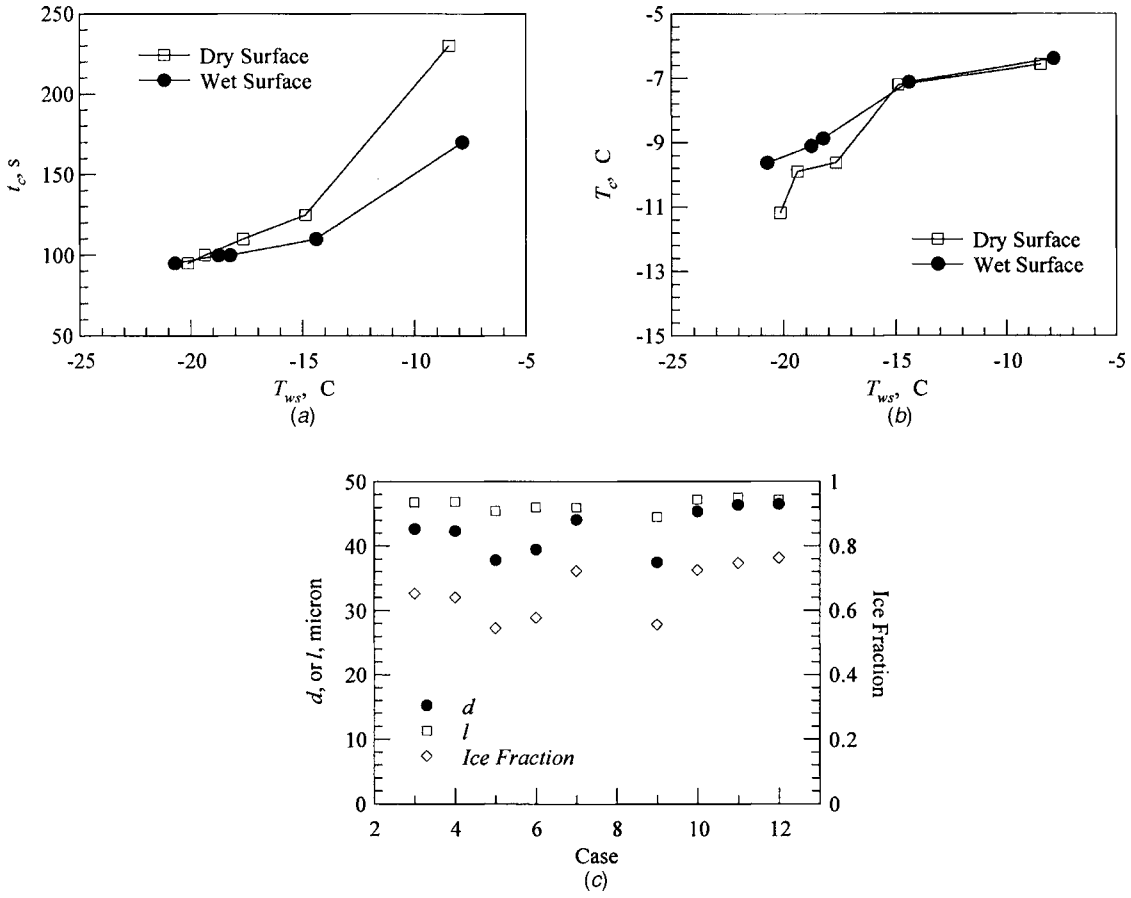

Fig. 2 (*a*) Critical time and (*b*) temperature under different conditions, and (*c*) droplet diameter and site-length scale for nucleation sites and ice fraction at the critical time

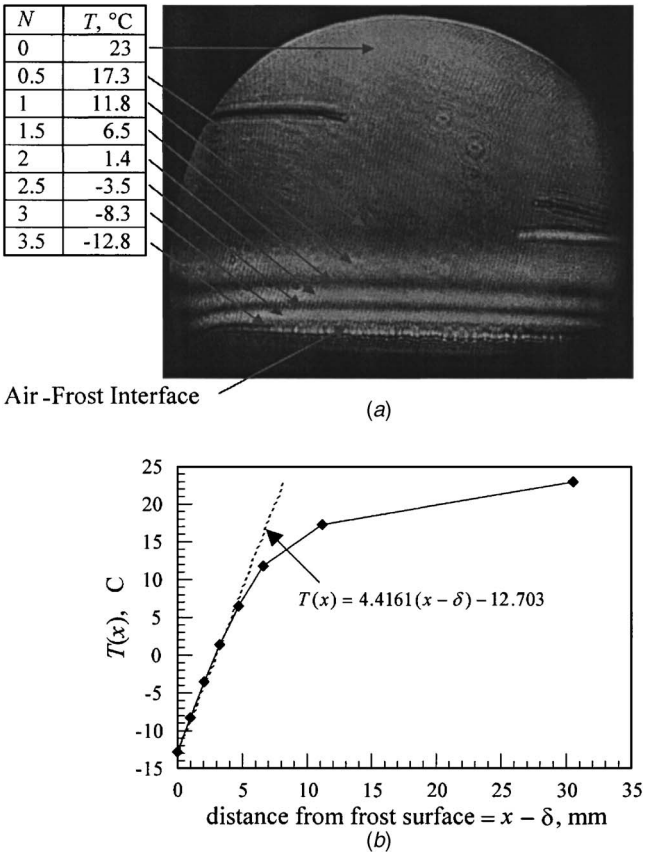

Fig. 3 Typical holographic image: dry surface—(*a*) holographic interferometry fringes and (*b*) temperature profile in the thermal boundary layer. T_a=23°C, RH_a=61%, T_w=−18°C, t=60 min

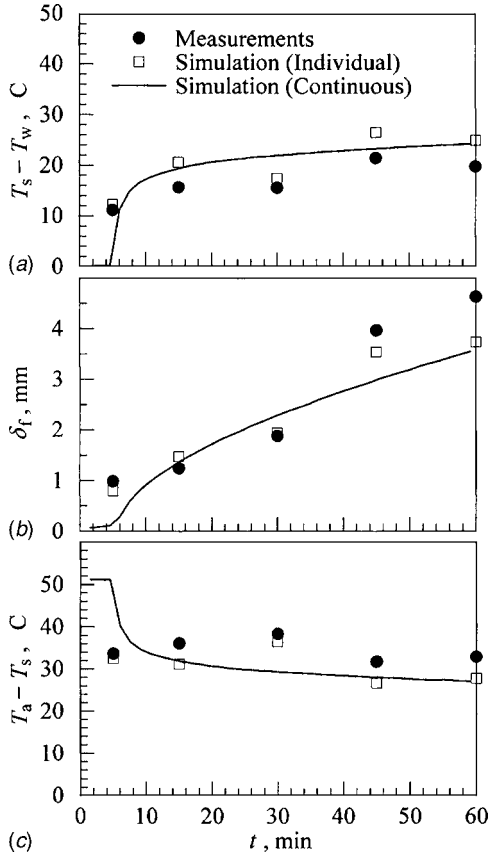

Fig. 4 (*a*) Variation of temperature difference between air-frost interface and cold surface with time, (*b*) variation of thickness of frost layer with time, and (*c*) comparison of the simulation and experiment results of the temperature difference between ambient and air-frost interface: dry surface, $\langle T_a \rangle$=23.2°C, $\langle RH_a \rangle$=56%, $\langle T_w \rangle$=−32.8°C

based on the Reynolds number. The DBG model assumes the frost as a continuous porous medium with variable thermal and geometric properties. In the numerical calculation, the root-mean-square convergence within 10^{-4}% is obtained for the cases studied. Extensive test runs have been carried out to come up with a better compromise between accuracy and computational efficiency requirements.

Results and Discussion

Transition From Drop-Wise Condensation to Solidification. A series of microscopic observations is conducted under the different steady-state temperature, T_{ws}. The test conditions are listed in Table 1. The tests have two types of initial surface state, dry and wet. The initial dry surface means that the test is not started until the surface is carefully dried using the soft lens paper with ethanol. The initial wet surface means that the test starts on the surface with a microlayer of moisture. For cases No. 1 and 2 in Table 1, the steady-state temperatures are −4°C; and the condensed, subcooled water on the surface never freezes. The critical times and temperatures for all other cases are shown in Figs. 2(*a*) and 2(*b*). It is shown that the critical time is reached faster for the lower steady-state temperature, and the corresponding critical temperature is also lower [Fig. 2(*b*)]. For most cases, the critical time for the initial dry surface is reached earlier than under the initial wet surface. The difference decreases with the decrease in the steady-state temperature. The critical temperatures are almost the same for the high steady-state temperature. The critical temperature for the initial dry surface is lower than that of wet surface when the steady-state temperature is lower than −15°C. For this case, the difference increases with the decrease in the steady-state temperature. The results of fractal analysis of droplet distribution at the critical times indicate the mean diameters of droplets, d, are within the range of 37.4–46.5 μm, shown in Fig. 2(*c*). There is a tendency for the mean diameter to slightly increase with the decrease in the steady-state temperature. On the other hand, the mean length scale of nucleation site, ℓ, is less sensitive to the cold surface temperature. The value is within the range of 44.5–47.6 μm. The ice fraction on the surface at the critical time is within the range of 0.556–0.763. The tendency to increase with the decrease in the steady-state temperature is clearly seen in Fig. 2(*c*).

Air-Frost Interface Temperature. Figure 3(*a*) shows a typical holographic image to measure the distribution of air temperature in the field above the cold/frost surface. The first exposure was taken under the condition of uniform temperature distribution before the surface is cooled. The second exposure was taken a 60 min after the test started. A thin black horizontal line with small waves in the bottom area clearly shows the air-frost interface. The fringe pattern clearly shows the stratified temperature field between the ambient temperature and air-frost interface temperature. Figure 3(*b*) shows the temperature distribution of the thermal boundary layer in the central location of the image shown in Fig. 3(*a*). With the temperature profile $T(x)$ of the air above the frost surface, the heat transfer coefficient between the frost surface and ambient air by the natural convection can be determined as follows: $h=-k(dT/dx)/(T_s-T_a)$. A series of the holographic images was taken for different frost accumulation times but under the same desired ambient and cold surface temperatures. This ar-

rangement is made to simulate a continuous frosting process. There is a certain variation in ambient and cold surface temperature due to the setting and control limitation. Therefore, the results in Fig. 4 were reported as under average ambient and surface conditions to indicate the trend.

Figure 4(*a*) shows that the temperature difference between the air-frost interface and the cold surface increases with the growth of frost layer. In the initial period the temperature difference increases slowly as the frost growth rate is high. It tends to approach a quasisteady fashion later on. The variation of frost layer thickness is shown in Fig. 4(*b*).

Comparison With Simulation Results. The model simulation results are compared with the measurements and shown in Fig. 4. Considering the variation in boundary conditions for each experimental data point, two different simulations are conducted. One is that the experimental conditions for the individual experimental data point are used as an input in the simulation. The other simulation is based on the average ambient and cold-surface temperatures obtained from all the experimental data and assumed to maintain through the entire 60 min frosting period. Table 2 shows the specified input conditions for each simulation.

Table 2 Parameters used in simulation

Case No.	t_{test}, s*	T_a, °C	T_w, °C	t_t, s	ℓ_{eff}, μm	d_{eff}, μm	ϕ_i
13	300	21.1	–23.8	20	400	40	0.008
14	900	17.8	–34.1	300	400	40	0.008
15	1800	14.4	–39.6	240	120	40	0.00
16	2700	19.1	–34.1	300	500	40	0.005
17	3600	20.1	–32.6	20	500	40	0.005
Average	3600	18.5	–32.8	350	900	40	0.002

* t_{test} = Total test time for a frosting process

Because the frost thickness data are process dependent, i.e., the measured thickness is the result at the end of a frosting process, the individual data points in Fig. 4 are taken at the end of each corresponding experimental duration. They are not taken at different times during a same frosting process. The time indicated in the

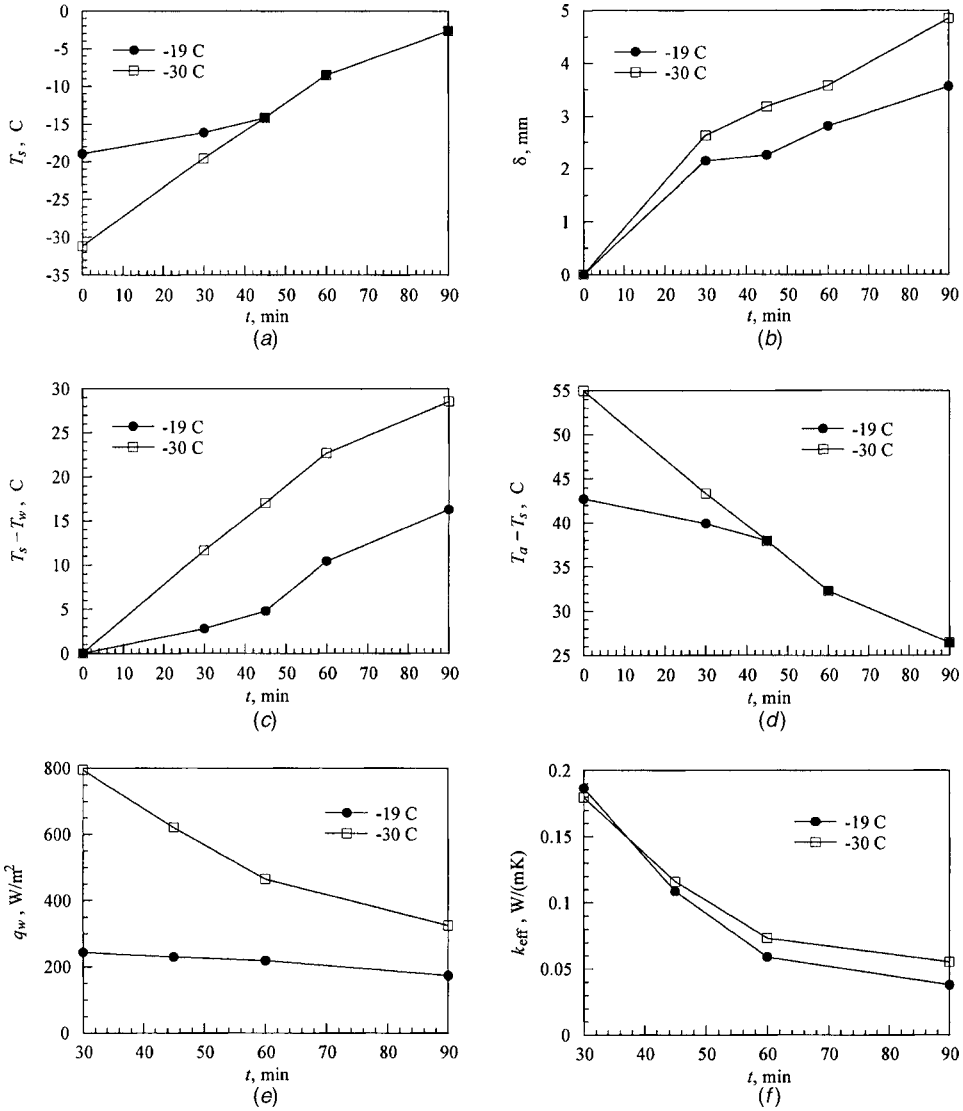

Fig. 5 Time variations of (*a*) air-frost interface temperature, (*b*) frost layer thickness, (*c*) temperature difference between air-frost interface and cold plate surface, (*d*) temperature difference between the ambient and air-frost interface, (*e*) heat flux through frost layer, and (*f*) bulk effective thermal conductivity of frost for two different cold plate temperatures: $\langle T_a \rangle = 23°C$, $\langle RH_a \rangle = 61\%$

figure for the individual results really represents the time elapsed in the corresponding frosting process. Despite various efforts, it is difficult to maintain the exact same initial conditions such as ambient temperature, coolant temperature, and cold surface thermal and moisture conditions, for all the experiments. Therefore there are variations in those conditions. The continuous numerical results simulate a longer period with the assumption of constant ambient and cold surface temperatures that are taken as the average values from all the experimental data, while the simulated individual results use the ambient, initial, and cold surface conditions from the corresponding experimental process. That is why there is a discrepancy, and the individual results compare better because they are more accurately close to the experimental condition.

The comparisons show that, in general, the simulation agrees reasonably with the measurement data. The simulation slightly overpredicts temperature differences between the air-frost interface and cold plate [Fig. 4(*a*)] while the temperature difference between the ambient and air-frost interface temperatures is more consistent with the experimental result. The above comparison illustrates a couple of important observations. One is that the investigative approach, combining both numerical modeling and experimental input, allows us to study the detailed heat and mass transport associated with the frosting phenomena. On the other hand, it indicates that a more comprehensive investigation on the general trends of indicative parameters characterizing the STG period is needed, because the generalization of effective parameters, ℓ_{eff} and ϕ_i, to other conditions remains unsolved despite the advance in determining d_{eff}. The results clearly indicate that there are significant variations in the temperature difference between the frost surface temperature and cooling surface temperature. For the example shown in Fig. 4, a 4-mm-thick frost layer formation within 1 h results in a difference of about 20°C in surface temperatures under natural convection, and a rate of 0.1°C/min in temperature increase can be observed. This sensitivity could lead to developing advanced sensing methodology and helping quantification of latent loads on cold surfaces.

Effect of Cold Surface Temperature. If the air-frost interface temperature can be treated as an indicator of dynamic balance between the heat released for frost growth (i.e., the heat removed by the cold plate) and the heat transfer from the ambient to the frost surface, it will be of interest to see if the air-frost interface temperature, T_s, depends on the cold plate temperature, T_w. Figure 5(*a*) shows the experimental results for two different cold plate temperatures (−19° and −31°C) under the same ambient temperature condition. It can be seen that for both cases, the frost surface temperatures are much lower than the freezing temperature and close to the cold surface temperature during the early growth period. That is because the frost layer was formed by subcooled or frozen droplets at the early growth period. The frost layer was thin, as shown in Fig. 5(*b*) and has relatively high effective thermal conductivity. After the DBG period is reached, the air-frost interface temperature reaches the same value for those two cases. This indicates that the convective heat transfer rate from the ambient to the frost surface remains the same for both. This confirms that the formation of frost reduces the ability of the heat transfer equipment to remove heat from the ambient, even though the amount heat transferred to the cold plate is higher in the case with the lower cold plate temperature [T_w=−31°C; Fig. 5(*e*)]. The insulation effect of the frost layer can be demonstrated by the increase in the temperature difference between the air-frost interface temperature and cold plate temperature as the frost thickness increases [Figs. 5(*c*) and 5(*d*)]. This heat transfer degradation is more pronounced in the T_w=−31°C case than in the −19°C case. Using the definition of a bulk effective thermal conductance that includes the transient effect, $\overline{k}_{\text{eff}}=q_w/((T_s-T_w)/\delta)$, we can see from Fig. 5(*f*) that $\overline{k}_{\text{eff}}$ decreases to about 31% of its initial value in a 90 min period for T_w=−31°C versus a reduction to about 22% of its initial value for T_w=−19°C. Figure 6(*a*) shows the heat transfer coefficient of the two cases obtained based on the temperature profile from the holographic measurement. An empirical correlation of Nusselt number and Rayleigh number based on all of the cases of holographic measurements in the present study can be obtained as

$$\text{Nu}_L = 5.35 \times 10^{-4}\text{Ra}_L^{0.823},$$

which is valid for $2.81\times10^4 \leqslant \text{Ra}_L \leqslant 6.62\times10^4$ and the characteristic length is defined as $L \equiv$ (surface area/perimeter). All of the properties are evaluated at the film temperature, $(T_s+T_a)/2$. An R^2 value for the correlation is 0.971. The comparison of the experiment data with the correlation is shown in Fig. 6(*b*).

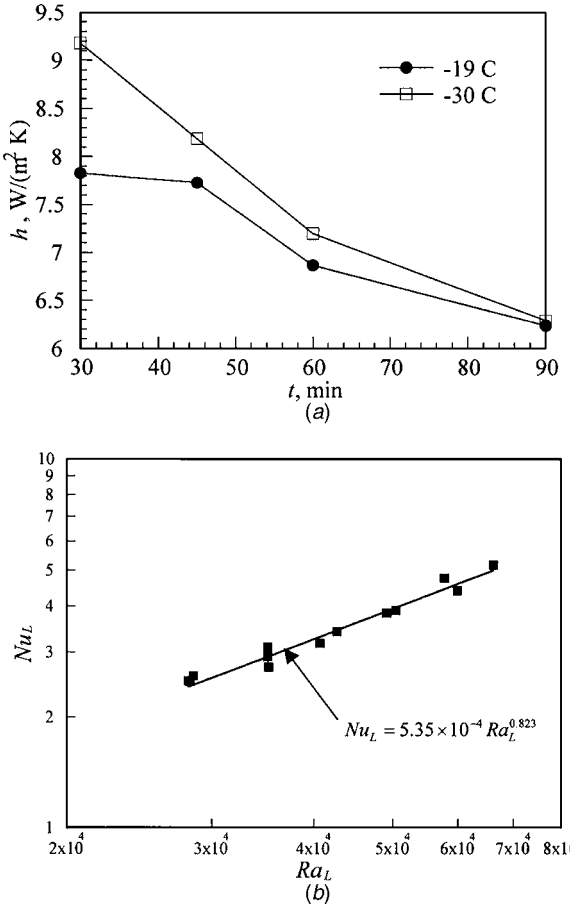

Fig. 6 (*a*) Time variations of convection coefficient for the two different cold plate temperatures: $\langle T_a\rangle$=23°C, $\langle RH_a\rangle$=61%, (*b*) correlation of Nusselt number and Rayleigh number

Acknowledgments

The authors thank the NSF for their financial support, and Heatcraft, Inc., for their equipment support. J. thanks the FIU Latin American and Caribbean Center (LACC) for the additional scholarship support. The experimental assistance from Ms D. Castro is also acknowledged.

References

[1] Majaron, B., Kimel, S., Verkruysse, W., Aguilar, G., Pope, K., Svaasand, L. O., Lavernia, E. J., and Nelson, J. S., 2001, "Cryogen Spray Cooling in Laser Dermatology: Effects of Ambient Humidity and Frost Formation," Lasers Surg. Med., **28**(5), pp. 469–476.
[2] Sklar, G. N., Koschorke, G. M., Filderman, P. S., Naslund, M. J., and Jacobs, S. C., 1995, "Laparoscopic Monitoring of Cryosurgical Ablation of the Prostate," Surg. Laparosc Endosc, **5**(5), pp. 376–81.
[3] Iragorry, J., Tao, Y.-X., and Jia, S., 2004, "A Critical Review of Properties and

Models for Frost Formation Analysis," Int. J. HVAC&R Res., **10**(4), pp. 393–420.
[4] Tao, Y.-X., Besant, R. W., and Mao, Y., 1993, "Characteristics of Frost Growth on a Flat Plate During the Early Growth Period," ASHRAE Trans., **99**(1), pp. 746–753.
[5] Sabau, A. S., Tao, Y.-X., Liu, G., and Vidhuvalavan, S., 1997, "Effective Thermal Conductivity for Anisotropic, Granular Porous Media Using Fractal Concepts," the *National Heat Transfer Conference, ASME HTD*, 349, pp. 121–197.
[6] Tao, Y.-X., Besant, R. W., and Rezkallah, K. S., 1993, "A Mathematical Model for Predicting the Densification and Growth of Frost on a Flat Plate," Int. J. Heat Mass Transfer, **36**(2), pp. 353–363.

Natural Convection Patterns in Right-Angled Triangular Cavities With Heated Vertical Sides and Cooled Hypotenuses

El Hassan Ridouane

Antonio Campo
e-mail: acampo@cem.uvm.edu

Department of Mechanical Engineering, The University of Vermont, Burlington, VT 05405

Jane Y. Chang
Department of Applied Statistics and Operation Research, Bowling Green State University, Bowling Green, OH 43403

The present investigation deals with the numerical computation of laminar natural convection in a gamma of right-angled triangular cavities filled with air. The vertical walls are heated and the inclined walls are cooled while the upper connecting walls are insulated from the ambient air. The defining apex angle α is located at the lower vertex formed between the vertical and inclined walls. This unique kind of cavity may find application in the miniaturization of electronic packaging severely constrained by space and/or weight. The finite volume method is used to perform the computational analysis encompassing a collection of apex angles α compressed in the interval that extends from 5° to 63°. The height-based Rayleigh number, being unaffected by the apex angle α, ranges from a low 10^3 to a high 10^6. Numerical results are reported for the velocity field, the temperature field and the mean convective coefficient along the heated vertical wall. Overall, the matching between the numerically predicted temperatures and the experimental measurements of air at different elevations inside a slim cavity is of ordinary quality. For purposes of engineering design, a $\overline{\mathrm{Nu}}_H$ correlation equation was constructed and also a figure-of-merit ratio between the $\overline{\mathrm{Nu}}_H$ and the cross sectional area A of the cavity was proposed. [DOI: 10.1115/1.2033903]

Introduction

When a gas or a single-phase liquid is trapped inside a stationary closed cavity, natural convective motion of the fluid is induced and sustained when a temperature difference is applied at two or more thermally active walls. This scenario represents an important subclass of buoyancy-induced flows arising in engineering, geophysics, environmental sciences, etc.

There is a wealth of publications dealing with the theory, numerical computation and experimentation of natural convection across two-dimensional stationary cavities of square, rectangular and annular cross sections as disclosed in the chapters written by Raithby and Hollands [1] and Jaluria [2] in specialized handbooks. However, certain cavities occurring in modern engineering applications often have shapes differing from the conventional configurations cited above.

The present paper addresses laminar natural convection in right-angled triangular cavities filled with air. These cavities are heated at the vertical wall and cooled at the inclined wall, whereas the upper horizontal wall is insulated from the surroundings. The motivation for undertaking this investigation gyrates around the experimental work of Oktay [3], who studied the beneficial attributes of boiling heat transfer for the efficacious cooling of an array of microelectronic LSI devices attached to a vertical wall and encapsulated inside an upright triangular cavity. Surprisingly, a literature survey on natural convection in cavities reveals no publications so far on this kind of right-angled triangular cavity and, consequently, the fluid physics of the unique assembly is not understood. As stated by Simons et al. [4] and Bar-Cohen [5], a prominent application of this particular cavity arises in the miniaturization of electronic packaging subjected to space and/or weight constraints. Despite the fact that the literature is scarce in the area of natural convection in vertical-placed right-angled triangular cavities, it is abundant in the area of horizontal-placed right-angled triangular cavities. Representative articles are those of Akinsete and Coleman [6], Poulikakos and Bejan [7], Karyakin et al. [8], Salmun [9], Asan and Namli [10], and Haese and Teubner [11].

Relying on the finite volume method, numerical predictions of the velocity and temperature fields induced by buoyant air in vertical-placed right-angled triangular cavities owing to various apex angles under the influence of low, moderate and large Rayleigh numbers are carried out in this paper. To validate the numerical predictions, experimental data were gathered for local air temperatures and mean convective coefficients from the publications by Elicer-Cortés et al. [12,13].

The body of the paper is divided into four sections. The first section describes the physical system and the mathematical formulation. The implementation of the finite volume method is explained in the second section. The third section contains the numerical-determined velocity and temperature fields as well as the total heat transfer rates through the heated vertical wall. Finally, the comparison between the numerical predictions and some experimental measurements available for air are included in the fourth section. In addition, this section contains a correlation equation needful for efficacious cavity design.

Physical System and Mathematical Formulation

Figure 1 is a sketch of the physical system that consists of compressible air inside a vertical-placed right-angled triangular cavity. A hot temperature is prescribed at the vertical wall, a cold temperature is prescribed at the inclined wall and the connecting top wall is covered with insulation. The variable apex angle α is assigned at the bottom vertex, the intersection formed between the heated vertical and the cooled inclined walls. The gravitational acceleration acts parallel to the hot vertical wall. The dimension perpendicular to the plane of the diagram is assumed to be long, so that the confined air is conceived as two dimensional. For the sake of generality, the air is assumed to be a non-Boussinesqian fluid, so that the thermophysical properties changing with temperature are incorporated in the analysis to mimic the experimental observations. Accordingly, the mathematical formulation is described by the system of conservation equations

$$\text{Mass: } (\rho u)_x + (\rho v)_y = 0 \tag{1}$$

$$\text{Horizontal momentum: } (\rho uu)_x + (\rho vu)_y = -p_x + (\mu u_x)_x + (\mu u_y)_y \tag{2}$$

$$\text{Vertical momentum: } (\rho uv)_x + (\rho vv)_y = -p_y + (\mu v_x)_x + (\mu v_y)_y + g(\rho - \rho_r) \tag{3}$$

$$\text{Energy: } (\rho c_p uT)_x + (\rho c_p vT)_y = (kT_x)_x + (kT_y)_y \tag{4}$$

Contributed by the Heat Transfer Division of ASME for publication in the JOURNAL OF HEAT TRANSFER. Manuscript received by the Heat Transfer Division April 12, 2004; revision received May 3, 2005. Review conducted by: B. Farouk.

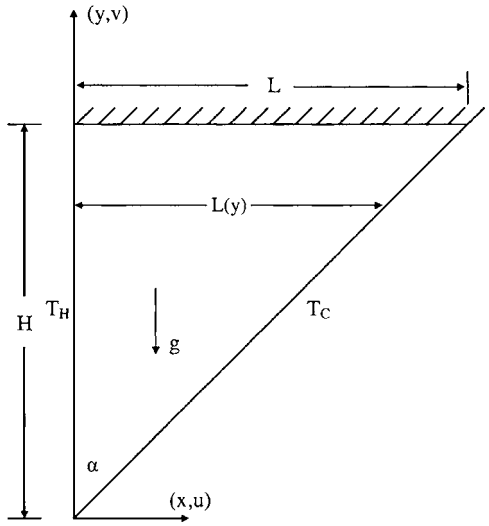

Fig. 1 Sketch of the upright right-angled triangular cavity

$$\text{Ideal gas equation of state: } p = \rho RT \tag{5}$$

The reference density ρ_r in Eq. (3) is evaluated at a reference temperature $T_r=(T_H+T_C)/2$.

The velocity boundary conditions rest on the assumptions that (a) the walls are solid, rigid and impermeable and (b) the trapped air does not slip at the walls. The thermal boundary conditions implicate prescribed temperatures at both the heated vertical wall and cooled inclined wall. Besides, a zero temperature gradient is assigned at the top horizontal wall.

Eqs. (1)–(5), subject to the set of boundary conditions, are discretized with the finite volume method in order to determine the velocity and temperature fields of the air. Owing to the asymmetry of the physical domain shown in Fig. 1, the computational and physical domains are coincident. Different apex angles α contained in the interval $5° < \alpha < 63°$ coupled with Rayleigh numbers Ra_H ranging from 10^3 to 10^6 are chosen.

The local wall heat flux along the hot vertical wall $q_w(y)$ is found by applying Fourier's law to the air temperature field. This step leads to the mean wall heat flux along the hot vertical wall

$$\overline{q_w} = \frac{1}{H}\int_0^H q_w(y)dy \tag{6}$$

Subsequently, the mean convective coefficient $\overline{h}$ and the mean Nusselt number $\overline{Nu}_H$ are obtained from the relations

$$\overline{Nu}_H = \frac{H\overline{h}}{k} = \frac{H\overline{q_w}}{k(T_H - T_C)} \tag{7}$$

Here, the air thermal conductivity k is evaluated at the reference temperature $T_r=(T_H+T_C)/2$.

Computational Procedure

The numerical computations are performed with the finite volume code FLUENT 6.1. The computational domain was created and meshed using the grid generation software Gambit 2.0®. Care was taken to increase the element density in vulnerable areas where high velocity and temperature gradients would occur, such as near the solid walls. Based on numerical experiments, various grid sizes having 30,000 triangular elements up to 90,000 were tried. For the largest $\alpha=63°$, the optimal computational mesh was constructed with 76,000 triangular elements carrying an error within 1%. Upon reducing α to 45°, 30°, 15°, 10°, and 5°, the number of triangular elements was diminished gradually to 65,000, 58,000, 52,000, 47,000, and 43,000, respectively. These grid layouts rendered reliable results for the velocity and temperature fields $u(x,y)$, $v(x,y)$ and $T(x,y)$ for all combinations of α and Ra_H selected. In Eqs. (1)–(4), the discretization of the convective term is accomplished by the second order accurate scheme QUICK, while the pressure-velocity coupling is handled with the SIMPLE scheme. Also, global convergence was guaranteed by controlling the residuals of Eqs. (1)–(4). After good convergence of the velocity and temperature fields was attained, we proceeded to calculate the streamlines and isotherms as well as the mean wall heat flux at the vertical heated wall $\overline{q_w}$, the ultimate quantity of interest.

Numerical Results and Comparison Against Experimental Data

Fluid motion was set up in the triangular cavities by heating the vertical wall to a uniform temperature T_H while simultaneously cooling the inclined wall at a uniform temperature T_C. The upper connecting horizontal wall was insulated.

When examining Fig. 2 for a low $Ra_H=10^3$, we observed contour plots of temperatures and stream functions for the three typical cavities owing apex angles $\alpha=63°$, 45° and 15°. From the trio of stream function plots, it can be seen that all three configurations exhibit a single rotating vortex. The direction of the vortex rotation can be determined by finding the sign of the gradient for the stream function in the x direction and remembering that the velocity in the y direction is opposite in sign to the stream function gradient. For the three cavities, the stream function gradient is negative from the hot wall to the center and positive from the center toward the cold wall. Therefore, the vertical velocity is positive along the hot vertical wall and negative along the cold inclined wall and the vortex is rotating in a clockwise direction. The effect on temperature of the clockwise vortex can be visualized in the isotherm plots. The vortex moves the warm fluid from the left wall along the top of the geometry and results in higher temperatures at the top half of each cavity. The overall orientation of the temperature isotherms is vertical signaling a heat transfer process dominated by conduction. The strength of the vortex rotation can be determined by calculating the magnitude of the stream function gradient. The 45° triangle displays the largest stream function gradient, while the 15° triangle displays the smallest. Therefore, we expected the vortex strength and velocities to be highest in the 45° triangle and lowest in the 15° triangle. The local Nusselt number Nu_y attains the largest value for the 15° triangle, an intermediate value for the 45° triangle and the smallest value for the 63° cavity. Essentially, the peculiar behavior of Nu_y must then be attributed to increased conductive heat transfer due to the small separation between the hot and cold walls and not to the increase in vortex strength.

Figure 3 displays the temperature and stream function contour plots for the high $Ra_H=10^6$. When comparing the stream function plots from Fig. 2 and Fig. 3, one noticed that the vortex for the 63° and 45° triangles has moved down toward the bottom corner when Ra_H is expanded three orders of magnitude. On the contrary, the location of the vortex in the 15° triangle literally is not affected. Calculating the sign of the stream function gradient showed that the direction of vortex rotation is the same as in Fig. 2. In addition to the new vortex locations, the strength of the vortex is also enlarged as seen by the magnitude of the stream function gradient. The effect of this vortex strength increment can be seen in the temperature contours where the isotherms are now arranged horizontally instead of vertically. This difference in the isotherm orientation highlights the importance of convection over conduction at this Ra_H number. Also, Fig. 3 revealed that the strongest vortex occurs for the 63° triangle, which is in sharp contrast to Fig. 2 where the 63° triangle had the intermediate rotation strength. As it happened in Fig. 2, the local Nusselt number Nu_y is the highest for the 15° triangle and the lowest for the 63° triangle. Furthermore, the percent amplification in Nu_y be-

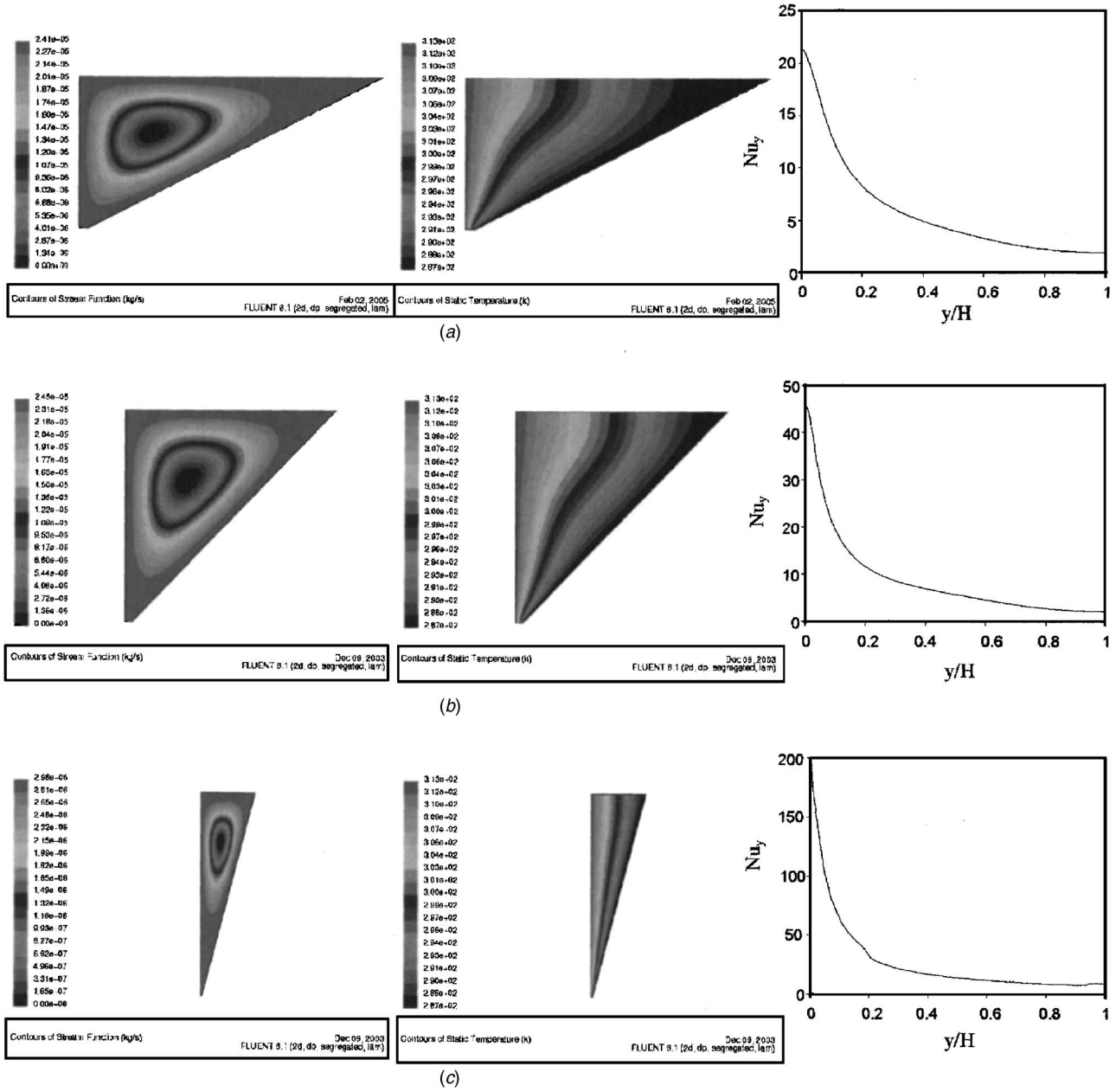

Fig. 2 Plots of stream functions, isotherms and local Nusselt numbers Nu_y for three apex angles $\alpha=63°$, 45° and 15° sharing a small $Ra_H=10^3$

tween Fig. 2 and Fig. 3 is connected to the 63° triangle. This large percent accretion is due to the fact that conduction is less important in the overall heat transfer process for this particular apex angle because of the relatively large separation between the hot and cold walls especially near the lower vertex. Consequently, any augmentation in convective heat transfer will have a greater impact on the overall heat transfer.

Experimental data for the local air temperatures $T(x,y)$ and mean convective coefficients $\bar{h}$ in slender upright triangular cavities were gathered from the publication by Elicer-Cortés and Kim-Son [13] to validate the numerical predictions. In their work, the vertical wall was heated by means of a stabilized electric power supply while the inclined wall was cooled with a precision thermostat containing water. In the experimental setup, three shapes related to slender upright triangular cavities holding apex angles of 5°, 10°, 15° were considered. The hot wall temperatures were set at $T_H=40°$, 60°, 80°, and 100°C. For the 15° triangle, Fig. 4 illustrates a reasonable parity between the numerically estimated and the measured air temperature profiles taken at three relative heights $y/H=0.1$, 0.58 and 0. 99. The lowermost curve for $y/H=0.1$ reveals that the numerical predictions overlap perfectly with the experimental measurements. It may also be inferred that in this lower corner region, the air is basically motionless and the transfer of heat occurs by conduction. The numerical temperatures slightly overpredicted the experimental observations at the other two heights $y/H=0.58$ and 0.99. The largest discrepancy occurs for the uppermost curve representative of $y/H=0.99$. This may be attributed to the fact that this location, being very close to the top horizontal insulated wall, experiences heat losses to the ambient air through the insulation [13]. Experimental error in the measurements is another possibility. Invariably, the same patterns prevailed in Fig. 5 for a more slender cavity having a smaller apex angle of 10°. Here, the measurements were taken at relative heights of $y/H=0.1$, 0.5 and 0.98. A feature showing up in the

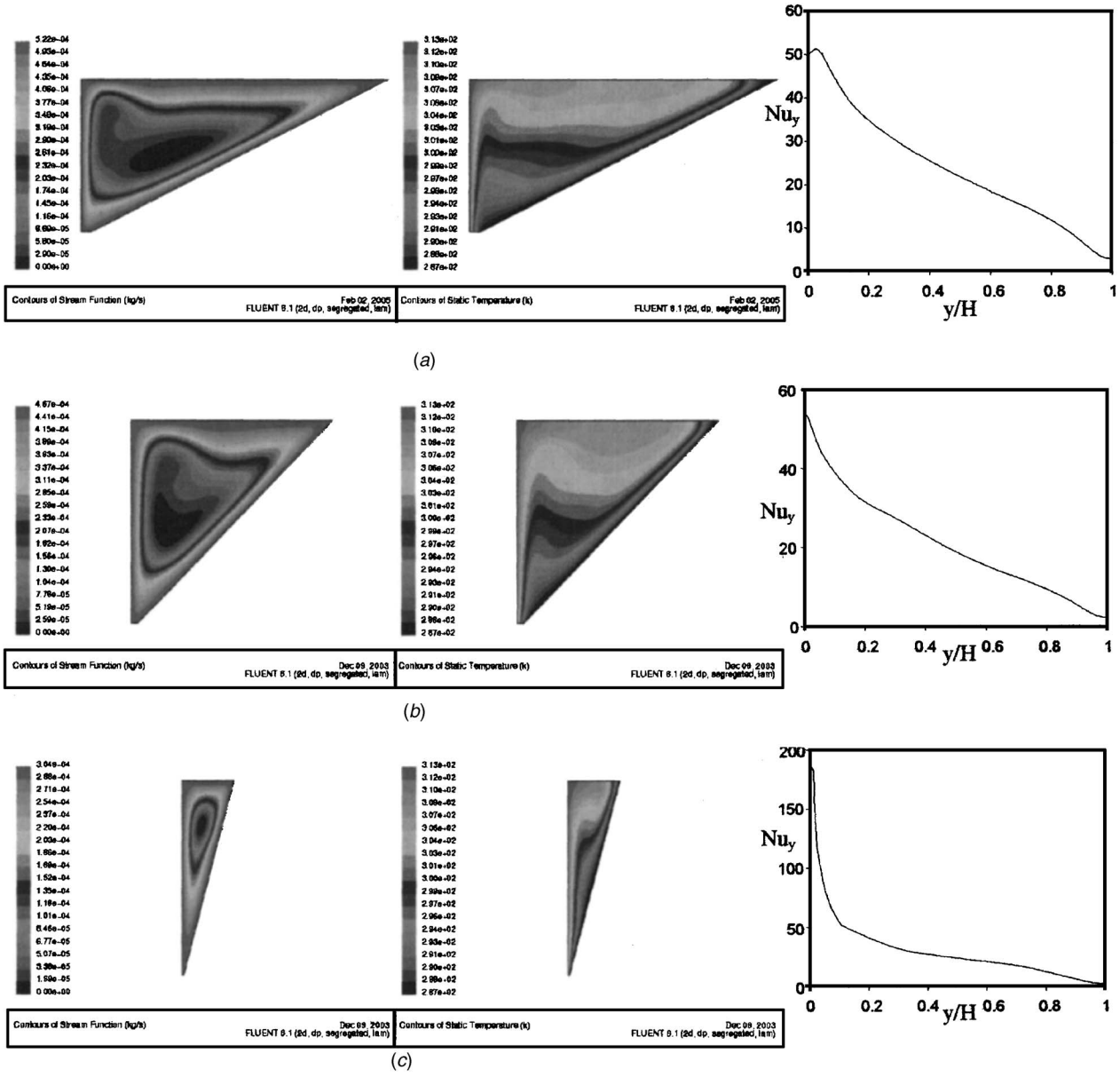

Fig. 3 Plots of stream functions, isotherms and local Nusselt numbers Nu_y for three different apex angles α=63°, 45° and 15° sharing a large $Ra_H=10^6$

figure indicated that the agreement between the numerical and experimental air temperatures at the three locations is acceptable. Overall, the matching between the numerical predictions of local temperatures and the experimental measurements of [13] tends to improve for the smaller upright cavity. Table 1 summarizes the comparison between the computed $\overline{Nu}_H$ and the $\overline{Nu}_H$ measured by Elicer-Cortés et al. [12] for the three apex angles α=5°, 10° and 15°. The level of matching is considered reasonable because the relative errors for $\overline{Nu}_H$ are located within a narrow band of 11%. Thereby, this kind of concordance lends credibility to the numerical computations to be used in computer-aided designs of upright triangular cavities.

The height-based mean Nusselt number $\overline{Nu}_H$ depends on two independent quantities, namely the apex angle α (a geometric quantity) and the Rayleigh number Ra_H (a thermo-geometric quantity). Correspondingly, the variability of $\overline{Nu}_H$ gives rise to a double-valued function $\overline{Nu}_H=f(\alpha, Ra_H)$ that generates a $\overline{Nu}_H$ surface. For purposes of visualization, it may be convenient to de-

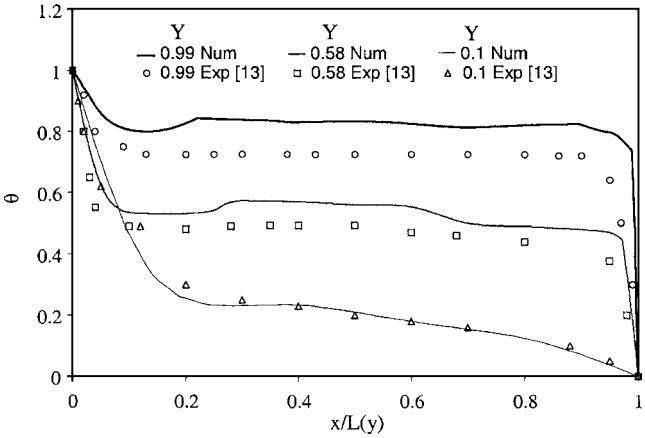

Fig. 4 Comparison between the numerical and experimental temperature profiles at three different elevations for a 15° triangular cavity

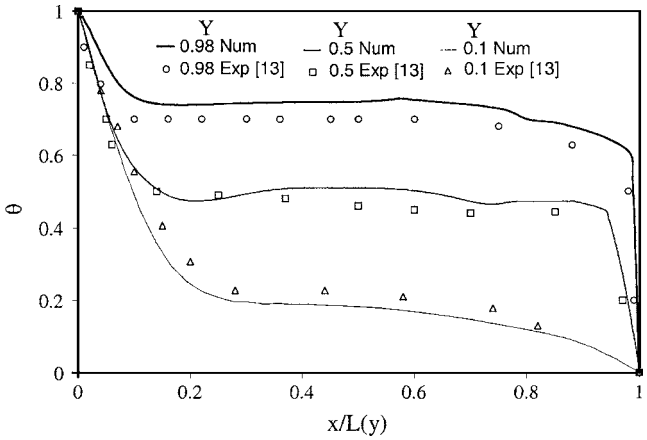

Fig. 5 Comparison between the numerical and experimental dimensionless temperature profiles at three different elevations for a 10° triangular cavity

couple the $\overline{Nu}_H$ surface into an equivalent family of $\overline{Nu}_H$ curves changing with Ra_H while retaining α as a parameter. This is shown in Fig. 6. For comparison purposes, the lowermost $\overline{Nu}_H$ curve representative of the 63° cavity constitutes the natural base line case in this study. When the apex angle is reduced to $\alpha = 45°$ the $\overline{Nu}_H$ curve moves up slightly but remains almost parallel to the $\overline{Nu}_H$ curve related to the 63° cavity as long as $Ra_H \leq 10^5$. However, above $Ra_H = 10^5$, the separation between both curves shrinks and the two curves eventually coincide at $Ra_H = 10^6$. Quantitatively, the $\overline{Nu}_H$ deviations, $\Delta\overline{Nu}_H$, amount to 1.5 units for the low $Ra_H = 10^3$ and to 1 unit for a high $Ra_H = 10^5$. These two numbers are referred to the values of $\overline{Nu}_H$ correlative to the 63° cavity. When the 45° cavity is cut diagonally in three equal apex angles, the leftmost wedge gives rise to a slim 15° cavity. For this specific geometry, the increments in $\overline{Nu}_H$ show remarkable gains. For instance, when $Ra_H = 10^3$, $\overline{Nu}_H$ raises from about 4.5 to 13.5, a threefold factor. Since the $\overline{Nu}_H$ curve for 15° flattens out in the vicinity of $Ra_H = 10^6$, it turns out that for $Ra_H = 10^6$, the $\overline{Nu}_H$ enlargement goes from 10.5 to 15.5—a modest factor of 1.5. For small and large Ra_H, the asymptotic slopes of the $\overline{Nu}_H$ curves increased with increments in the apex angle α; the increments are milder for low Ra_H. Moreover, it is worth mentioning that $\overline{Nu}_H$ for the 15° cavity is kept constant at a value of 13.5 for Ra_H up to 5×10^5. This number constitutes the critical Rayleigh number $Ra_{H,c}$, which is linked to the onset of natural convection currents. Conversely, this aspect is also a reassurance that the transfer of heat occurs by conduction whenever $Ra_H < 5 \times 10^5$.

Table 1 Comparison between the numerical and experimental mean Nusselt numbers $\overline{Nu}_H$ for different values of α and T_H

Angle α (Deg.)	T_H(°C)	$\overline{Nu}_H$ Num.	$\overline{Nu}_H$ Exp.
5	40	361.87	345.19
	60	373.99	342.10
	80	379.47	348.16
	100	369.30	341.19
10	40	334.60	300.58
	60	375.38	348.78
	80	368.69	347.25
	100	380.25	343.73
15	40	354.61	375.07
	60	387.35	392.35
	80	419.71	387.01
	100	420.12	393.21

Second, Fig. 7 portrays the other view of the $\overline{Nu}_H$ surfaces, namely a family of $\overline{Nu}_H$ curves changing with α being parameterized by Ra_H. All $\overline{Nu}_H$ curves exhibited monotonic decreasing behavior. As expected, for a fixed α, $\overline{Nu}_H$ gets energized with increments of Ra_H. The separation between two consecutive $\overline{Nu}_H$ curves increased gradually as Ra_H becomes intensified and α gets larger. Thus, the largest separation occurs between $Ra_H = 10^3$ and 10^6 at $\alpha = 63°$.

A non-linear multiple regression analysis was carried out with the collection of numerically data generated. Its outcome produced the predictive correlation equation

$$\overline{Nu}_H = 26.37 + 1.43 \times 10^{-5} Ra_H - 68.86\alpha - 1.28 \times 10^{-11} Ra_H^2 + 74.13\alpha^2 - 27.82\alpha^3 + 5.44 \times 10^{-6} \alpha Ra_H \quad (8)$$

where α is expressed in radians. The nearly perfect R-square value of 99.4% means that 99.4% of the variability in $\overline{Nu}_H$ caused by changes in α and Ra_H can be explained by the six predictor variables in Eq. (8). The range of validity of Eq. (8) is $5° \leq \alpha \leq 63°$ and $10^3 \leq Ra_H \leq 10^6$. The maximum error between the numerical and predicted $\overline{Nu}_H$ is less than 12%.

The two primordial goals in packaging engineering using cavities for natural convection cooling may be enunciated as follows: (1) to transfer large amounts of heat across the cavities and (2) the placement of the cavities in reduced spaces. To fulfill these two

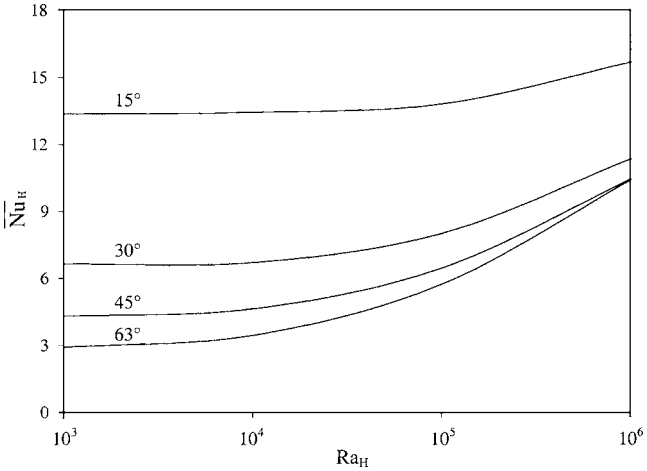

Fig. 6 Variation of the mean Nusselt number $\overline{Nu}_H$ with the Rayleigh number Ra_H parameterized by the apex angle α

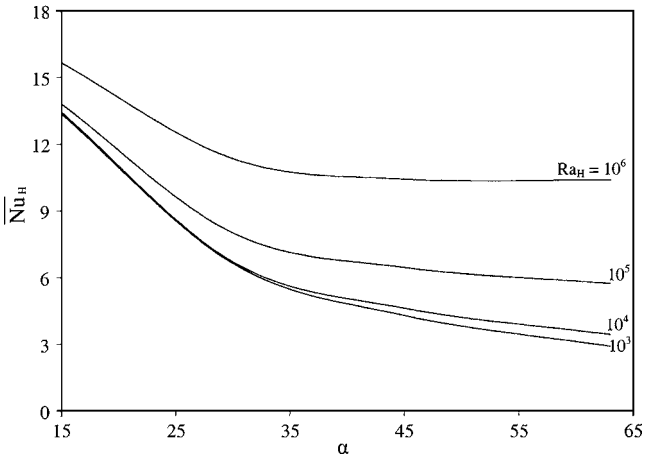

Fig. 7 Variation of the mean Nusselt number $\overline{Nu}_H$ with the apex angle α parameterized by the Rayleigh number Ra_H

Table 2 Relationship between the mean convective coefficient $\bar{h}$, the cross section area A and the Rayleigh number Ra_H

Ra_H	$\overline{Nu}_H/A$			
	63°	45°	30°	15°
10^3	2.91	8.45	22.57	49.86
10^4	3.45	9.08	22.81	50.16
10^5	5.73	12.67	27.23	51.54
10^6	10.55	20.49	38.59	58.45

goals concurrently, we proposed a figure of merit forming a ratio between the $\overline{Nu}_H$ and the cross sectional area A of the cavity. Table 2 lists the corresponding numbers for all combinations of apex angles α and Rayleigh numbers Ra_H utilized in this work. First, for a low $Ra_H=10^3$, the $\overline{Nu}_H/A$ ratio jumps from 2.91 to 8.45 between the 63° cavity and a 45° cavity; this action translates into a factor of 3. Moreover, the $\overline{Nu}_H/A$ ratio jumps from 2.91 to 49.86 between the 63° cavity and a 15° cavity, a factor of 17. When Ra_H is enlarged to 10^6, the $\overline{Nu}_H/A$ ratio jumps from 10.55 to 20.49 between the 63° cavity and the 45° cavity, a factor of almost 2. In addition, the $\overline{Nu}_H/A$ ratio leaps from 10.55 to 58.45 between the 63° cavity and a 15° cavity, a factor of 5.5. Given this thermo-geometric background, it may be concluded that within the spectrum of apex angles and Ra_H numbers tested, the heat transfer enhancement gets accentuated when both the apex angle α and the height-based Rayleigh number Ra_H diminishes. In other words, this statement is synonymous with conduction-dominant cavities. This condensed information channeled through $\overline{Nu}_H/A$ may be useful to engineers engaged in thermal design optimization.

Acknowledgments

The authors are appreciative of the help received from Mathew McGarry during the early phase of the investigation.

Nomenclature

a = thermal diffusivity
A = cross sectional area of cavity
g = acceleration of gravity
$\bar{h}$ = mean convective coefficient
H = height of vertical wall
L = length of horizontal wall
k = thermal conductivity
Nu_y = local Nusselt number, hy/k
$\overline{Nu}_H$ = mean Nusselt number, $\bar{h}H/k$
p = pressure
q_w = local wall heat flux
$\bar{q}_w$ = mean wall heat flux
R = gas constant
Ra_H = Rayleigh number, $g\beta(T_H-T_C)H^3/av$
T = temperature
u,v = velocities in the x- and y- directions
x,y = horizontal and vertical coordinates

Greek Letters

α = apex angle
β = volumetric thermal expansion coefficient
v = kinematic viscosity
θ = dimensionless temperature, $(T-T_C)/(T_H-T_C)$
ρ = density

Subscripts

x = derivative with respect to x
y = derivative with respect to y

References

[1] Raithby, G. D., and Hollands, K. G. T., 1998, *Handbook of Heat Transfer*, 3rd. ed., Mc-Graw–Hill, New York, Chap. 4.
[2] Jaluria, Y., 2003, *Heat Transfer Handbook*, Wiley, New York, Chap. 7.
[3] Oktay, S., 1982, "Departure from Natural Convection in Low Temperature Boiling Heat Transfer in Cooling Microelectronic LSI Devices," *Proc. Int. Heat Transfer Conference*, Paper No. PB 17, pp. 113–118.
[4] Simons, R. E., Antonnetti, V. W., Nakayawa, W., and Oktay, S., 1997, *Microelectronics Packaging Handbook*, 2nd. ed., pp. 1–315 to 1–403, Chapman and Hall, New York.
[5] Bar-Cohen, A., Watwe, A. A., and Prasher, R. S., 2003, *Heat Transfer Handbook*, Wiley, New York, Chap. 13.
[6] Akinsete, V. A., and Coleman, T. A., 1982, "Heat Transfer by Steady Laminar Free Convection in Triangular Enclosures," Int. J. Heat Mass Transfer, **25**, pp. 991–998.
[7] Poulikakos, D., and Bejan, A., 1983, "The Fluid Mechanics of an Attic Space," J. Fluid Mech., **131**, pp. 251–269.
[8] Karyakin, Y. E., Sokovishin, A., and Martynenko, O. G., 1988, "Transient Natural Convection in Triangular Enclosures," Int. J. Heat Mass Transfer, **31**, pp. 1759–1766.
[9] Salmun, H., 1995, "Convection Patterns in a Triangular Domain," Int. J. Heat Mass Transfer, **38**, pp. 351–362.
[10] Asan, H., and Namli, L., 2000, "Laminar Natural Convection in a Pitched Roof of Triangular Cross Section: Summer Day Boundary Condition," Energy Build., **33**, pp. 69–73.
[11] Haese, P. M., and Teubner, M. D., 2002, "Heat Exchange in an Attic Space," Int. J. Heat Mass Transfer, **45**, pp. 4925–4936.
[12] Elicer-Cortés, J. C., Kim-Son, D., and Coutanceau, J., 1990, "Transfert de Chaleur dans un Diedre a Geometrie Variable," Int. Comm. Heat Mass Transfer, **17**, pp. 759–769.
[13] Elicer-Cortés, J. C., and Kim-Son, D., 1993, "Natural Convection in a Dihedral Enclosure: Influence of the Angle and the Wall Temperatures on the Thermal Field," Exp. Heat Transfer, **6**, 205–213.